The Effect of scan speed on lack of fusion formation during electron beam melting of Ti-6Al-4V alloy and crack growth behaviour of the alloy under impact and fatigue loading

Mona Aziziderouei

A thesis submitted to Auckland University of Technology in fulfilment of the requirements for the degree of Doctor of Philosophy (PhD)

2018

School of Engineering, Computer and Mathematical Sciences

Auckland University of Technology

Abstract

Electron beam melting (EBM) is a powder-bed fusion additive manufacturing process suitable for fabricating metallic parts with a high degree of shape complexity, opening EBM's application potential with the Ti-6Al-4V alloy for biomedical and aerospace components. Due to the additive nature of part building track-by-track (TbT) and layer-by-layer (LbL), track size and track spacing coordination is required to coalesce tracks via overlapping and to prevent the formation of lack of fusion (LOF) for EBM to be efficient. To date, how Scan Speed (*v)* affects the morphology (size and shape) of the melt pool during EBM of Ti-6Al-4V has been insufficiently understood hence, this thesis opens with the expansion of knowledge on this.

Heat flow direction during EBM of Ti-6Al-4V contributes to the columnar growth of β (bcc) phase predominantly along the build direction (BD) during solidification. Subsequently, upon cooling, $\beta \rightarrow \alpha$ (hcp) + β in colony form takes place with α phase lining along the prior solidified β grain boundaries. Heat cycles imparted from TbT and LbL consolidation means transformation takes place multiple times. Thus, the microstructure formed during EBM is complex, with its influence on crack propagation under impact and fatigue loading yet to be sufficiently understood. This knowledge is important for microstructure control during EBM and for producing parts of satisfactory mechanical properties. Hence, understanding how EBM build orientation affects crack propagation under impact and fatigue loading are covered in the second and third part of this thesis respectively.

In the first series of EBM experiments, the speed function was decoupled so that *v* could vary from 5 to 18 m/s for constant beam current of 28 mA. Samples were then examined metallographically with defect levels measured and quantified. In the second part of experimental/testing work, impact test samples were built applying EBM conditions common for Ti-6Al-4V. Samples were made with notches orientated in 0, 45 and 90° to the EBM BD. After impact testing, the fracture surface and cross sections of test samples were analysed, and defect measurements were made. In the third part of experimental/testing/analytical work, fatigue crack growth (FCG) samples were built and machined with notch orientations also at 0, 45 and 90° to EBM BD. After FCG testing and obtaining the fatigue curves of crack increment per cycle (da/dN) versus the change of stress intensity factor (ΔK), fracture surface cross-sections were examined in detail with an emphasis on colony dependent crack growth.

A direct relationship between the LOF frequency and v has been established and will be explained in detail. It has been found that increasing v not only reduced the size of melt pool but also the stability of the shape of pool and that the reduction of melt pool size and shape stability resulted in insufficient overlapping, increasing the amount of LOF. Varying v is also found to impart a shape change of the melt pool, as well as influencing the height of the crown and depth of the melt pool. Explanation of the change of melt pool shape and size instability as a function of v is discussed in detail, including consideration of the Marangoni flow's effect on the melt pool through varying v.

Impact energy (IM) values of a range of samples have been found to vary widely from 26 J to 49J. The variation has been identified to be caused from two sources: BD dependent microstructure and batch dependent fraction of LOF. The dependence of IM on BD appears to originate from the mode of solidification during EBM. Cracks have been found to propagate through $\alpha + \beta$ colonies in vertically built samples with propagation barely affected by the α phase lining normal to the crack growth, along the prior β phase grain boundaries during columnar solidification. The effect of the α phase lining in samples built with other orientations on lowering IM will be shown and explained. The batch effect will be explained by LOF size variation in different batch and by LOF orientation which aids crack growth.

FCG tests showed similar behaviour in region II for all notch orientations, with exponential constants determined to be $m = 3.1$ and $C = 1 \times 10^{-8}$ mm/cycle. It will be shown that LOF in favourable orientation may affect crack growth but the low level of LOF at up to 1% has not contributed to an overall faster growth rate. The low level of porosity at 0.1% has affected crack growth little. It is also found that locally crack advancing in a specific orientation in a $\alpha+\beta$ colony and thus the striation orientation in one colony is different from another. The combined growth direction is then the same as the direction that the global crack front moves during crack growth. This crack growth feature is suggested to be the reason for the lack of the dependence of Paris law constants on notch/BD relationship.

In summary, the effect of v on LOF formation and on fraction of LOF area have been quantified, along with introducing Type 4 LOF. Two major factors that affect IM the most, which are BD and maximum LOF area, have been identified. Furthermore, it has been found that the fatigue crack growth region II is independent of LOF, porosity and BD. In addition, a significant role of β phase in $\alpha+\beta$ colonies has been revealed.

Acknowledgement

Contents

List of Figures

ix

Attestation of Authorship

I hereby declare that this submission is my own work and that, to the best of my knowledge and belief, it contains no material previously published or written by another person (except where explicitly defined in the acknowledgements), nor material which to a substantial extent has been submitted for the award of any other degree or diploma of a university or other institution of higher learning.

Auckland,   Signature

10/10/2018

List of Tables

Nomenclature

v	Scan Speed
β	(BCC) Phase
α	(HCP) Phase
BD	Build Direction
LOF	lack of fusion
EBM	Electron Beam Melting process
AM	Additive manufacturing process
SLM	Selective Laser Melting process
ΔK	Stress Intensity
da/dN	Crack growth rate
FCG	Fatigue Crack Growth
IM	Impact Energy
C	Fatigue Paris law constants
m	Fatigue Paris law constants
TbT	Track-by-Track
LbL	Layer-by-Layer
E	Energy Density
f_{LOF}	LOF area fraction
$F_{porosity}$	Porosity area fraction
GB	Grain Boundary
t	Powder layer thickness
h	Hatch Space
l	Beam Current

P	Beam Power
d	Depth of melt pool
W	Width of melt pool
a	The distance that the crack travels in one cycle of loading
ΔK_{th}	Fatigue Crack Threshold
K_C	Fracture Toughness (K_{IC})

1. CHAPTER. Introduction

1.1 Titanium and Titanium Alloys

Titanium (Ti) is the fourth most plentiful earth's crust element and is named in honour of the Titans of Greek mythology that first discovered by William Gregor in 1791 in Cornwall (U.K.) (Gerd Lütjering et al., 1998). Initially, it was extracted from ilmenite or black sands, however, its extraction cost was high limiting is an application. Through technological improvements harbouring low-cost Ti production, use of Titanium escalated in a wide range of applications, bringing its mechanical properties to the fore. Titanium is the centre of attention in many industries including aerospace and biomedical because of its outstanding combination of properties, which are rare for one element. Titanium offers high strength, low density (4.5 g/cm^3), and excellent corrosion resistance. Examples of its applications include; biomedical devices requiring corrosion resistance with high strength, and the demand for high strength, low density, and excellent creep resistance up to ~550°C in aero-engine components. In comparison with aluminium, titanium has a higher melting temperature of ~1670°C as compared to 660°C, making it more desirable for critical temperature applications, however, aluminium has a lower density. Titanium's density is 40% lower than that of steel and nickel-based superalloys making it one of the highest strength to density ratio elements (Donachie, 2000).

The mechanical properties of titanium and its alloys originate from their phase composition and structure. Titanium alloy classifications are based on the volume fraction of the phases at room temperature (Gerd Lütjering et al., 1998).

Titanium alloys are known to contain four phase categories; alpha (α), near-alpha (α), alpha-beta (α-β) and beta (β). The structure of commercial pure titanium (CP) consists of pure α -phase and through the addition of alloying elements the other microstructures are formed. The most popular and widely used commercially is Ti6Al4V by virtue of its ideal properties including; high strength, good toughness, heat treatability, excellent corrosion resistance and low thermal expansion rate (Balasubramanian et al., 2011; Facchini et al., 2010; Ritchie et al., 1999; Yunlian, Ju, Quan et al., 2000). Stabilising the α-phase in Ti6Al4V is achieved primarily through the use of the Al alloying element. The shortcoming of α-phase alloys is that they are single-phase alloys, preventing the use of heat treatment to improve mechanical properties. Two phase alloys facilitate phase transformation and refinement. In this situation, some β-phase is retained at low

temperatures. The advantage of α-β alloys if heat treated appropriately is a great combination of strength and ductility, stronger than either α or β alloy grades. The β-phase alloys are known as metastable as they have a tendency to transform into other phases (Donachie, 2000).

1.2   Ti6Al4V and phase transformation

The attractive properties of Ti6Al4V to the aerospace and biomedical industries, including its high strength and corrosion resistance are directly influenced by the microstructure and to a greater extent, the processing conditions and thermal treatment conditions.

Ti6Al4V is a dual-phase α+β alloy in which an equilibrium microstructure occurs at a mixture of both α and β phases, with microstructural variations resulting from differences in its time-temperature history. As the name implies, Ti6Al4V has two major alloying elements, the α-phase (hcp) stabilising aluminium (Al) and β-phase (bcc) stabilising vanadium (V). Therefore, by increasing the content of Al in the alloy, the α-phase will become more stable at higher temperatures conversely, β-phase is more stable at lower temperatures by increasing V content in the alloy.

The equilibrium microstructure of Ti6Al4V contains a combination of α and β phases at room temperature. In equilibrium, the α-phase dominates with β-phase retained in the microstructure in a small fraction. Microstructural differences at room temperature are highly dependent on the cooling rate and heat treatment history of the alloy. At slow cooling rates less than ~100°C/min, the Ti6Al4V alloy liquid at a melting point of ~1670° begins cooling until temperature reaches the β transus temperature ~995°C. With the β transus temperature defined as the temperature at which β phase begins the transformation into primary α phases, as shown in Figure 1-1 (Donachie, 2000).

2
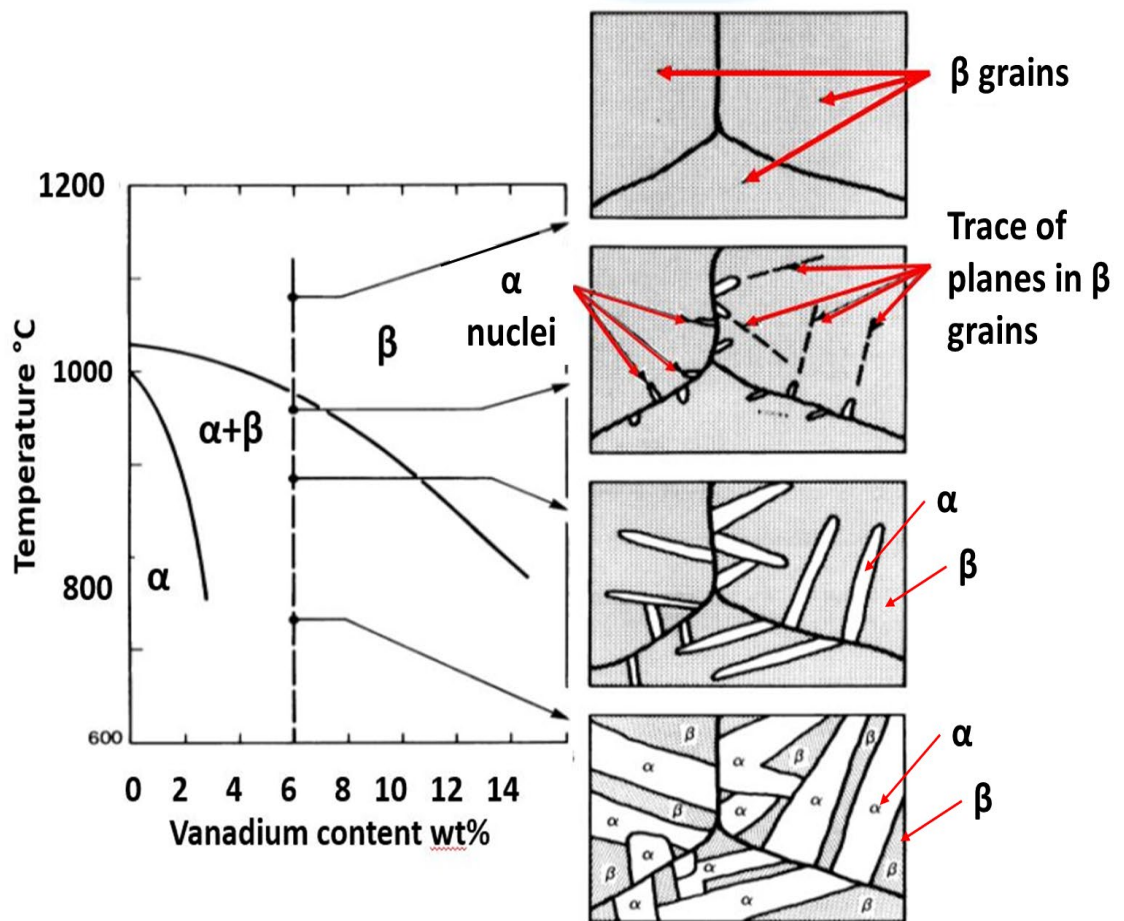
Figure 1-1 Illustration of the transformation process of α-β Ti6Al4V alloy showing α formation in the β matrix. (Donachie, 2000).

During the continuous cooling process, α-phase nucleates either at the interface of existing α platelets or at β grain boundaries, with growth propagating parallel to each other based on Burgers relationship which is known as an α colony. The growth of α colonies continues from grain boundaries until they meet each other. The retained β matrix separates each α plate from one another in an α colony. The α and β plates are known as α and β lamellae with the resulting microstructure known as lamellar as presented in Figure 1-2. The transformation of two phases from bcc β to hcp α follows the Burgers crystallographic relationship of (110) β ∥ (0002) α and [111] β ∥ [1120] α, through which the bcc crystal can transform to hcp crystal in twelve different orientations (Gerd Lütjering et al., 1998).
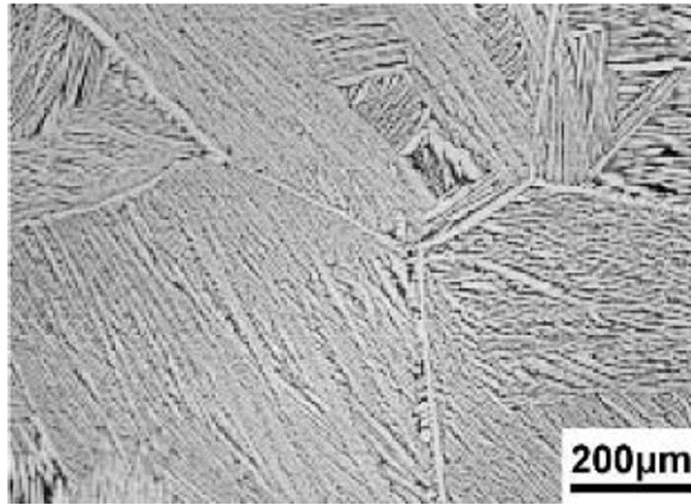
Figure 1-2 Optical micrograph showing lamellar structure formation of α+β Titanium alloy at a slow cooling rate (Semiatin et al., 2001)

As the cooling rate increases, the α-phase sizes and α colonies decrease, with the existing colonies at β grain boundaries unable to fill the inside of the grains completely, facilitating new colony nucleation at the boundaries of existing colonies. In order to minimise the total elastic strain, the new α plates nucleate on the existing α plates almost perpendicularly by point interaction. The number of α plates inside the colonies is smaller than lamellar structures. This type of nucleation and growth mechanism is known as basket weave or Widmanstätten structure (Gerd Lütjering et al., 1998). An example of the Widmanstätten structure produced in two different methods is presented in Figure 1-3. The light grey shows the needle like β phase and dark grey α plates and α boundaries.
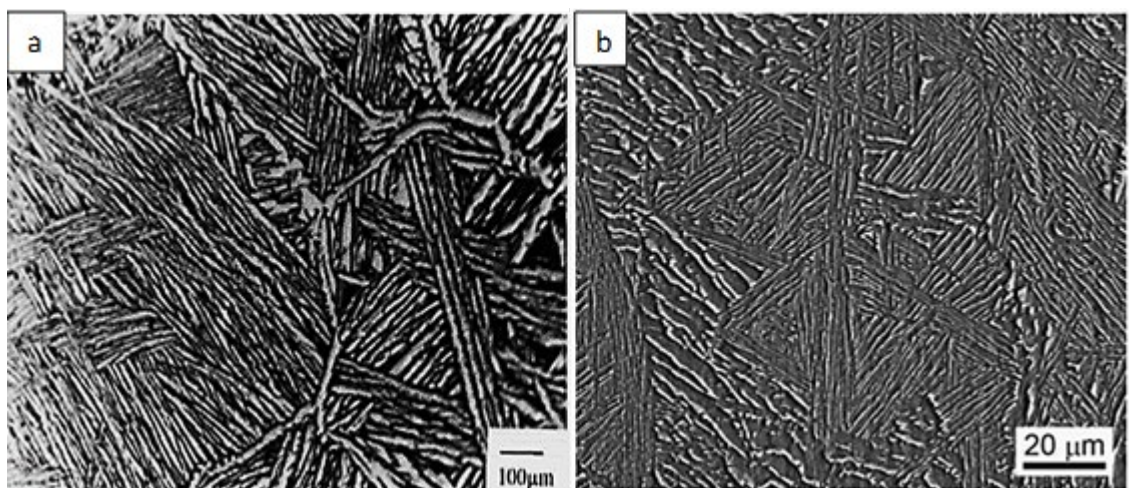
Figure 1-3 Widmanstätten microstructure of Ti6Al4V alloy a) of 0.81°C/s cooling rate (Gil et al., 2001) and b) produced via EBM (Rafi et al., 2013).

As the cooling rate increases, the nucleation rate of α phase on the β phase grain boundaries increases accordingly. This increase leads to faster growth of α plates into the β grains, all the while the diffusion process in the α phase decreases. At even greater cooling rates smaller and thinner α plates form, thereby concluding that the width and length of α platelets are dependent on cooling rate. At an extreme cooling rate (more than ~1000°C/min), α phase does not have enough time to grow during solidification and instead of α-phase nucleation, ά-phase known as martensite nucleates and grows. At these cooling rates the ά phase is so fine as compared to the α-phase hence, at rapid cooling rates there is ά phase with limited retained β phase (Donachie, 2000).

1.3 Electron Beam Melting (EBM) Process

Ti6Al4V alloy fabricated by AM has been used widely in many fields such as biomedical, aircraft and aerospace industries due to a great combination of high corrosion resistance and outstanding biocompatibility of Ti6Al4V and unique manufacturing technique of AM which combining these two material and method offer more opportunities for industries and markets in the long term of usage. It is also employed in other areas such as cameras, jewellery and sports equipment(Balasubramanian et al., 2011; Facchini et al., 2010; Ritchie et al., 1999; Yunlian et al., 2000). Despite this, the aerospace industry is still the largest user of AM Ti6Al4V alloy, which is required high strength, high and low cycle fatigue.

EBM is one of the most commercially popular additive manufacturing processes, attracting the attention of many industries. The EBM machine specifications vary depending on the version however, they commonly have a maximum beam power between 3-3.5 KW with a Voltage of 60 KV, a beam diameter between ~0.1 - 0.4 mm and operate in a vacuum pressure of 10^{-4} - 10^{-5} mbar, with a maximum build size of 200 × 200 × 200 mm. The electron beam used to melt the metal powder is generated by a tungsten filament inside the electron gun which is heated to above 2000°C by the filament current, driving the flow of electrons out of the gun (Arcam AB, 2014; Tan et al., 2014). Through an applied voltage of 60 KV between the filament and the anode, the generated electrons are accelerated and are focused via electromagnetic lenses. These concentrated electrons are bent by deflection coils used to control the motion of electron beam on the platform. The focused electrons melt the powder particles, with the amount of the area on the powder bed surface that electron gun melts known as the spot size and is governed by the degree of focusing of the electromagnetic lenses (Tan et al., 2014). A small spot

size causes the electron to penetrate deeper with higher intensity thus, melting a deeper power layer. Conversely, a large spot size leads to a decrease in penetration (depth) but, with a larger molten area on the top surface (Cheng et al., 2013; Mladenov et al., 2016).
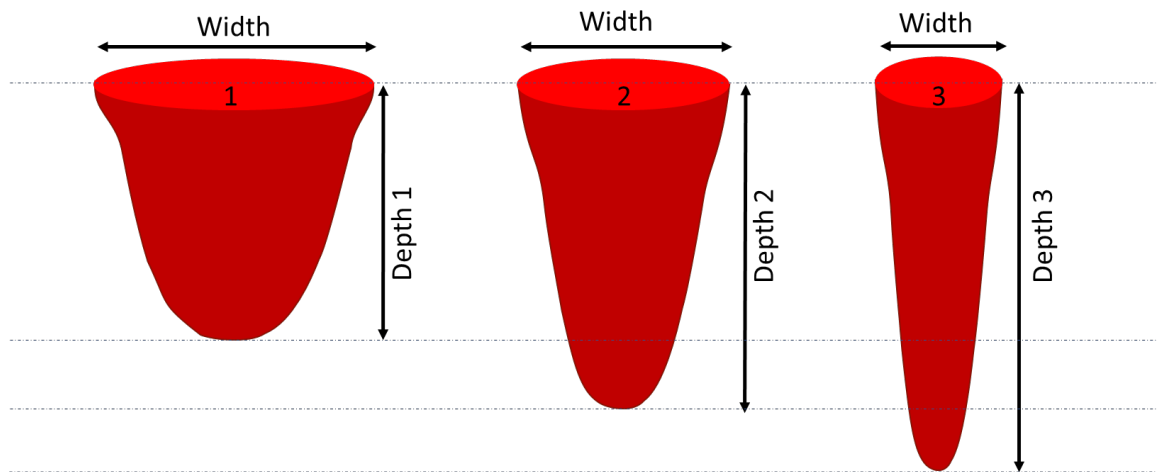
Figure 1-4 Schematic of a single melt pool (width = length) when spot size decreases from large diameter (1) to small diameter (3), the depth of penetration increases while the width decreases.

The spot size on the powder bed is controlled by the focus offset of the electron beam in the EBM process and is signified by the unit mA. A positive focus offset relates to the focusing point of the electron beam above the powder bed (defocused) with, a negative focus offset resulting in a focus point deep inside the powder bed (Al-Bermani, 2011). Electrons strike the exposed powder particles which, absorb the electron energy inducing melting by virtue of the temperature increase, higher than the melting point of the powder particles and generating a half segmental molten metal pool. The molten pool thermo-capillary motion occurs as a result of the surface tension gradient from the centre of the electron beam recording the highest temperature with heat flow flowing to the melt pool boundary measuring a lower temperature. The turbulent flow in the molten area induced by the heat transfer mechanics causes phenomena such as splashing and moving molten liquid out of the melt pool area (Galati et al., 2018; Hebert, 2016). The characteristic teardrop melt pool shape evident in Figure 1-5 is due to the movement of the electron beam from one point to the next point (Wang et al., 2017).
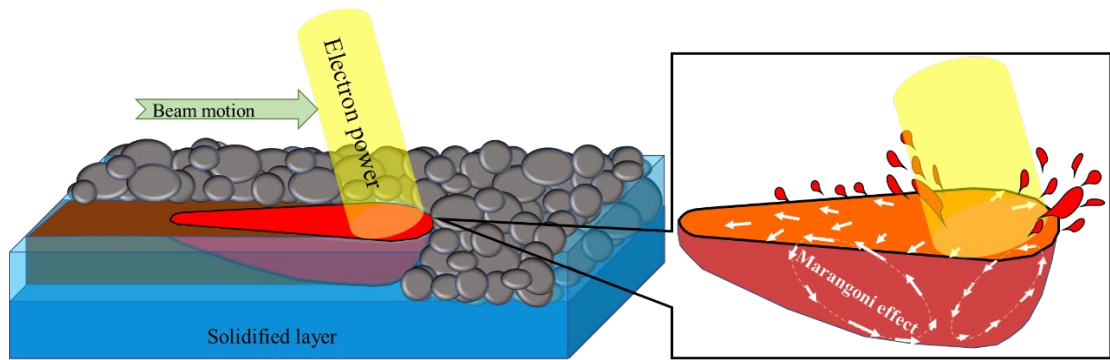
Figure 1-5 Schematic of the melt pool and mechanism of Marangoni effect during the melting process.

The EBM process consists of the formation of many layers on top of each other fused together producing a part. The steps used in EBM manufacture are presented in Figure 1-6 and described below. The process starts with 3D CAD data which is sliced into many layers of identical thickness (50, 70 or 100 μm). Each of these 2D layers is converted into the electron beam paths. In order to produce the first slice, a layer of powder particles is deposited by the rake system on the build-platform as seen in Figure 1-6a, which itself is connected to a vertical piston allowing it to move to build the layers. Prior to melting, the electron beam starts preheating by scanning over the powder layer with defocused beam to reduce the possibility of residual stress in part. Following the 2D image of the first slice, the electron beam starts scanning and melting the powders and generating the melt pools evident in Figure 1-6b. As the electron beam moves to the next spot, the temperature of the generated melt pool decreases from above melting temperature to room temperature solidifying as the heat is dissipated. After completing the first layer, the piston moves build-platform down equal to the thickness of the layer thickness and fresh powder is deposited on top of the solidified layer. In this subsequent layer, the electron gun starts scanning at a rotation of 67° about the previous path. This cycle is repeated by depositing a new layer on top of the last one following Figure 1-6c until part completion.
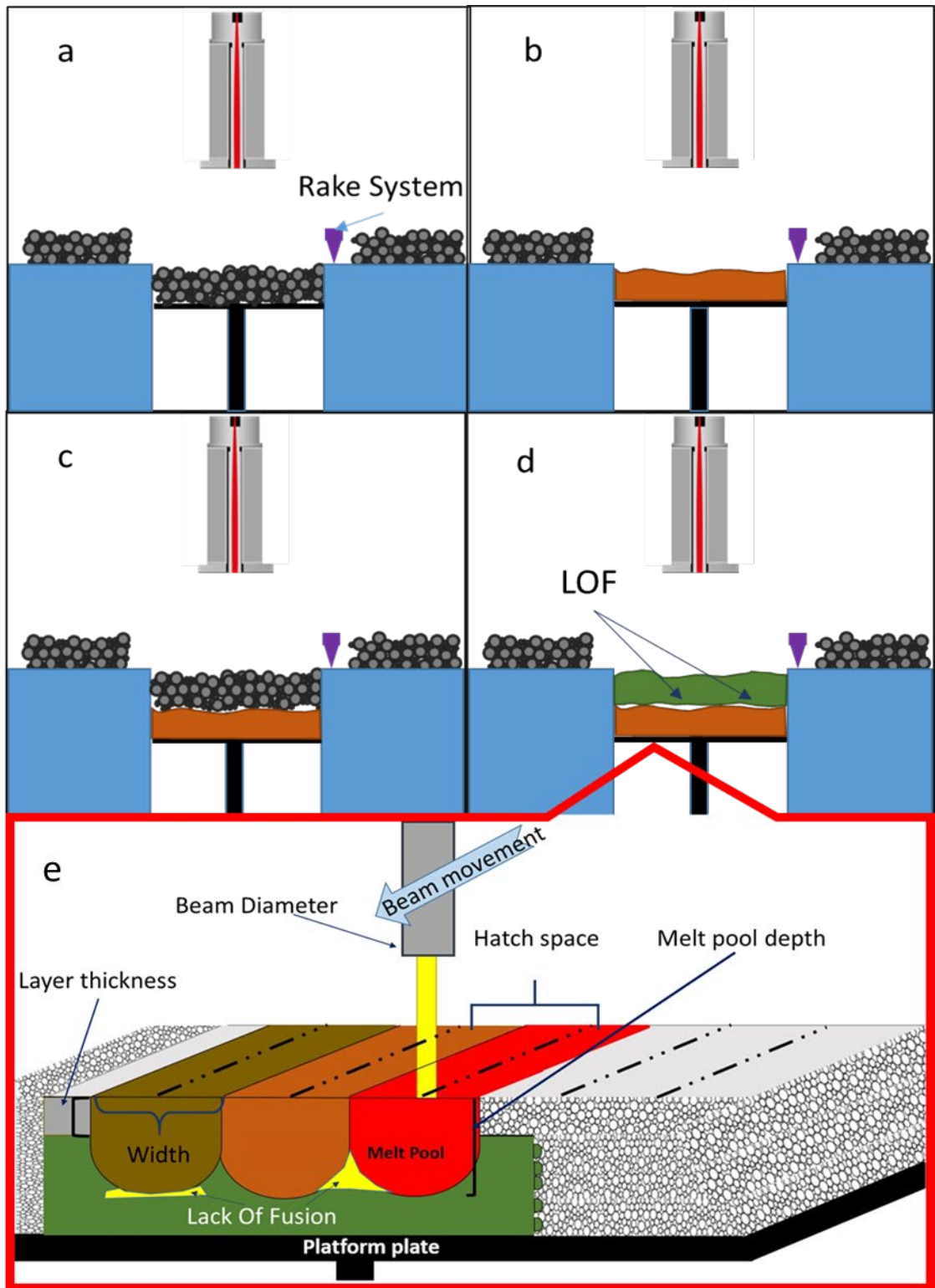
Figure 1-6 Illustration of EBM system in two layers and LOF formation during the process.

During the EBM process, the powder is spread on the platform uniformly and is influenced by the flowability of the powder including its; sphericity, packing density and compressibility (Arce, 2012; G. Lütjering, 1998). When the build process is finished, the

part is cooled using helium gas, increasing the cooling rate (Arcam AB, 2014; Svensson et al., 2009).

Each part is manufactured in two steps in the EBM process, the first consists of melting the outer part boundary known as the contour. The contour builds a fence between the accurate figure and the surrounding powder, providing a solid surface structure. The second step is melting inside the bordered part forming the bulk of the part and is referred to as the Hatching or Squares area (Murr et al., 2009). For the hatching area, there are two types of patterns used to produce each layer, the S-shaped scan line and a Z-shaped scan line as shown in Figure 1-7. In the S-shaped pattern, the beam moves from one side to the other, from that position the beam makes a U-turn starting a new line to melt. While in the Z-shaped scan the beam melts from one side to the other and after finishing one line, the beam returns to the beginning side to start a new line. Meaning that in a single layer, the beam starts only from one side of the layer (Ge et al., 2014; Tammas-Williams et al., 2015).

Build Direction

a) Z-Shaped scan line   **b) S-Shaped scan line**
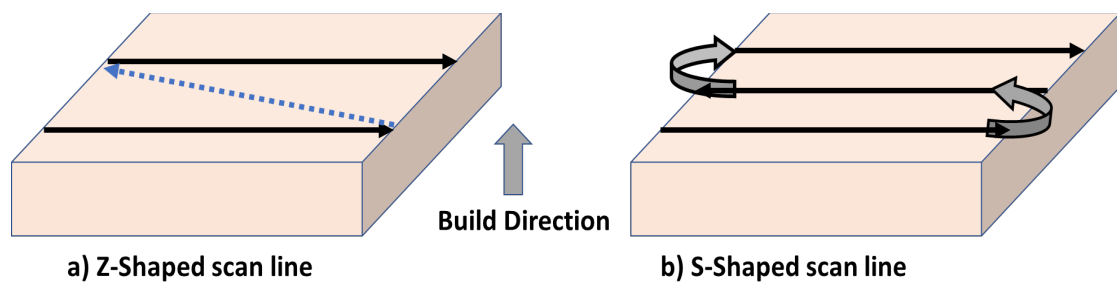
Figure 1-7 An illustration of typical scan patterns used in the EBM process

During the EBM process, some areas between layers are left unfused as shown in Figure 1-6d. Also, between two adjacent melt pools, some powder particles are left un-melted or partially melted because of incomplete overlapping of two adjacent melt pools as seen in Figure 1-6e. These un-melted or partially melted areas form a lack of fusion (LOF) causing a reduction in mechanical properties, such as toughness and fatigue, making LOF a critical factor in the quality of AM products. Melting powders depends on the amount of energy the electron gun produces and is commonly referred to as Energy density or Energy Input (E), with it playing an important role in powder-based AM processes (SLS, SLM and EBM). If the energy input is not sufficient enough to melt the powder completely, LOF will form in the melt (Karlsson et al., 2014; Rafi et al., 2013).

Energy input is affected by scan speed, beam power and the line offset between melt tracks, with each of these parameters represented as the Equation 1-1 below (Gerd Lütjering et al., 1998).

Equation 1-1

$$E = \frac{P}{\vartheta.h.t}$$

The energy input equation consists of electron power P (J/s), scan speed ϑ (m/s), hatch spacing h (m) and deposited powder layer thickness t (m). Power (P) is defined by Beam Current (I) and Electron Beam Voltage of 60KV (Cheng et al., 2014). Energy input is a result of focusing or defocusing of the electron beam which is called "Focus Offset (FO)" with the unit of mA. A positive value for focus offset gives the beam's focal point overhead the surface of deposited powders, and negative focus offset gives the opposite position (Al-Bermani, 2011). Energy input has an inverse relation with scan speed thus, through increasing scan speed the energy input decreases leading to defect formation during the EBM process. It should be mentioned that this equation is defined for SLM, which is a powder base and it is used for EBM as well (Thijs et al., 2010). There is a parameter known as a "Speed Function (SF)" index which controls the scan speed and beam current, however, in the latest versions of EBM machine such as Q10, there is a possibility of setting scan speed and beam current by switching speed function off. The range of SF which is usually used is from 20 to 65 (Cheng, Price, Gong, et al., 2014). The actual relationship between speed function and both, scan speed and beam current are not known outside of the machine manufacturer (Arcam co.) however, it is known that as long as the beam current is kept constant, the scan speed increases when the speed function is increased.

The powder bed AM technologies of EBM and SLM have a lot of similarities in technique and procedure to produce highly dense products however, there are some differences. The main difference between these processes is the heat source beam, which is a laser for SLM and electron beam for EBM. The second obvious difference is the processing atmosphere which in SLM is commonly Argon or Nitrogen gas however, the EBM process occurs within a vacuum system to decrease the possibility of powders reaction with oxygen at high temperatures (Muthu et al., 2016).

One of the significant advantages of using AM technique like EBM is a unique manufacturing technique fusing powder layer-by-layer to produce products with highly

precise geometries that traditional manufacturing techniques cannot achieve. Hence, EBM Ti6Al4V alloy products are widely used for replacing bones in the hip and joint, teeth in biomedical industries, blades of the jet engine and airframe for aircraft. Although AM shows great promise for manufacturing products with complex shapes, improving production speed and efficiency, the extensive investigations carried out by the researchers show that there are some limitations in the mechanical properties that lead to poor performance and shorter life in comparison with traditional techniques.

A minimum mechanical properties standard such as toughness, strength under cyclic loading and fatigue crack growth resistance are required in order to apply Ti6Al4V alloy components produced by EBM in biomedical and aerospace industries. Due to high aspect ratio of LOF, there is possibility of LOF/defects serving as a source of preferential crack propagation, unfavourably affecting the mechanical properties of EBM parts. Hence, a preliminary study was done to examine the effect of LOF on mechanical properties of EBM Ti6Al4V parts (Leuders et al., 2013; Levy et al., 2003).

1.4   The microstructure of Ti6Al4V alloy produced by EBM

Ti6Al4V processed via EBM is characterised by a Widmanstätten structure containing lamellar α phase and a small portion of β phase inside the prior β columnar grain boundaries which is the current α columnar grain boundaries. The α and β phases of differing sizes and orientations inside the columnar grain boundaries are orientated along the build direction. During the EBM process, the build chamber is kept at a temperature of 650-700°C, slowly cooling down after processing to room temperature facilitating α platelets growth (Rafi et al., 2013). This is evident in the cross-sectional optical micrograph Figure 1-8 as light grey α columnar grain boundaries. In Figure 1-8a, the light grey α platelets located inside the α colonies are shown with the build direction on the left bottom side. During the EBM process, the predominant downward direction of heat flow results in columnar growth of β (bcc) phase in Ti6Al4V along the build direction during solidification. Subsequently, upon cooling the phase transformation of $\beta \rightarrow \alpha$ (hcp) $+ \beta$ occurs, with α phase lining the prior β grain boundaries and β phase columnar grains transforming into colonies of $\alpha + \beta$.
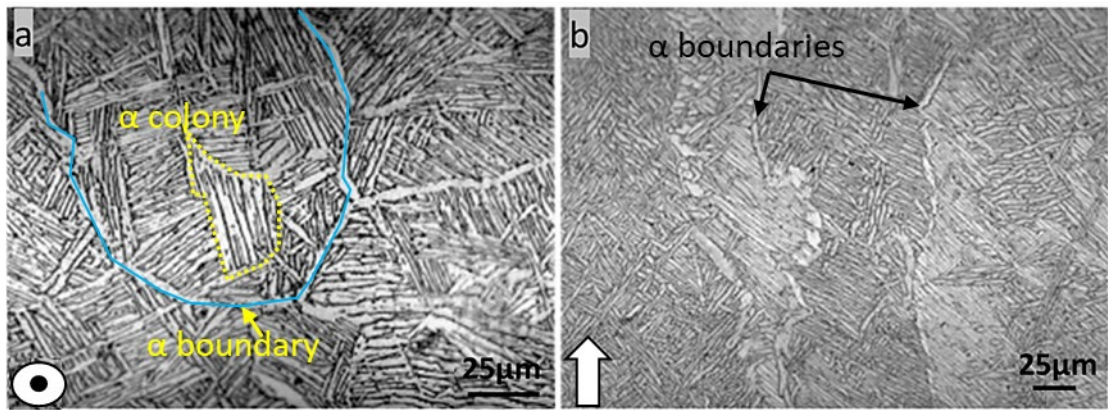
Figure 1-8 The optical micrograph of EBM produced Ti6Al4V alloy with the Widmanstätten structure, the light grey shows α phase and dark colour represents β phase, a) the α platelets inside the α colony b) the α grain boundaries (Rafi et al., 2013).

Some literature on EBM notes the formation of many porosities with an average size of 10μm and LOFs with lengths between 100 to 400μm, causing a considerable reduction in elongation (Karlsson et al., 2014; Mohammadhosseini et al., 2012; Svensson et al., 2009). The LOF forms due to the un-melted powder particles left between two adjacent melt pools which are because of insufficient heat input from the electron beam. The reason for low elongation values was reported to be due to the existence of defects like porosity and LOF (Karlsson et al., 2014). Examples of such LOF and porosity shapes are presented in Figure 1-9. The presence of LOF with having stress concentration areas at the corners of the LOF shape affects the mechanical properties of the samples dramatically.
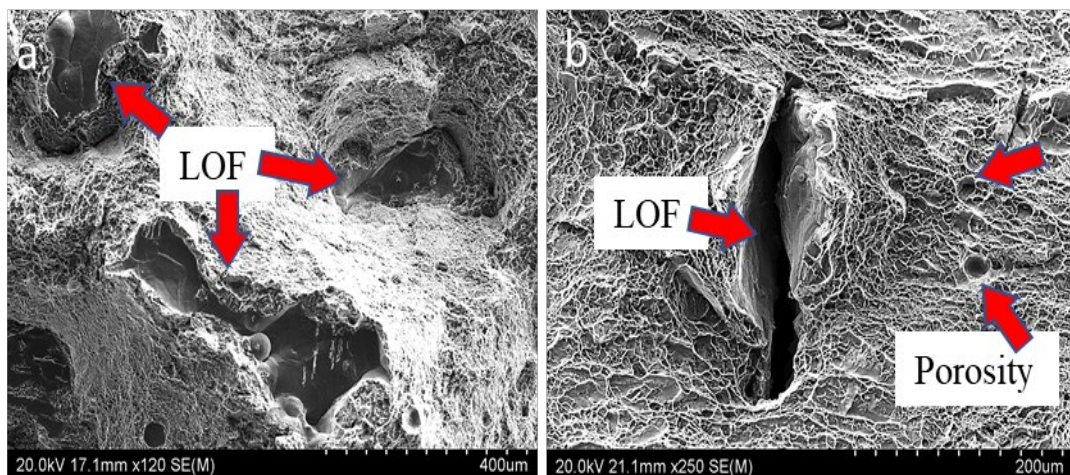
Figure 1-9 The SEM images of LOF and porosity with the different build directions, a) vertical, and b) horizontal.

Thus, the influence of LOF on mechanical properties become a more severe issue. There is a challenge how drastically LOF affect mechanical properties such as toughness and fatigue crack growth, which are a great challenge for the quality and performance of EBM products.

Ti6Al4V alloy produced by EBM contains many overlapping melt pools. Consequently, LOF formation relates to melt pools shape and their overlap as shown in Figure 1-10. Therefore, understanding the shape of the melt pool plays a crucial role in learning the formation of LOF.
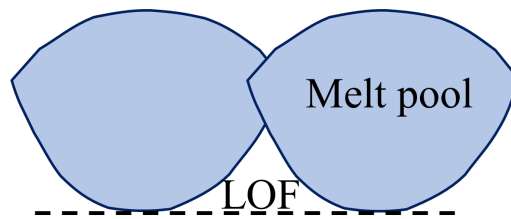
Figure 1-10 An illustration of two adjacent melt pool with LOF.

The prior discussion briefly introduced the importance of melt pool geometry effects on LOF formation in the EBM process. Therefore, it is crucial to study the melt pool geometry of the Ti6Al4V alloy and the influence of process parameters on its shape. The melt pool shape can be a great tool in understanding the LOF formation of this alloy. Further, due to the effect of LOF on mechanical properties, there is a requirement to study the relation between LOF and mechanical properties such as toughness and fatigue crack growth.

2. CHAPTER. Literature Review

This chapter attempts to explain 1) how the melt pool size and shape of Ti6Al4V alloy during the EBM process were identified, 2) how the process parameters affect the geometry of the melt pool, 3) how LOF forms in relation to the melt pool shape and process parameters, specifically the scan speed, and 4) the effect of scan speed on the microstructure and the top surface of the part. It also studies the effect of LOF on the mechanical properties of Ti6A14V alloy produced by EBM involved with a sudden load like impact energy and a cycling load like fatigue crack growth.

2.1 Melt pool geometry in EBM

In powder-based additive manufacturing (AM) like EBM, the built part is produced by several melt pools which are affected by the EBM process parameters. In order to understand and study the melt pool geometry, the effect of the EBM process parameters on the melt pool is crucial (Cheng et al., 2013; Soylemez et al., 2010). Some of the process parameters of EBM are scan speed, beam current, speed function and beam diameter (Murr et al., 2009).

Bo Cheng et al. investigated melt pool geometry by using thermal modelling of three process parameters, beam speed, power and beam diameter, and there is no observation on the actual sample. Figure 2-1 shows an illustration of a simulated modelling view (Cheng et al., 2013). A schematic drawing of melt pool geometry is provided for better understanding of length, width and depth as shown in Figure 2-2.
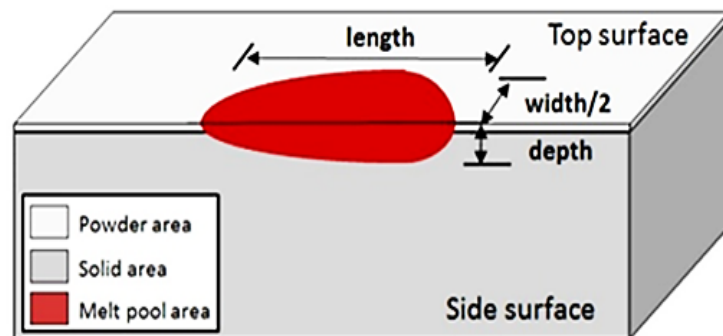
Figure 2-1 Schematic of the melting pool geometry of the simulated melt pool area (Cheng et al., 2013).
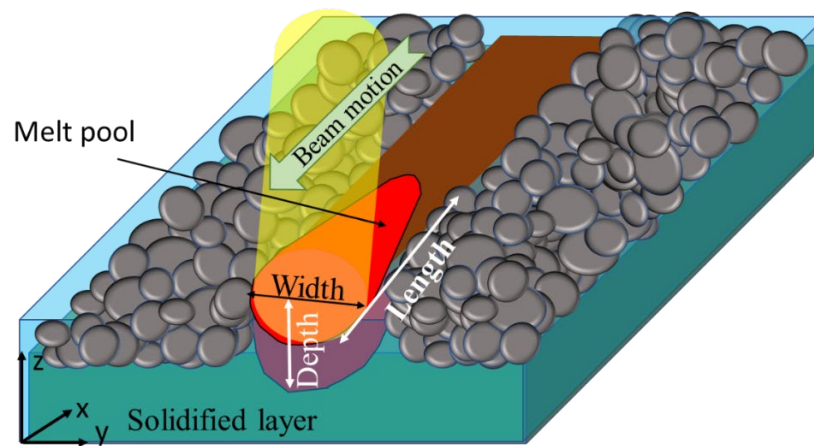
Figure 2-2 The schematic geometry of a melt pool in one beam pass.

During simulation, by increasing beam speed or scan speed from 100mm/s to 1000mm/s when power and beam diameter were kept constant (120W and 0.4mm respectively), the depth of the melt pool decreased from 0.2 to 0.1mm respectively. In this simulation study, the shape of the melt pool was assumed to be a half-ellipse. However, there was no explanation why this shape of the melt pool was suggested (Cheng et al., 2013). Soylemez et al. studied the relationship between length and depth of the melt pool with two thermal finite element simulation and experimental techniques. A disagreement was found between the numerical and experimental value of the melt pool size. The experimental value was higher than the value that the numerical method indicated. In addition, with a constant power, when the scan speed was increased from 0.004 to 0.007 and 0.014 m/s, the length to depth (L/d) ratio of the cross-section of the melt pool changed from 0.016 to 0.0132 and 0.0134. However, the actual length and depth of the base on the different scan speeds were not mentioned and explained. In addition, Hernandez-Nava et al. studied the influence of heat treatment on the microstructure above and below the β transus temperature with numerical and experimental methods. The depth of the melt pool was measured to be 176 μm in the numerical method and 148 mm the experimental method in one single beam pass. In both articles, Soylemez et al. and Hernandez-Nava et al. studied the melt pool size with two thermal finite element simulation and experimental techniques to maintain melt pool size (Hernández-Nava et al., 2016; Soylemez et al., 2010). However, numerical and experimental methods in both studies were done for a single bead, which cannot represent the melt pool shape of the EBM process because during production of a part, many adjacent melt pools are involved that may affect each other's shapes, and, also, the top surface should be considered as a part of the melt pool (Figure 2-3). In a one bead melt pool, there is no adjacent melt pool to understand if and how they affect each other. Besides, the condition of the scan speed on melt pool shape

is eliminated if, in reality, the scan speed factor exists. By eliminating the scan speed for revealing the shape of the melt pool, in fact the shape of the melt pool during producing a product is still unknown.
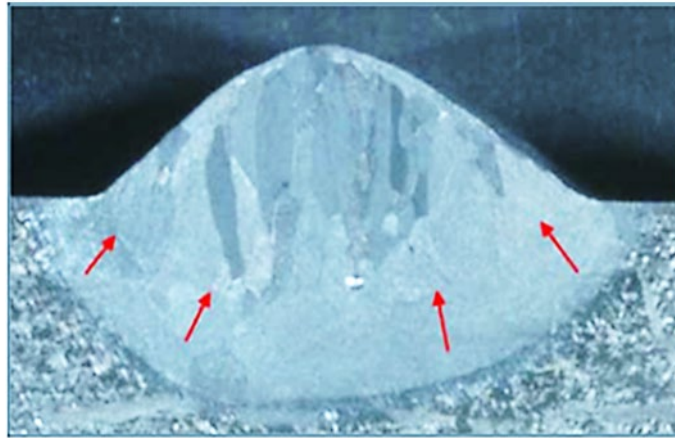
Figure 2-3 A cross-section of one bead and the arrows show the boundary of the re-melted substrate (Soylemez et al., 2010).

Bo Cheng et al., investigated EBM process parameters such as scan speed to analyse and measure melt pool size in two methods of simulation with ABAQUS software and measuring the build part surface temperature with a LumaSense MCS640 NIR camera during the EBM process (Cheng et al., 2014). By increasing scan speed from 481mm/s to 1595mm/s, the length of the melt pool decreased from 1.72mm to 1.26mm. Because at the high scan speed, there is less time for the electron beam to transfer the energy to the surrounding powder than for a slow scan speed, the amount of the melted powder at high scan speed is less than at the slow scan speed. It was explained that the higher scan speed induced the possibility of insufficient melting during the EBM process. By increasing scan speed, the length of the melt pool decreased from 2.35mm to 1.25mm. For scan speeds of 481 and 853mm/s, the width was 0.9mm while in 1193mm/s, and 1595mm/s, the width of the melt pool decreased to 0.8mm approximately. Therefore, by increasing scan speed from 481mm/s to 1595mm/s, the length decreased while the sensitivity of the width was not as much as the length. Although the dimensions of the melt pool were measured, the actual shape of the melt pool was still not clear.

As the melt pool forms, the heat transfer from the highest temperature to the lowest temperature provides a thermal gradient and consequently thermal flows are formed. These flows increase the heat transfer and this leads to a decrease in temperature inside the melt pool. Consequently, the thermal gradient increases even more. The surface

temperature distribution leads to turbulent flow which is the Marangoni phenomenon and the temperature distribution from the surface to the depth creates flotation forces. The Marangoni phenomenon in the melt pool leads to Rayleigh instability (Gusarov et al., 2007). Rayleigh instability makes the melt pools change into droplets, which is known as balling which causes a rough top surface (Attar, 2011). In another article, it was reported that the balling effect is produced by the high temperature difference between the melting and non-melting powder since the molten metal easily generates spheres because of surface tension. The higher the temperature gradient, the more the balling phenomena and instability happens (Galati et al., 2018). Kruth et al. investigated the effect of high thermal gradients and vaporisation on the balling effect. As reported, the low scan speed improves the balling effect with discontinuous melt pools in the samples (Kruth et al., 2004). Jamshidinia et al. investigated the effect of flow convection in temperature distribution and melt pool geometry via a 3D thermal-fluid flow model of EBM (Jamshidinia et al., 2013). The outward molten flow occurs as shown in Figure 2-4 due to the negative temperature coefficient of surface tension in the molten material which could affect the melt pool size and temperature distribution. The highest temperature in the centre of the melt pool, where the powder starts melting in one melt pool, has the lowest surface tension because molten material flows toward the edge of the melt pool where the surface tension has the highest level.
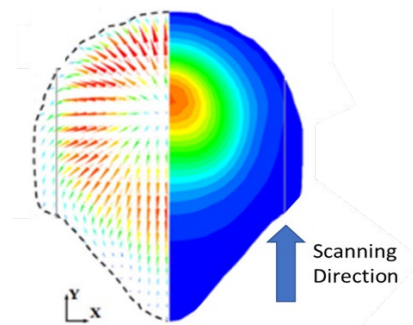
Figure 2-4 The model of the fluid convection patterns at the top view of the melt pool at 100mm/s scan speed and 14mA beam current of the electron beam moving direction (Jamshidinia et al., 2013).

Consequently, molten material flows from the center toward the edges of the melt pool area due to the Marangoni phenomenon. This two-sided overflow of the melt pool could cause a wider and narrow melt pool. When the electron beam is moving forward in one hatch line (beam moved away), the end of the teardrop shaped melt pool starts solidifying (Shrestha et al., 2017). Besides, some literature where the simulation method was used in

additive manufacturing techniques (EBM and SLM), has indicated the melt pool shape as a tear-drop (Cheng et al., 2014; Cunningham et al., 2016; Jamshidinia et al., 2013; Shrestha et al., 2017). During the melting process, the electron beam starts transferring the electrons to the selected powders to melt the selected area which has the highest temperature in the powder-bed. Thus, as the electron beam moves to the next adjacent area to melt the newly selected powders, the highest generated temperature points move along with the electron beam movement. As the electron beam makes a new melt pool, the previous melt pools become completely or semi-solidified. The electron beam movement pushes the molten liquid against the electron movement (opposite the direction of the electron beam movement), which generates ripples on each hatching line during the melting process. The ripple is a result of the solidification process in one shot of the beam gun and when the beam gun moves to melt the next spot (next melt pool), the end of the tear-drop-shaped melt pool starts solidifying (Parry et al., 2016; Zhou et al., 2015).

Narra et al. investigated the relationship between the width of prior β boundaries of Ti6Al4V alloy with melt pool size by changing the speed function index (Narra et al., 2015; Narra et al., 2018). Since speed function controls the scan speed and beam current, hence, by increasing the speed function from 7 to 130 when the rest of the process parameters were kept constant (including beam current), the scan speed increased. For each speed function, one single bead melt pool was formed and the cross-section of the melt pool parallel to the build direction was analysed. Analysis showed that by increasing the speed function, the melt pool size decreased as shown in Figure 2-5. Although the relationship between speed function and melt pool area is indicated, the length, width and the actual shape of the melt pools were not shown or explained for each speed function. No figures of the melt pools were given, and also, the method of measuring the melt pool area was not described.
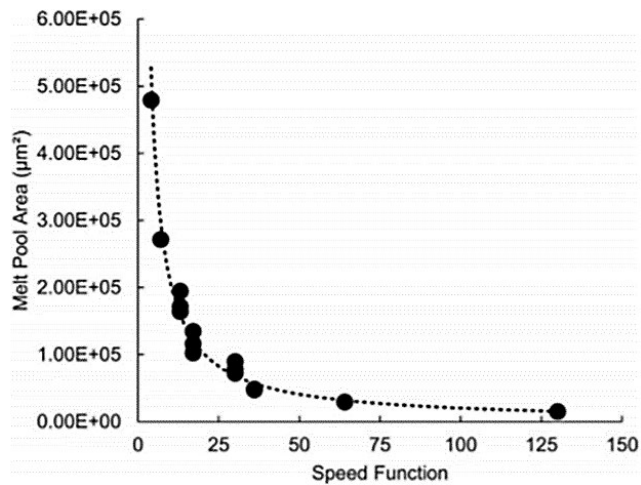
Figure 2-5 The relationship between cross-sectional area of melt pool and speed function (Narra et al., 2015, 2018).

Furthermore, in this work, the melt pool areas were measured and shown in Figure 2-6, however, the solidified melt pool has a crown which was not considered as melt pool area.
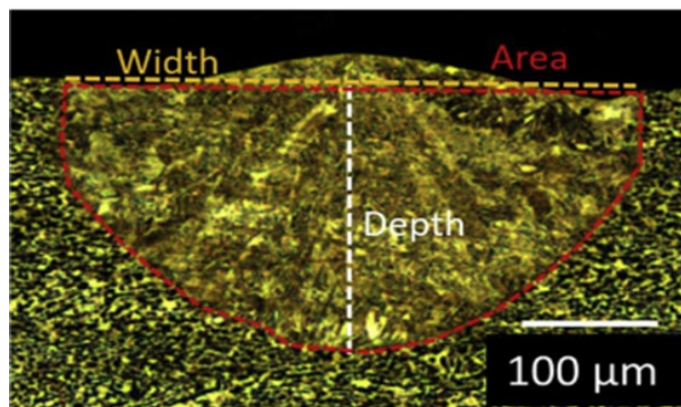
Figure 2-6 Micrograph of a single bead melt pool of Ti6Al4V alloy with the measured outlines (Narra et al., 2015, 2018).

Although was explained, by keeping all parameters constant, an increase in speed function means that the scan speed increased, it was not clear what each speed function corresponded to what value of the scan speed. Also, Mahale et al. explained that due to the difficulty in finding a relationship between the speed function number and the scan speed, by keeping all parameters constant, increasing speed function shows an increase in the scan speed (Mahale, 2009).

The melt pool geometries in other materials which were produced by the EBM process have been observed experimentally, as shown in Figure 2-7. Helmer et al. observed the melt pool shape in the nickel-based superalloy, Inconel 718, as shown in Figure 2-7a. The

observation of the line features on the optical image such as the width and depth of the melt pool on the top layer were measured and reported to be ~800μm and 250- 350μm respectively with a scan speed of 200mm/s. The half part of the melt pool that was vanished by the next melt pool was mirrored and the width of the melt pool was estimated; thus, the expected shape of the melt pool was measured (Helmer et al., 2014). Lodes et al. investigated the EBM process on pure copper whose thermal conductivity is too high, 60 times higher than Ti6Al4V, to compare the melt pool size with other materials, specially Ti6Al4V alloy (Lodes et al., 2015). Zhong et al. investigated the microstructure and mechanical properties of 316L stainless steel whose line-like features of the melt pools could be observed in the optical micrographs, however, the geometry of the melt pools was not mentioned and from the presented micrograph is difficult to measure (Figure 2-7b). Also, Körner studied the relationship between process features and grain structures in different materials of pure copper, Ti6Al4V in SLM and EBM processes (Körner, 2016). The pure copper melt pool was observed but the width, length and the depth were not measured. Even, from the presented optical micrograph, which is shown in Figure 2-7c, due to the melt pools overlapping, the width and depth of the melt pool cannot be measured. In Figure 2-7d, the micrograph of Ti6Al4V alloy shows that there is no sign of the shape of the melt pool. Liu et al. observed and showed a melt pool geometry in β-type Ti24Nb4Zr8Sn produced by Arcam A1 EBM with a thickness layer of 70μm and scan speed of 130mm/s (Y. J. Liu et al., 2016). The melt pool width and depth were 280 ± 23μm and 152 ± 15μm in SLM and 146 ± 17μm and ~172 ± 21μm in the EBM process respectively, which are shown in Figure 2-7e and Figure 2-7f. In these studies, it seems that the shape, length, width and depth of the melt pools for different materials are different. Most of the melt pool shapes of different materials were not measured or considered like Figure 2-6. In the studies that presented one bead of melt pool shape, the melt pool crown was not considered in the depth measurement. The melt pool has a crown on top, which is a part of the melt pool shape, and should be considered for presenting the melt pool. because each top melt pool is a base ground for the next powder layer. That is why the shape of the crown is critical as the bottom of the melt pool which was not considered in the mentioned studies.
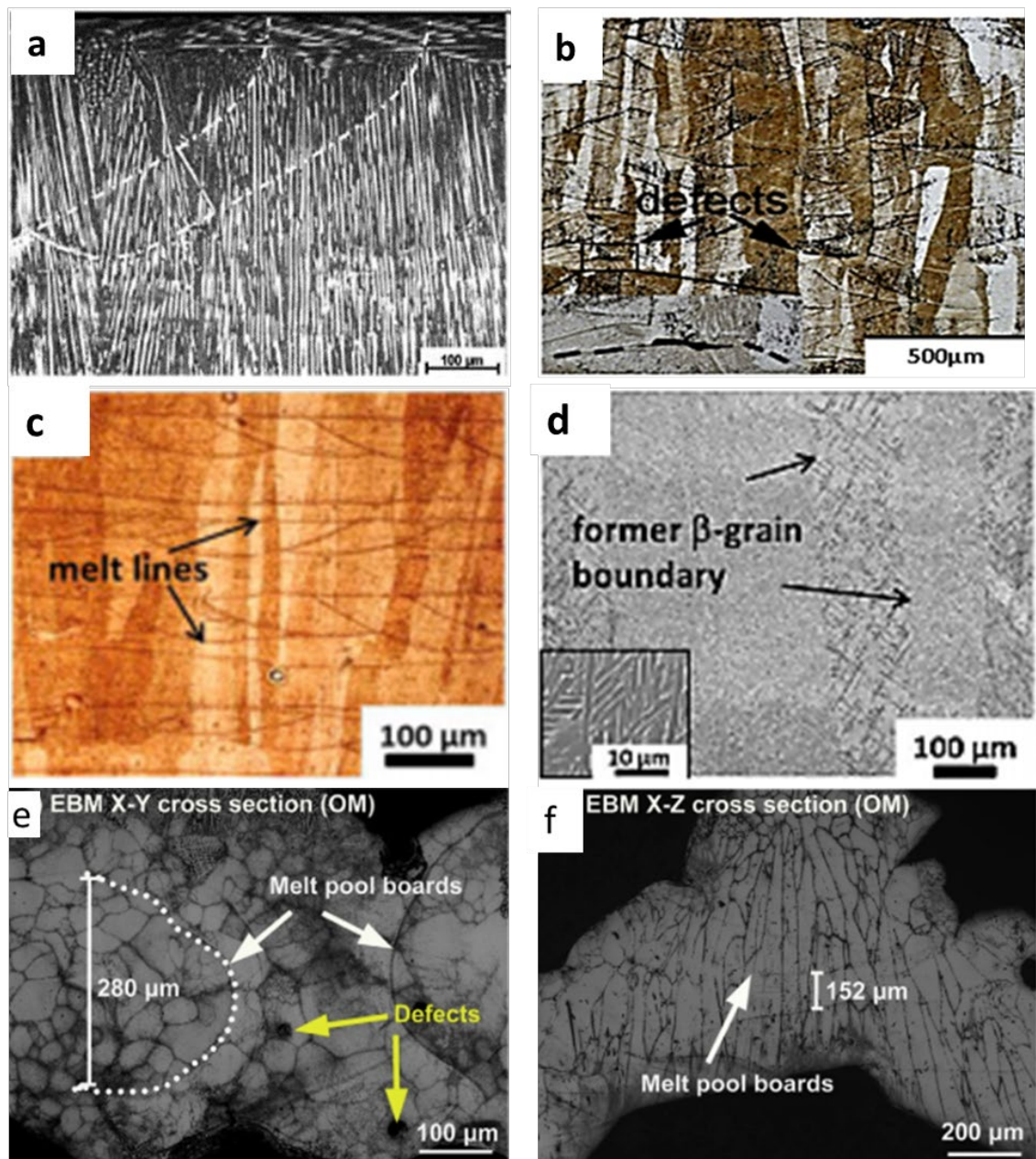
Figure 2-7 Optical micrographs of melt pool shape in different materials in EBM process: a) nickel-based superalloy Inconel 718 (Helmer et al., 2014), b) 316L stainless steel (Zhong et al., 2017), c) pure copper, d) Ti6Al4V (Körner, 2016), e) and f) β-type Ti24Nb4Zr8Sn (Y. J. Liu et al., 2016).

In addition, during the EBM process, Ti6Al4V alloy re-melted and re-solidified a couple of last solidified layers along with the new powder layer. Therefore, each solidified layer re-melt and re-solidified many times. Therefore, the microstructure became homogenised and made the melt pool boundary difficult to identify. By comparing the width and depth of the melt pools in different materials produced by EBM, the sizes are not similar or even close because every material has different heat loss and thermal conductivity properties. Therefore, Ti6Al4V melt pool geometry cannot be understood by comparing

with other materials' melt pool geometries. Consequently, it is important to identify the Ti6Al4V alloy melt pool shape experimentally.

2.2   Formation of Lack of Fusion (LOF)

When two adjacent melt pools overlap each other and during overlapping some un-melted or partially melted powder particles remain between them, LOF forms. If the molten metal fails to wet the previous solidified layer and adjacent melt pools, a gap between the new melt pool and the previous solidified materials produces LOF (Ek, 2014; Gong et al., 2013; Karlsson et al., 2014; Q. Liu et al., 2014; Svensson et al. 2009). Two neighbouring melt pools join each other by flowing one above the other and consequently some un-molten powder is trapped between the two melt pools, as shown in Figure 2-8 (Gong et al., 2013). In other words, LOF is a result of the effect of geometrical melt pool shape and lack of overlap between two adjacent melt pools or two layers that may cause some powders to be partially melted during the EBM process (Ek, 2014).
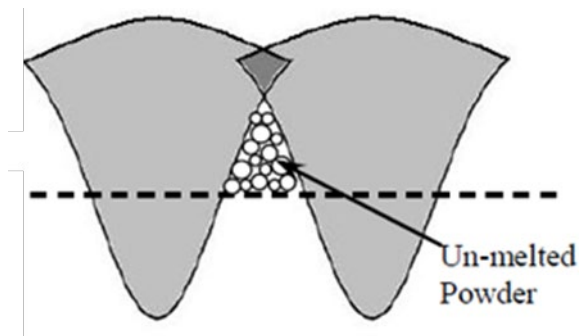
Figure 2-8 Illustration of defect formation between two adjacent melt pools (Gong et al., 2013).

In a recent publication by Williams et al., they identified the location, size, and shape of defects in samples using X-Ray Computed Tomography (XCT). However, the resolution of this device is only accurate for defects with larger than ~5µm in diameter (Tammas-Williams et al., 2015).
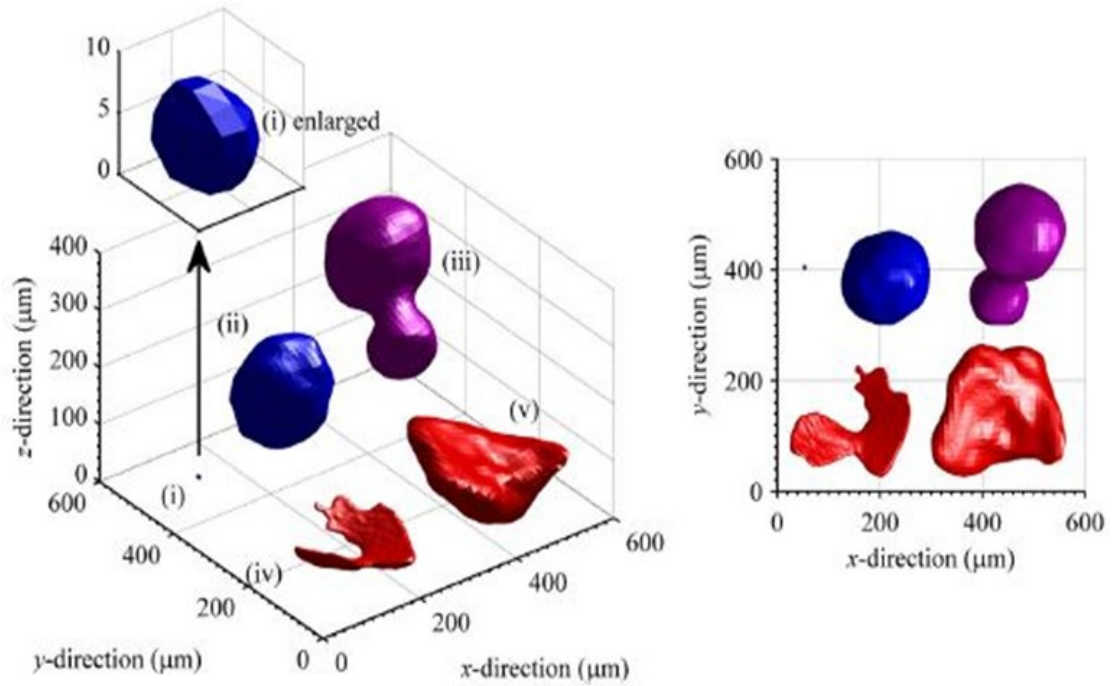
Figure 2-9 XCT image of different defect types; (i) and (ii) spherical pores, (iii) two joined spherical pores. (iv) and (v) two shapes of LOF (Tammas-Williams et al., 2015).

Different defect morphology images, that were taken by XCT are shown in Figure 2-9. In this figure, common spherical pores are shown by i and ii. It should be mentioned that pores and LOF that are shown in (i) and (iv) belonged to the centre of the sample which were so small they needed a high-resolution scan while the coarse pores (ii, iii and v) were detected with a lower resolution scan. In addition, in another study, which was done by Kristofer, LOF was observed (Ek, 2014). However, it was classified as a porosity. Despite observing defects, no further analysis for quantifying was done.

Tammas-Williams et al. stated that the length of LOF is usually found bigger than 100μm and spherical pores 10μm in the EBM process (Tammas-Williams et al., 2015). Ross Cunningham et al. quantified the volume fraction of pores by Synchrotron XCT, as a function of the melt pool shape (Cunningham et al., 2016). However, the melt pool geometry was employed from Narra et al.'s work (Narra et al., 2015).
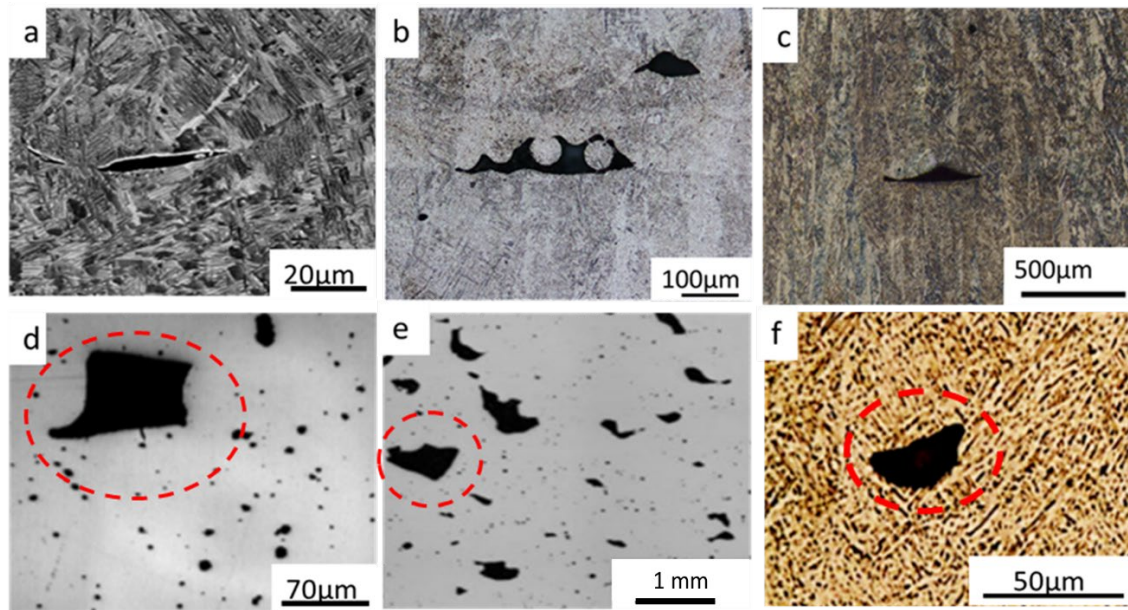
Figure 2-10 Various LOF shapes from a-e) literatures (Aboulkhair et al., 2014; Cunningham et al., 2016; Galarraga et al.2017) and f) preliminary study on LOF.

Different shapes of LOFs from some literature and preliminary study are shown in Figure 2-10. Most of the LOF shapes in Figure 2-10a-c can be attributed to the reasons mentioned in the literature, which are empty spaces, un-molten or partially molten powders left between two adjacent melt pools and discontinuities in fusing layers together (Cunningham et al., 2016; Gong et al., 2014; Gong et al., 2013; Léonard et al., 2012; Tammas-Williams et al., 2015). That means that the melt pool shape highly influences LOF formation but there is a lack of explanation of various LOF shapes in Figure 2-10d-f. Therefore, investigating the formation of all shapes of LOF is needed.

2.3 Effect of process parameters on formation of defect/LOF

During the EBM process, different process parameters could affect the generation of defects, specially LOF. Although EBM technology has been used commercially in industries, some of the process parameters such as scan speed affect the formation of defects, specially LOF, which may have an influence on the performance of EBM products (Cheng et al., 2014; Zäh et al., 2010). In first versions of EBM machines such as Arcam S400, there is no possibility of changing the scan speed in the EBM machine. Scan speed is set automatically by the speed function, which controls scan speed and beam current during the EBM process. Therefore, for changing the speed function and keeping other process parameters constant, the scan speed increases during producing a part in the EBM machine (Al-Bermani, 2011; Gong, 2013). However, in recent versions

such as Q10, the scan speed can be altered. Furthermore, it was stated that the formation of a defect has a direct relation to value of energy input. Energy input could be changed due to change of some or one of the process parameters like scan speed in Equation 1-1. Therefore, when energy input is insufficient, powders melt partially so defects are generated.

Puebla et al. investigated the influence of scan speed on porosity formation in two build directions of vertical and horizontal (Puebla et al., 2012). It was reported that by increasing the scan speed from 100mm/s to 1000mm/s, the amount of porosity increased as a result of incomplete molten powders in a deposited layer of the EBM process as shown in Figure 2-11. Although the image of porosities in 100mm/s was not provided, as scan speed increased from 100 to 1000mm/s, the percentage of porosity increased from 4.7% to 12.5%. The percentage of porosity was calculated by (1 - relative density) ×100. Relative density ρ/ρ_s was provided by measuring the sample's density ρ and divided by the density of Ti6Al4V alloy ρ_s. Although Puebla et al. explained the relationship between scan speed and defects in two different build orientations of horizontal and vertical samples, the percentage of porosity in different build parts was not discussed or analysed. In addition, the definitions of porosity and LOF were not distinguished and the formation of defects was not clearly explained. By increasing the scanning speed, the size of the melt pool decreases. Consequently, overlapping of two adjacent melt pools decreases, when the empty or un-melted powders make LOF in a part (Cunningham et al., 2016; Gong et al., 2014, 2013; Léonard et al., 2012; Tammas-Williams et al., 2015). Consequently, the existence of LOF increases. Although in Cunningham's investigation, melt pool size was mentioned, the data was borrowed from Narra et al.'s research (Narra et al., 2015).
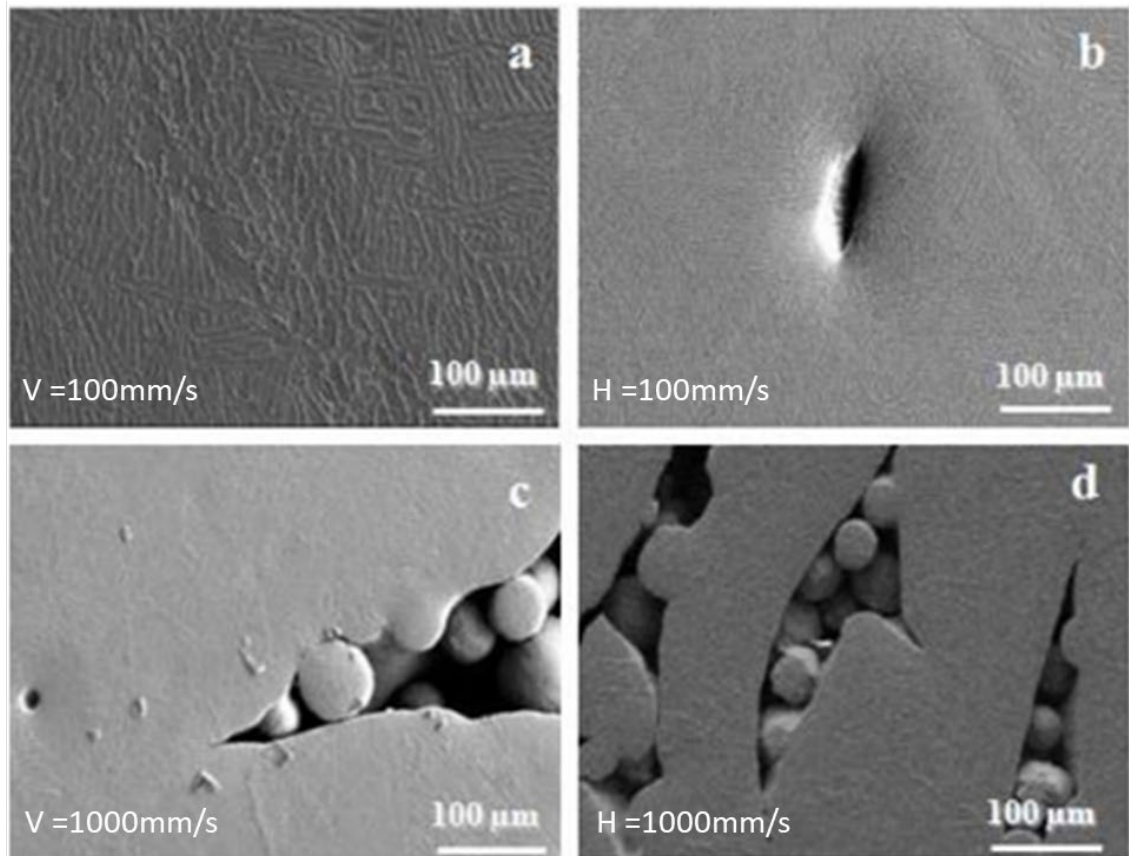
Figure 2-11 SEM images of LOF in different scan speeds in two build orientation samples of: a) and c) vertical, b) and d) horizontal (Puebla et al., 2012).

The effect of speed function on defects was investigated by Haijun Gong (Gong, 2013). The percentage of porosity in each sample was provided by measuring the relative density and equation ($R_D = 1 - (\rho/\rho_s)$). The percentage of porosity increases by increasing speed function as shown in Figure 2-13. Although the effect of speed function on the percentage of porosity was analysed, there was no investigation of LOF. In addition, Galarraga et al. examined the percentage of porosity in two locations, centre and edge, using Elements-D software. It was reported that the centre sample had a higher porosity percentage in comparison to the edge sample. In the centre sample, porosity level in the top area is 0.31% while this value drops to 0.2% at the bottom area. However, this trend changes in the edge sample with 0.08% porosity at the top area. By reaching the bottom area, this value increased to 0.1%. However, there is a doubt whether porosity means defect or spherical porosity (Galarraga et al., 2017). The number and overall volume fraction of pores reduces considerably when the melt pool area increases as shown in Figure 2-12. In Figure 2-12, among changing speed functions from 7 to 157, the melt pool area with speed function 36 was selected to be X in Figure 2-12, the nominal value. Therefore, the melt pool areas were divided into the nominal melt pool area value to define each melt

pool area relative to the nominal melt pool area; then, the relationship between the relative melt pool area was a function of speed. Hence, the relationship between the melt pool area and volume fraction of spherical porosity is illustrated. Although the fraction of LOF was not quantified in Cunningham et al.'s work, it was mentioned that by reducing the melt pool area, the volume fraction of LOF outstandingly increases (quantification was done by observation, not measurement) (Cunningham et al., 2016).
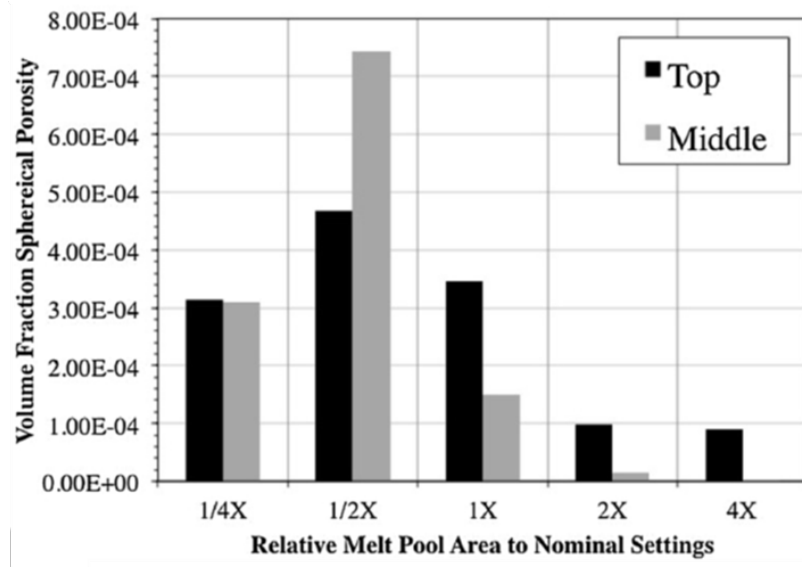
Figure 2-12 The volume fraction of porosity size as a function of melt pool size
(Cunningham et al., 2016)
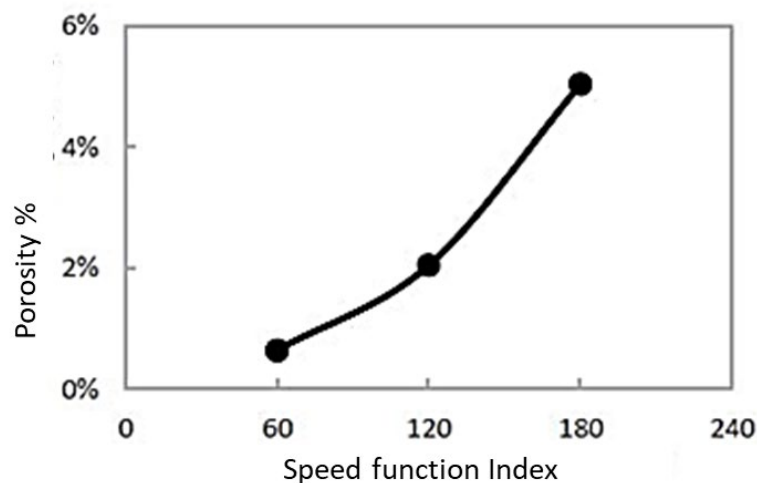
Figure 2-13 Illustration of the effect of speed function index on porosity (Gong, 2013).

Kirchner et al. investigated the effect of scan speed and beam current on porosity formation in the EBM Arcam A2X machine (Kirchner et al., 2014). It was stated that changing scan speed affected the percentage of porosity level of parts. Increasing scan speed leads to an increase in porosity level (1.1%), especially when the scan speed

increases from 10m/s to 12m/s, which was considerably steep, as shown in Figure 2-14. It described the different types of porosity as a spherical pore and LOF, however, it did not mention the percentage of which type of defect was affected by scan speed. Yet, there was no further explanation why this severe defect occurred. Besides, by measuring apparent density, the volume fraction of spherical pores was 0.27%, however, the volume fraction of LOF was not quantified. Another study stated that by increasing scan speed, melt pool size decreased due to insufficient time for transferring melt pool heat (Juechter et al., 2014). Although they presented an uneven and visible porosity on the top surface due to an increase in scan speed, there was no further explanation how Ti6Al4V melt pool size of was measured and how a sample with an uneven top surface of more than 2mm could have just 0.5% porosity, while the layer thickness was 50μm.
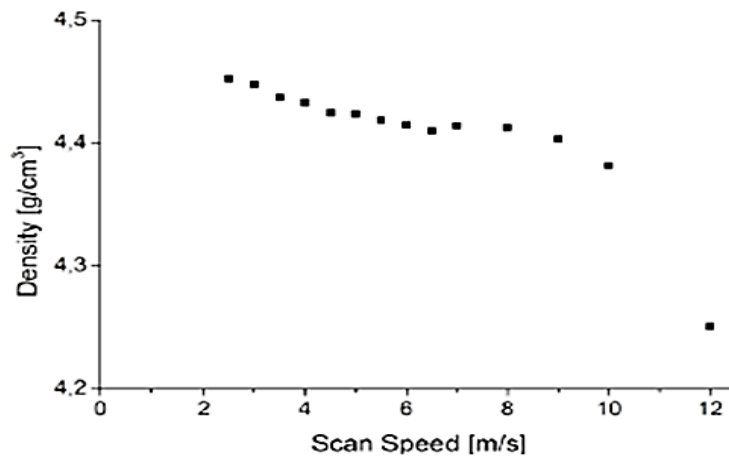
Figure 2-14 The relationship between scan speed and density of Ti6Al4V alloy samples (Kirchner et al., 2014).

Since LOF shape and size depend on the shape and size of the melt pool in Ti6Al4V alloy, investigating both melt pool shape and LOF are essential keys for improving mechanical properties. Although many studies have attempted to explain the melt pool shape simulatively and experimentally, the melt pool shape of Ti6Al4V is still unclear due to no evidence of line-like features (the melt pool boundary) on the micrograph images. The reason for not observing the line-like features is attributed to the heat cycle of the several previous layers each time the new powder layer begins to melt during the EBM process. When a new melt pool is formed by the electron beam on the top of the solidified layer, a part of the melt pool beneath is melted. Therefore, a part of underneath melt pool re-melts and re-solidifies, so a new microstructure starts nucleating and growing along with the columnar grain structure. In addition, a zone around the melted area is a heat affected zone which makes the microstructure as heat treated. Because this area is not melted, it is

28

suggested that its temperature is below the β transus, hence, α phases in this area begin to transform to β phases partially. As soon as the temperature drops, the transformed β phases start transferring to α phases. The previous melt pool shape vanishes due to these several phase transformations. In addition, many studies have been done on the formation of defects, however, the formation of all kinds and types of defects (porosity and LOF) has not been classified and distinguished.

2.4 Effect of scan speed on the prior β grain boundaries of Ti6Al4V alloy

During the EBM process, the predominant heat flow direction of downwards results in the columnar growth of β (bcc) phase predominantly along the build direction during solidification of the Ti-6Al-4V alloy. Then, upon cooling, the phase transformation β → α (hcp) + β takes place, with α phase lining formed along the prior β grain boundaries and β phase columnar grains transformed into colonies of α + β. Bo Cheng et al. employed two methods of simulation with ABAQUS software and a LumaSense MCS640 NIR camera to analyse the melt pool size and prior β columnar grains (Cheng et al., 2014). It was reported that by increasing scan speed from 481 to 1595mm/s, the cooling rate increased, which led to a really fine α phase and in some areas of ά phase. In addition, by increasing cooling rate in the part, the solidification rate increases, thus, the columnar grains width decreased from 109.7 to 37.1μm when scan speed increased from 214 to 529mm/s. Pushilina et al. investigated the influence of process parameters on the microstructure behaviour of Ti6Al4V parts produced by the EBM. By increasing the speed function from 85 to 98 with a constant beam current, the average of the α width decreased. The majority of the α plates of width in speed function of 85 was 0.4 to 0.6 μm and in some areas this width reached 1.4 to 1.6 μm. By increasing the speed function to 98, the width of the α plates decreased to an average of 0.2 to 0.5 μm (Pushilina et al., 2018). Narra et al. investigated the relationship between the width of prior β boundaries of Ti6Al4V alloy and the width of the melt pool (Narra et al., 2018, 2015). By increasing the speed function from 7 to 130 for a one bead melt pool, different widths of melt pools were achieved. By measuring the width of each melt pool and comparing them to the average width of prior β grain boundaries, the relationship between these two factors was analysed as shown in Figure 2-15. By increasing the width of the melt pool, the average of prior β columnar grains increased linearly. It should be mentioned that some of the width samples were too narrow to be measured, therefore, they were eliminated in the width measurement.
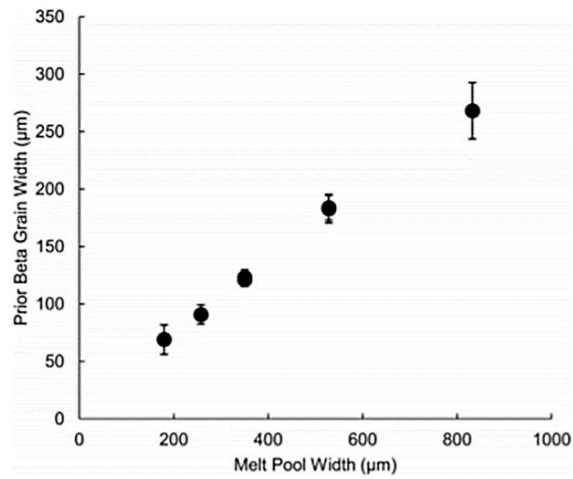
Figure 2-15 The average of the width of prior β grain boundaries of Ti6Al4V alloy as a function of the melt pool width (Narra et al., 2018, 2015).

In Figure 2-16, the average width of some prior β grain boundaries in EBM are shown. Although the melt pool width in Figure 2-16 was not mentioned, based on data of Figure 2-15, the melt pool width for the prior β grain boundaries of 91, 177 and 277µm were estimated to be 265, 520 and 820µm, respectively.

Prior β width=91µm   Prior β width=177µm   Prior β width=277µm
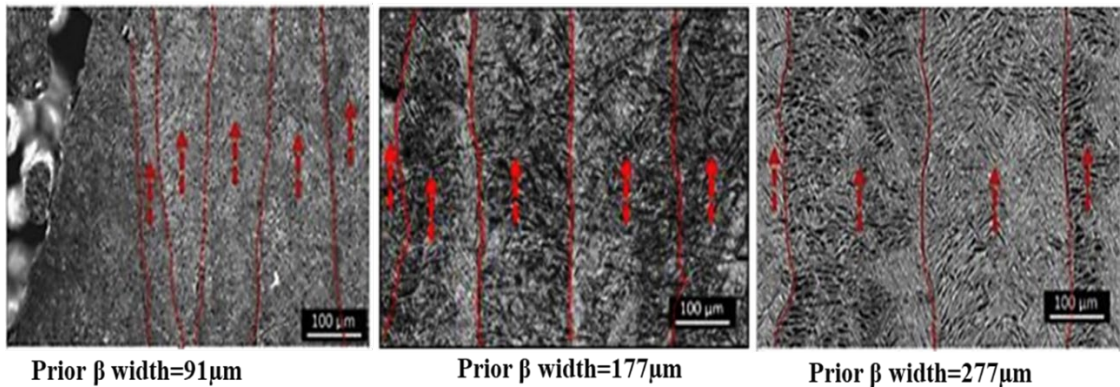
Figure 2-16 SEM images of the average of the prior β grain boundaries width (Narra et al., 2018).

According to Körner and Narra et al., by decreasing the scan speed the melt pool size increased, thus, the width of the columnar grains increased. However, the authors did not provide any evidence of the melt pool shape and size of either Ti6Al4V and Ti48Al2Nb2Cr (Körner, 2016; Narra et al., 2018).

2.5   Effect of process parameters on top surface features

The top surface of built samples shows the top surface of the melt pools in the last layer of the part produced by the EBM. Therefore, any irregularity like rough surface or defect

on the top surface shows the possibility of these matters to the previous layers. In addition, by studying the top surface, the behaviour of melt pools during overlapping with adjacent melt pools can be studied and investigated. Therefore, the focus of this section is the relationship between process parameters with the top surface of the EBM part.

Bo Cheng et al. examined the top surface of samples that were produced by different speed functions from 20 to 65 (Cheng et al., 2014). By increasing the speed function, the track line pattern from a smooth line becomes wavy with visible pores, as shown in Figure 2-17. Juechter et al. and Bo Cheng et al. stated that too much energy input could make an uneven top surface in EBM components. In addition, it was explained that increasing the scan speed makes an uneven surface and as a cross-section of the uneven surface, the top surface becomes wavy, Figure 2-18 (Cheng et al., 2014; Juechter et al., 2014). However, the reason for the wavy and uneven surface was not explained.
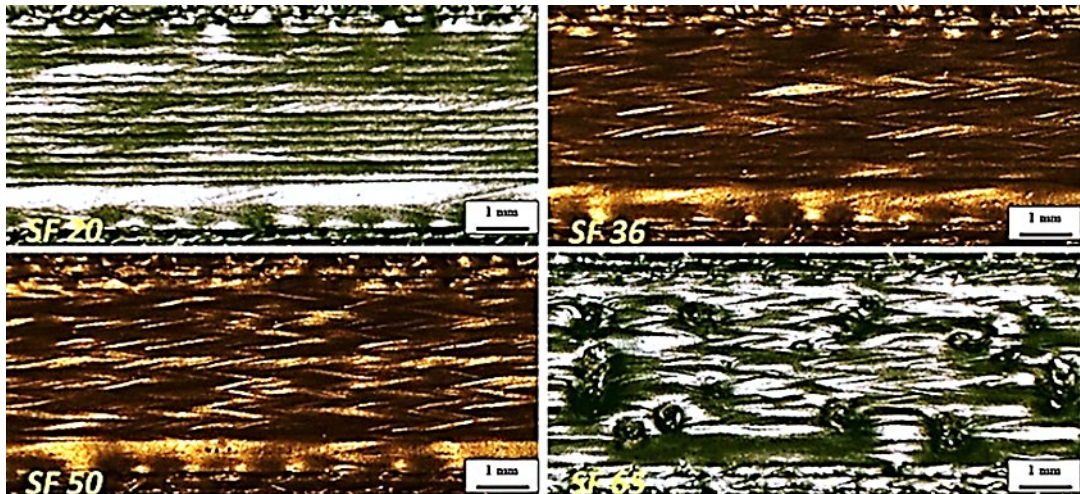
Figure 2-17 Top surfaces of Ti6Al4V samples produced by the EBM with different speed function values (Cheng et al., 2014).
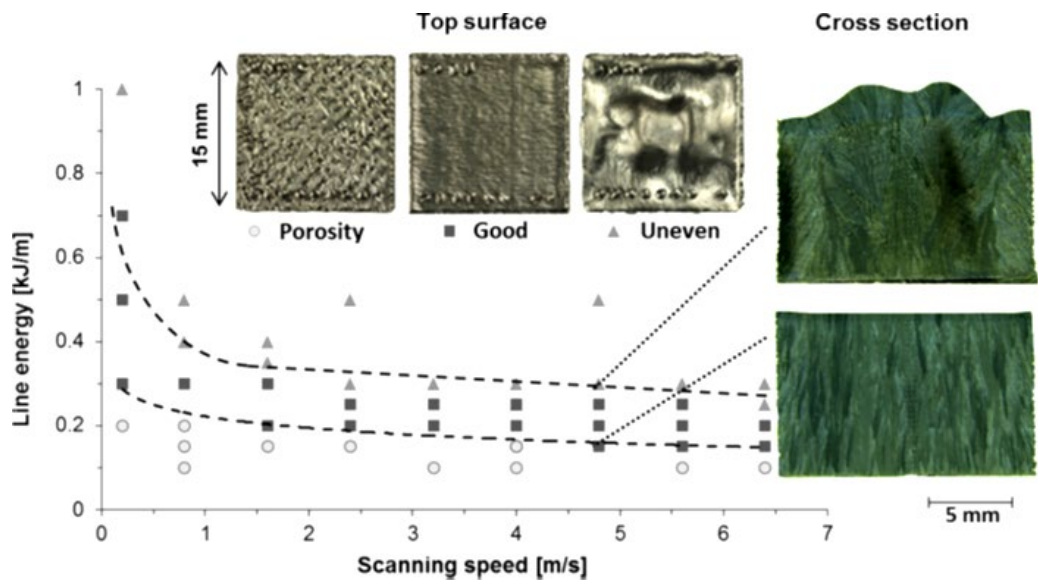
Figure 2-18 Ti–6Al–4V samples with different scan speed produced by Arcam S12 machine EBM machine (Juechter et al., 2014).

2.6 Effect of LOF and an anisotropic EBM Ti6Al4V orientation on mechanical properties

The product performance depends on not only the mechanical properties such as tensile strength, toughness and fatigue, but also the top surface roughness and micro-hardness which play an important role in product quality.

2.6.1 Effect of LOF and directional built samples on toughness

A few studies have been done on understanding the effect of build directions and LOF on impact energy, particularly on as-built Ti6Al4V alloy produced by EBM. Toughness is one of the important mechanical properties for EBM products for many industries applications such as biomedical, aerospace, etc.

Yasa et al. studied the directional build orientations of vertical in form of Z and horizontal in two different notch positions (notch a side Y and notch on top X) in different materials (Yasa et al., 2010). In Ti6Al4V and stainless-steel alloys, the impact energy of Y samples with 14J and 15J, have the highest value in comparison to X (~12J and 10J) and Z (~7J and 8J) samples respectively; which stated that impact energy was not a function of build direction. In addition, the Z direction of both alloys had the lowest impact energy compared to the horizontal samples (X and Y notch positions) that was related to existence of defects (Yasa et al., 2010). The fracture surface of SLM Ti6Al4V showed a mixture of brittle and ductile features, Figure 2-19.

32
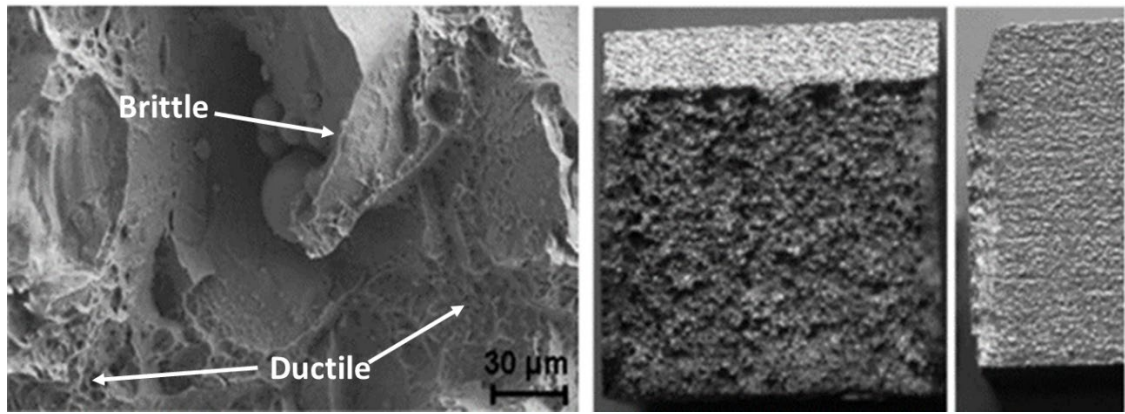
Figure 2-19 Ti6Al4V fracture surface of a) SEM image in high magnification and b) the top and side images of sample in low magnification (Yasa et al., 2010).
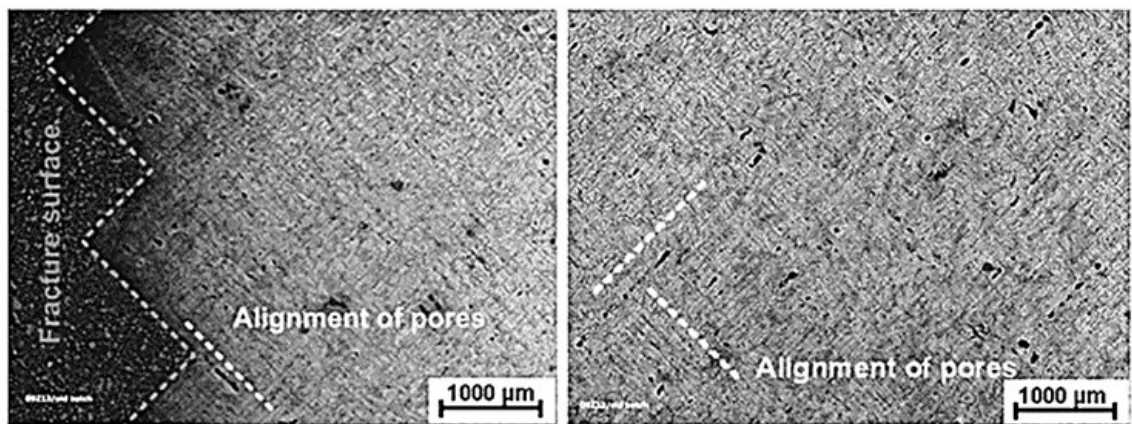
Figure 2-20 The cross section of Stainless-steel AISI 316L fracture surface which is perpendicular to build direction (Yasa et al., 2010).

The cross section of stainless-steel showed a wavy fracture path which was attributed to aligned pores along the fracture, which means that the effect of defects on the fracture path, as shown in Figure 2-20. However, there was no further explanation about the fraction of Ti6Al4V LOF compared to other materials.

In addition, the anisotropy of SLM Ti6Al4V alloy on toughness in two directions, horizontal and vertical, were investigated by Wu et al. (Wu et al., 2016). The density of both samples was 99.5%. The impact energy for vertical and horizontal directions was reported to be 4.9J and 9.6J respectively, which means that the impact energy for the horizontal direction was 96% higher than the vertical one. In both vertical and horizontal sample cross sections, some different spherical and linear (LOF) defects with a size of several hundred micrometres were observed. Furthermore, the defects could be seen in the fracture surface of both samples as shown in Figure 2-21. The low toughness of the vertical sample in comparison to the horizontal sample was attributed to the orientation

33

of LOF, which was along with impact energy that reduces the load bearing in the vertical sample. While in the horizontal sample, the LOF disk-shape orientation is perpendicular to loading direction (notch direction), which increases the resistance of the sample to impact loading. Therefore, the orientation of LOF caused the low toughness in the vertical sample compared to the horizontal sample. The directional LOF suggests that the coherency of joined layers in the powder-based process is not strong (Wu et al., 2016).
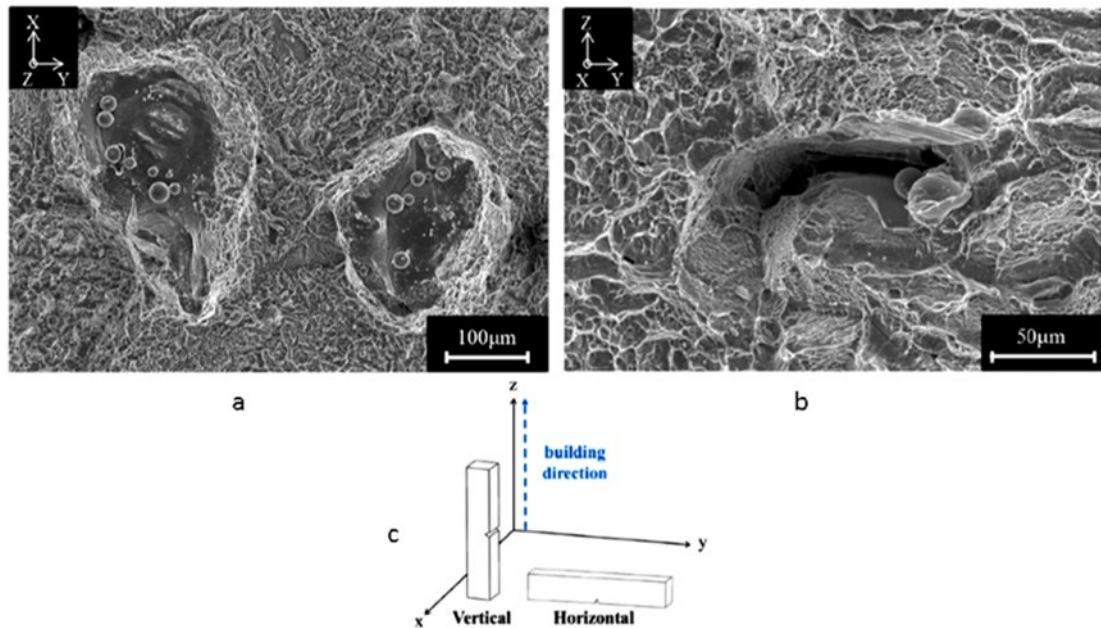
Figure 2-21 The SEM images of LOF on the fracture surface: a) vertical b) horizontal orientations. Regarding build direction, the vertical and horizontal samples are schematically shown (Wu et al., 2016).

2.6.2 Effect of oxygen and build direction on impact toughness

EBM powder recycling is one of the advantages of using AM but by reusing them, their distribution may change, or powders may have been contaminated (absorb oxygen). Therefore, in some studies powder shape, size and oxygen level were investigated. The studies showed that oxygen levels of samples produced by reused powders increased along with the strength while the ductility decreased (Grell et al., 2017; Tang et al., 2015; Yan et al., 2014). Correspondingly, not only is the strength of samples affected by oxygen level, but also the ductility of samples as well. Tang et al. reported that recycling of powders could be done 21 times with resulting good tensile properties if, based on ASTM F294, the percentage of oxygen level keeps below 0.20% (Tang et al., 2015). In addition, Grell et al. studied the effects of oxygen level on Charpy impact energy of as-built and Hot Isostatic Pressing samples (HIP) in vertical and horizontal directions (Grell et al., 2017). HIP is used for improving material properties with inert gas pressure (Argon) for

pressing the material (105 MPa) at elevated temperature (around 920°C) (Donachie, 2000; Grell et al., 2017). Some samples were fabricated from some powders with different conditions: first-time used, fifth-time used, and a mixture of fifth-time used, artificially oxidized and highly oxidized powders. The first-time and fifth-time used powder batches showed a small amount of oxygen in the fabricated samples. The other two samples with a mixture of fifth-time used and artificially oxidized samples had a lower oxygen level in the built-up samples. The ZX orientated samples had the highest absorbed energy levels which means that the ZX samples in all conditions had the highest impact toughness. When the oxygen level increased, the impact energy that the Charpy sample absorbed decreased and the effect of HIP process and build direction decreased in the highly oxidized specimens. In addition, the highest ductility belonged to the sample with the lowest oxygen level and the highest brittleness belonged to the highly oxidized specimens while the mix-powdered sample (mixture of fifth-time used and artificially oxidized sample) had the medium performance. It was demonstrated that the influence of level of oxygen on impact energy in EBM Ti-6Al-4V value is high with an oxide layer which reached 3μm thickness (Grell et al., 2017).
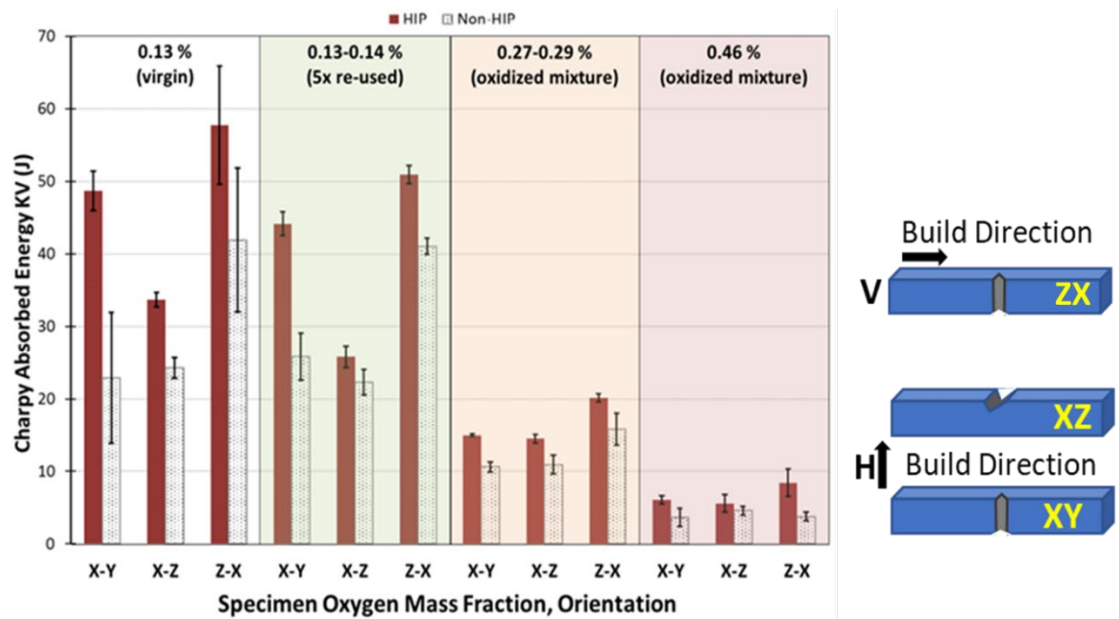
Figure 2-22 The effect of oxygen levels in three different build orientations of XY, XZ and ZX (Grell et al., 2017).

It was stated that the vertical samples (ZX) had the highest impact energy in comparison to horizontal samples XY and XZ (which notch was placed on the side and top respectively) with the fraction of oxygen up to ~0.4%. Even in HIP processed samples, vertical samples owned the highest impact energy. It should be mentioned that the

horizontal samples in XY and XZ directions both had a quite similar range of impact energy value at each fraction of oxygen level, which means that the notch position in the horizontal sample did not affect the impact energy result. The impact value of ~0.13% fraction of oxygen level was ~47, 30 and 55J in respect of XY, XZ and ZX directions, respectively. LOF was observed in all areas of EBM samples, especially in the first layers, regardless of direction of the samples. It was stated that fracture occurred in the Charpy samples 10mm away from the notch. The fracture occurred in this location due to the LOFs between the layers that were generated during the EBM process. Charpy impact energy is a function of oxygen level. Oxygen level has more influence on impact energy than build orientation and HIP processing. For instance, by increasing oxygen level of the sample from 0.29% to 0.46%, impact energy value drops from ~12J, 12J and 16J to 3J, 4J and 3J in respect of XY, XZ and ZX direction in as-built samples. While HIPed samples for the same oxygen content shows the same trend, which Grell et al. concluded is obvious proof that oxygen level has the most influence on EBM samples, even more than build direction (Grell et al., 2017). Figure 2-23 shows the LOF shape that was found on the fracture surface of the vertical sample. Although it was stated that the existence of LOF affected impact energy value severely even more than oxygen level, there was no further explanation or analysis of LOF. Also, it was claimed that the strong directional effect in Charpy impact energy was found to be vertical (ZX), however, not all build orientations were examined such as angled build samples.
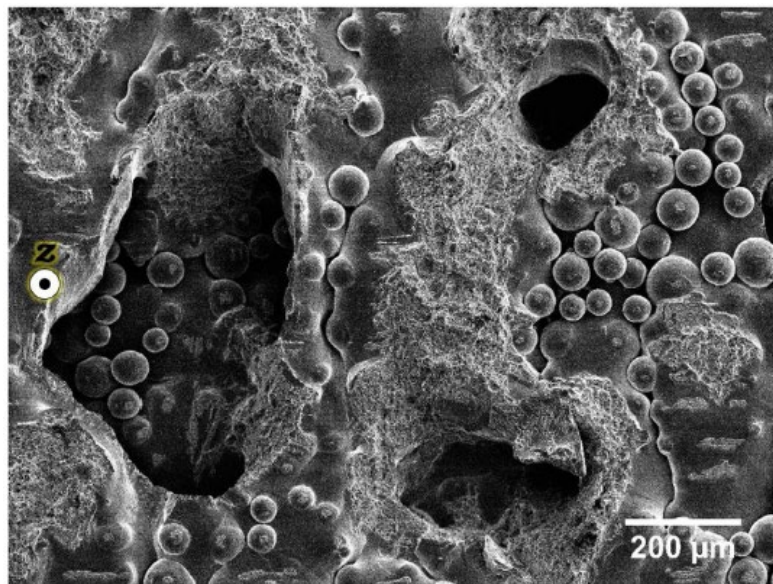
Figure 2-23 SEM image of LOF on the fracture surface of vertical sample (Grell et al., 2017).

Grell et al. stated that the build direction had no significant effect on the impact energy of the samples (Grell et al., 2017). In addition, LOF affected impact energy by choosing to fracture in the layers with LOF presence, instead of fracturing on the notch area. However, there was no further explanation and analysis of the amount of LOF. Besides, Buirette et al. demonstrated that impact energy was affected by microstructure which plays a significant role in changing mechanical properties (Buirette et al., 2014). The above discussions about the effect of LOF and build direction on impact energy are summarized and presented in Table 2-1.

There are limited studies about the relationship of build direction and LOF with toughness in Ti6Al4V alloy produced by EBM. Two directions of vertical and horizontal have been included in their studies while the samples that are built with an angle to the relative of the horizontal plane were not studied. Therefore, investigating the effect of build direction and LOF on the toughness of Ti6Al4V produced by EBM is crucial. In addition, it is not yet clear how LOF affects the built parts, whether it is due to the fraction of LOF or its size and distribution in the parts.

Table 2-1 The summary of Charpy impact energy data from various articles

Ref.	Geometry (mm)	Notch	O%	TD-ND	RD-ND	TD-RD	RD-TD	Material / Microstructure	Pendulum Energy (Joule) & speed m/s	Process technique	Surface	Reason
(Christophe Buirette 2014)	Non-standard 55x10x6	Yes		11	21	8	8	Ti6Al4V / α-β annealed	300 & 5.23	Hot Rolled	No Info	Microstructure & crystallographically
		Yes		21	20	14	22	Ti6Al4V / β annealed				
Ming-Wei Wu 2016	Standard 55x10x10	Yes		H 9.6		V 4.9		Ti6Al4V / ά in widmanstatten	No Info	SLM	No Info	LOF
Evren Yasa 2010	Standard 55x10x10	Yes		X 11	Y 18	Z 10		Ti6Al4V	No Info	SLM	As-Built	No significant effect on build orientation
		No		X 52	Y 71	Z 45						
		Yes		X 10	Y 18	Z 10		Maraging steel				
		No		X 60	Y 101	Z 105						
		Yes		55	No Info on direction			AISI 316L stainless-steel				
		No		200								
W.A. Grell 2016	No Info	Yes	0.13	XY 23	XZ 25	ZX 42		Ti6Al4V	No Info & 5.5m/s	EBM		Oxygen level & LOF (more effective)
			0.13	48	34	58		Ti6Al4V (α-β annealing)		HIP		
			0.13-0.14	26	22	41		Ti6Al4V		EBM		
			0.13-0.14	44	26	51		Ti6Al4V (α-β annealing)		HIP		
			0.27-0.29	12	12	17		Ti6Al4V		EBM		
			0.27-0.29	15	15	20		Ti6Al4V (α-β annealing)		HIP		
			0.46	3	4	3		Ti6Al4V		EBM		
			0.46	6	5	8		Ti6Al4V (α-β annealing)		HIP		
Qizhen Li et al. 2008	No Info	-	-	16.1				Ti6Al4V alloy	-	Wrought	-	-
Marleen Rombouts et al. 2009	No Info	Yes	-	15				Ti6Al4V alloy	-	Cast	-	-

2.6.3 Fracture path

During fracture, the crack passes either inside the grains or along grain boundaries (follows the grain boundaries). When the crack propagates along grain boundaries, it is known as intergranular fracture. In this kind of crack, the boundary is a weak area for a crack to propagate. On the contrary, if the crack passes through the grains and does not follow the grain boundary path in metal microstructure, it is called transgranular fracture (Gerd Lütjering et al., 1998; Schijve, 2009). Christophe Buirette et al. investigated the crack propagation of Charpy samples in two different ring-rolling Ti6Al4V alloys with α–β annealed (equiaxed) and β annealed (lamellar) microstructures (Buirette et al., 2014). The β phase length and colony size in the equiaxed microstructure was larger than lamellar ones. The crack propagation in the α–β annealed microstructure was intragranular. The crack at small grain size propagates a short length rather than larger microstructure. Unlike the α–β annealed microstructure, the crack propagation in the β annealed microstructure occurs at either the grain boundary, the colony interface or between two α platelets. The reason that crack propagates on the α phase referred to the α thickness of less than 1mm and the length of 100mm which makes an easy path for the crack. The difference between the crack path of the two different microstructures was attributed to the colony size and the quantity of α+β interfaces which count as obstacles during crack propagation.
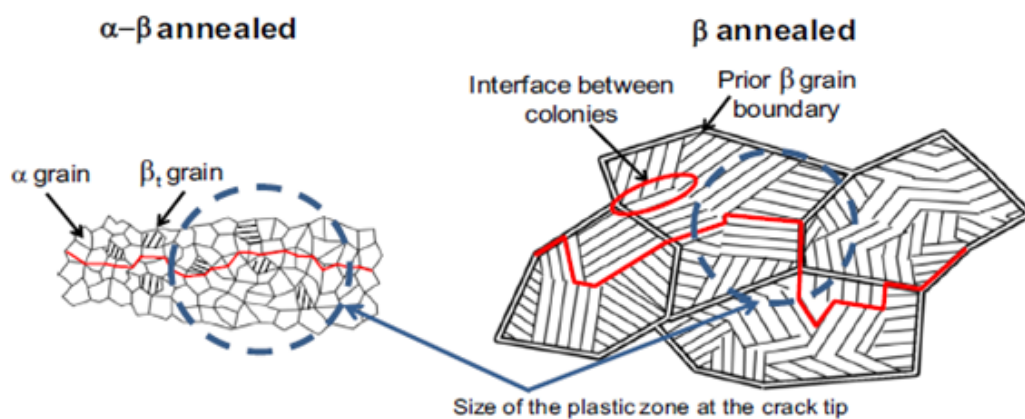
Figure 2-24 The illustration of crack propagation behaviour in two different equiaxed and lamellar microstructures. The red line shows the crack path in the microstructures (Buirette et al., 2014)

Also, Sarrazin categorized the crack path into three groups: transgranular stage I, transgranular stage II and intergranular (Sarrazin-Baudoux, 2003). In transgranular stage I, the

crack propagates through and along grain boundaries while in transgranular stage II, the crack just passes through the grains as shown in Figure 2-25.
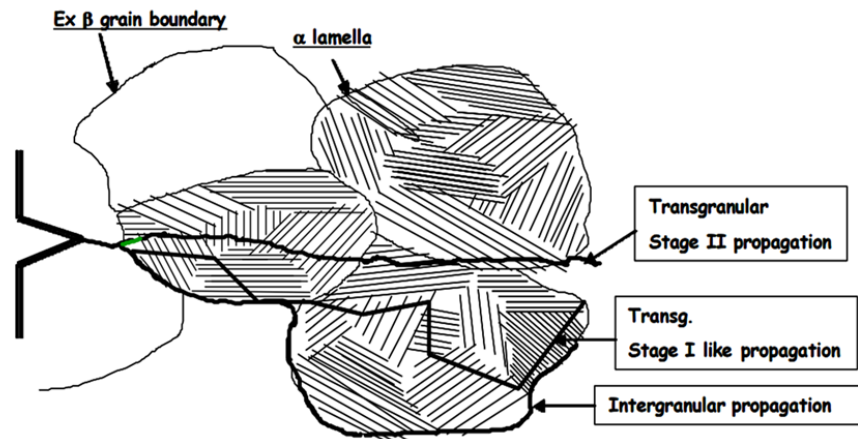
Figure 2-25 Illustration of three crack paths (Sarrazin-Baudoux, 2003)

2.6.4 Fatigue crack growth

Fatigue on a material happens when it is exposed to cyclic loads. When the failure cycle range is less than 5×10^4, it is known as low cycle fatigue (LCF) and if the failure cycles exceed more than this range, it is called High Cycle Fatigue (HCF) (Donachie, 2000).

Fatigue life has three main stages to complete the entire process from crack initiation until the fracture occurs. Crack initiation is categorized into two phases: the first phase belongs to crack nucleation and small crack growth; the second phase belongs to long crack propagation and final fracture. Despite the fact that the nucleation size is related to the size of one grain, the size of small crack growth could contain around ten-grain sizes. These two phases together form stage I or region I in the fatigue crack growth diagram which is shown in Figure 2-26 (Perez, 2004; Schijve, 2009; Tudose et al., 2016). Fatigue crack growth depends on the stress ratio of applied load, material and the temperature of environment. The crack growth rate in stage I is 10^{-6} mm/cycle. The second region belongs to stage II or region II, which shows the crack growth behaviour power, that well-known Paris law. The crack grows steadily and linearly in the Paris law region; however, it somehow gets affected by stage I parameters. The Paris law relationship is given in Equation 2-1, where C and n are known as constants related to the material. The C and n values can be calculated by measuring the slope of the linear line in the Paris law area that is bounded by two points.

Equation 2-1

$$\frac{da}{d\mathcal{N}} = C.\Delta K^n$$

The first point on the left that separates the region I from region II is known as the fatigue crack threshold ΔK_{th}, stress intensity. The "a" is the distance that the crack travels in one cycle of loading and N is known as the number of cycle da/dN. The other point is the right-side limit between the two areas of region II and region III, where fracture occurs, that is fracture toughness K_C or (K_{IC}). In region III where the crack growth accelerates quickly regardless of microstructures and barriers is known as the unstable crack growth region (Schijve, 2009).
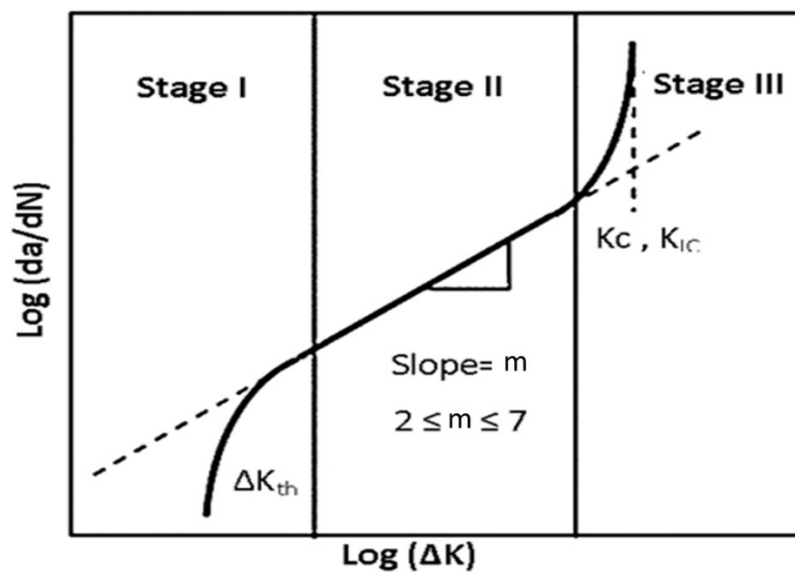
Figure 2-26 Illustration of fatigue crack growth (Tudose et al., 2016).

Daniel Greitemeier et al. investigated the factors influencing the fatigue performance of HIPed, annealed, heat-treated laser powder bed Direct Metal Laser Sintering (DMLS) and EBM TiAl6V4 for different stress ratios (Greitemeier et al., 2017). The crack growth resistance in ΔK_{th} for HIPed samples of DMLS and EBM with values of DMLS: 4.4MPam$^{0.5}$ and EBM: 4.8MPam$^{0.5}$ were higher than the annealed ones with values of DMLS: 3.2MPam$^{0.5}$, EBM: 4.2MPam$^{0.5,}$ respectively. Regardless of the different processes of Ti6Al4V, the data showed a similar crack propagation value for region II in all conditions with a stress ratio of 0.1. According to the crack growth graph, C and m values of the annealed EBM sample are 6×10^{-8} $\frac{mm}{cycle}$ and 2.7 respectively. In addition, Yuwei Zhai et al. studied the effect of different process parameters of Laser Engineered Net Shaping (LENS) and Electron Beam Melting (EBM) on microstructure and mechanical properties (Zhai et al., 2015). Fatigue crack growth of EBM, and Laser

Engineered Net Shape (LENS) Ti6Al4V at different low stress ratios were investigated. The c and m values of as-fabricated EBM vertical sample (crack propagation is perpendicular to build direction) are 1.7×10^{-11} and 3.2, while in the horizontal sample (crack propagation is parallel to build direction), these values changed to be 2×10^{-12} and 3.7 respectively. Although c and m values were measured in this study, the reason for this difference in region II was not explained and discussed. Contrarily, in Edward et al.'s paper, horizontal and vertical orientated samples showed a similar fatigue crack growth behaviour in both regions I and II (Edwards et al., 2013). Therefore, there was no noticeable difference in crack growth rates for both samples as a function of directed build sample and loading direction. Even by comparing EBM Ti6Al4V alloy with a wrought one, region I was similar to the EBM samples, while there was a little difference in region II with the EBM sample curve which was attributed to slower crack growth rate for a given ΔK in the EBM sample which means that the crack growth resistance in the EBM Ti6Al4V alloy due to the microstructure being higher than the its wrought alloy. In addition, Joshi et al. investigated the influence of directional crack propagation on electron beam orientation of the EBM Ti6Al4V alloy by a four-point-bending test (Joshi et al., 2013). It was demonstrated that the fatigue resistance in samples with vertical build direction (perpendicular to crack growth path) is higher than the sample with horizontal one (a crack path parallel to build direction) due to maximum stress evaluation of 105 - 186 MPa for the vertical and 75.4 - 130 MPa for the horizontal build direction. In region II when the effect of the stress ratio R on $\frac{da}{d\mathcal{N}}$ decreased, ΔK_{th} increased. By increasing the stress ratio, not only ΔK_{th} but also near-threshold FCG rates increased for all conditions of as-fabricated and β-annealed samples in both directions of horizontal and vertical samples. The ΔK_{th} values for as-fabricated EBM samples in horizontal and vertical orientations for stress ratio 0.1 were 3.7 and 4.7 $MPam^{0.5,}$ while in annealed samples, these values increased incredibly to 6 $MPam^{0.5}$ for both orientated samples (Galarraga et al., 2017).

Table 2-2 The summary of fatigue crack growth data of AM samples

Ref.	Condition	Build Direction	m	C	FCG Diagram	Microstructural analysis on Region II	Type of Test
(Seifi et al., 2015)	As-Built	H-LS Start	3.1	-	No	No	Fatigue Crack Growth
		H-LS END	2.9	-	No	No	
		V-LT BOTH	2.9	-	No	No	
(Joshi et al., 2013)	As-Built	V	-	-	-	-	4-point bending
		H	-	-	-	-	
(Greitemeier et al., 2017)	HIP	V	2.7	$6*10^{-8}$	Yes	No	L Bracket
	β Annealed	V	2.7	$6*10^{-8}$	Yes	No	
(Zhai et al., 2015)	As-Built	V	2.25	$2*10^{-7}$	Yes	Yes	Fatigue Crack Growth
		H	2.37	$1.7*10^{-7}$			
	Heat-treated	V	2.37	$1.7*10^{-7}$	Yes	No	
		H	3.57	$8*10^{-9}$			
(Seifi, Salem, Satko, Shaffer, & Lewandowski, 2017)	As-Built	H-LS Start	4.1		Yes	No	Crack Growth
		H-LS END	3.5				
		V-LT BOTH	2.9				
	As-Built	V		-	-		3-point bending
	HIP	H		-	-		
(Galarraga et al., 2017)	As-Built	V	2.9	$5*10^{-8}$	Yes	Yes	Crack Growth
		H	3.37	$1*10^{-8}$			
	β Annealed	V	2.9	$2*10^{-8}$			
		H	2.9	$2*10^{-8}$			
(Edwards et al., 2013)	As-Built	V	2.28	$2.5*10^{-7}$	Yes	No	Crack Growth
		H	2.28	$2.5*10^{-7}$			
	Wrought	-	2.67	$9*10^{-7}$			

2.6.4.1 Effect of LOF on Fatigue crack growth

The existence of defect/LOF in samples may affect the fatigue crack growth, therefore many studies have been done to investigate this matter. In the Seifi et al. study, large sizes of LOF and porosity were observed in three-point bend tested samples specially in samples with lower fracture toughness (Seifi et al., 2017). However, LOF was mentioned

in this work but was not measured separately. Edward et al. explained that due to crack growth rate in the FCG diagram for horizontal and vertical samples being the same, defects did not have a noticeable effect on crack growth behaviour (Edwards et al., 2013). Also, Greitemeier et al. stated that fatigue performance is controlled by defects in annealed Direct Metal Laser Sintering (DMLS) and EBM specimens while in HIPed samples controlled it is by microstructural inhomogeneity (Greitemeier et al., 2017). In EBM samples, the average of the defect area is approximately 108×10^3 μm^2 while in the DMLS sample this value decreased dramatically to approximately 2×10^3 μm^2. The average of defect area in these two samples makes fatigue performance different which means that fracture occurs in EBM samples faster than DMLS samples due to the average defect area. The pore size in annealed EBM samples was 320µm and DMLS less than 240 µm while in HIPed samples, no pore was spotted. Different defects size and shape are shown in Figure 2-27. Although Greitemeier et al. investigated the influence of defect on fatigue performance, the defect shapes were not distinguished as to which defect types of porosity or LOF had more influence on decreasing fatigue performance (Greitemeier et al., 2017).
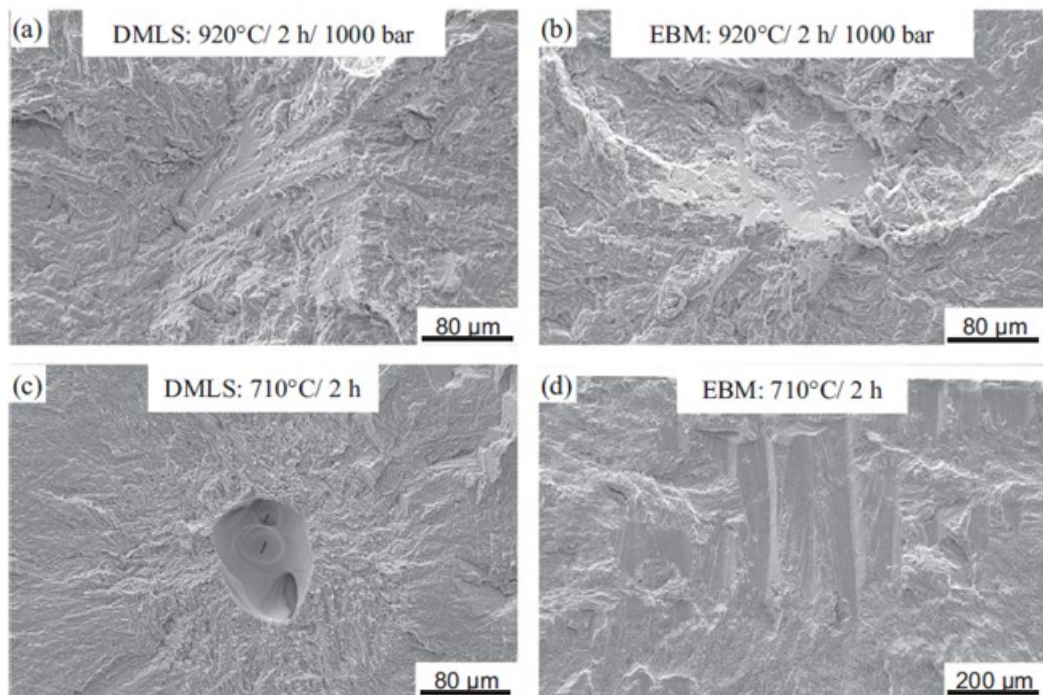
Figure 2-27 Fractographic analysis of different processed TiAl6V4 with R=0.1: (a) HIPed DMLS, (b) HIPed EBM, (c) annealed DMLS (d) annealed EBM (Greitemeier et al., 2017).

Many studies have been performed on fatigue crack growth in two build directions. In some works, the fatigue crack growth of region II was similar, but the reason was not microstructurally studied. Also, in some studies, there was a slight difference between fatigue crack growth graph of vertical and horizontal directions of the as-fabricated EBM Ti6Al4V alloy; however, there was no explanation provided for region II. Although two directions of vertical and horizontal were studied in the literature, the 45° build sample of the alloy was not studied or compared in fatigue crack growth. Consequently, there is a need to study the crack growth propagation in all three directions, vertical, horizontal and 45° build, in the region II microstructurally to understand the anisotropic properties of phases of region II.

2.6.4.2   Effect of microstructure on the crack propagation

In Ti6Al4V microstructure with lamella morphology, when a crack propagates due to different crystallographic orientations in two adjacent α colonies with fine structure, it may propagate out of the plane and continues in different slip planes that are adjacent to the main propagation plane (in the neighbourhood area). The crack changes direction from the main propagation plane to adjacent planes that have a suitable distance. Therefore, the crack tips divide into different planes with Z distance which is related to α plates size in fine lamella structures and perpendicular to the prior main crack plane, as shown in Figure 2-28. In order for the crack to propagate, it needs to travel through unfavourable directions and orientated crystallographic planes. Since distance Z is related to α plate size in a lamella structure, distance Z has a direct relation to the barrier strength of crack propagation. The finer the microstructure is, the less crack propagation resistance exists in the material (Gerd Lütjering et al., 1998).
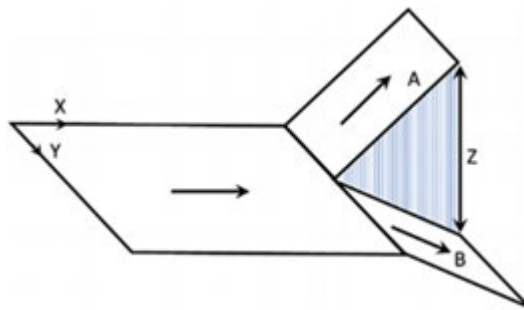
Figure 2-28 Illustration of crack propagation in two adjacent colonies and planes with different directed crystallography (Gerd Lütjering et al., 1998).

The fatigue behaviour of EBM and SLM were studied and compared by Rafi et al. (Rafi et al., 2013). The fatigue limit for samples built by EBM and SLM were 340 MPa and

550 MPa respectively. The SLM Ti6Al4V process has a fine martensitic phase that acts as a hindrance for dislocation motion, therefore, a strengthening effect occurs and the plastic strain in the material during strain amplitude of fatigue test decreases. While the EBM Ti6Al4V alloy has a lamellar microstructure, the fatigue strength of the Ti6Al4V alloy in the SLM process is higher than the alloy produced by the EBM process. In addition, Seifi et al. studied fatigue crack propagation behaviour in five directions based on build orientations in the EBM process due to the existence of anisotropy in properties (Seifi et al., 2015). Also, EBM parts were compared with cast and wrought Ti6Al4V, which were reported to be comparable. In this work, the dependency of build direction with anisotropic properties and microstructure were investigated, however, their relationship is still uncertain.

Zhai et al. investigated the fatigue crack growth of mill-annealed, EBM, and Laser Engineered Net Shape (LENS) Ti6Al4V at different low stress ratios (Zhai et al., 2015). In a stress ratio of 0.1, the fatigue crack growth of the β annealed sample in both vertical and horizontal directions was similar which was attributed to the equiaxed microstructure of β annealed meaning that both vertical and horizontal samples have an identical microstructure regardless of crack growth direction. Consequently, the behaviour of fatigue crack growth in both vertical and horizontal directions is identical. In crack propagation, the crack interacts with α lath and colonies to grow in EBM Ti6Al4V (Zhai et al., 2015). Although the β annealed condition showed similar fatigue crack growth behaviour, different orientated EBM samples had contrast in not only region I, but also region II. The data for region II was provided but was not microstructurally studied sufficiently. Also, it is stated that in LENS fabricated Ti6Al4V, the crack interacted with α'/α phases which is the primary propagation mechanism; and in EBM crack growth was controlled by α lath and colonies however no evidence was presented for this statement. In addition, the relationship between microstructure with FCG and crack path has been hardly addressed.

Benedetti et al. investigated the behaviour of small cracks during propagating from the notch in two different microstructures, bi-modal and lamellar, in the Ti-6Al-4V alloy with a four point bending fatigue test (Benedetti et al., 2004). A lamellar structure consists of coarse prior β grains with length of 600μm while bi-modal microstructure had primary α grains of 20μm with a lamellar colony of α and β plates inside the small β grains with 20-40 μm μm length. In stage I for the lamellar microstructure, in areas where the α lamellar colonies' orientations aligned with the load axis, the crack cut across the lamellae α and

β producing a transgranular path. In the area where the lamellar colony orientation had an angle of close to 90° with the load axis, the crack propagated along α lamellar colonies which means that the crack propagated in favour of α lamellar colonies' orientations. In the lamellar structure in stage II, the crack had a tortuosity and bifurcation path with a high angle to the crack direction in comparison to the bi-modal crack path. This difference was attributed to the interaction between the crack and the size of the colonies and grains which in the lamellar structure reached approximately 500μm while the bi-modal structure had a fine microstructure with grain size of approximately 20μm.
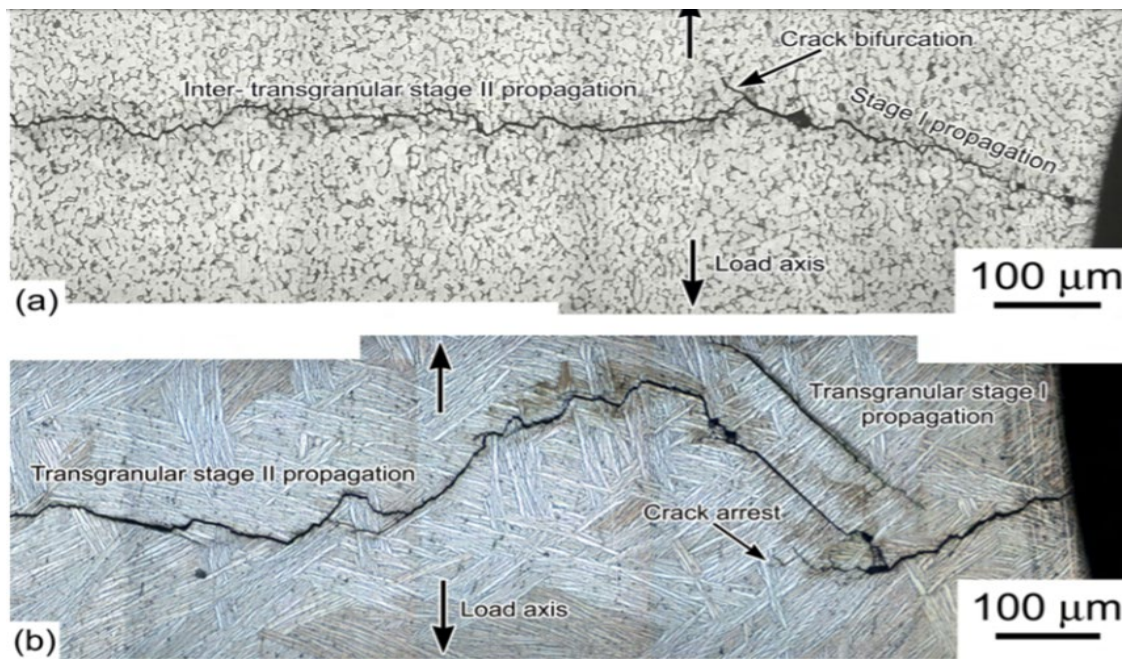
Figure 2-29 Micrographs of crack path from crack initiation at the notch in the right side to crack propagation at the left side in two microstructures of a) bi-modal and b) lamellar (Benedetti et al., 2004).

Seifi et al. studied the crack growth using a three-point bend test on two groups of samples, each group being produced by different EBM machines A2X and A2 (Figure 2-30) (Seifi et al., 2017). In the A2X processed sample, the crack propagated regardless of α laths, α colonies, prior β grain boundaries and α/β interfaces, while in the A2 processed sample, the crack deflected and propagated along the α/β interface and crossing β phases. The EBSD scan of the crack area in A2 processed was shown in Figure 2-31 and Seifi et al. described that the crack crossed the prior β grain boundaries during propagation. Although two groups of samples in two different EBM process versions were compared, the crack deflection due to changing the crack direction for traveling along α/β interfaces was not supported clearly (Figure 2-30). In addition, the crack propagation in the A2 sample was analysed with EBSD scan; however, it is difficult to

observe the crack interaction with α and β phases in the presented EBSD scan image. Also, there was no EBSD scan for crack propagation of the A2X sample to compare with the A2 sample. Moreover, the SEM image of the crack path of the A2-processed sample did not clearly show the β orientation during crack deflection. In the A2X-processed sample's crack path shown in the lower SEM magnification it was difficult to observe the difference. Thus, there is lack of support for the crack path statement (Seifi et al., 2017).
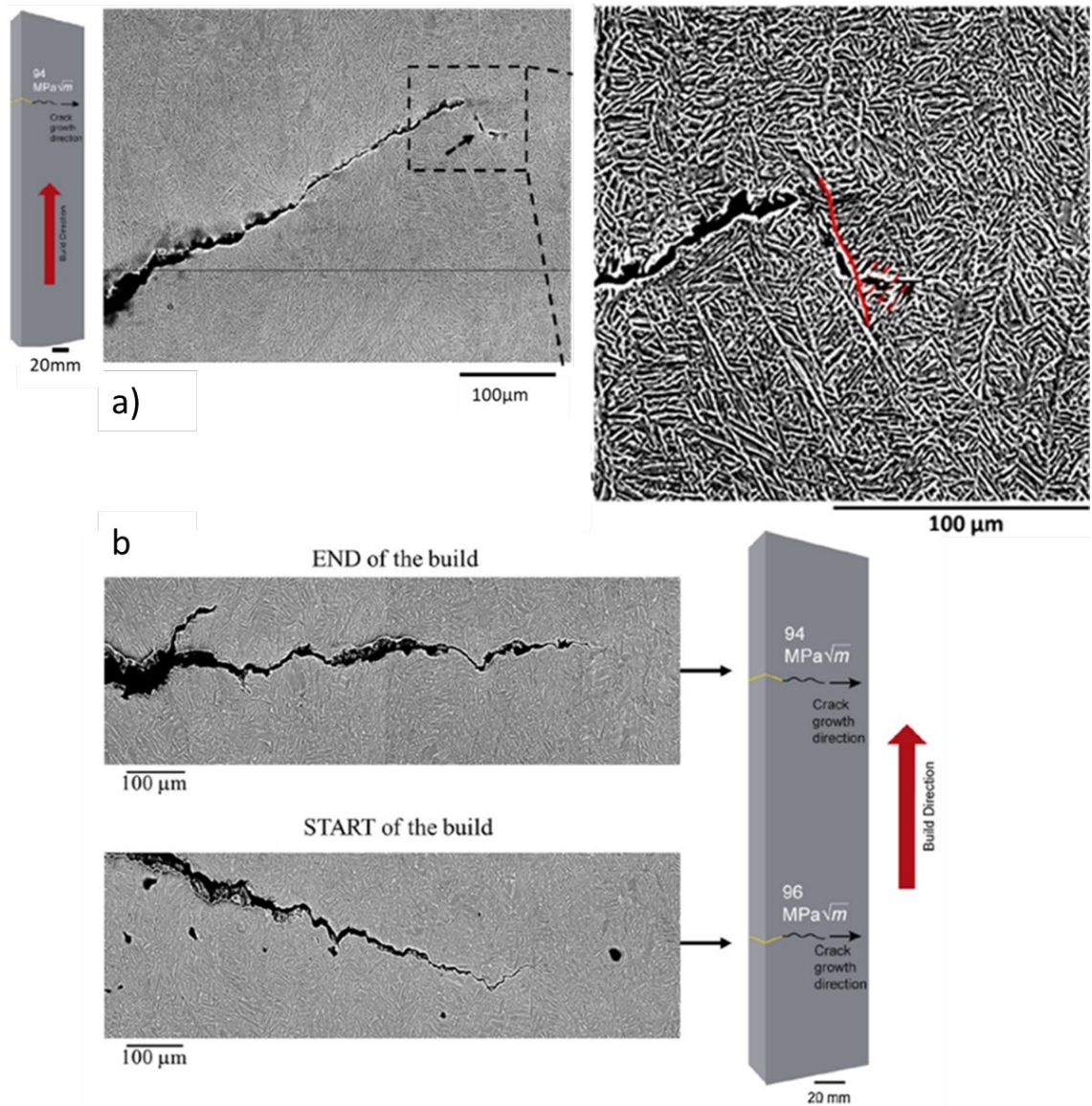
Figure 2-30 Crack path at the end of the build for microstructural Ti6Al4V alloy in two different versions of EBM process a) A2 b) A2X (Seifi et al., 2017).
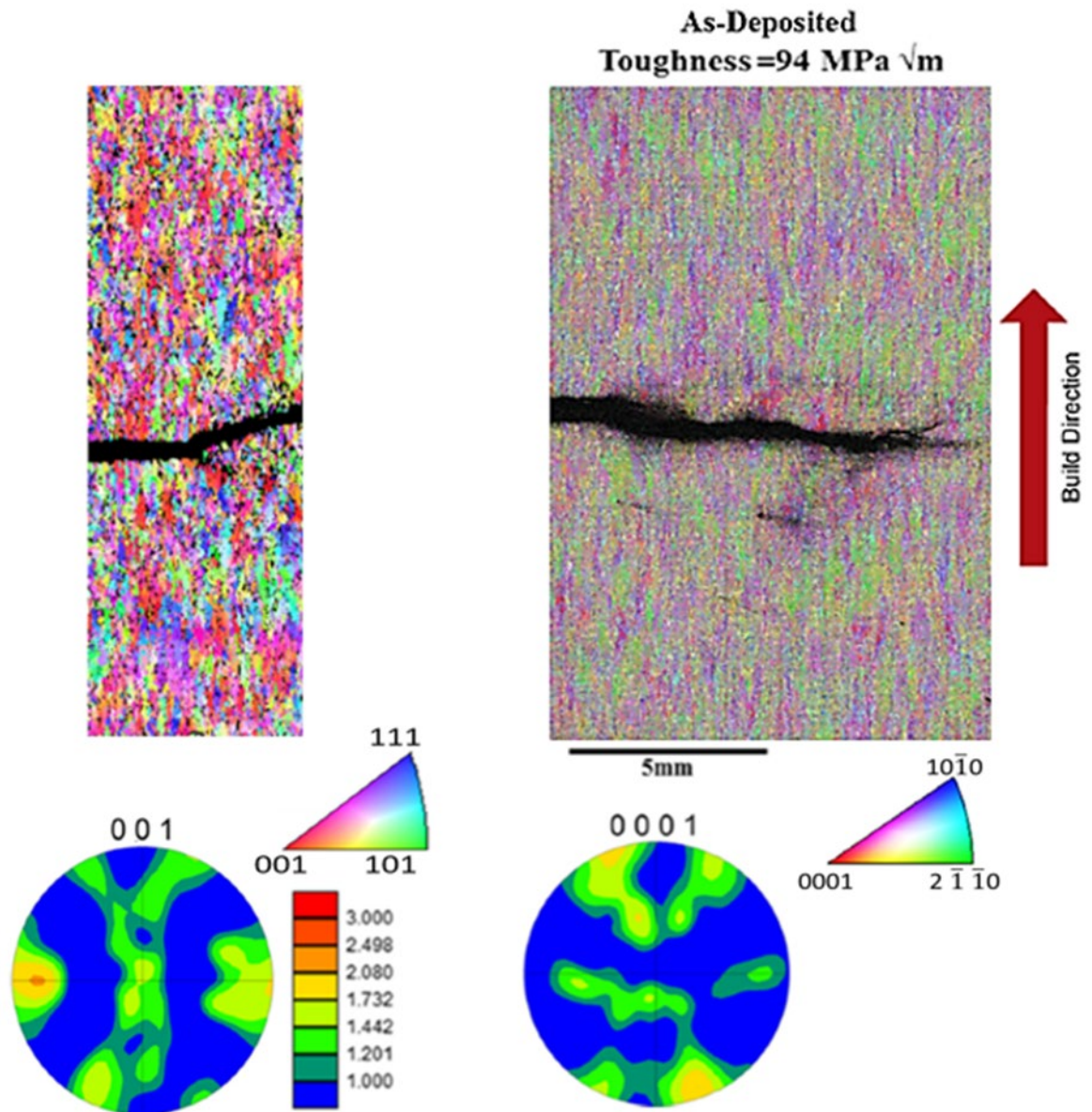
Figure 2-31 EBSD result of IPF map for the crack propagation in A2 processed sample (Seifi et al., 2017).

The fracture toughness of both build directions was examined and since the fracture toughness of the vertical sample (with values of 95-105 MPam$^{0.5}$ in A2X- process and 83-95 MPam$^{0.5}$ in A2 process) was higher than in the horizontal sample (with value of 82 MPam$^{0.5}$), it was expected that the crack path had so many prior β grain boundaries to pass through during travelling, while in the horizontal sample, the crack propagates along prior β grain boundaries, so there was more resistance of crack propagation in vertical sample than horizontal one (Seifi et al., 2017).

Zhai et al. reported that the main mechanism of fatigue crack growth in the Ti6Al4V alloy is a crack interaction with the α/ά phase. The fatigue crack growth is controlled by α lath

and colonies (Zhai et al., 2015). However, there is no further explanation or evidence of demonstrating the crack interaction with the α/ά phase at a high magnification. The microstructures of the EBM Ti-6Al-4V crack path in all three regions of region I, Paris region II and region III are shown in Figure 2-32. In region I or the threshold regime, not only crack closure, but also crack front geometry and intrinsic material properties act as key factors that affect fatigue crack growth resistance. The influence of these factors may change for different stress ratios. For instance, in the low stress ratio like 0.1, crack closure is the main influence in fatigue crack growth resistance, while in higher stress ratios, the key factor is crack front geometry. All these factors are related to the size and morphology of the microstructure such as α colony. In as-fabricated EBM Ti6Al4V alloy, due to possessing a much smaller α colony size compared to β annealed material with equiaxed structure, the influence of crack closure and crack front geometry factors increases; which means that the material resistance to crack growth increases. Therefore, increasing fatigue crack growth resistance in a material is due to finer microstructure (α colony and grain size) (Galarraga et al., 2017).
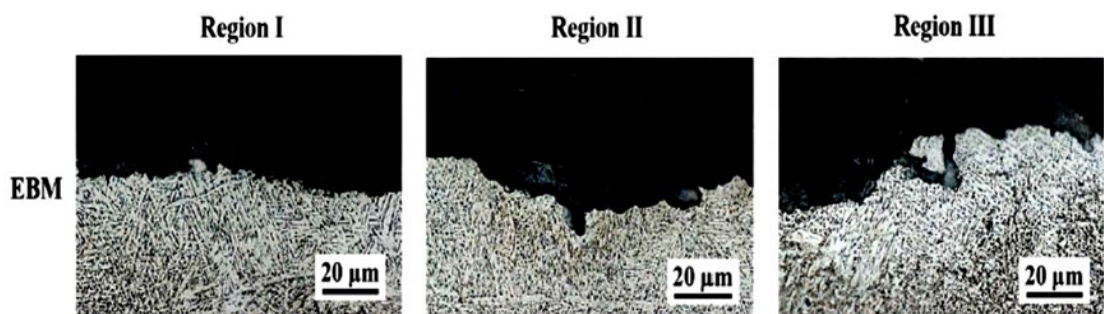
Figure 2-32 Three regions of fatigue crack growth in EBM Ti6Al4V alloy (Zhai et al., 2015)

Haize Galarraga et al. studied the relation between fatigue crack growth of two different build directions and microstructures of Ti6Al4V alloy produced by EBM and heat-treated ones (Galarraga et al., 2017). The microstructure of the EBM as-fabricated Ti6Al4V ELI alloy with columnar prior β grain boundaries parallel to build direction Z is shown in Figure 2-33a. In the higher magnification of the as-built sample, the prior β columnar grain boundary (α layer) can be seen well in Figure 2-33b. In addition, the equiaxed microstructure of β-annealed with heat-treatment above the β transus temperature shows in Figure 2-33c that the slow cooling rate in the heat treating process changed the lamella α+β Widmanstätten morphology and size in the equiaxed microstructure (Galarraga et al.,

2017). By applying heat treatment, the volume fraction of the ductile β phase increases (Greitemeier et al., 2017).
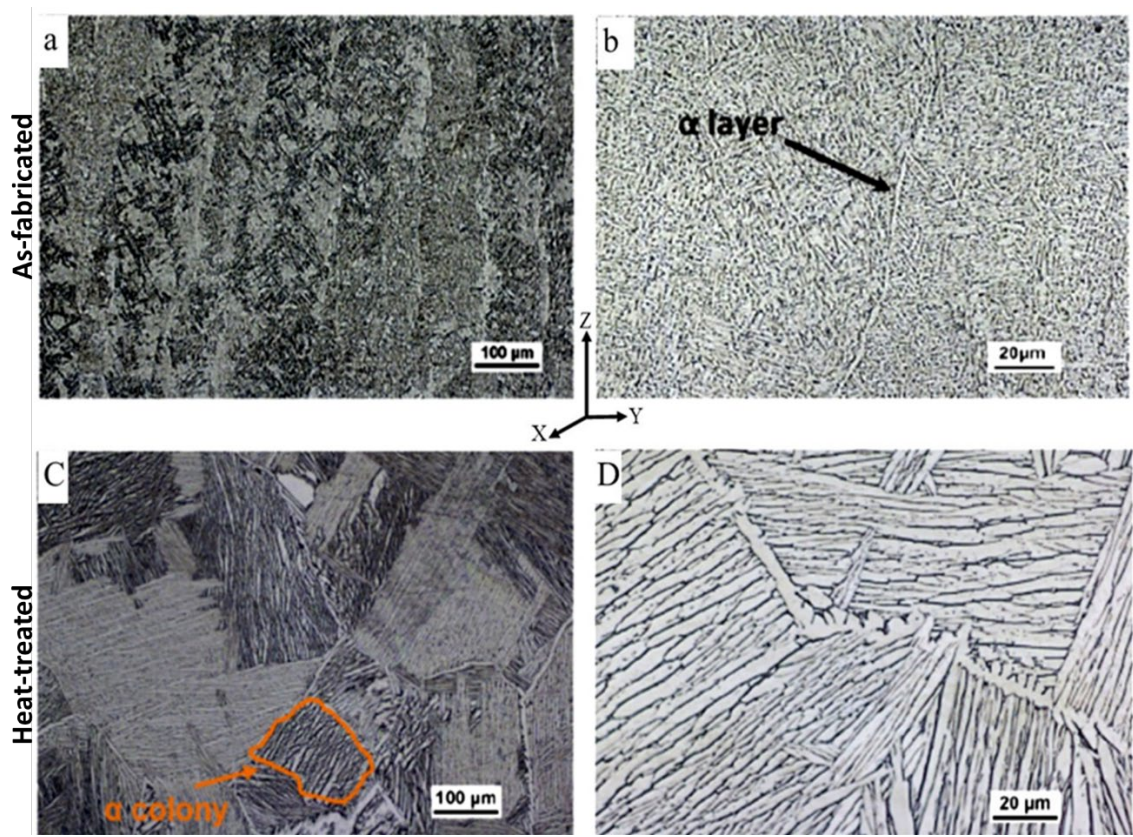
Figure 2-33 SEM microstructure images of EBM Ti6Al4V alloy in the as-fabricated sample shows: a) the columnar grain boundaries, b) α boundary or the prior ß grain boundaries, and in heat-treated sample: c) the equiaxed β-annealed microstructure the α colony area, d) the high magnification for showing the ß phase length (Galarraga et al., 2017).

Galarraga et al. investigated the crack path in region II for two different microstructures: as-fabricated EBM and β annealed samples (Galarraga et al., 2017). Figure 2-34 shows crack branching in the as-fabricated EBM Ti6Al4V alloy in both directions, vertical and horizontal, while crack branching is not observed in the β annealed samples. The branching behaviour of the horizontal sample of the as-fabricated EBM Ti6Al4V alloy was reported to be more noticeable and prominent, where the crack direction is parallel to the build direction compared to its vertical direction where the crack direction is perpendicular to the build direction (Galarraga et al., 2017). Crack deflection occurs when it interacts with larger α lath regions in comparison with finer α lath regions. Since the α phase has a preferential orientation in the Ti6Al4V microstructure, it affects the crack growth path, especially when the cracking direction and preferential direction of α phase

51

are more or less aligned. The schematic of this statement is shown in Figure 2-34. The crack needs energy to propagate and grow; consequently, when branching and tortuosity occur during crack travel, the crack needs more energy to continue propagating. The crack interaction with α colonies in the β annealed microstructure causes deflection in the crack path and this deflection is not usually favourable for crack propagation. However, the authors did not provide any evidence to explain the statement. Also, because of the large α colony size in the β annealed microstructure, the tortuosity distance between the two deflections is larger than in the as-fabricated EBM sample with a fine α colony size. The β annealed crack path is shown just in the horizontal sample due to having the same equiaxed morphology in both samples (Galarraga et al., 2017).
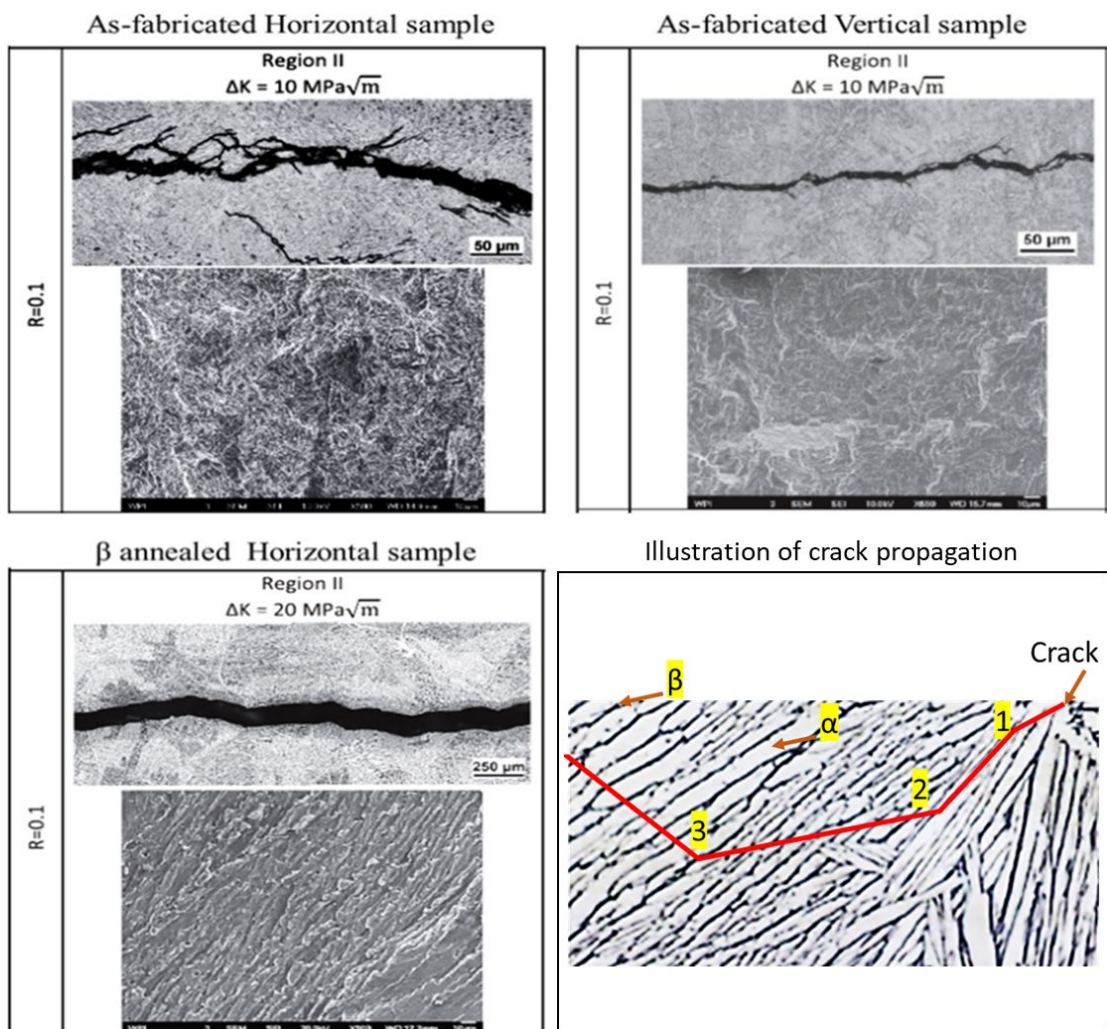
Figure 2-34 Fatigue crack growth of region II in the as-fabricated EBM Ti6Al4V alloy in different orientations of horizontal and vertical compared to the β annealed samples, which represent both horizontal and vertical due to having a similar microstructure (Galarraga et al., 2017). The illustration is sketched based on the literature crack propagation statement.

Galarraga et al. suggested that in the horizontal sample, the crack passes through so many scan layers, where the boundary between two adjacent deposited layers of the EBM process is. Hence, those deflections were attributed to the scan layer, with thickness of ~0.05mm as a barrier. When the crack reaches a region that needs more energy to propagate this is known as a barrier. In Figure 2-35, the scan layers in the EBM sample are shown. During the EBM process, an amount of powder is deposited and melted, and the next powder layer is deposited again. The boundary between the two deposited layers is called a scan layer and it was stated that these scan layers are barriers and the crack need more energy to propagate through them.
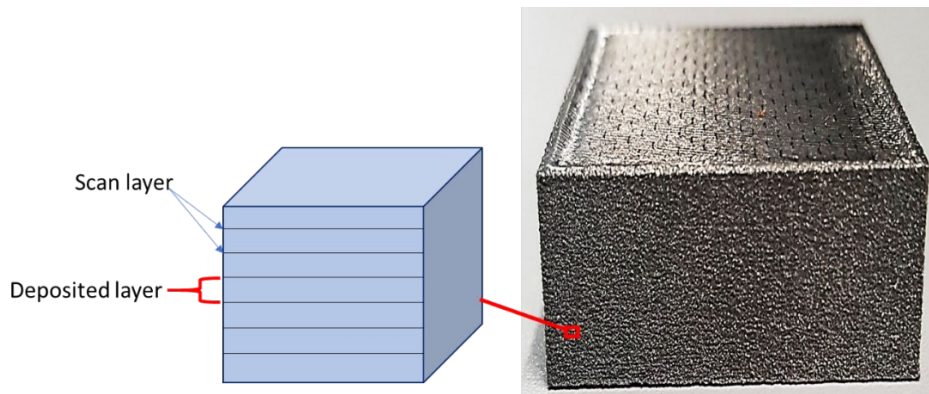
Figure 2-35 Schematic of scan layer in the EBM sample.

The vertical sample crack does not interact with scan layers, it interacts with another barrier, columnar grain boundaries, which are shown in Figure 2-36. Crack growth rate ($\frac{da}{dN}$), which is the amount of crack extension in a cycle, in the horizontal sample is higher than in the vertical one. It implies that the horizontal sample needs more energy to propagate than the vertical sample. Since in the horizontal sample (crack parallel to the grain boundary) the crack travels through not only scan layers, but also grain boundaries, this means that the crack passes through two kinds of barriers, while in vertical sample (crack perpendicular to the grain boundary), there is only one barrier. The number of barriers during crack propagation and the rate of crack growth is contradictory to Galarraga et al.'s hypothesis and deduction. In addition, it was explained by Yuwei Zhai et al. that in horizontal crack growth, which is parallel to columnar boundaries, the layer boundaries (scan layers), which are the deposited layers during production of the part, act as a barrier (Zhai et al., 2015). When the crack reaches scan layers and columnar prior β grain boundaries, a rough fracture surface is generated in comparison to the vertical sample. Because scan layers and prior β columnar boundaries act as barriers in the horizontal sample that leads the crack path to become rougher than in the vertical sample,

which is perpendicular to columnar grain boundaries and parallel to scan layers. In the vertical sample, the crack has only one type of barrier which is grain boundaries due to the crack being parallel to the scan layers and perpendicular to the grain boundaries. In addition, there is a doubt about the scan layer as a barrier due to lack of evidence. In the EBM sample, there are so many scan layers and if the scan layers are barriers, the energy required by a crack to pass all those scan layers is much higher than a crack which propagates parallel to the scan layers. In addition, during the EBM process, for producing a new layer, more than two layers are re-melted. Hence, the last scan layer microstructure is heat-treated several times and homogenized with the rest of the microstructure.
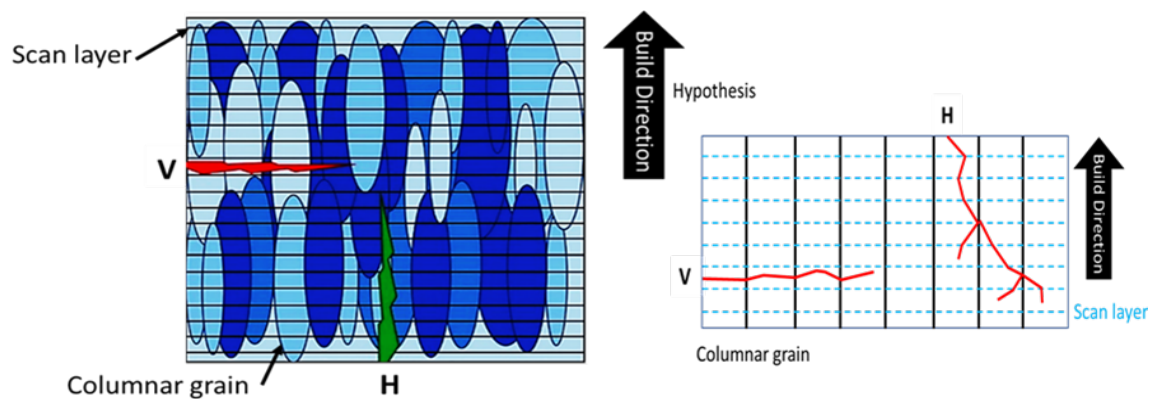
Figure 2-36 Hypothesis of how crack interacts with the scan layer and the columnar grain during propagation in two different orientated samples (Galarraga et al., 2017).

In addition, not only Zhai et al. but also Sandgren et al. stated and showed an α columnar boundary on the fracture surface, as shown in Figure 2-37, but there was no evidence or support how the grain boundary was identified on the fracture surface (Sandgren et al., 2016; Zhai et al., 2016).
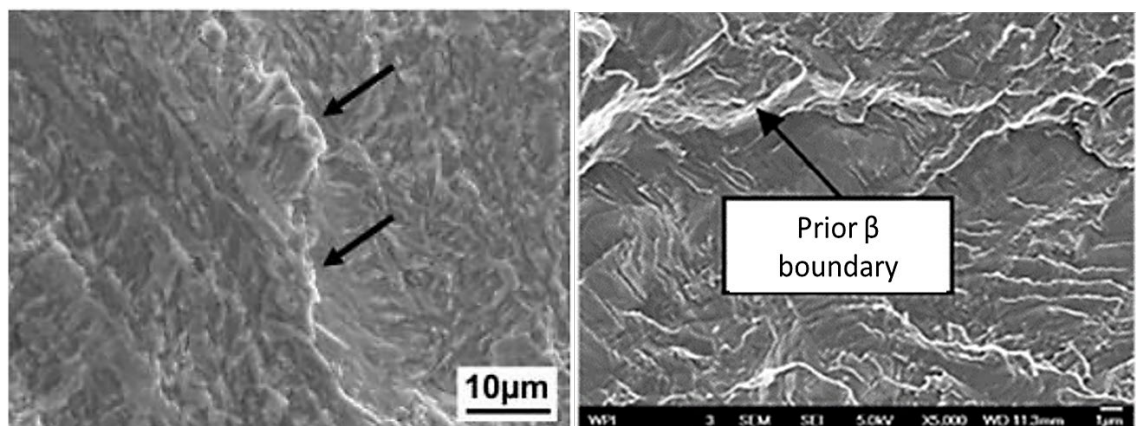
Figure 2-37 SEM image of the fracture surface in region II that shows prior β grain boundaries in horizontal crack growth (Sandgren et al., 2016; Zhai et al., 2016).

Summarising the studies above shows that many studies have been done on crack growth or crack paths in Ti6Al4V alloy produced by EBM in different orientations. However, the effect of the directional structure of this alloy on fatigue crack growth propagation in three different (vertical, horizontal and 45°) anisotropic orientations has not been studied sufficiently, particularly for region II. As was discussed in the last section, the α grain boundary is a barrier for the crack to propagate, so the crack propagation behaviour in different directions needs to be studied, particularly, the sample which is built with an angle of 45° to the deposited powder layer, which has not been studied in the Ti6Al4V alloy. In addition, there is doubt about the scan layer (the boundary between two adjacent deposited solidified layers) as a barrier due to lack of evidence. Therefore, the aim of this study is understanding the crack propagation path of EBM Ti6Al4V alloy in linear region II in different orientations.

Edwards et al. studied fatigue crack growth graphs of two EBM vertical and horizontal directions and the region II of both directions were identical, but the reason was not microstructurally explained and studied (Edwards et al., 2013). Also, there is little difference between the region II fatigue crack growth graph of two vertical and horizontal as-fabricated EBM Ti6Al4V alloys in the Mohsen Seifi et al. study; however, there was no explanation provided (Seifi et al., 2015).

2.6.4.3 Relation of crack growth and striation formation

In fatigue crack growth, the crack propagates more or less perpendicular to the applied load direction. After crack initiation from the material's free surface, the crack involves slip deformation on slip planes which can be explained by the crack mechanism during a single load cycle (Figure 2-38a). When a load is applied on an initiated crack, the crack tip is opened up on two symmetric slip planes with maximum shear stress in the plastic deformation zone, which is around the crack tip. The first applied load is a tension load that causes a two-symmetrical plane slip in front of the crack tip. By unloading the tensile load, it becomes a compression load because, during tensile loading, the deformation that occurred on the slip planes is completely un-reversible due to strain hardening and plastic deformation, so, two other slip planes, which are almost mirrored with the tension loaded slip system, get activated with a compression load. Thus, the first cycle of fatigue crack growth forms, which contains tension and compression loads. This single generated fractured area is called a striation and the direction of the striations usually indicates the main crack direction (Dubey, Soboyejo, & Soboyejo, 1997; Schijve, 2009).
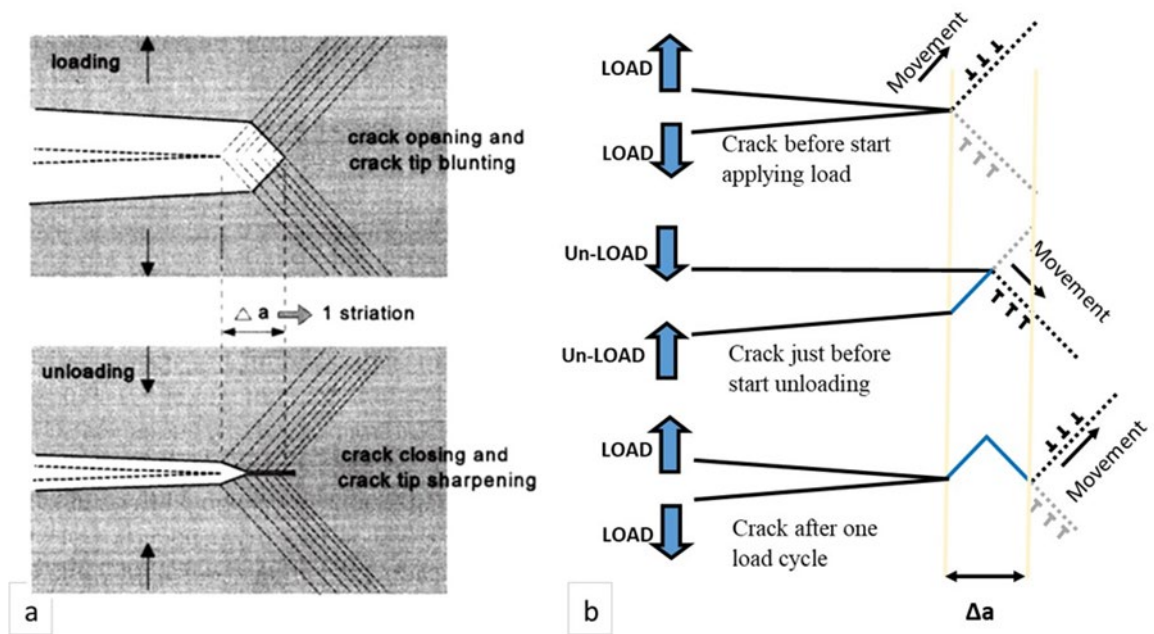
Figure 2-38 Schematic of a) Crack growth mechanism of one load cycle (Schijve, 2009), b) Step by step movement of crack growth mechanism of slip systems for generating a striation.

The primary stage of fatigue crack growth is characterised by the initiation of cracks with the coincidental striations, if there is any. This step typically creates at the surface and continues for a very short distance into the material. The second stage is characterised by striations that normally continue until final fracture or the cessation of cyclic loading (Connors, 1994). During fatigue crack growth, the stress concentrates at a sharp crack tip. It is assumed that one cycle of loading is a combination of one tension load and one compression load. In a tension load, two sides of the crack come apart in opposite directions then the sharp crack tip drives the crack to propagate. During the tension load, the crack tip becomes less sharp and more rounded which is not affective to support the crack growth anymore. In this point, stress intensity happens by plastic hardening and plastic flow at the crack tip. The tension load changes to a compression load, therefore the two parted materials try to go back to the previous place before tension started. In the meantime, the crack tip starts to become sharp from a radiused tip. The compression load prepares the crack tip for another crack propagation recognized as subcritical crack growth as its microscopic process generates a striation on the fracture surface (Figure 2-39). This cycle of loading continues until the stress intensity at the crack tip exceeds the fracture toughness when the crack propagation is catastrophic and recognised as critical crack growth (Connors, 1994).
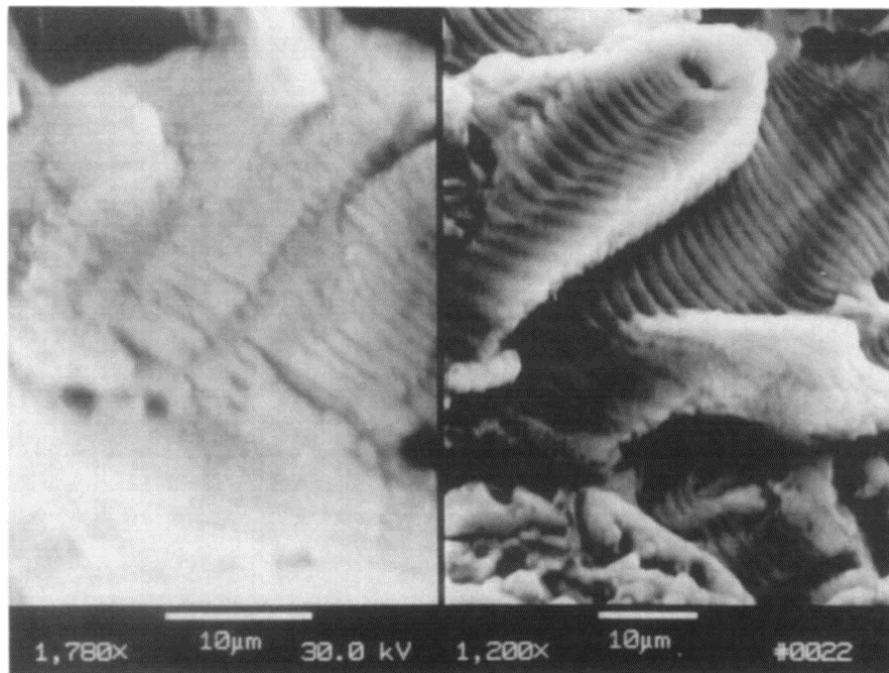
Figure 2-39 The striation feature that occurred from in distance of 14.32 mm from the surface side in the region II (Connors, 1994).

A.L. Pilchak et al. investigated the formation of the facet of crack growth at low ΔK in cast and HIPed Ti6Al4V alloy (Pilchak et al., 2009). It was stated that a striation represents one cyclic load. During cycle loading, opening displacement in the crack tip increases and creates ridging and by unloading the load, the crack tip is re-sharpening, which makes a feature of a striation on the fracture surface (Figure 2-40).
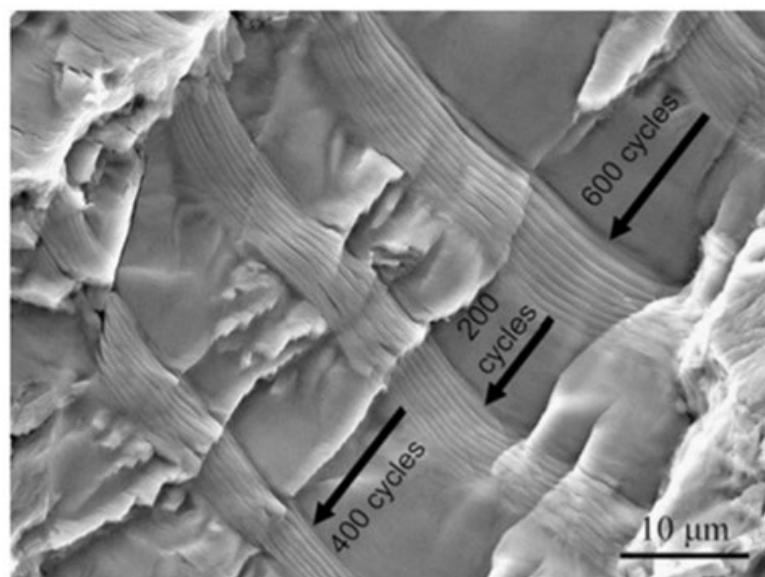
Figure 2-40 Influence of ΔK on fracture feature representing striation during overload cycle (Pilchak et al., 2009).

M. Janecek et al. described the fatigue behaviour of Ti6Al4V alloy. The striations are usually oriented normal to the main crack propagation direction. However, different striation directions in one area were seen and the reason for different local striation directions was not explained (Janeček et al., 2015).
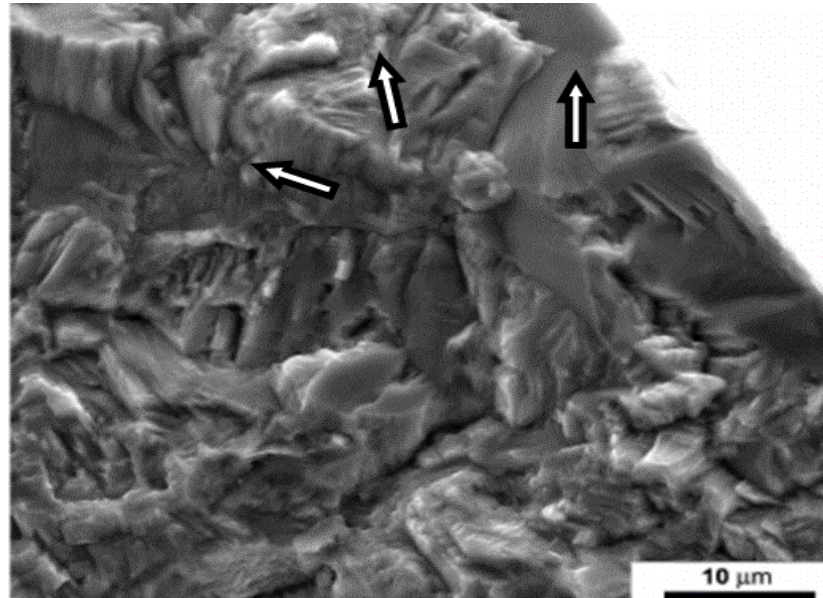
Figure 2-41 The different striation directions in one area of Ti6Al4V alloy (Janeček et al., 2015).

In another study, Sandgren et al. studied fatigue crack behaviour in LENS fabricated Ti-6Al-4V and striations were measured using an SEM and microtomography (Sandgren et al., 2016). The measured striation value showed an agreement with FCG data in the upper Paris region II. It should be mentioned that the linear Paris region is divided into two areas: the upper side, which is from middle to the start point of region III, and a lower region, which starts from the end of region I until the middle of region II.

2.7   The objective of this PhD thesis

From literature reviews and preliminary work, defects which are generated during the EBM process play an important role in detrimentally affecting the mechanical properties and performance of the parts. The formation of defects, particularly LOF, depends on the melt pool shape and size. Many studies have attempted to identify melt pool geometry in the EBM process and melt pool geometry in different materials has been observed experimentally except in Ti6Al4V alloy. When a new melt pool is formed by the electron beam on the top of the solidified layer, a part of the melt pool beneath is melted. Therefore, a part of the underneath melt pool re-melts and re-solidifies, so a new

microstructure starts nucleating and growing with the columnar grain structure. In addition, a zone around the melted area is a heat affected zone which makes the microstructure heat treated. Because this area is not melted, it is suggested that its temperature is below the β transus, hence, α phases in this area begin to transform to β phases partially. As soon as the temperature drops, the transformed β phases start transferring to α phases. The previous melt pool shape print vanishes due to these several phase transformations. From the melt pool shape and geometry of different materials, it turned out that the sizes are not similar because of the different thermal properties of the materials. Therefore, the Ti6Al4V alloy melt pool could not be understood by knowing other materials' melt pool geometries. In addition, from reviewing the literature, the LOF is a sensitive process and the influence of defects/LOF in different build directions on toughness has not been studied sufficiently. There were limited and incomplete studies on the effect of defects/LOF on toughness such as not distinguishing the defect types (porosity and LOF) to understand how detrimental each type is in EBM processed parts. Also, the crack propagation path of a Charpy fracture surface in Ti6Al4V alloy has not been studied.

Apart from that, many pieces of literature have been focused on region I where crack growth is affected microstructurally. According to the linear Paris law equation, region II is affected by the microstructure of the alloy, however, the sensitivity of crack growth in regard to the microstructure is less than in region I. The fatigue crack growth path in region II has not been studied sufficiently. In some articles, the fatigue crack growth of Ti6Al4V alloy was performed in two different build directions. Region II for both build directions in the fatigue crack growth graph was identical. In addition, in some other works, the fatigue crack growth graph of this region for different build directions behaved differently. However, for both different and identical fatigue crack growth graphs, no further explanation was given for the region's behaviour. Therefore, there is a need to study and investigate the fatigue crack growth path of region II and how a crack propagates in an anisotropic Ti6Al4V alloy and, in addition, to understand if defects/LOF have any influence on crack propagation in this region. Furthermore, although fatigue crack growth in vertical and horizontal directions has been included in many studies, samples that were built with an angle relative to the horizontal plane were not studied. Thus, this thesis research on EBM of Ti6Al4V alloy aims to answer the following questions:

1. How does scan speed, as one of the process parameters of EBM, affect melt pool shape in Ti6Al4V?

2. How does scan speed and melt pool shape affect the formation and fraction area of LOF in Ti6Al4V?

3. How does a defect/ LOF affect impact toughness?

4. How does the build direction affect toughness?

5. How does the crack propagate in the microstructure of Ti6Al4V Charpy samples?

6. How does the crack propagation path behave in region II of an anisotropic Ti6Al4V alloy for three different build directions?

7. How does a defect/ LOF affect fatigue crack propagation in region II for three different build directions in the Ti6Al4V alloy?

8. Which factors of LOF, build directions and microstructure affect fatigue crack growth in Ti6Al4V and how?

In the Chapter 3, the experimental procedures and the analytical facilities are described and explained. In Chapter 4, detailed results of experiments and analysis for questions 1 and 2 are presented and discussed. Chapter 5 covers questions 2 to 5 and questions 6 to 8 will be answered in Chapter 6.

3. CHAPTER. Experimental Design and Procedures

This chapter details the experimental strategy process for each study and the application of different tests in the investigation of factors including, defect/LOF and the build direction on mechanical properties, microstructural responses and EBM Ti6Al4V performance.

3.1 EBM Machine

Samples were fabricated on an Arcam Q10 EBM machine operated by Zenith Tecnica Co. from Ti6Al4V ELI alloy powder. The Arcam Q10 EBM has a maximum beam power of 3KW with a voltage of 60KV and a beam diameter of 0.4mm. parts are fabricated within a build chamber with a maximum size of 200mm (X) ×200mm (Y) ×180mm (Z). Prior to build commencement, the build chamber is pressurised to 1×10^{-5} mbar, and as the build commences, helium gas is added into the chamber at a 2×10^{-3} mbar.

Figure 3-1 "Arcam Q10 EBM machine"(Prabhakar, Sames, Dehoff, & Babu, 2015)

During the build process, the helium gas pressure is maintained at ~2×10^{-3} mbar in order to keep the chamber environment free from contamination and to maintain the chemical composition of the produced parts. Further temperature control is achieved through heating the build platform to 700°C, reducing the effect of residual stress on the fabricated part.

3.2 Ti6Al4V powder

The Ti-6Al-4V ELI powder used in all experiments were supplied by APA Co. with the composition as given in Table 3-1.

Table 3-1 Composition of Ti6Al4V alloy in wt%

Ti	Al	V	N	H	C	Fe
Balance	5.5-6.5	3.5-4.5	<0.05	<0.012	<0.08	<0.25

The powder particles size range as specified by the supplier is between 45-106μm with the powder distribution provided by Arcam (AP&C) Co. following the ASTM B214-07 standard to be 3.2% 0-45μm, 53.2% 45-75μm, 40.7% 75-106μm and 2.9% 106-250μm. Furthermore, as evident in Figure 3-2 the powders are of spherical morphology with an apparent density of ~ 2.7 g/m^3. In Figure 3-2 it can also be seen that the powder particles are a combination of sizes, ensuring ideal distribution mechanics and powder packing density.
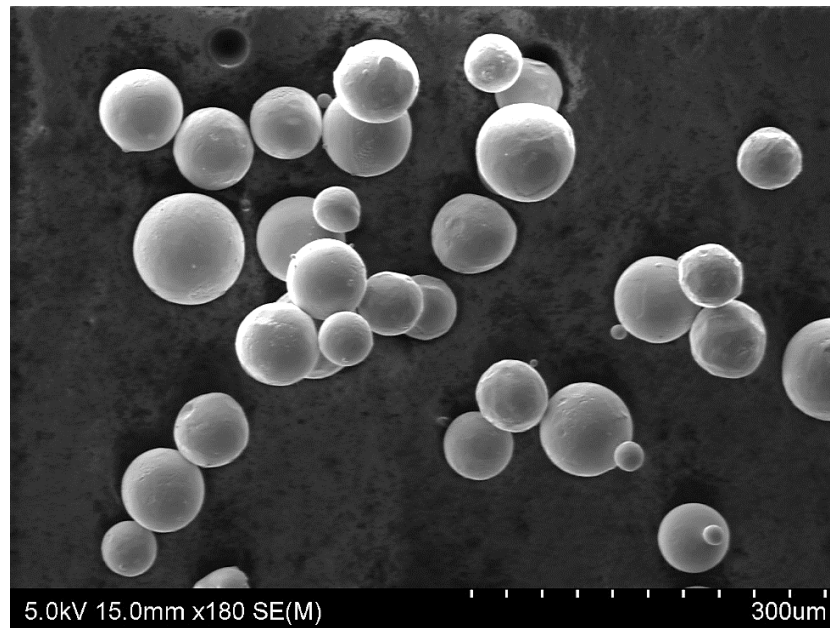
Figure 3-2 SEM of Ti6Al4V powders

Evident in Figure 3-2 is Ti6Al4V particles smaller than 45μm which are sintered to the larger particles, forming in a particle within the powder range of 45-106 μm.

3.3 EBM parameters

The default processing parameters of the Arcam Q10 EBM were provided by Arcam Company and are shown in Table 3-2.

Table 3-2 The EBM processing parameters for samples on the Arcam Q10 EBM

Sample	Scan speed (m/s)	Beam current (mA)	Hatch space (mm)	Focus offset (mA)	Layer thickness (mm)	Layer rotation (°)	Beam diameter (mm)	Speed Function -	Line order
Default	-	-	0.4	26	0.05	67	0.4	28	1
1	5	28	0.4	26	0.05	90	0.4	-	1
2	9	28	0.4	26	0.05	90	0.4	-	1
3	12	28	0.4	26	0.05	90	0.4	-	1
4	16	28	0.4	26	0.05	90	0.4	-	1
5	18	28	0.4	26	0.05	90	0.4	-	1

A z-shape scanning strategy was incorporated in melting each layer. As presented in Figure 3-3, this scanning strategy consisted of the electron beam started melting from Point 1 until termination at Point 2 followed by melting continuation at an angled line (red dashed line), arriving at the next scan line location at Point 3. This scanning strategy repeated until all the hatching lines were completed. Each point on the Figure 3-3 is divided into two lines, one that follows the started track line and the other joining to the next track line. Thus, for each track line, the electron beam returned to the D side from T via the transfer route to begin melting the subsequent line.
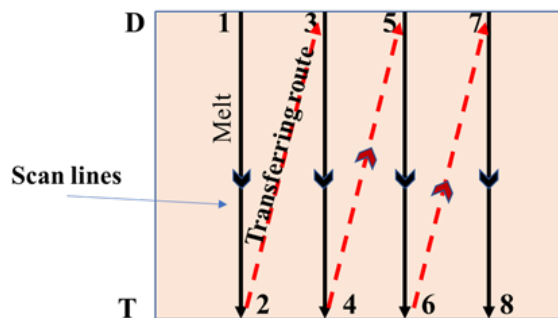
Figure 3-3 Illustration of the scan strategy procedure of a single layer from left to right.

3.4 Mechanical polishing and etching process

Preparation of metallurgical samples for SEM and optical microscopy analysis consisted of cutting the sample with a Struers Lotom-3 abrasive saw and a Buehler slow cutting

machine. The cut sample was then mounted in PolyFast phenoic powder resin in a Struers LoboPress-3 metallurgical mounting machine and heated to 180° at 20N of force for 6mins followed by water cooling for 5 minutes.

Mounted samples were ground manually with 180, 500, 1200 and 2400 grit SiC papers on a Metaserv rotary grinder. Following, a Struers TegraPol 21 automatic metallurgical polishing machine was used to polish samples with a 6μm diamond suspension (DP) and a 1μm standard colloidal silica suspension (OP-S) polishing paste. The final stage consisted of cleaning samples in a Techspan ultrasonic cleaner with 95% ethanol.

Etchant:

Mounted samples were etched by Kroll's reagent: 92% H2O distilled water + 2% HF + 6% HNO3 for metallurgical examination.

Optical microscope (Opt):

For microstructure observation at low magnifications, an Olympus BX51M optical microscope was employed at magnifications of; 50x, 100x, 200x and 1000x.

Image J Software:

Image J image analysis software was used to analysing the size, shape and the volume fraction of particles from the SEM image.

Scanning Electron Microscopy (SEM) and Energy Dispersive Spectroscopy (EDS):

A Hitachi SU-70 Schottky field emission scanning electron microscope (SEM) was used for high magnification observation of microstructure, phases, grain boundaries and fracture surface analysis. SEM micrographs are obtained at different accelerating voltages, 5, 15 and 20 kV, depending on the microstructural features examined, and the magnification required. Energy Dispersive Spectrometer (EDS) on the SEM was employed to analyse the chemical characteristics and phases differentiation by incorporating the Noran System 7 (NSS) software. EDS is a chemical analysis method that determines the concentration of elements in a given sample and thus was used in quantifying the aluminium (Al) and vanadium (V) concentrations in different parts of the Ti6Al4V alloy microstructure. However, EDS technique has a limitation as the smoother the surface is, the stronger and more accurate the recognition of elements is (Nasrazadani & Hassani, 2016). During EDS analysis, the scattering of X-rays at a single point is obstructed by the rough surface, and the X-ray deflections cannot be accurately identified

by the EDS detector, and further complexities occur when surfaces are considerably steep and fluctuated (AZONetwork, n.d.).

3.5 Scan Speed parameter

In order to study the melt pool shape, LOF and the influence of these effects on each other, five groups of Ti-6Al-4V ELI samples were prepared. Samples were produced with dimensions of $25 \times 25 \times 20$ mm^3 and at scan speeds of; 5, 9, 12, 16, 18m/s while, maintaining other process parameters unchanged as presented in Table 3-2. Each subsequent layer was rotated 90° to the prior layer in order to investigate the effect of scan speed within the hatching area (Figure 3-4) with respect to sample location on the built-platform.
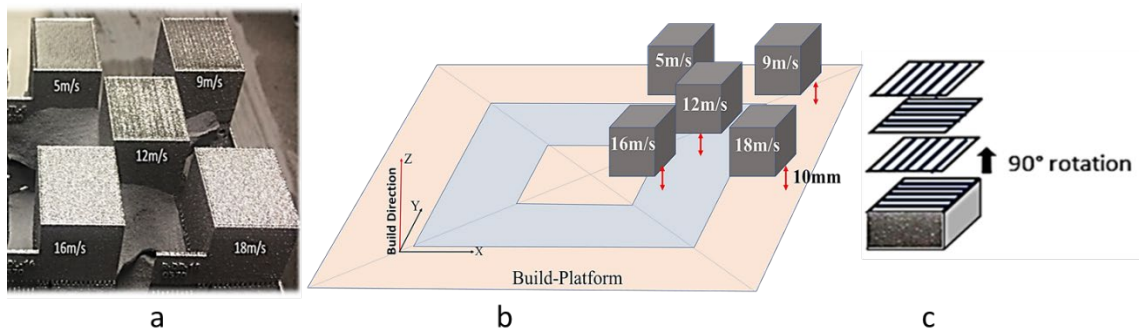
Figure 3-4 Samples with different scan speeds b) illustration of the locations on the built-platform and c) the scan pattern rotation for each layer.

Sample top surface and cross-sectional microstructure were studied using optical microscopy, and scanning electron microscope (SEM) with the samples cut perpendicular to the scan tracks/ track lines of the last layer on the surface as shown in Figure 3-5 and mounted as per Section 3.4.
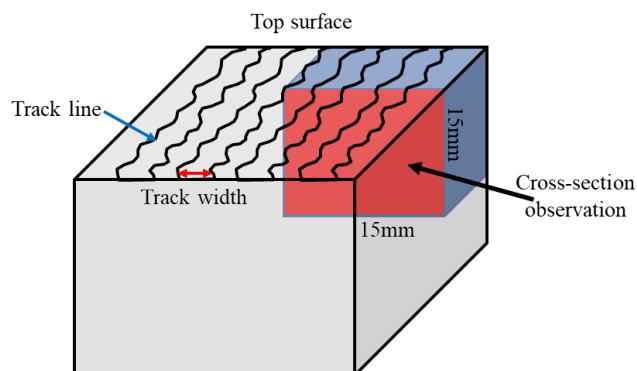
Figure 3-5 Illustration of the cut direction of all samples perpendicular to the final scan track represented by the black line on the top surface.

Microstructural observation, LOF and surface track lines of selected pieces for each scan speed group were done by SEM and optical microscopy with, Image J analysis software used in the evaluation of α columnar grain boundary width as evident in the illustration shown in Figure 3-6. SEM Images were taken from different locations on the sample where were possible in the analysis of α columnar grain boundaries.
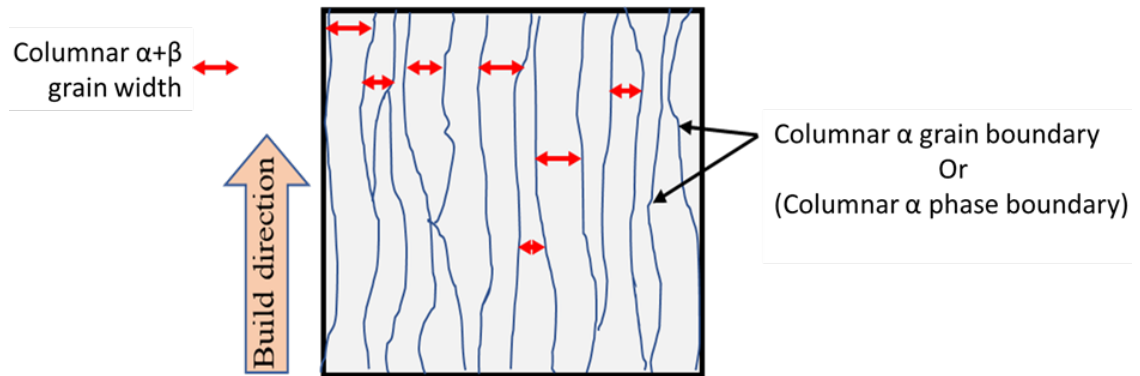
Figure 3-6 Illustration α grain boundary width measurement procedure.

Image J was further used in LOF area measurements taken at the cross-section depicted in Figure 3-5. It should be noted that the fraction of LOF that was measured for samples 5, 9, 12, 16 and 18m/s was from the SEM images of cross-section samples were prepared.

Also, this software was used for measuring the top surface from the cross-section side, as shown in Figure 3-7. Top surface roughness measurements indicate the crown of melt pool shape, necessary in the understanding of the effect of scan speed on melt pool shape. The optical microscopic image from the cross-section region Figure 3-5 was prepared by taking sequential images and merging them in a single total cross-sectional region image. A base line perpendicular to the build direction was outlined in a way to place on the lowest top surface area. Hence, according to the base line when the reference height is 0 mm, the roughness of the top surface was measured positively as shown in Figure 3-7.
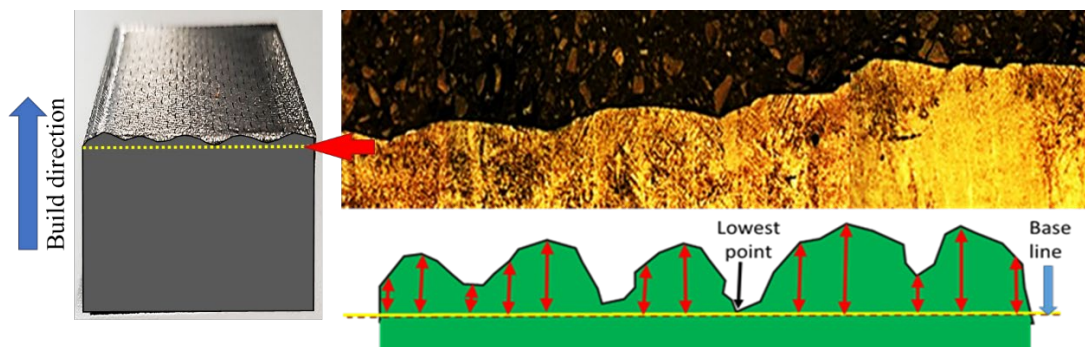
Figure 3-7 Cross-sectional micrograph of a samples top surface and illustration of the surface roughness measurement locations

3.6 Samples location vs defects

As mentioned in Chapter 1 and 2, defect formation significantly influences the mechanical properties and performance of EBM parts. As presented in Figure 3-8, three samples positioned at the centre, middle and the edge of the build-platform were used to evaluate the fraction of LOF and porosity along the build height. EBM processing parameters were consistent for each sample produced. The default processing parameters were used for producing these samples which are mentioned in Table 3-2. The build-platform as depicted in Figure 3-8 is separated by colour into regions denoting the sample positioning areas. Samples were further evaluated for a fraction of LOF and porosity along the build direction from the build-platform (from $Z = 0$ to $Z > 0$).
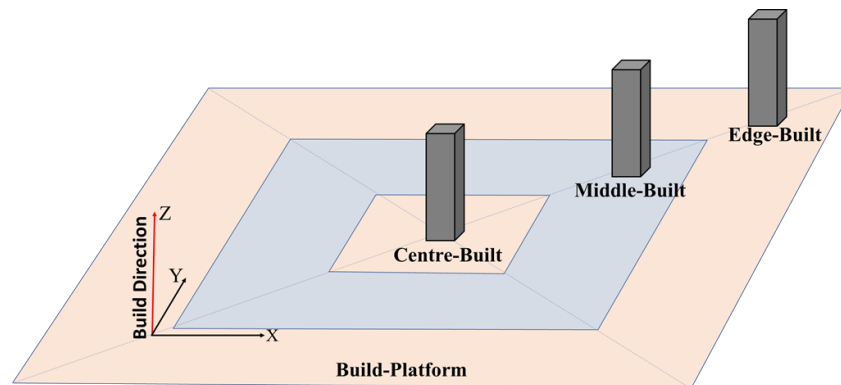
Figure 3-8 Location of samples on EBM platform in three areas; centre, middle and edge (See Figure 3-9 for details).

Synchrotron tomography:

A slow cutting saw machine was used to cut $3 \times 3 \times 2$ mm samples in three areas located at; 0, 25 and 50mm from the build platform as shown in Figure 3-9. These cubic pieces were prepared for synchrotron tomography analysis.
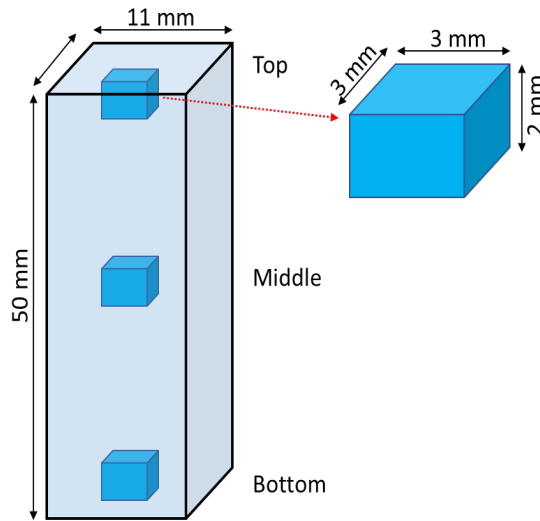
Figure 3-9 Illustration of sliced locations of the 3 × 3 × 2 mm samples for CT analysis.

Synchrotron tomography (CT) at the Imaging and Medical Beamline (IMBL) is a 3 GeV national synchrotron radiation which was employed in the evaluation of LOF and porosity level. Synchrotron tomography was invented in the mid-1980s and has seen considerable improvement over the recent years with particular growth in image resolution. It provides a practical way to obtain information on the shape and position of defects in the sample over a reasonable processing time and cost. CT consists of a monochromatic beam which penetrates the sample projecting X-ray attenuation profiles on the sensor. A 70 KeV monochromatic beam energy was used to penetrate into the sample fully. The sample is rotated from 0 to 180°, with a single image taken of the sample by CCD camera in half degree increments. A Scintillator screen is placed directly in front of the CCD camera to detect the context of monochromatic x-rays. The Scintillator screen thickness depends on the X-ray energies; therefore, the scintillator thickness layer can be optimised as the beam energy changes. Computers are connected to the X-ray source to control scanning parameters and to convert the 2D radiographs to 3D images. Settings used in the synchrotron test are summarized in Table 3-3 with a schematic of the synchrotron presented in Figure 3-10.

Table 3-3 Synchrotron setting parameters

Energy (KeV)	70
Pixel Size (μm)	5.7
Acquisition time (s)/Projection	0.07

Rotation Range (°)	0-180
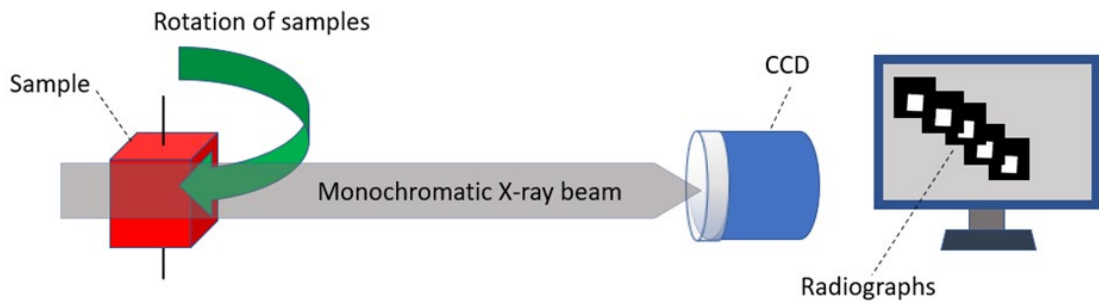
Figure 3-10 Schematic of synchrotron

The video taken by the synchrotron is converted to 2D images as presented in Figure 3-11a, with a single image from each area chosen to represent the location and height of each sample. A representation of the LOF and porosity 2D converted image is enlarged in Figure 3-11b.
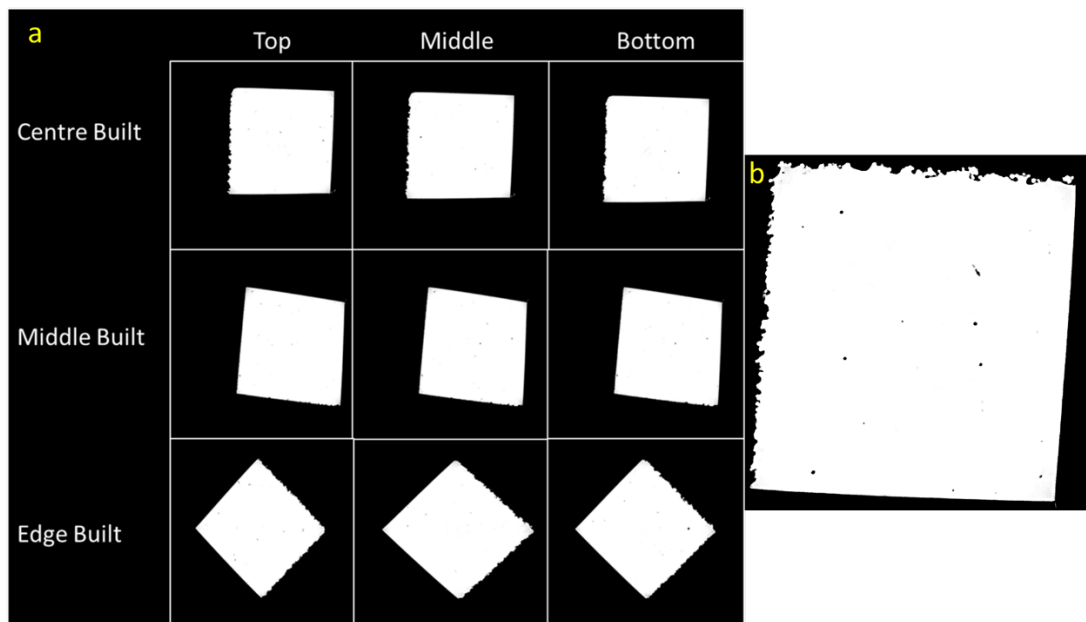
Figure 3-11 2D synchrotron images a) at the; top, middle and bottom for each of the three build locations and b) the high magnification of a 2D synchrotron image.

Detection of LOF's can be achieved by both high-resolution synchrotron and optical microscopy, however, the synchrotron could not identify any defects less than 6 μm in size.

The volume and total area of LOF and porosity were measured in each image through the use of ImageJ analysis software. The fraction of LOF area is represented as a percentage of the sample by the equation presented below:

Equation 3-1

$$f_{LOF}\% = \frac{\sum area \ of \ LOF \ for \ each \ 2D \ converted \ image}{total \ number \ of \ images \times (area \ of \ the \ sample)} \times 100$$

Sample area is noted as the length × width multiplied by the number of images and is repeated in principle for the fraction of porosity area.

3.7 Charpy Impact Energy

The Charpy impact test is the widely used destructive testing method in evaluating impact strength and absorbed the energy of the metal samples. The default parameter settings presented in Table 3-2 were used in the production of the Charpy samples. The V-shape Charpy samples were produced with the geometry of 11×11×56 mm and machined via CNC electrical discharge machining (WEDM) to 10×10×55 mm as per ASTM standard E23, with a 45° notch angle, 2mm notch length and 0.25mm core radius.

The Charpy impact test, type 6703 made by AVERY Birmingham, consists of a load that swings in a pendulum motion from a fixed height suddenly striking the sample. The specimen was positioned horizontally, with the notch location away from the pendulum motion as shown in Figure 3-12. The pendulum was released in a single swing hitting the sample, and the energy absorbed in fracturing the sample was measured on the indication dial prior to removal of the sample.

Three groups of specimens were built in three different orientations of; 90° (H), 45° and 0° (V) as shown in Figure 3-13. Each group was manufactured in the middle of the EBM build platform with identical processing parameters. From each batch, three samples in each orientation (V, 45° and H) were tested with a pendulum of 300J maximum energy at a speed of 5 m/s. The pendulum struck the Charpy samples in the middle on the un-notched side in room temperature conditions. The default processing parameters were used for producing these samples which are mentioned in Table 3-2.
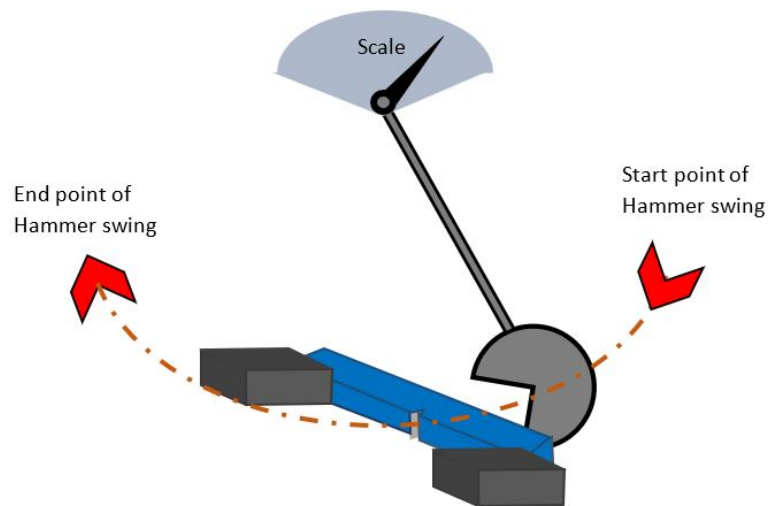
Figure 3-12 Illustration of Charpy impact test machine
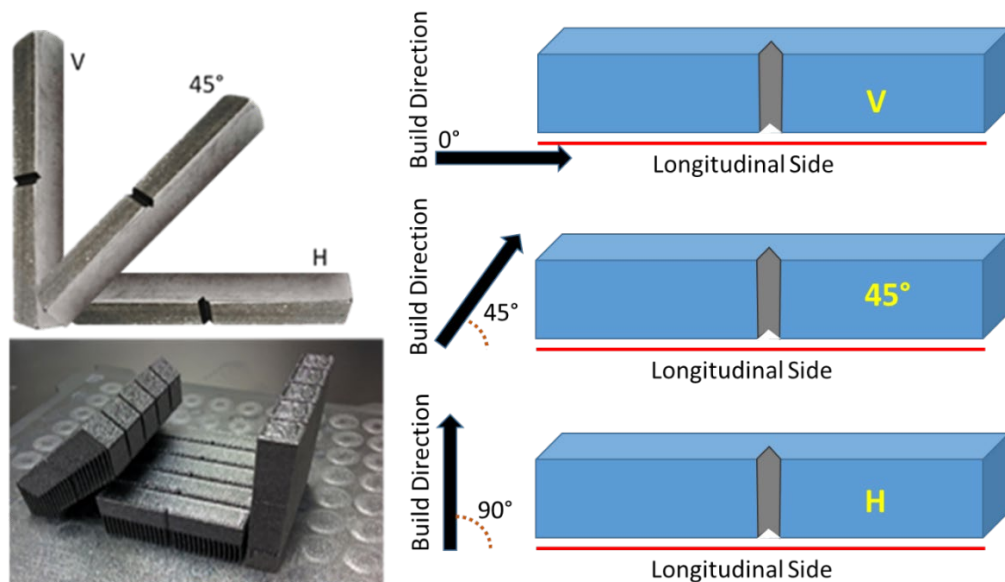
Figure 3-13 Sample positions on the build platform and Charpy sample design in each orientation. Angles between samples build direction, and the longitudinal side are detailed on the right side.

The Charpy Impact test was performed to investigate the effect of the build orientation and defects/LOF on the impact toughness of EBM parts. For each sample, the factors below were analysed with respect to their influence on impact toughness:

- Number of pores

- Number of LOF

- Fraction of pore

- Fraction of LOF

- Max pore area

- Max LOF size

- Microstructural differences (β phase length, α lath width and columnar α+β grain width)

- The oxygen level in the samples

LOF and porosity measurements:

After testing one of the two fracture surfaces was selected for SEM imagery, with ~95 sequential images captured and mapped from each Charpy fractured surface for all three orientations at a constant magnification. Each SEM image was used to measure the size, diameter, length and number of LOF, and porosity via the ImageJ image process software. The entire procedure is detailed in Figure 3-14 below.
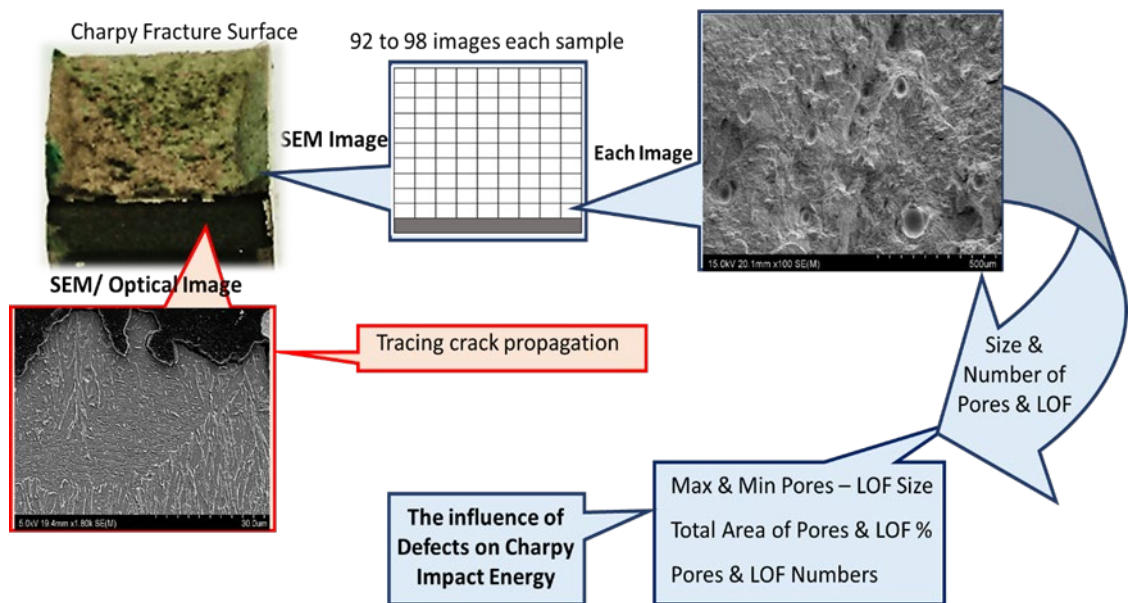
Figure 3-14 The procedure of gaining data from each Charpy sample

For each SEM image of the fracture surface, porosity and LOF areas were measured, as shown in Figure 3-15. Following, the total area of LOF/porosity was divided by the total area of the fracture surface. Therefore, the fraction of LOF/porosity area, the number of LOF/porosity defects and the largest LOF/porosity area was evaluated. Each of the LOF areas was measured by ImageJ software for each SEM image, and the total LOF area was calculated and divided by the fracture plane area (10×8 mm^2), defining the fraction of LOF. Each of the measured LOF areas used in the fraction of LOF calculation was sorted from the lowest to the largest area in Microsoft Excel software for each sample and used

to determine the highest LOF area. The LOF direction is determined by the concentrated area around the disk-like shape which may be detrimental for crack propagation. The LOF direction is always perpendicular to the build direction. Also, the longest length of LOF was chosen to be measured for length of LOF.
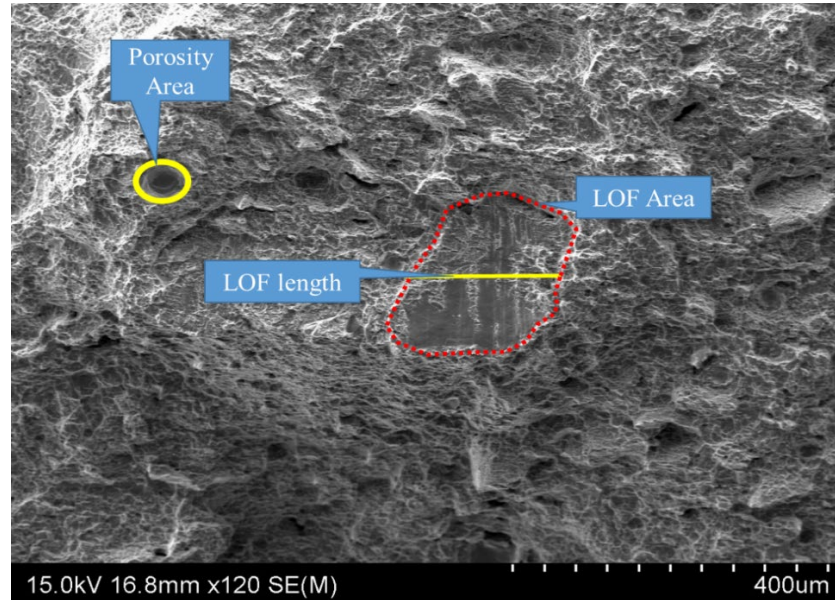
Figure 3-15 The example of how the LOF and porosity areas are measured (the longest length of LOF is chosen for measuring).

Sub-micron voids:

A number of sub-micron voids from 0 to 200µm (close to fracture surface) and 1800 to 2000µm (far from fracture surface), as represented in Figure 3-16 were measured along the cross-section (in the middle) of the fracture surface.
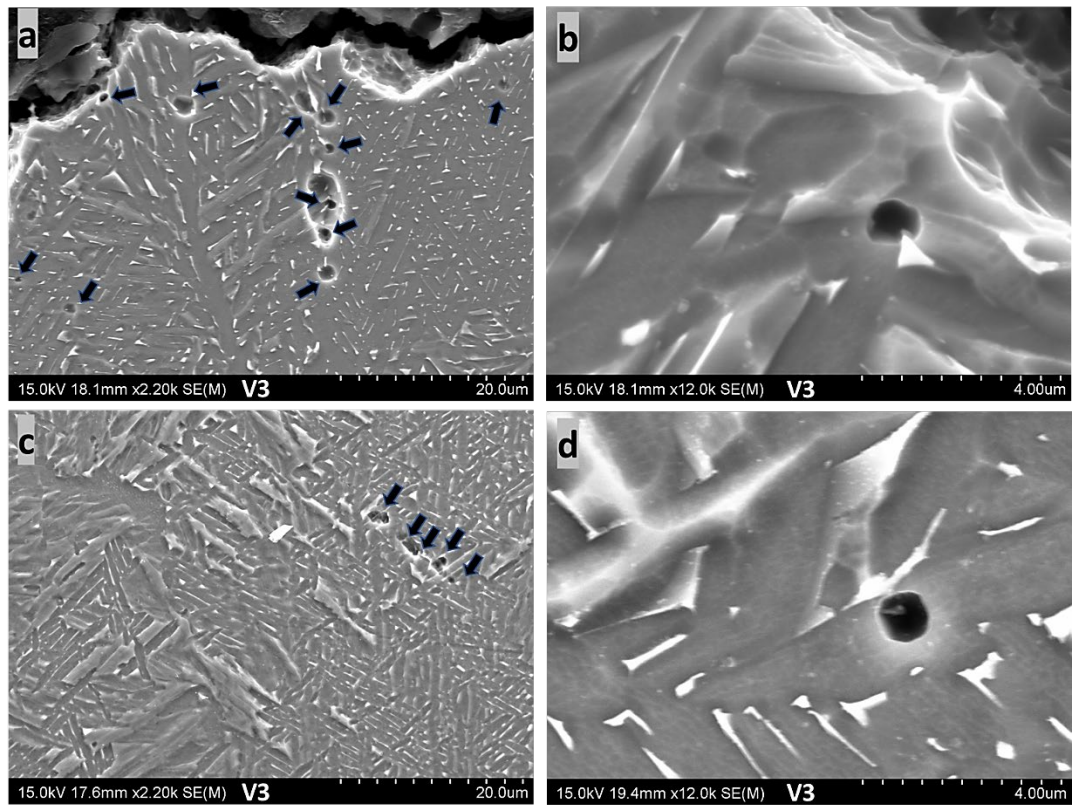
Figure 3-16 SEM micrograph cross-section of a) and b) close to the fracture surface (in 200 μm distance, c) and d) far from the fracture surface from 1800 to 2000μm.

These sub-micron voids are as the result of the applied load on the sample and are commonly less than 5μm in diameter. Sequential SEM images are taken in high magnification to evaluate the numbers of the sub-micron voids in the vertical samples. Sub-micron voids were observed in all samples, however, only the vertical samples are evaluated.

β phase length, α lath and grain width measurements:

Through slowing of the cooling rate during solidification, β phase becomes longer and thicker, and the α lath thickens. Figure 3-17 represents the details of measuring the average width of the α lath and phase length, obtained by using SEM. Further represented in Figure 3-17, the length of β phase and the width of α lath are measured from more than eight SEM images taken of different grains, with ImageJ image analysis software applied to determine if the cooling rate of the samples is identical.
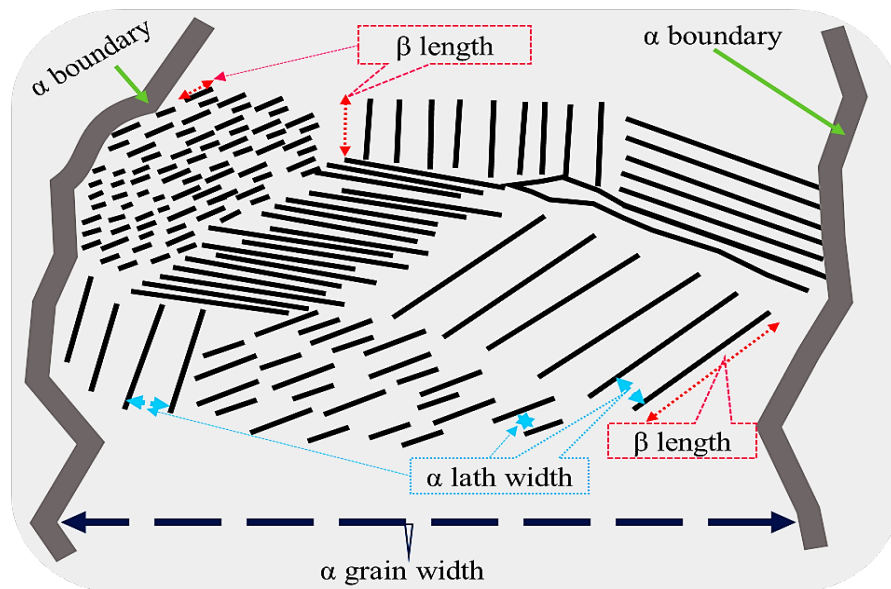
Figure 3-17 Illustration of how β phase length and α lath width are measured.

The other half of the Charpy sample is used in metallographic analysis across its fracture surface. In order to observe the fracture path and microstructure around the fracture area, a cross section cut was done for each fractured sample along the notch as shown in Figure 3-18.
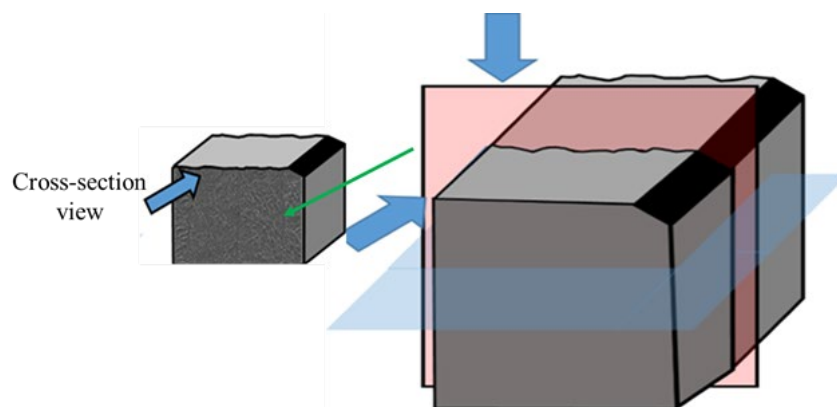
Figure 3-18 Illustration of cross-sectioned Charpy sample observing the fracture path.

Oxygen level measurement:

The oxygen level in the Charpy samples is measured by taking $3mm^3$ sections from three separate areas of each sample. A LECO ON736 Elemental Analyzer is used to measure

the oxygen and nitrogen level and to determine if the level of oxygen affects impact energy in different build orientations.

Notch positioning:

The notch was positioned on different sides of the Charpy samples, to examine the effect of notch position on the impact energy as shown in Figure 3-19. With six samples produced in the 45° direction and six samples in the horizontal directions. The default processing parameters were used for producing these samples which are mentioned in Table 3-2.
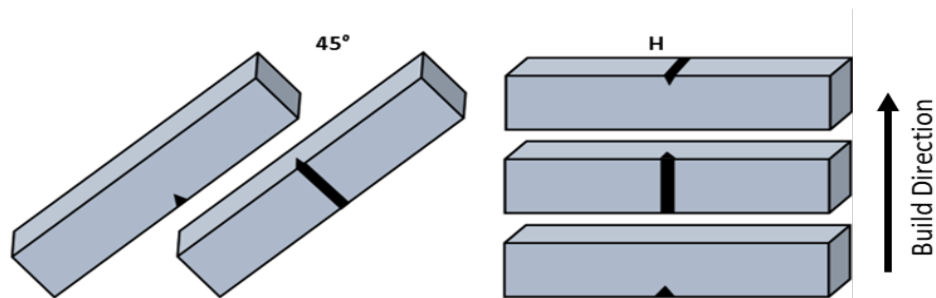
Figure 3-19 Notch positions on Charpy samples

3.8 Fatigue Crack Growth

Fatigue crack growth (FCG) experiments in three different orientations were performed, in order to investigate the influence of build orientation angle with load direction on the anisotropic properties of Ti6Al4V.
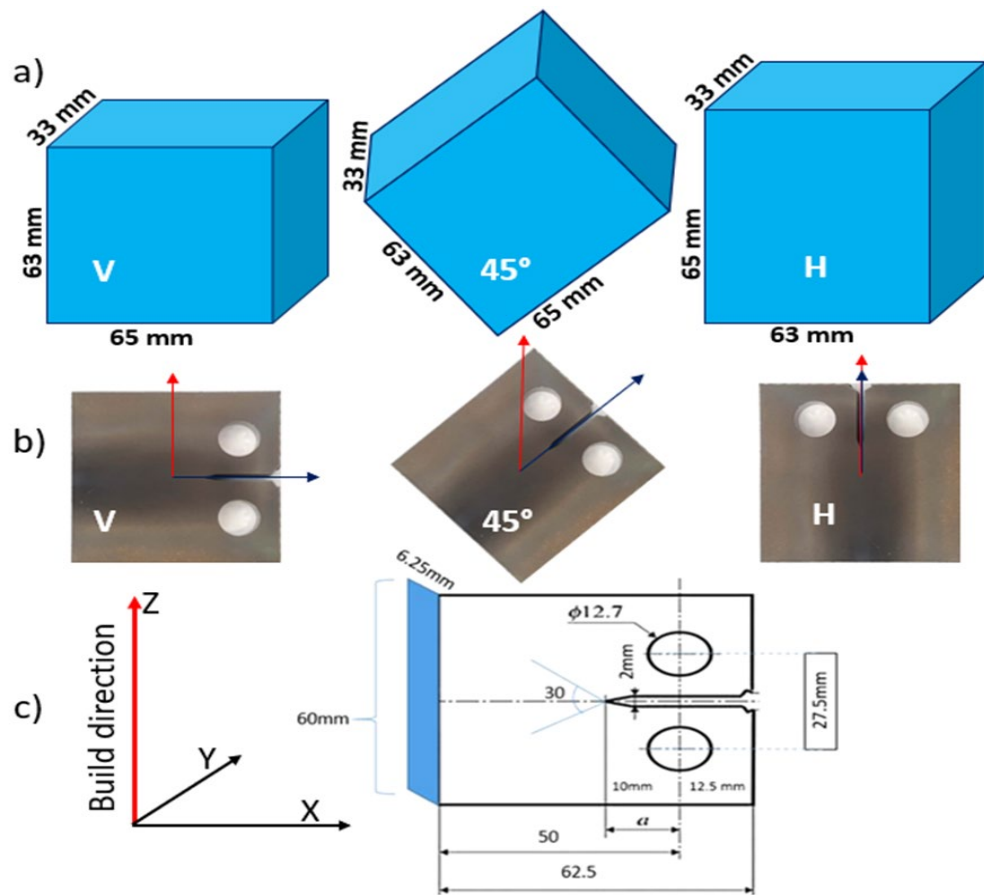
Figure 3-20 Illustration of a) bulk samples in three different directions, vertical, 45° and horizontal samples, b) notch angles with the build direction, and c) The geometry of the samples.

Three bulk samples were produced on the Arcam Q10 EBM with the default parameter settings and dimensions as shown in Figure 3-20a. According to ASTM standard E647, each bulk sample was cut into five FCG samples were cut via CNC electrical discharge machining (WEDM) to the dimensions presented in Figure 3-20c. Wire cutting machine. In the vertical (V) samples the notch is perpendicular to the build direction (90°), while the 45° and horizontal (H) samples are 45° and 0° to the build direction respectively, as presented by the red and blue arrows in Figure 3-20b.

The Fatigue crack growth test was performed on a MTS Landmark Servohydraulic Test System. First, the pre-crack procedure was applied to form the pre-crack with a length of 2mm using the pre-crack conditions presented in Table 3-4.

Table 3-4 The given Pre-crack values in MTS process

Final crack limit	2 mm
Frequency	20 Hz
Final K	11 MPa.m$^{0.5}$

As presented in Figure 3-21, the crack growth rate is determined by clip gage under repeated loading. The clip gage measures the displacement in the sample through the sensing of movement via two metallic arms instrumented with strain gages, notched to fit into the sharp edges of the samples used as reference points for displacement measurement. Each time the load is applied (a cycle of applied load), the crack-opening displacement (COD) is recorded by the clip gage with the crack length calculated and measured after each loading cycle. The control computer employs a functional relationship between crack length and the sample geometry to obtain the crack length value (Schijve, 2009). The initial crack length is 10mm, thus, in one cycle of the load, the crack is measured as shown in Figure 3-21.
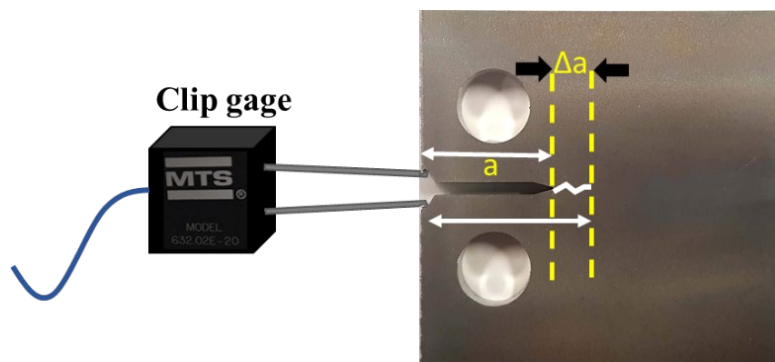
Figure 3-21 Illustration of clip gage used in providing the displacement measurement.
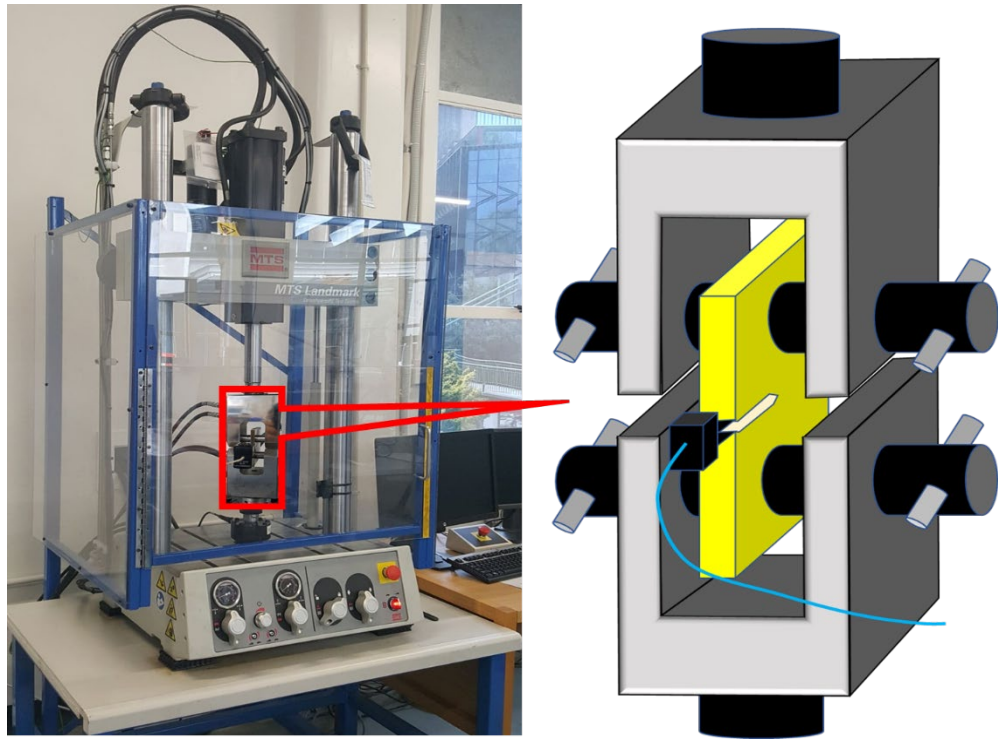
Figure 3-22 The position of the fatigue crack growth (FCG) sample used in the test.

From the final pre-crack result, the crack growth parameters were provided to the machine. A constant load was applied to produce region II crack growth with and applied load of 3400 N, stress ratio (R) of 0.1 and cyclic frequency of 15 Hz at room temperature. The produced fatigue crack growth data was plotted to investigate the effect of the crack propagation direction with build direction, itself influencing the directional microstructure and the columnar grain boundaries. One half of the fractured part was used for metallographic examination with respect to the crack path while the other half was prepared for fracture surface investigation via SEM microscopy.

Select metallurgical samples within this experimental work were prepared differently to the bulk and were not mounted in resin. Hot glue was used in the mounting of selected samples fractured in the region II area, as to study both fractured surface and the cross-section. After grinding, polishing and etching, the samples were removed from the mounted glue and analysed by SEM tilted at a 40° to the fracture surface and the cross-section microstructure to investigate the orientation of β phase with respect to the striation as depicted in Figure 3-23.
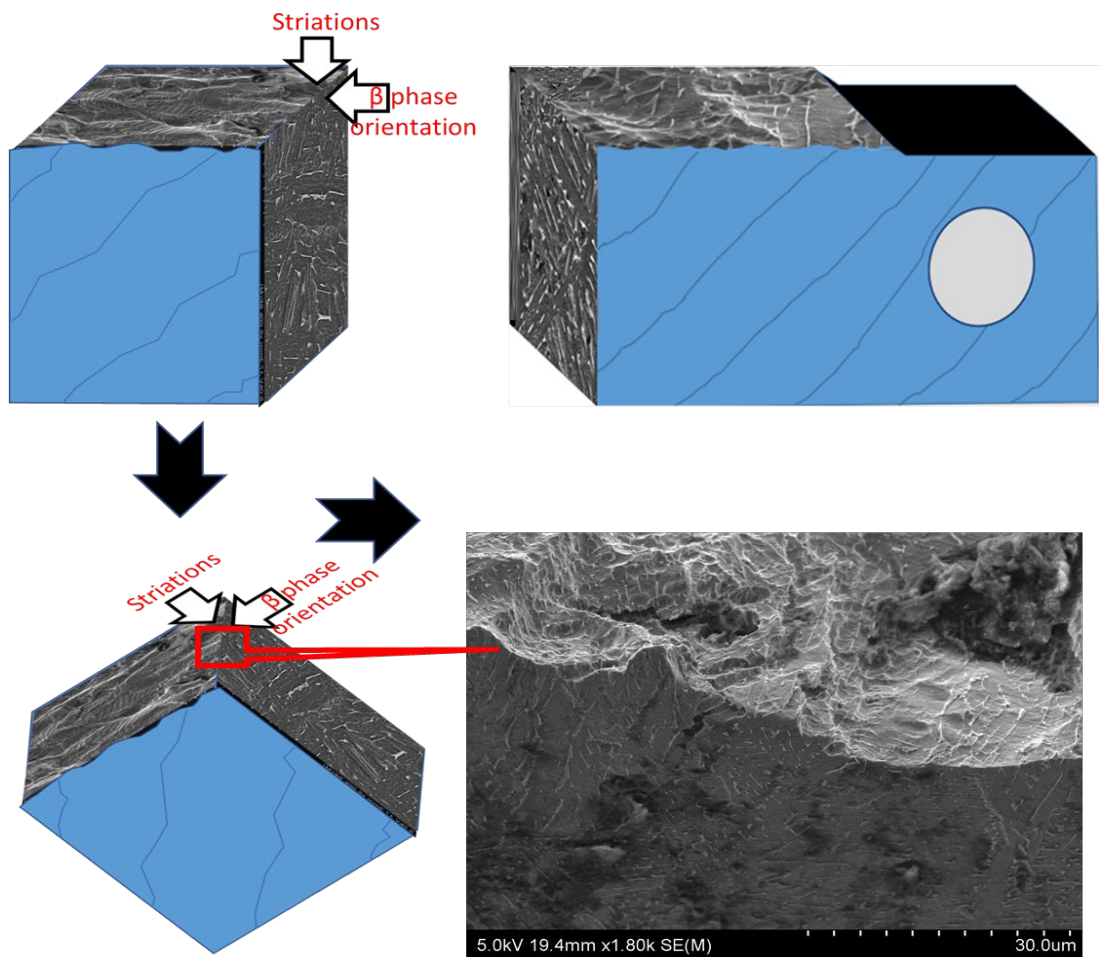
Figure 3-23 The analysed microstructure area beneath striations in the 45° sample.

Energy Dispersive Spectroscopy (EDS) is used in analysing and finding the α+β colonies and α phase boundaries along the fracture surface. Due to the limitation of EDS requiring a smooth surface to project an accurate reading, areas with the least amount of surface deviation were selected for the EDS analysis.

4. CHAPTER. Effect of Scan Speed on Melt Pool and Lack of Fusion (LOF)

The formation of LOF is a sensitive process in parts produced by EBM, with its formation drastic on part quality and strength. Therefore, samples were produced at a range of scan speeds and evaluated for their influence on the melt pool and LOF characteristics. Firstly, the track line on the top surface of the samples was studied and used to establish the stability of the melt pool shapes for each sample, followed by melt pool shape analysis at different scan speeds. The formation mechanism of LOF and the shape category was defined through the use of optical microscopy and ImageJ image analysis software, to determine the relationship between scan speed and area fraction of LOF. Finally, the relationship between LOF formation and top surface roughness is defined through surface roughness analysis.

As mentioned in Chapter 2, Ti6Al4V melt pool shape is unable to be observed during the EBM process, yet the melt pool geometry is reported to be influenced by scan speed. Hence, a wide range of scan speeds from 5 to 18 m/s are chosen to identify the melt pool shape by experimental means similar studied by Cheng, Price, Gong et al, Cheng and Chou, Hernandez-Nava, Narra et al. and Soylemez et al. (Cheng et al., 2013; Cheng et al., 2014; Hernández-Nava et al., 2016; Narra et al., 2018, 2015; Soylemez et al., 2010). Additionally, this wide scan speed range is used to study the effect of scan speed on the LOF area and geometry.

Five cubic samples with scan speeds of 5, 9, 12, 16 and 18m/s were produced in the locations shown in Figure 4-1, with supplementary parameters defined in Chapter 3, Table 3-2.
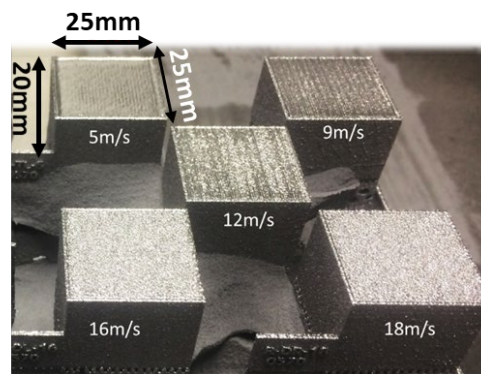
Figure 4-1 The EBM as-fabricated samples with respective scan speeds.

4.1 Morphological features of track lines

In order to understand the melt pool characteristics; the top surface of each sample was analyzed by SEM as presented in Figure 4-2. As the scan speed is increased from 5 m/s to 18 m/s, track lines were observed to increase in unevenness and eventually disappear completely at 16 and 18m/s. This is seen to agree with the result published by Juechter et al. (Juechter et al., 2014), scan speed has a direct relation with top surface of EBM components. Further, as seen for all samples in Figure 4-2, there is no sign of melt pool ripples between track lines. The ripples represent the process of solidification. The existence of ripple is a consequence of solidification process in one melt pool. When electron beam moves to melt the next spot (next melt pool), the end of the melt pool which is tear-drop-like shape, which is due to the electron beam movement and speed, starts solidifying. By the time the next melt pool is created, a part of the previous melt pool solidifies, and ripples appear on the top surface of the components, as illustrated in Figure 4-3a. Similar ripples were detected on the top surface of SLM parts by Gong et al., Parry et al. and Zhou et al. (Gong et al., 2013; Parry et al., 2016; Zhou et al., 2015).
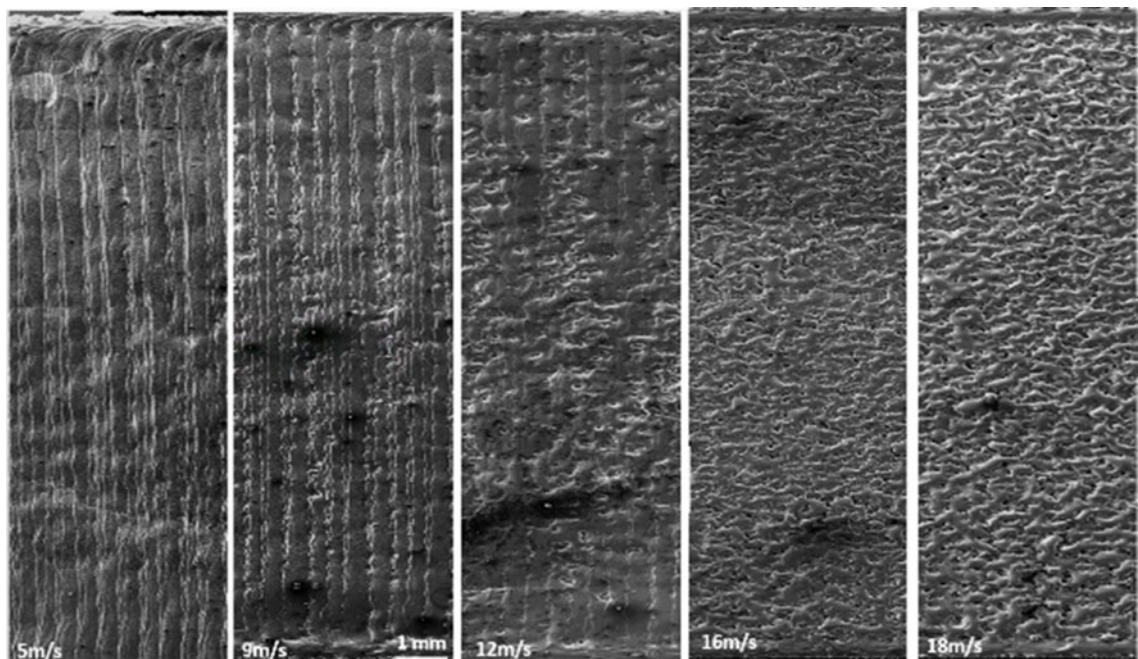
Figure 4-2 Top surface feature from 5, 9, 12, 16 and 18 m/s, track line from straight to wavy and finally disappeared.

Consequently, the process of multi welded melt pools could be traced by ripples. However as observed in Figure 4-2 a single hatch-line in the EBM process is in the molten state as the electron beam starts melting the adjacent powder in the subsequent line. By the time the electron beam moves to the next hatch line, the previous hatch line is still in the liquid

state. Therefore, each hatch line would still be liquid when the electron beam is about to move to the next hatch-line. Hence why no ripple is observed as schematically shown in Figure 4-3b. Track lines are not linear and have curves and waves which are seen along the melt pool side as the electron beam moves and are observed in top surface images. Therefore, it can be suggested that the track line consists of melt pool side ripples as presented in EBM images by Cheng et al. and Juechter et al. (Cheng et al., 2014; Juechter et al., 2014).
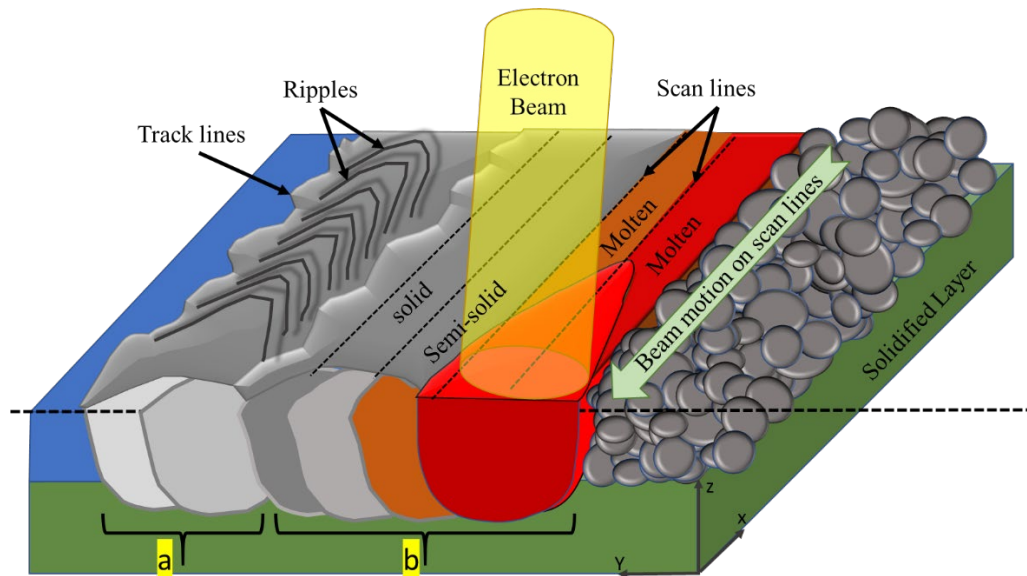
Figure 4-3 Schematic image of melting process a) when a melt pool solidifies as the next melt pool forms with the resulting ripple, and b) when melt pool stays molten until electron beam moves to the next scan line for melting (no ripple).

A representation of the electron beam melting process for a single layer is illustrated in Figure 4-4A and depicts the characteristic z-shaped pattern. The electron beam melting process begins at Point D1 and follows a line to Point T2, before following a diagonal vector denoted as a red dashed line to the adjacent scan line start location at Point D3 and is repeated along the whole hatching layer. Each point on the Figure 4-4A is divided into two lines that one follows the started track line and the other joins to the next track line. The printed track lines Figure 4-2 suggest that when the electron beam was located along the D side, it moved to the next line from side D to start melting the next line. However, during positioning to the next consecutive scan line along the D end the electron beam continued melting resulting in the z-shape pattern on the top surface in Figure 4-4A, representing the melting process in Figure 4-2. Ge et al. and Williams et al. observed the z-shape pattern and concluded its formation was due to the electron beam traversing to the new melt location. They further highlighted that the travelled route to arrive to the

next scan line was not supposed to melt (Ge et al., 2014; Tammas-Williams et al., 2015). In this study, a z-shaped pattern was used as presented in Figure 4-4, ideally following the path presenting in Figure 4-4 (A). Conversely, the melting occurs along the beam transfer path as evident in Figure 4-2 with the z-shape scan pattern presented in Figure 4-4B occurring as the electron beam returns to the D side of the sample.
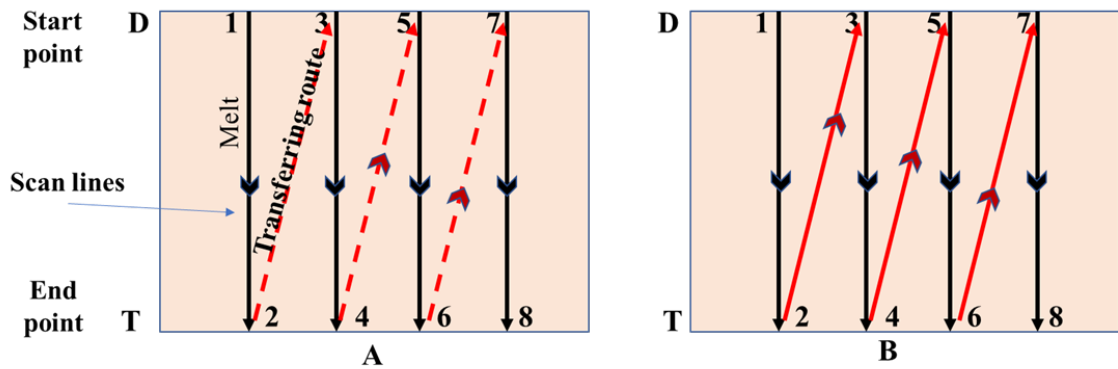
Figure 4-4 Illustration of how the electron beam melts one single layer from left to right, A) The expected z-shaped scan strategy melts on the solid black lines and B) the observed z-shaped scan strategy whereby the whole route melted.
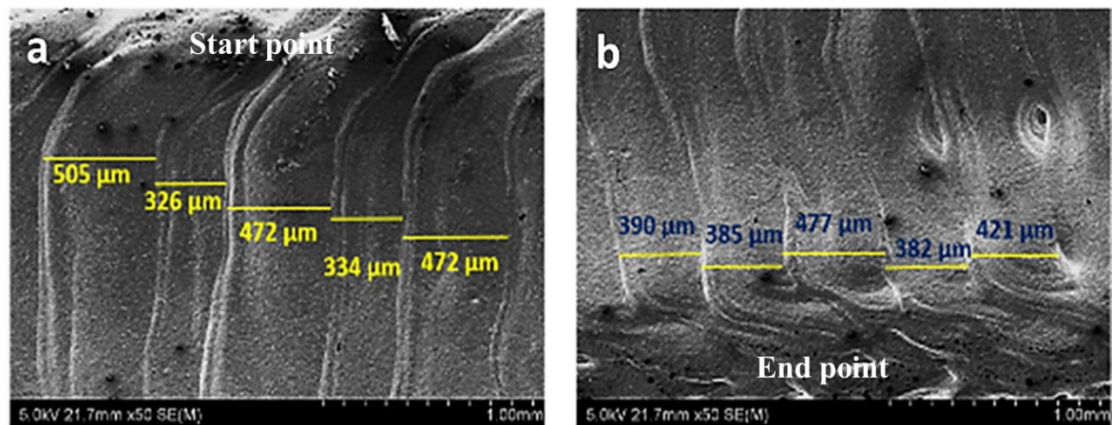
Figure 4-5 SEM images of 5m/s sample's top surface, a) start side (D) and b) end side.

The start and end sides of six track lines in the 5 m/s sample are presented in Figure 4-5. The measured distance of two sequential track lines shows that the width of the tracks is approximately close to the width of the hatch space of 400μm. The track line widths of the 5, 9 and 12m/s samples presented in Figure 4-6 are uneven, which is likely the result of different melt pool sizes and an instability in the melt pools. Furthermore, the track lines over flow onto the previous solidified side, producing the enlarged track line presented in Figure 4-3b. As scan speed increases, the distance between two adjacent track lines (the width of track) increases. This suggests that the volume of overlapping between two adjacent melt pools decreases hence, resulting in an increase in the number

of defects as evident in Figure 4-6. On the top surface of the 16 and 18m/s samples, discontinuous tracks can be observed, likely forming due to the high instability in the melt pools with the presence of many irregular pores.
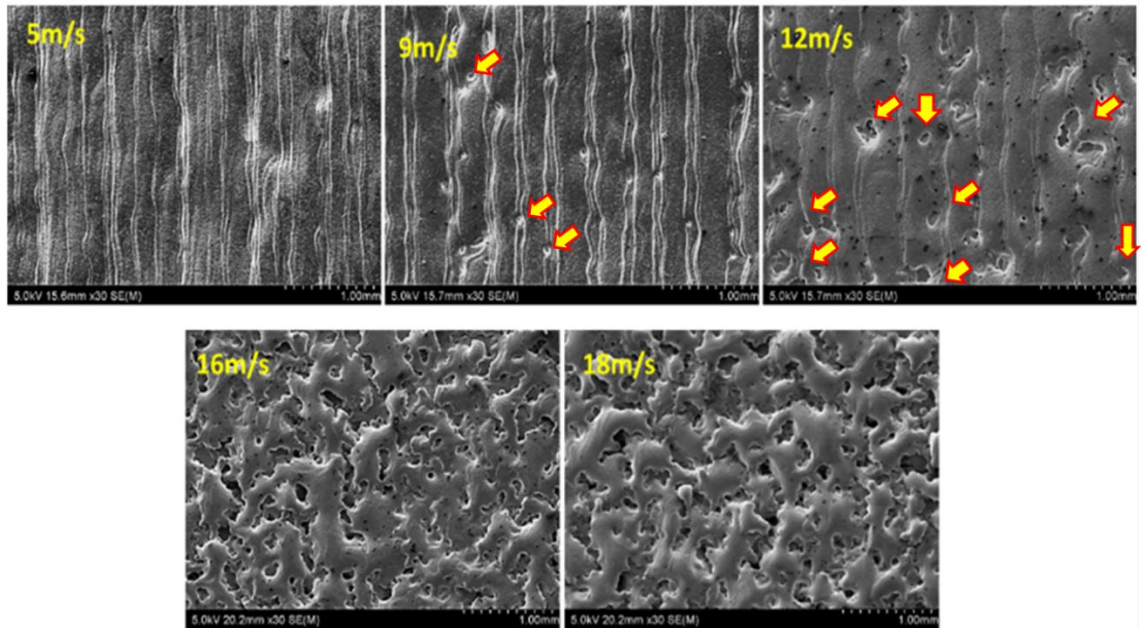
Figure 4-6 SEM top surface images of the samples with different scan speeds. Defects are indicated by arrow.

A cross-sectional microstructural analysis of all the samples was taken perpendicular to the track lines as presented in Figure 4-7.
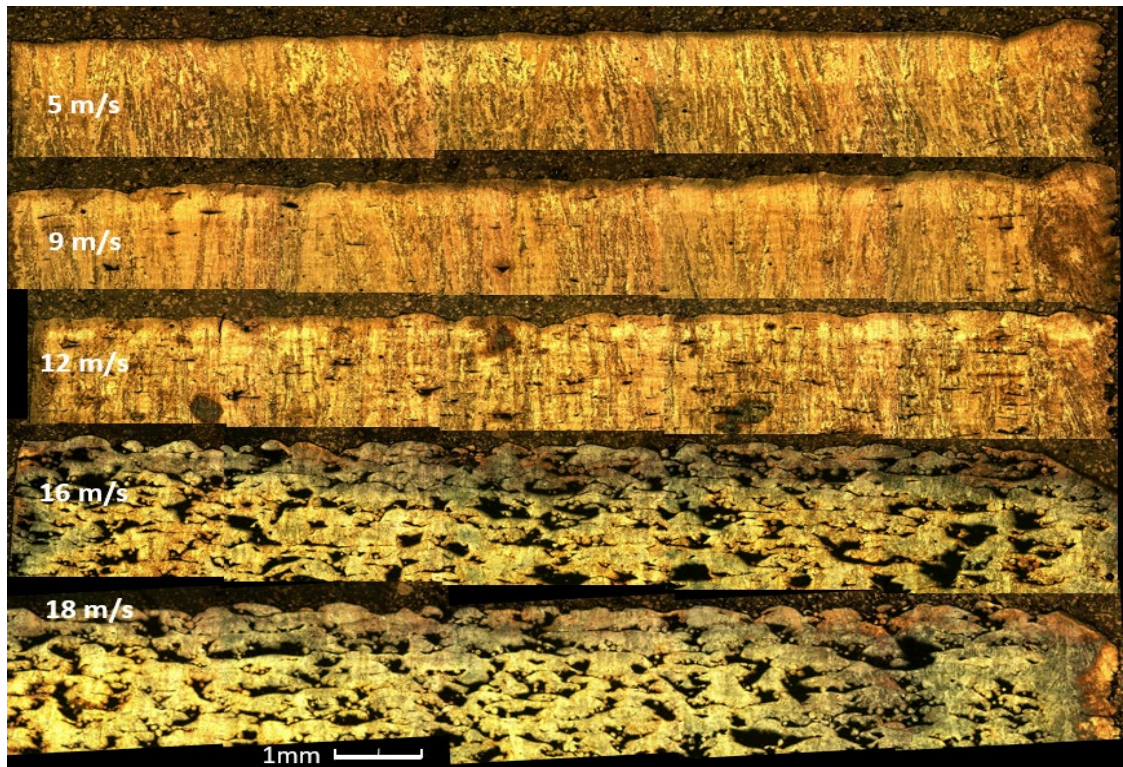
Figure 4-7 Cross-sections of samples with different scan speed.

Track lines were generated following the electron beam motion therefore, the cross-sections cut perpendicular to the track lines display a width and depth view of the melt pool for the final layer. Hence, track lines help to identify the area of top melt pools (width) and consequently, the width of the melt pool can be measured.
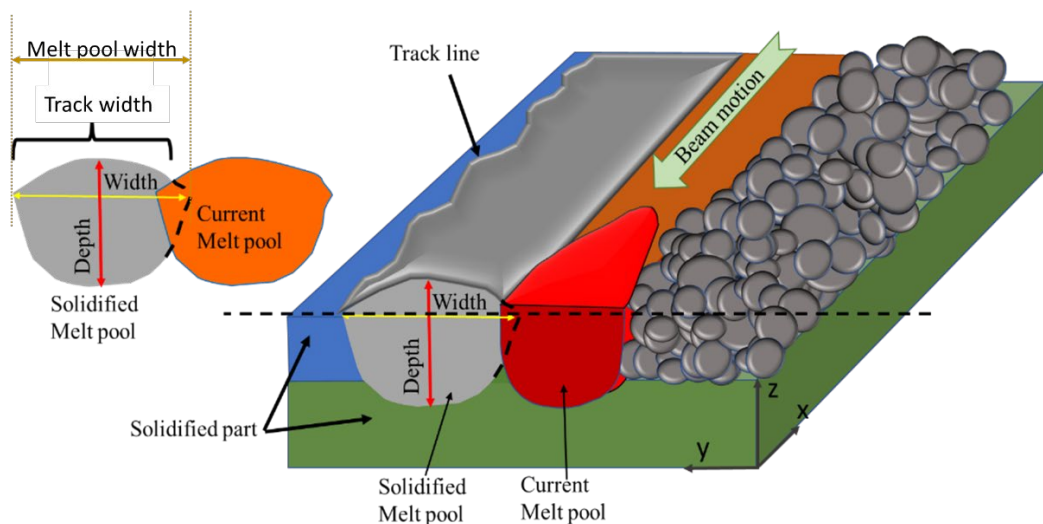
Figure 4-8 Schematic of a cross-sectioned sample during the EBM process.

As shown in Figure 4-8, it should be noted that the distance between two track lines is a portion of track width and may not provide information on the actual single line track width due to partial coverage by the overflowing molten metal on last generated melt

pool. In order to be able to measure the width of the melt pools, a horizontal reference line taken as shown in the black dashed line between the melt pool corners in the overlapping area.

4.2 Melt pool shape

Cross-sectional images taken of the 5m/s sample show no evidence of LOF in the hatching area as opposed to images taken of the 9m/s sample whereby, many LOFs were observed as evident in Figure 4-9. Some LOFs close to the surface can be connected through a patterned line that fluctuates along the length of the sample as presented in Figure 4-9. By following the LOF shapes connected by the dashed white line, it is proposed that the line represents the bottom of the melt pool for the final layer.
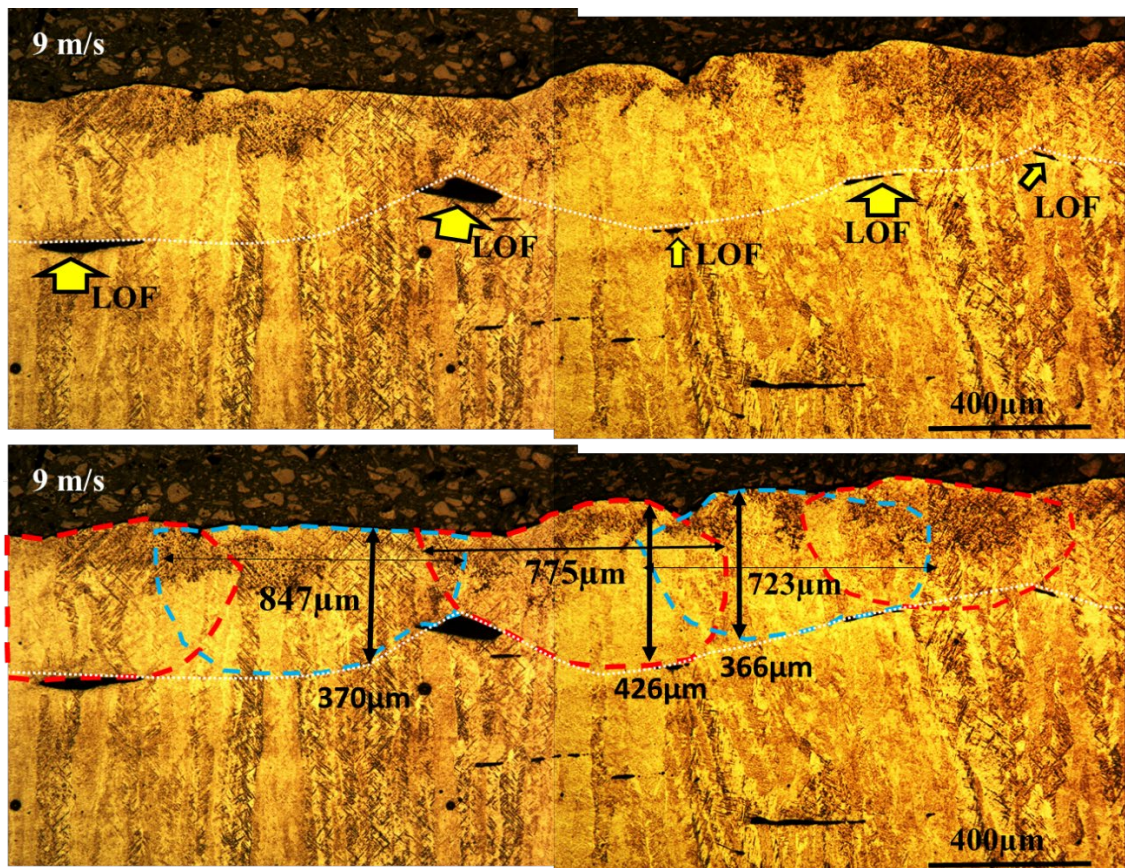
Figure 4-9 Cross-sectional image of the 9m/s sample with melt pool shapes.

The shape of the melt pools in the 9m/s sample can be predicted from the white dashed line and the connected LOF. The average melt pool depth for the last layer in the 9m/s sample is ~410 µm and, based on the shape of LOF, and the track lines positions, the average melt pool width of the 9m/s sample is around 750 µm.

At a scan speed of 12m/s, the melt pool discontinuity occurs due to the limited time for transferring heat into the powder bed, forming melt pools as shown in Figure 4-10. Another possibility for the missing melt pool is due to an increase in the scan speed leading to the electron beam travelling too fast to consolidate the powder. The average melt pool depth for the 12m/s sample is 200 - 210 μm with the melt pool width ranging from 584 to 682 μm. However, only a select few melt pools were measured on the top surface, as melt pools joined and overlapped making measurements difficult.
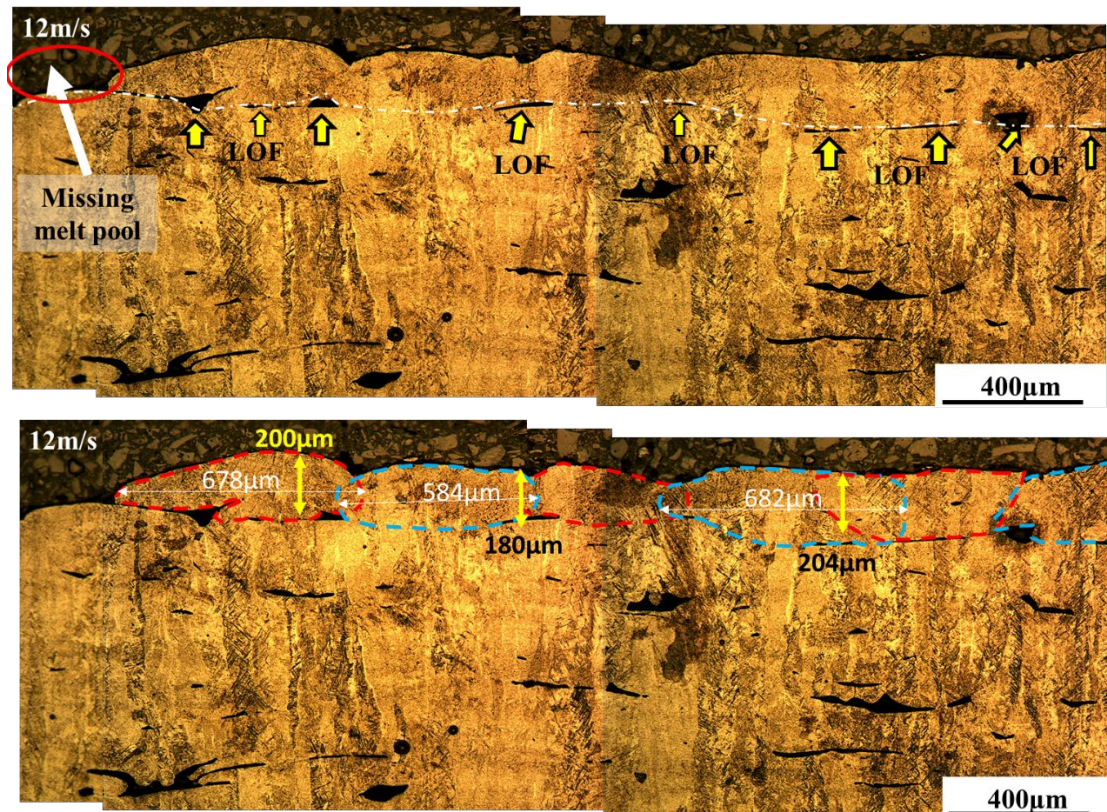
Figure 4-10 The melt pool shape in the 12m/s sample cross-section with a missing a melt pool on the top left side.

Samples produced at scan speeds of 16 and 18 m/s show melt pools to partially overlap with adjacent melt pools, allowing for measurement of melt pool size and shape. The melt pool depth and width vary along the top surface as observed through the measurement of the melt pools. The variance in melt pool depth in each sample is due to the uneven surface of the previously solidified layer, which in turn affects the subsequently deposited powder layer thickness. The other plausible reason is that according to energy input equation Equation 1-1, by increasing scan speed from 5 to 9, 12, 16 and 18m/s, the energy input available to melt the powder is reduced from 16.8 to 9.33, 7, 5.25 and 4.66 J/mm^3, hence, dramatically reducing the stability of the melt pool. The discontinuity in the track line of

samples produced at 16 and 18 m/s lead to more accurate measurements for the melt pool width and depth. The width and depth for the 16m/s sample are 460 - 863 μm and 86 - 204 μm respectively, while these values for the 18m/s sample changes to 400 - 829 μm and 133 - 196 μm respectively. As the energy input of 5 to 18m/s samples reduces from 16.8 to 4.66 J/mm^3, the depth and width of the melt pools reduce correspondingly. Following the melt pool shapes in Figure 4-9, Figure 4-10 and Figure 4-11, as scan speed increases, energy input decreases, creating a discontinuity in the melt pool. The discontinuity in the melt pools and the surface tension of the molten metal, create a shape of a melt pool seen in Figure 4-11 at a scan speed of 16 and 18m/s. This discontinuity in the melt pool occurs because of the heat transfer from the highest temperature to the lowest temperature, producing a thermal gradient. Consequently, the thermal flows are formed leading to an increase in the heat transfer and decrease of the temperature inside the melt pool, increasing the thermal gradient. By increasing the thermal gradient in the melt pool, Marangoni phenomena increases leading into Rayleigh instability, breaking the melt pools into droplets. Increasing the scan speed from 5 to 18m/s leads to the generation and predominance of the balling phenomena leading to the melt pool breaking up into spherical globules, as was observed by Attar, Galati and Iuliano, Gusarov et al. and Kruth et al. for powder bed additive manufacturing (Attar, 2011; Galati et al., 2018; Gusarov et al., 2007; Kruth et al., 2004). Therefore, the melt pool shape changes from approximately half circle to more droplet and spherical as shown in Figure 4-11c and d, from 9 to 18m/s.

The tear-drop melt pool shape was reported by Cheng et al. and other authors in EBM processing as viewed along the melt pool length while, the melt pool presented in this study considers the front view of the melt pool showing its width and depth (Cheng et al., 2014; Cunningham et al., 2016; Jamshidinia et al., 2013; Shrestha et al., 2017).

The existence of LOF provides insight into the melt pool shape of the EBM process. By increasing the scan speed for each sample, the energy required to melt powders in that spot decreases. Therefore, the penetration depth decreases with increasing scan speed.
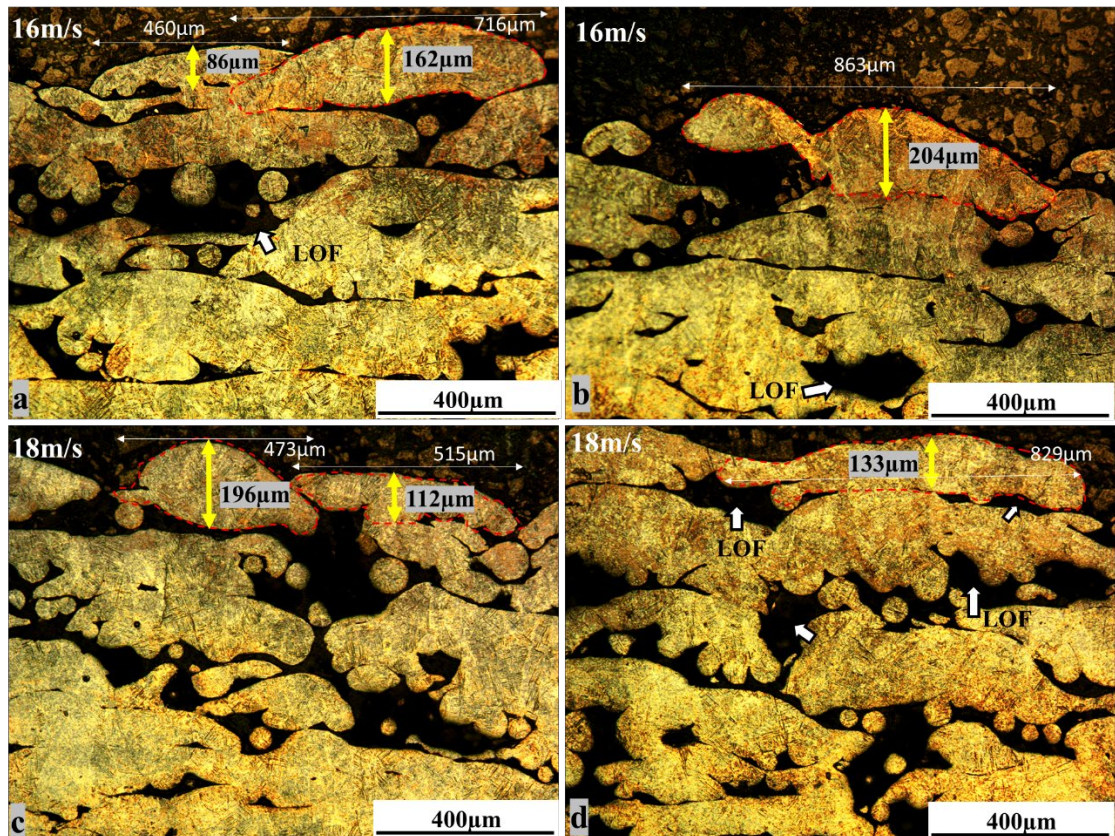
Figure 4-11 Cross-section images are showing the melt pool shapes of the 16 and 18m/s samples, with no or partial overlapping.

There was difficulty in measuring the melt pool depth of the 5m/s sample, due to no LOF present in the overlapped melt pool as seen in Figure 4-12. Therefore, the LOF in the zone between hatching and contour region was used to determine the melt pool depth of ~ 600 to 700 μm, consistent with melting approximately 10-12 powder layers of 50 μm thickness. Therefore, the possibility of LOF formation of between layers decreases outstandingly. As noted prior, the 5 m/s sample shows no evidence of LOF in hatching area, however, some LOFs less than 150 μm in width were observed in the joining zone of the hatching and contour area and were attributed to the lack of energy input. There is a decreasing trend in the melt pool size with increasing scan speed, with melt pool sizes significantly larger in the 5 and 9 m/s samples than samples produced at; 12, 16 and 18m/s which contain partial or no overlapping leading to many LOFs in the hatch area. This trend was observed in the work by Cheng et al., Juechter and Soylemez et al. for EBM processing of Ti6Al4V (Cheng & Chou, 2013; 2014; Juechter et al., 2014; Soylemez et al., 2010). By increasing the scan speed from 100mm/s to 1000mm/s in a thermal model of the EBM process, Cheng et al. reported a decrease in the melt pool size particularly the depth (~0.1mm) (Cheng et al., 2013). An experimental study on the EBM process by

Cheng et al., proved the length of the melt pool to decrease by ~0.36mm though increasing the scan speed from 481mm/s to 1595mm/s (Cheng et al., 2014). Additionally, Soylemez et al. and Juechter et al. experimentally observed a decrease in the melt pool size of EBM processed Ti6Al4V with increasing scan speed (Juechter et al., 2014; Soylemez et al., 2010).
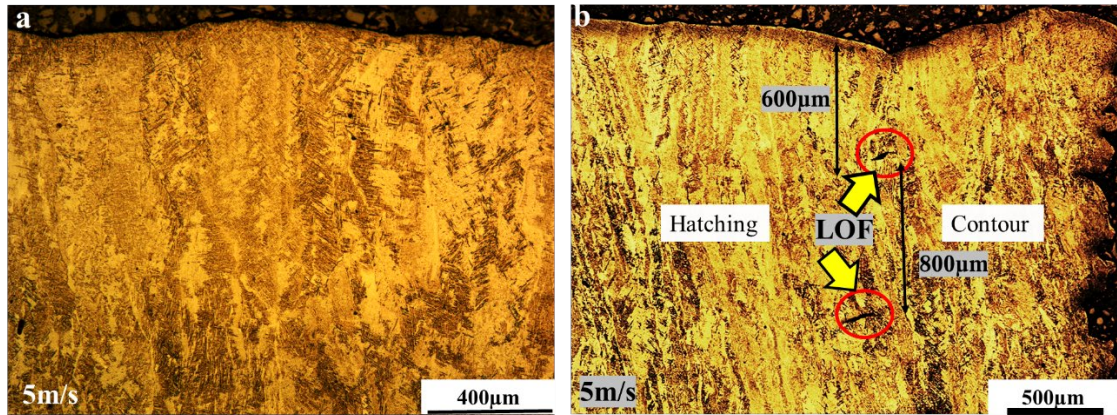
Figure 4-12 Optical micrographs of the 5m/s sample cross-section from a) hatch area and b) the joint area between the hatching area and contour area.

The schematic drawing of the melt pool shape from 5 to 18 m/s is shown in Figure 4-13. The increased scan speed induces differing melt pool sizes as the energy input decreases, leading to melt pool discontinuities with the surface tension of the molten metal is greater than between the molten metal and the powder. Consequently, the shape of melt pool changes from half circle-like to corn-like with increasing sphericity. Additionally, the melt pool width decreases as scan speed increases, leading to fewer powder particles melted as observed by Galati et al. as well (Galati et al., 2018). Due to the re-melting and re-solidifying of the Ti6Al4V alloy several times, all boundary-tracks of the melt pools vanished during the EBM process. Therefore, the shape of the melt pool is determined from the last layer of the samples. By increasing scan speed from 5 to 18 m/s, the shape of melt pool body presented in Figure 4-13 changes from semi-circle to more conical in shape. Further, the height of the melt pool crown increases, while the melt pool body shape becomes smaller. It should be noted that in the literature, the depth was used to evaluate the height of the melt pool body (depth of the melt pool body), different from the depth of the melt pool shape. The melt pool depth is defined as the distance from the lowest point of the melt pool boundary of the body melt pool to the highest point on the top of the melt pool crown. In the literature measuring the depth of the melt pool, the

crown was not considered. The crown of the melt pool is considered as the base for the following powder layer.
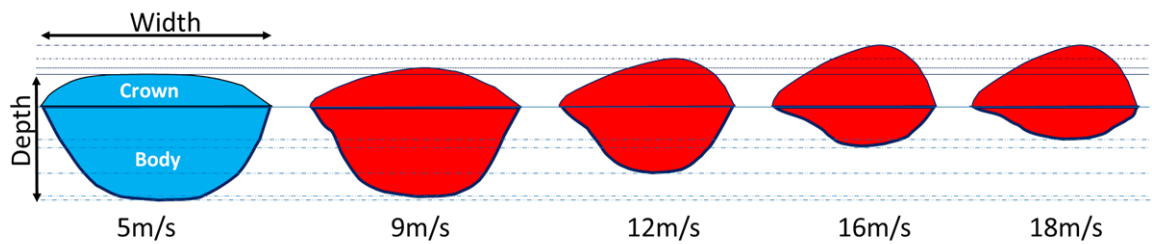
Figure 4-13 Schematic melt pool shapes of from the ideal form to the high scan speed form during EBM process (based on the actual shape of the last melt pools in 9, 12, 16 and 18 m/s).

Increasing the scan speed from 5 to 12 m/s results in an interrupted melting process. If the scan speed is increased above 12 m/s to 18m/s, melt pools may not have small contact with adjacent melt pools. Although the melt pool shape and size changes, the rate of change in the depth of the melt pool is greater than the width. This was similarly observed by Bo Cheng et al. (Cheng et al., 2013; Cheng et al., 2014) in two separate investigations in which they reported that by increasing scan speed, the geometry of the melt pool decreases, however, the sensitivity of the width to scan speed increases was not as significant as the depth and length.

4.3 Shape, formation and types of LOF

No LOF was observed in hatching area of the 5m/s sample, however, as the scan speed increases to 9 m/s, a flat isolated LOF forms in the hatching area as shown in Figure 4-14a. Increasing scan speed from 9 to 12m/s, the shape of LOF changed from flat isolated LOF into flat and irregular isolated shapes as shown in Figure 4-14b. While from 12 to 16 and 18m/s LOF shape changes from flat-isolated to an open LOF form. Continuous LOF forms with the size of LOF increasing as is seen in the 16 and 18 m/s samples in Figure 4-14c and d. When the beam speed is too fast, there is less electron transfer to melt a melt pool, and the energy input in the melting area decreases dramatically and forming open-LOF.
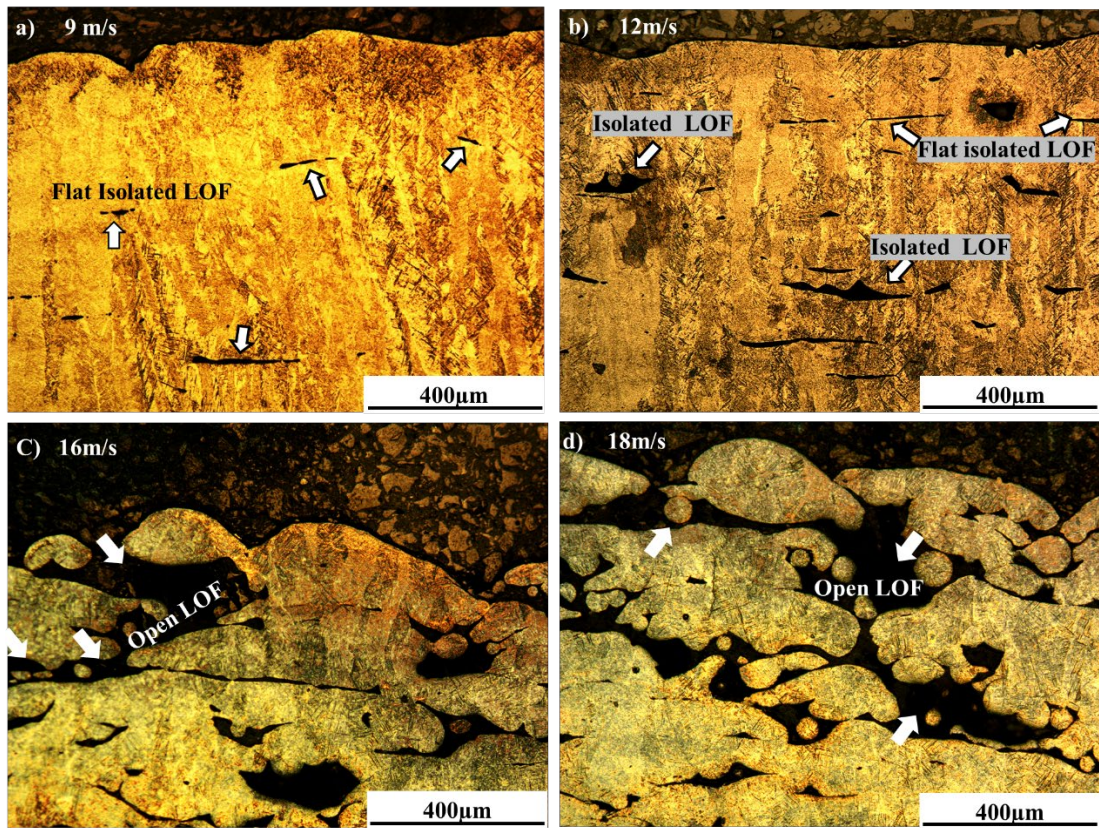
Figure 4-14 Effect of scan speed on the shape of LOF in samples at; 9, 12, 16 and 18m/s.

Some of the isolated LOF forms are a result of two adjacent melt pools that did not overlap entirely leading to an un-melted triangle-like area which sometimes has un-melted powder particles trapped inside as shown in Figure 4-15 (LOF number 1). Further, the triangle can form in reverse because of LOF occurring between two adjacent melt pool crowns and the following layer, as seen in Figure 4-15 (2A and 2B) and Figure 4-16 in red circles. Further LOFs formed between two deposited layers that did not fuse together and which were observed in other samples as well as those shown in Figure 4-15 (LOF numbers 3) and Figure 4-16 with arrows. This form of LOF formation can be attributed to a lack of melting penetration occurring due to insufficient energy input. During melting, as the scan speed increases the energy input supplied to the powder particles decreases, therefore, resulting in a smaller melt pool size. Additionally, there is a third shape of LOF that is detected more in 9 and 12m/s samples and is shown in Figure 4-15 (LOF number 4) and Figure 4-16b within the rectangular outline.
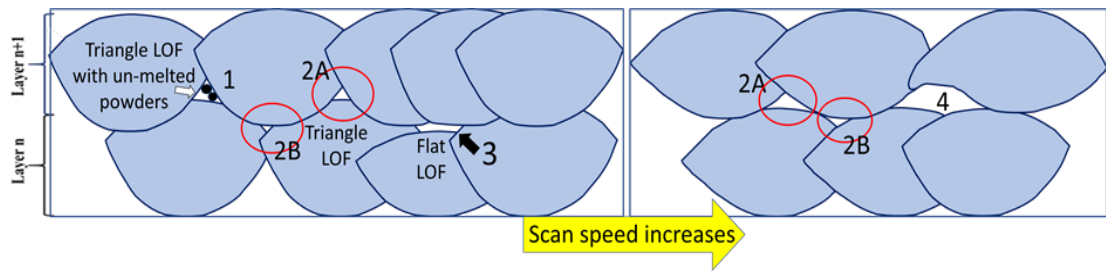
Figure 4-15 Illustration of isolated LOF shapes (LOF number 1, 2, 3 and 4) based on melt pools and the layers in a sample as scan speed increases, based on LOF formation from the 9 and 12m/s samples.
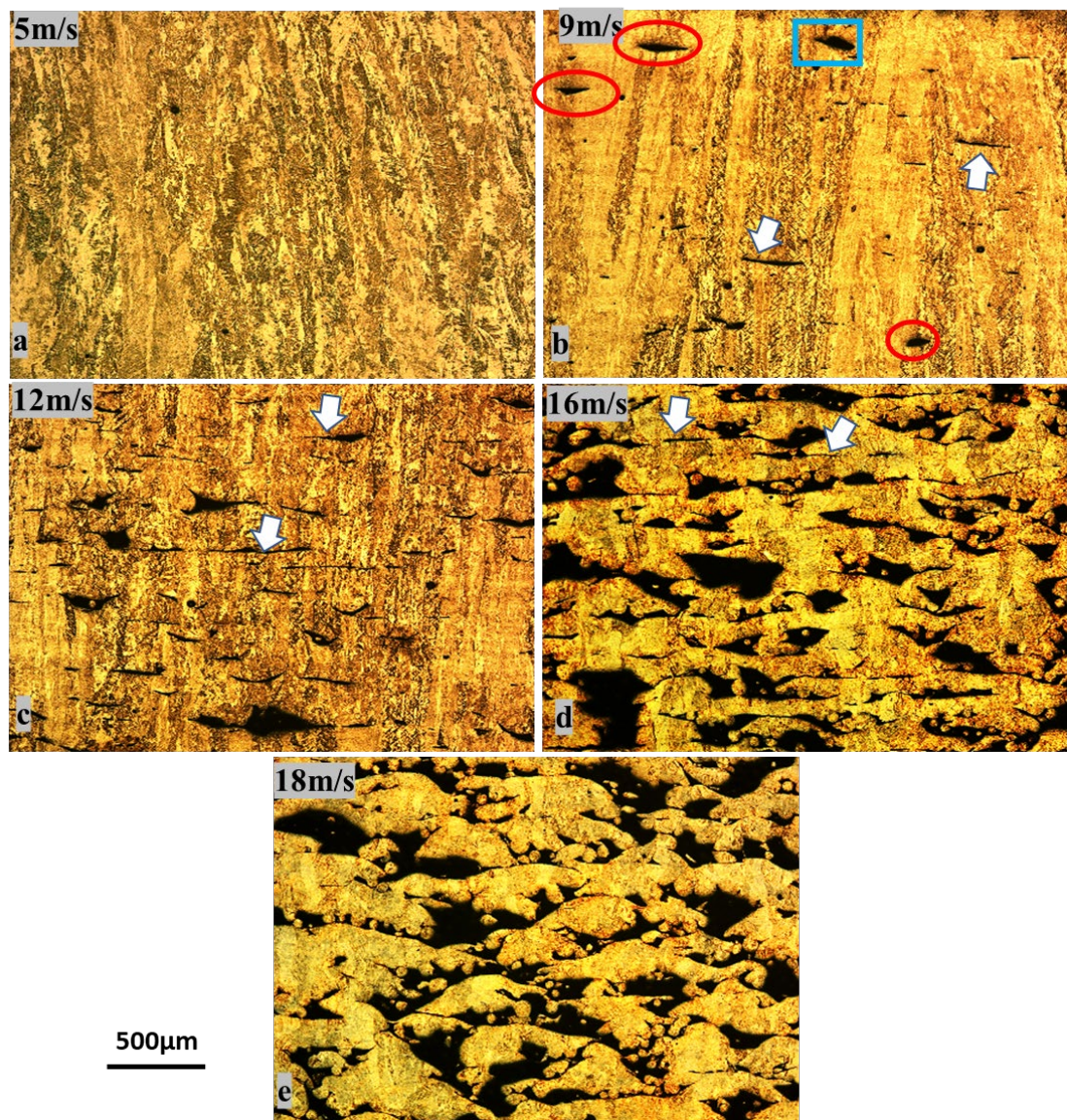
Figure 4-16 Optical micrographs of samples with scan speeds from 5m/s to 18m/s showing the characteristic shapes of LOF.

When the electron beam melts the powders bed, the Marangoni phenomena occurs due to thermal flow and heat transfer in the molten liquid from the highest to the lowest

94

temperature. When this phenomenon is accompanied with an increase in scan speed, turbulent (unsteady flow) results due to the heat transfer in the melt pool driving the molten metal to overflow into the last solidified melt pool side. Overflowing increases by increasing scan speed, as the molten liquid leaves the pool inducing greater overflowing. Molten metal solidifies during flowing over the solidified area, thus, generating LOF as shown in Figure 4-15 (LOF type 4) and in the blue rectangular outline in Figure 4-16b. The cross-section image of the 12 m/s sample's melt pool in Figure 4-17 shows the formation of a LOF type 4 observed in Figure 4-15, with a melt pool width of 600μm. Some articles use the terminology "porosity" as any kinds of defects including spherical porosity and LOF. However, these two kinds of defects need to be distinguished between each other due to their shapes differences and how they are generated (Kirchner et al., 2014; Puebla et al., 2012). Spherical or near-shaped spherical defects caused by trapped gas are porosities conversely, defects not spherical in shape are known as LOF. LOF can form with different types of shapes related to the generation process. Therefore, the shape and size of melt pools have an important role in LOF generation. Since the shapes of LOF differs from one another, they are categorized into 4 types as shown in Table 4-1. According to the shape of the LOFs observed in this study, the LOFs are categorized with the reason of each one of them based on adjacent melt pools illustrated. The reason for the shapes of LOF, categorized as types 1, 2 and 3 in this work is explained in detail in literature while the LOF type 4's shape has not been explained (Cunningham et al., 2016; Gong et al., 2014, 2013; Léonard et al., 2012; Q. Liu et al., 2014; Svensson & Ackelid, 2009; Tammas-Williams et al., 2015).
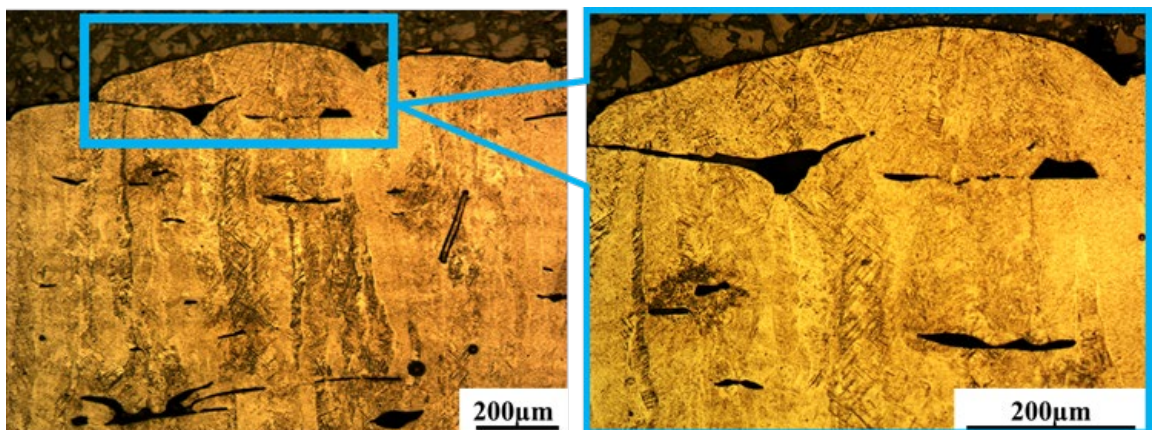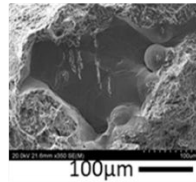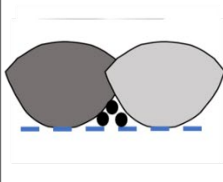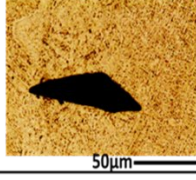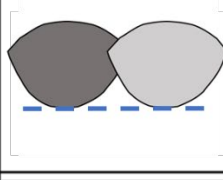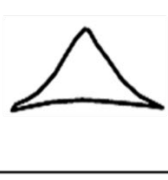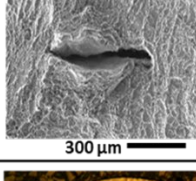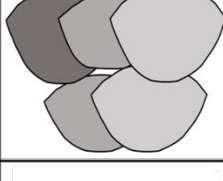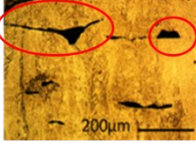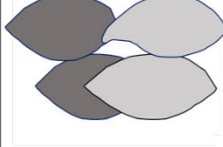
Figure 4-17 Cross-sectioned optical micrograph of 12m/s sample from the top surface (type 4).

Table 4-1 The category of LOF shapes in EBM manufactured specimens

Defect Type	Feature description	Feature	Relation with melt pool	Sketched Feature
Type 1	LOF with un-melted powder particles	100µm		
Type 2	LOF with triangular shape with no powder particles	50µm		
Type 3	LOF with flat shape	300 µm		
Type 4	Triangular /half circle LOF with no powder particles	200µm		

Samples produced at the scan speed of 9 and 12 m/s have LOF with an average length of 150 and 530 µm respectively, highlighting the direct relationship between scan speed and LOF. Further, the increased fraction of LOF induces a wavy and uneven top surface correlating the top surface with the percentage of LOF. The melted area is seen to flow over the previous solid hatch-line side during beam melting upon observing the cross-section taken perpendicular to the hatch line direction.

4.4   Effect of scan speed on the fraction of LOF

The fraction of LOF in the cross-section area for all samples was examined by ImageJ software and the results presented in Figure 4-18. By increasing the scan speed, the fraction of LOF increases sharply while the depth of the melt pool drops. Thus, the fraction of LOF increases meaning less fusion between layers and melt pools as the scan speed has a direct relationship with the number and size of LOF. As shown in Figure 4-18, the fraction of LOF is inversely proportional to the melt pool depth. By increasing scan speed from 5 to 18 m/s, not only the number of LOF but also the area of LOF increased as well. In addition, the shape of LOF changes by varying the scan speed in the specimens. It should be mentioned that the width of 5m/s could not be measured due to

melt pool overlapping. However, based on the LOF in the join area of the hatching and contour, the melt pool size of 5m/s should be greater than 700µm for both width and depth. The width and depth result of the melt pool by through increasing scan speed was similarly observed by various researchers (Cheng, Price, Gong, et al., 2014; Galati & Iuliano, 2018; Helmer et al., 2014; Narra et al., 2015).
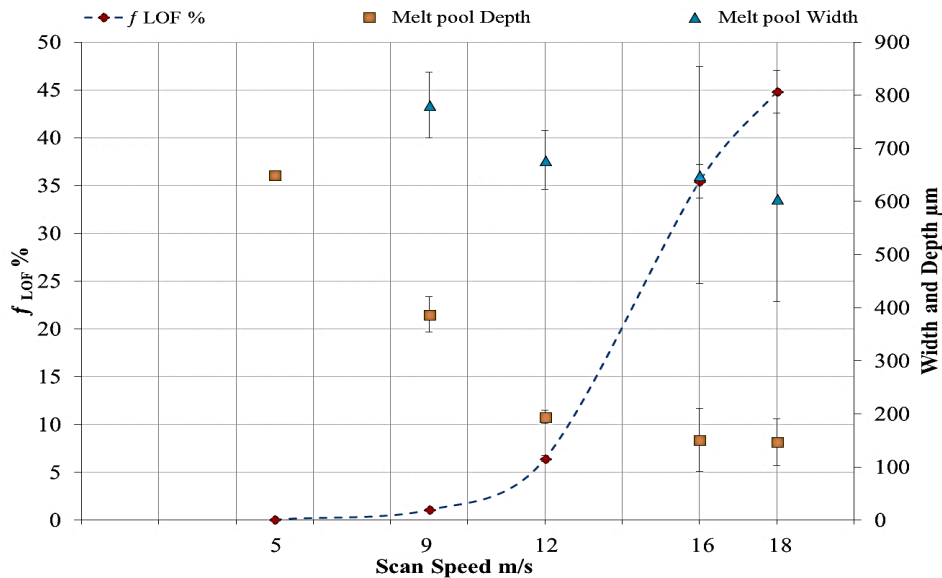
Figure 4-18 The percentage of fraction of LOF and melt pool width and depth vs scan speed.

Similar observations were made by Cunningham et al., Gong et al. and Léonard et al. in the EBM processing of Ti6Al4V with a direct relationship determined between scan speed and fraction of LOF resulting from the decrease in melt pool size (Cunningham et al., 2016; Gong et al., 2014, 2013; Léonard et al., 2012; Tammas-Williams et al., 2015).

4.5   Top region cross-section feature

The variation in the height of the top surface, as is observed in Figure 4-7, in samples with scan speeds of 5, 9 and 12m/s was measured by ImageJ software. On the cross-section of each sample, the lowest point on the top surface is chosen as the base line (Figure 3-7). The height of roughness was measured from the top of the surface to the base line, and the results were plotted in Figure 4-19. The range of the top surface roughness for the 5m/s sample is less than 0.05 mm; while the range for the 9m/s sample is between 0.08 and 0.125mm, and for 12m/s sample, the range is between 0.08 and 0.2mm.
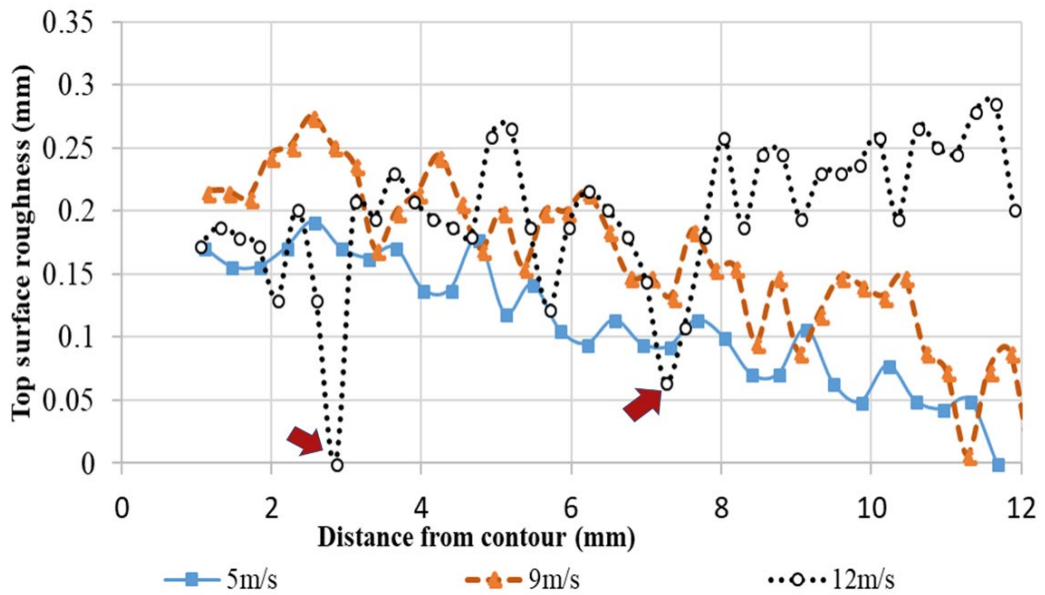
Figure 4-19 Surface height roughness measurements from the minima to the maxima of the samples produced at scan speeds of; 5, 9 and 12m/s.

The decreasing trend in the top surface height (top surface roughness) results due to the scan strategy. As the built wall in the contour area is fabricated before the hatching area it solidifies first with just the surface of powders melted in the contour area. Then, in the hatching area, the electron beam begins to melt the powder completely causing the melt pool height close to the contour to be higher than the middle of the hatch area. Due to this melting process, the height of the contour is not shown and considered in Figure 4-19. The lowest points in the 12m/s sample occur in the area that the electron beam missed to melt, which is actually the top surface of the previous layer as there is no melt pool in the areas shown with arrows. An increase in the melt pool crown of the previous layer would lead to a thinner deposition of powder in the consecutive layer, or possibly no powder in some locations. Since the beam energy is constant for all layers, the thinner layer would melt completely. Conversely, the area with thicker powder layer would produce LOF due to shallower penetration in comparison to 5m/s sample. By increasing the scan speed, the surface roughness is seen to increase. Juechter et al. and Cheng et al. observed similar findings, with the results explained that the increasing scan speed forms an uneven top surface characteristic to EBM components (Cheng, Price, Gong, et al., 2014; Juechter et al., 2014). Figure 4-20 shows this LOF formation due to an increase in the top surface roughness as an illustration. In the actual case, there is LOF formation which affects this process, and the beam gun melts some select areas in powder bed (layer n) forming humps hindering the distribution of powder for the consecutive layer. Therefore, when the beam gun melts the next powder layer (layer n+1), voids are formed due to the absence of

powder or poor wettability restricting fusion with the previous layer (layer n). The partially molten and unmolten powders left in layer n+1 aren't consolidated in the subsequent layers as the energy input is insufficient to melt two layers together. Therefore, the existed LOF in the previous layer does not heal and recover during the process at high scan speeds. Conventionally, the melting process for a single layer in EBM consolidates one or two underlying layers due to the high energy density and long melt duration. This is reduced at higher scanning speeds, as the transfer of energy into the melt is time limited resulting in a reduction in melt pool depth. This, in turn, leads to some layers not fusing together and a morphological change in the shape of melt pool with a wider crown on the top and a narrow root on the bottom.
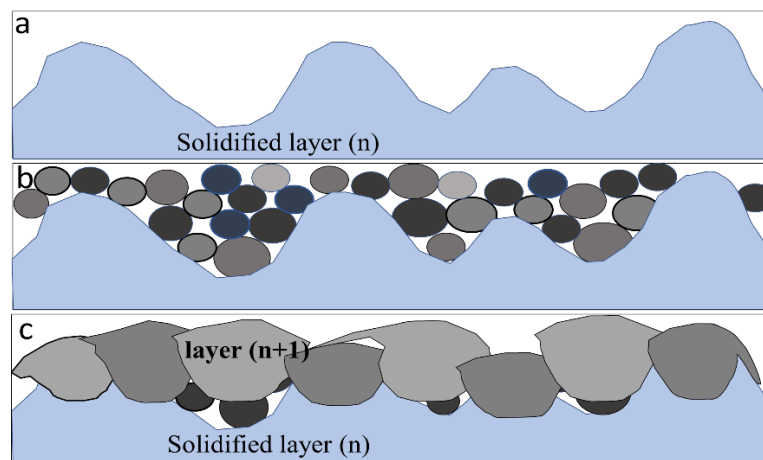
Figure 4-20 Illustration of producing layer n+1 on top of the solidified layer n.

As detailed above, by increasing scan speed, the surface height (top surface roughness) increased due to overflowing of the melt liquid on top of the solidified melt pools and due to the uneven distribution of powder on the previous rough surface. Hence, the new top new surface height follows the roughness of the previous layer. As the overflowing of the melt increases, LOF caused by melt overflowing (LOF type 4), increased as evident in Figure 4-19. At excessive scan speeds, the molten liquid overflows out of the pool and solidifies, reducing the liquid left in the pool area, worsening as the scan speed increases with increased melt pool instability in turn leading to higher top surface roughness. As the melt pool instability increases leading to melt discontinuity, the amount of LOF present and the size of LOF eventually increase. This phenomenon was further observed in EBM processing by the following authors (Attar, 2011; Galati & Iuliano, 2018; Gusarov et al., 2007; Jamshidinia et al., 2013). From their work, the authors explain that as melt pool forms, the heat transfers from the highest temperature to the lowest temperature leads to the surface turbulent flow as Marangoni phenomenon and the

temperature distribution from the surface to the depth generates flotation forces. As scan speed increases, this flotation forces in the melt pool leads to Rayleigh instability in the melt pool and breaks it into droplets thus, balling occurs. The balling phenomenon causes a rough top surface, consequently, the next deposited powder layer spreads unevenly and increases instability in the melt pool, and the uneven powder layers cause defects.

Although the range of the highest point to lowest point of the top surface, (highest top surface roughness (HTSR)), in the 5m/s sample is approximately 0.05mm, no LOF was observed. This proves that the melt pool size is large enough to prevent the formation of any LOF. The HTSR increased in the 9m/s sample to be in the range of 0.08 to 0.125mm with LOF mainly types 1 and 3 (Table 4-1). The surface height difference from the lowest point on the surface until the highest point in the samples at; 5, 9, 12, 16 and 18m/s are 120, 160, 240, 260- 310μm and 400μm respectively as presented in Figure 4-21. Through the comparison of the fraction of LOF area with the surface roughness range, the surface roughness increases with increasing scan speed in the samples in addition to the fraction of LOF area. Also, increasing a fraction of LOF induces wavy and uneven track lines on the top surface, showing the relationship of the top surface with the percentage of LOF.
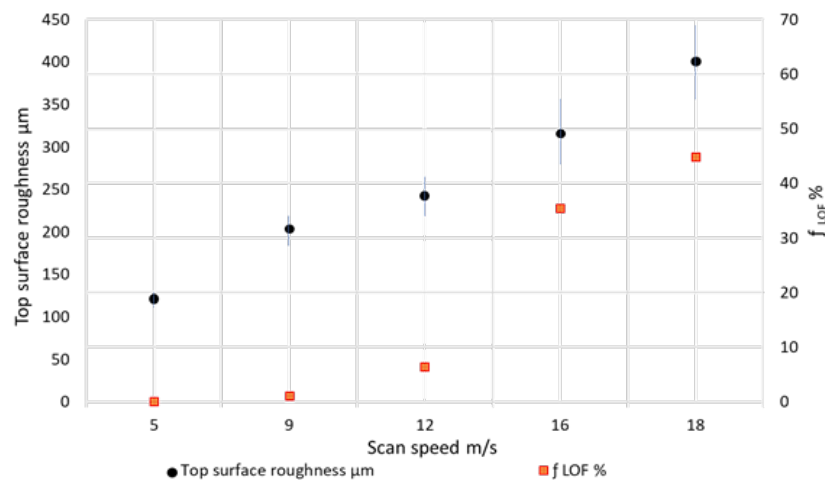
Figure 4-21 Comparison of the top surface roughness with the fraction of LOF area as scan speed increases from 5 to 18m/s.

The top surface roughness increases with increasing scan speed and is accompanied with an increase in the fraction of LOF area resulting from a decrease in melt pool width and depth. Thus, proposing that the top surface roughness is in a reverse relationship with the melt pool depth and width. Therefore, when the top surface roughness exceeds 0.05 mm, the possibility of LOF formation inside the samples increases and induces an unsteady

flow in the molten metal in the samples, leading to the expectation of more LOF especially type 4 grades.

4.6   Effect of the scan speed on the microstructure

The microstructures of Ti-6Al-4V processed by EBM consist of α+β lamella phases inside the columnar grains of prior β phase boundary (current α columnar grain boundary) along the build direction with intersecting Widmanstätten α platelets. During the EBM process, the predominant direction of heat flow downward results β phase columnar grains transform into colonies of α + β. Heat cycles due to track by track and layer by layer building mean transformation taking place multiple times. A varied width of columnar α grain boundaries were observed in planes parallel to the build direction as seen in the SEM images presented in Figure 4-22 with the α and β phases revealed in SEM micrographs. It can be observed from Figure 4-22 that, as the scan speed increases from 5 to 18m/s the β phase size decreases. The difference in cooling rates results in a non-uniform distribution of phases and variation in their sizes. Therefore, the width of the α columnar grain boundary was measured in many areas across the cross-section with the average width for each sample presented in Figure 4-23.
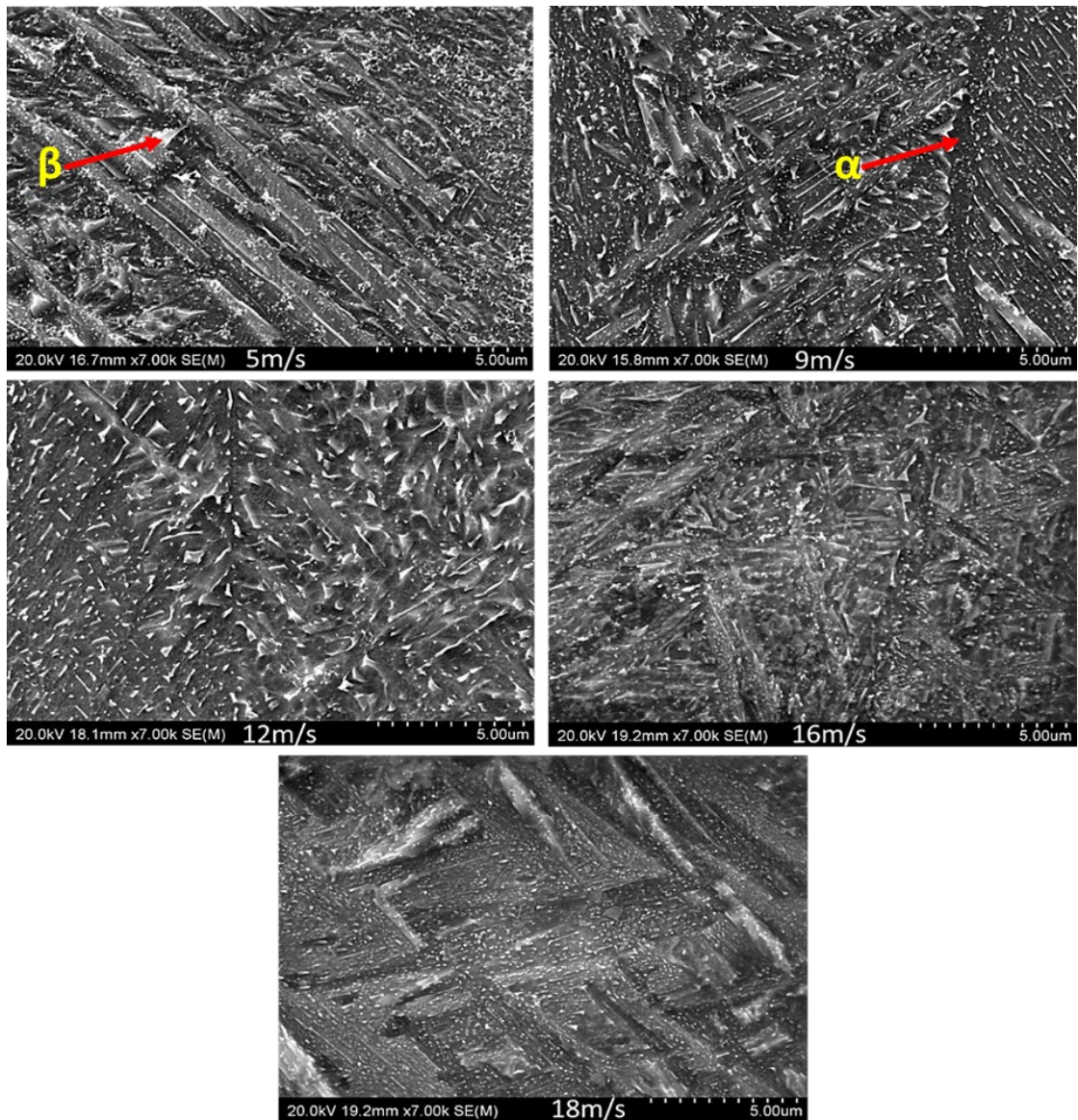
Figure 4-22 SEM micrographs of sample cross-section parallel to the build direction
with scan speeds of; 5, 9, 12, 16 and 18m/s.

As scan speed increases from 5 to 12 m/s, the width of the columnar boundary decreases simultaneously. It was predicted that this decrease in columnar boundary width continued to the 18 m/s sample. However, it was observed that in increasing scan speed from 12 to 18 m/s the width of columnar boundaries remained between 80 to 120 µm. Therefore, scan speeds influence on the width of columnar boundaries is predominantly in the range of 5- 12 m/s and exceeding the scan speed from this point has a relatively minor influence on the width of the columnar boundaries. Increasing scan speed further leads to a decrease in the melt pool depth and width, concluding that the average width of columnar boundaries has a relationship with not only the width also the depth of the melt pool. As melt pool depth decreases from ~650 to 147 µm, the melt pool width follows the same trend gradually decreasing from 800 to 600 µm and, the width of the α columnar grains

decreases slightly from 132 to 95 μm. As the scan speed affects the melt pool width and depth consequently, less molten liquid is available for solidification producing columnar α+β grains with smaller widths. However, the percentage change in columnar α+β grain width is not as significant as compared to the melt pool size change with, the greatest changed observed in the melt pool depth.
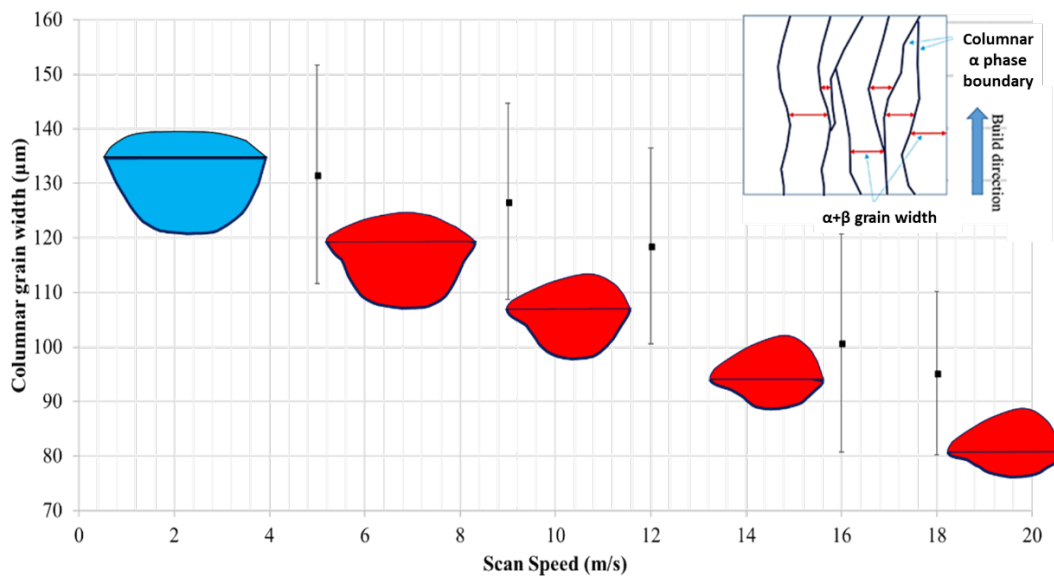
Figure 4-23 Average of the α+β grain width with scan speed accompanying the melt pool shapes.

This result was similarly observed by Cheng et al. and Körner et al. and Narra et al. in their work on EBM alloys (Cheng, Price, Gong, et al., 2014; Körner, 2016; Narra et al., 2018, 2015).

4.7 Effect of the sample location on the formation of LOF

In order to evaluate the effect of sample location on percentage fraction of LOF, a few samples were fabricated in three separate locations on the build-platform and analysed by synchrotron tomography. These samples were additionally evaluated for their percentage of LOF and pore area along the build height in three locations with the results presented in Figure 4-24.

The synchrotron results revealed that the percentage of defects in the Edge-built sample with 0.453% is greater than Centre (0.382%) and Middle build samples (0.183%) respectively. By distinguishing the difference between the percentage of porosity and LOF formation, it was found that the largest percentage of fraction of LOF occurred in the edge sample, with LOF decreasing in the centre and Middle-built samples (0.304%,

0.152% and 0.127% respectively). However, this percentage drops dramatically by increasing the distance from built-platform in edge and centre samples with the opposite observed for the middle-built samples. The results lead to the conclusion that the amount of LOF is not strongly related to the sample height and its location on the build-platform. Galarraga et al. evaluated the percentage of porosity in the sample produced in the centre of the platform finding a result consistent with our observations. The sample located on the edge in Galarraga et al.'s work, possessed 0.02% less porosity in the top area than the bottom area. Same in this study, the percentage of the porosity and LOF are lower in the top area, and both the percentage of LOF and porosity reduce accordingly moving down the sample reaching the bottom (Galarraga et al., 2017).
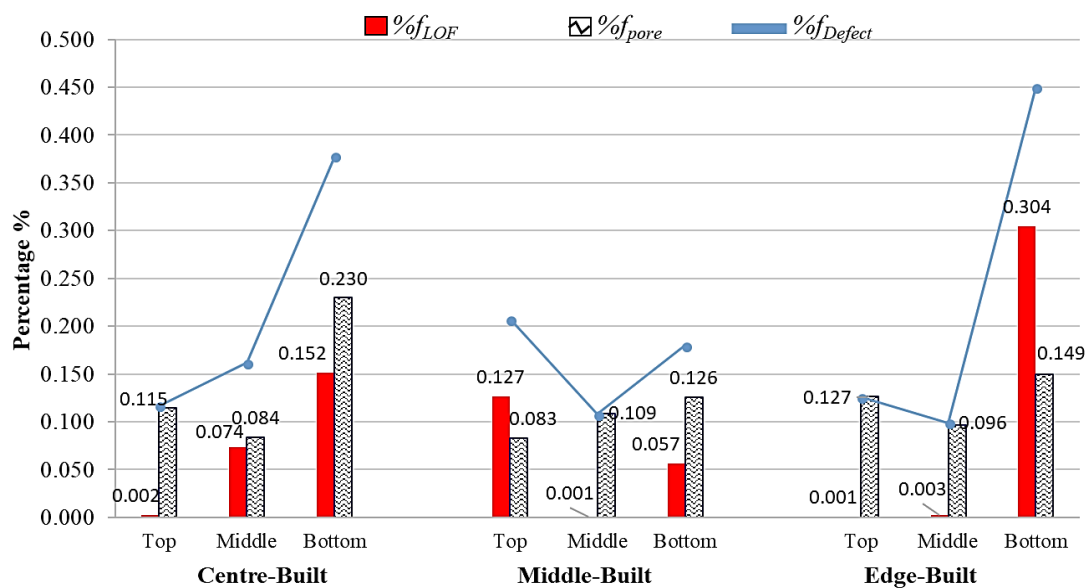
Figure 4-24 LOF and pore fraction obtained from synchrotron analysis for three different locations on the build platform.

In order to verify the LOF fraction calculated manually with ImageJ, a 2D cross-section plane of 5m/s sample was compared with the synchrotron result. This sample, as shown in Figure 3-4, was produced with 5m/s and was built at the sample location on the platform as the synchrotron edge-built sample. The 5m/s sample as shown in Figure 3-4 was built 10mm above the built-platform in the edge area. The edge-built synchrotron sample with area of 15×15 mm^2 as shown in Figure 3-8 was built 20mm above the platform. The position of both samples is shown in Figure 4-25. The fraction area with using ImageJ was obtained on one cross-section plane, while the synchrotron result took into account many planes with a result that is more accurate than measuring a single cross-section plane. The result of the 2D cross-section for 5m/s sample shows that there is no

LOF inside the hatching area and the result of synchrotron confirms the result of the 2D cross-section fraction of LOF area. The tested area of the 5m/s sample is located in the middle height of the edge-built sample where the fraction of LOF was measured to be 0.003% proving the consistency of two results.
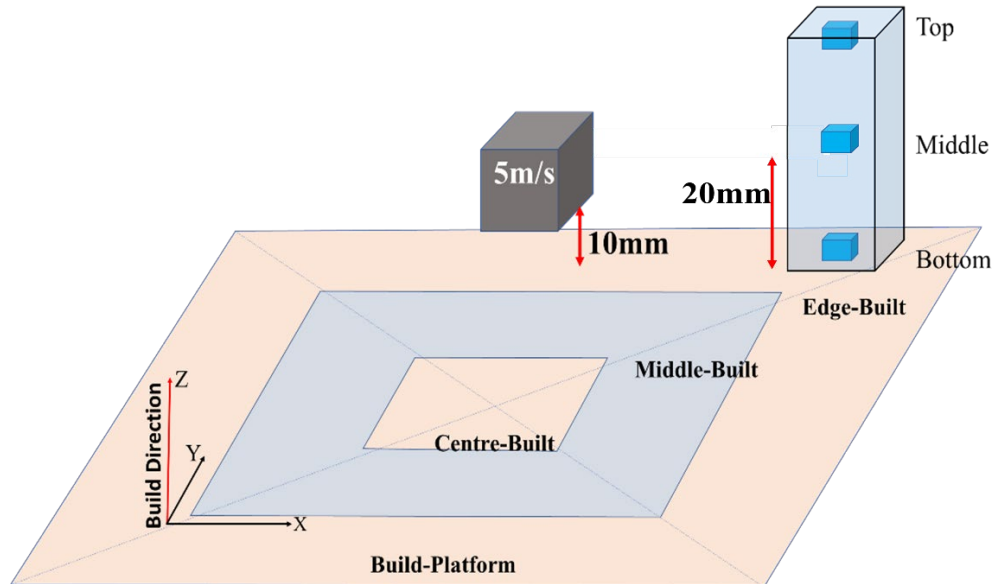
Figure 4-25 The location of the 5m/s sample built in the edge area.

4.8   Summary

The Ti6Al4V microstructure consists of an α+β lamella inside columnar α phase boundaries that re-melts and re-solidifies several times; and the layers become heat treated due to stay on the heat affected zone during EBM processing. This cyclic heat input results in the disappearance of the melt pool boundary lines and complexities in the observation of melt pool shapes, geometry and boundary. Furthermore, the formation of LOF is sensitive to EBM processing parameters, and so a range of scan speeds were employed to study its formation mechanics and its effect on the melt pool shape and size.

From the work contained within, it was revealed that the shape of the melt pools is a direct function of the scan speed and through increasing the scan speed from 5 to 18m/s, the melting width on the powder bed decreases, leading to a decrease in the melt pool depth. By applying the energy input Equation 1-1, for the scan speed range, the energy input available to melt the powder reduces proportionately with the increasing speed, from 16.8 to 4.66 J/mm^3. Melt pool width is expected to be more than 750 μm, with a depth of 700 μm for the 5m/s sample. Whilst for samples produced at the greater scan speeds, melt pool width decreased from 750 to ~ 400 μm, with an equivalent decrease in the melt pool

depth from ~410 to 100 μm, resulting from the increasing scan speed reducing the time for heat penetration. The decrease in energy input leads to discontinuity in the melt pool due to heat transfer from the highest to the lowest temperature, producing a thermal gradient. Through increasing of the melt pool thermal gradient, the Marangoni phenomena increases leading to Rayleigh instability, breaking the melt pool into droplets in inducing balling. Increasing the scan speed from 5 to 18m/s leads to the generation and predominance of the balling phenomena leading to the melt pool breaking up into spherical globules. The height of the melt pool crown increases with increasing scan speed, while simultaneously the melt pool body depth decreases. From literature, melt pool depth was used to evaluate the height of the melt pool body excluding the crown height and does not take into account the melt pool crown. The true melt pool depth is the distance from the lowest point of the melt pool boundary of the body, to the highest point on the top of the melt pool crown. With increasing scan speed, the melt pool shape and size changed and the rate of the reduction in the depth of the melt pool was much greater than the width (decrease of ~79% in depth compares to ~18% in width).

Classification of LOF by their shape into four types was illustrated and explained within this study. By increasing a sharp increase in the amount of LOF from 0 to 45% is observed by increasing the scan speed from 5 to 18m/s, while the corresponding energy input drops. Increasing scan speed from 5 to 18m/s increases the distance between track lines on the top surface, signifying the decrease in overlapping between two adjacent melt pools. When the electron beam melts the powders bed the Marangoni phenomena occurs within the pool, increasing in intensity with scan speed, causing turbulent flow leading to molten metal overflowing onto the last solidified melt pool side. This overflowing increase to form type 4 LOF defects with both the top surface roughness and the fraction of LOF increasing as well. The top surfaces relationship with LOF is evident when the top surface roughness exceeds 0.15 mm, the possibility of LOF formation inside the samples increases thus, resulting in the direct relationship of the melt pool crown with the fraction of LOF. Furthermore, the scan speed has a direct relationship with LOF length. An increase in scan speed induces a wavy and uneven top surface, accompanied with an increase in the fraction of LOF proving a direct relationship between the top surface and the fraction of LOF.

5. CHAPTER. Effect of defects/LOF and build direction on Impact Toughness

In this chapter, testing and metallographic examination have been conducted to investigate how defects and build-orientation affect the impact energy of Ti6Al4V specimens built using EBM. The amount, maximum size, percentage of fraction of LOF and porosity, and the percentage of oxygen level in different build orientations are analysed and presented. The cross-sections of fracture surfaces in three different orientations are presented and compared. The analysed results of placing a notch in different sides of each orientated sample to study the effect of notch positions on impact energy are also discussed.

5.1 Effect of build direction on Impact Energy

The Charpy test results of three groups, which are presented in Figure 5-1, show that the specimens with different build directions absorb quite different energy values before fracture. The range of impact energy values also varies from one batch to another, but all batches have a common trend from 0° (vertical - V) to 45° and 90° (horizontal - H). Impact energy decreases as the angle between the sample's longitudinal side and the build direction increases (Figure 3-13).
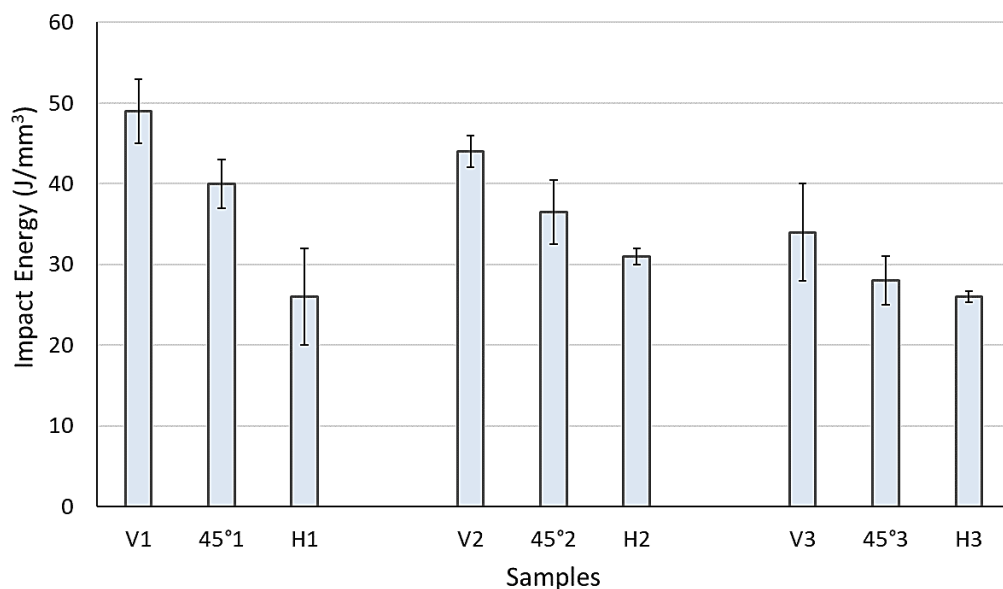
Figure 5-1 The Impact energy value of Charpy samples in three different build directions.

The impact energy result of the vertical samples is higher than the horizontal samples with values of 49, 44 and 34J versus and 26, 31 and 26J, respectively. This is in disagreement with Wu et al. and Yasa et al.'s work which reported that the impact energy in horizontal samples was higher than in vertical samples (Wu et al., 2016; Yasa et al., 2010).

For understanding the reason of the common trend among all impact energy tested samples, LOF and porosity levels were analysed by distinguishing maximum area, the number and fraction area of LOF, and porosity.

5.2   Effect of defects on impact energy

On the fracture surface of all Charpy samples, LOF and porosity were detected with different shapes. The build direction of the vertical sample is perpendicular (90°) to the fracture surface, while for the horizontal samples is parallel (0°) to the fracture surface.
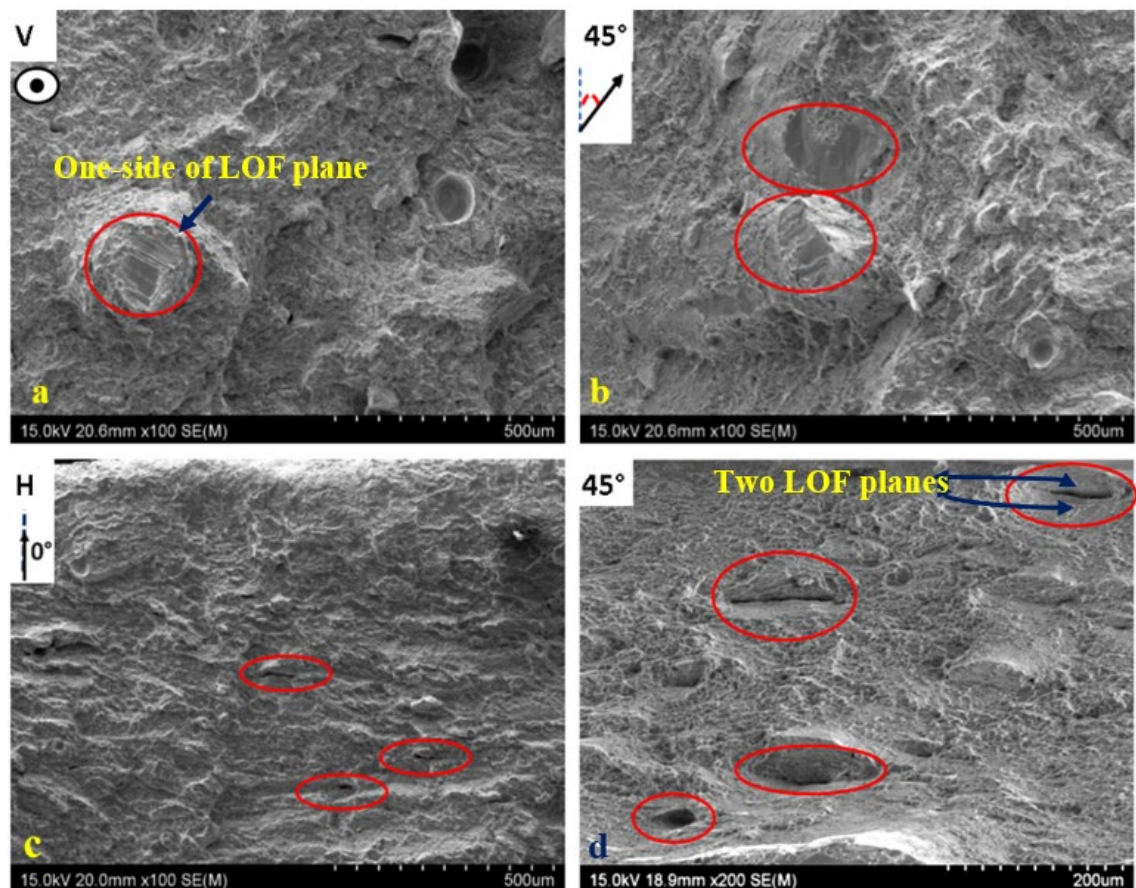
Figure 5-2 LOF in three fracture surface orientations, vertical, 45° and horizontal samples.

In the 45° sample, the build direction (arrow) has a 45° angle with the fracture surface as illustrated next to each image in Figure 5-2. The LOF observed in the horizontal samples is two flat planes or an opened plane without fusion, while just one surface of these two flat planes can be observed in the vertical samples. Both shapes of LOF in the vertical and horizontal samples are detected in the 45° sample's LOF.

All mentioned shapes of LOF are shown by red lines and in order to show both shapes of LOF in the 45° samples, two SEM images are used in Figure 5-2b and d. It should be mentioned that the different shapes of LOF are because of the direction of the sample's orientation and the position of the Charpy notch. Although the LOF direction is in favour of the fracture direction in the vertical samples, their impact energy values are higher than the other samples in each group. By comparing the orientated shape of LOF with the fracture direction and the impact toughness value, it is believed that the direction of LOF does not affect the impact energy in this work which disagrees with Wu et al.'s result. Wu et al. reported that the low toughness of the vertical sample in comparison with the horizontal sample is because of the orientation of LOF, which was along with impact energy that reduces the load bearing in the vertical sample; though, in the horizontal sample, the LOF disk-shape orientation is perpendicular to the fracture direction, which increases the resistance of the sample to impact loading (Wu et al., 2016). While our finding shows that regarding the high value of impact toughness in the vertical samples and the LOF shape orientations, the impact energy does not have a relationship with LOF orientation. It should be mentioned that this result is valid when the LOF areas are not more than 1.1%.

The LOF and porosity areas were measured in each SEM image from the sequential images of the fracture surface. Then, the total area of the LOF/porosity was divided by the total area of the fracture surface. Therefore, the fraction of LOF/porosity area, the number of LOF/porosities and the maximum LOF and porosity areas were evaluated and analysed. Analysing the number of LOF reveals that by increasing the angle between sample longitudinal sides with build direction, the average number of LOF rises from (0°, vertical) ~160 to (45°) ~184 to (90°, horizontal) ~235, as shown in Figure 5-3. In all three groups, vertical and horizontal orientated samples have fewer and higher numbers of LOF, respectively. But as indicated in Figure 5-2, the orientation of LOF in the horizontal samples does not affect the impact energy, at least not as much as in the vertical samples. Consequently, the angle of sample longitudinal side and build direction affects the sample's impact energy (Figure 3-13). This result demonstrates that the impact energy is

affected by build direction, while Yasa et al. (Yasa et al., 2010) stated that the impact energy is not a function of the build direction. In addition, it is evidenced that as the number of LOF increases, the crack propagates faster and easier with lower energy absorption in the samples. Therefore, the impact energy is a function of the number of LOF. In groups two and three, vertical samples with impact energies 44 and 34J, have 180 and 170 numbers of LOF, respectively.
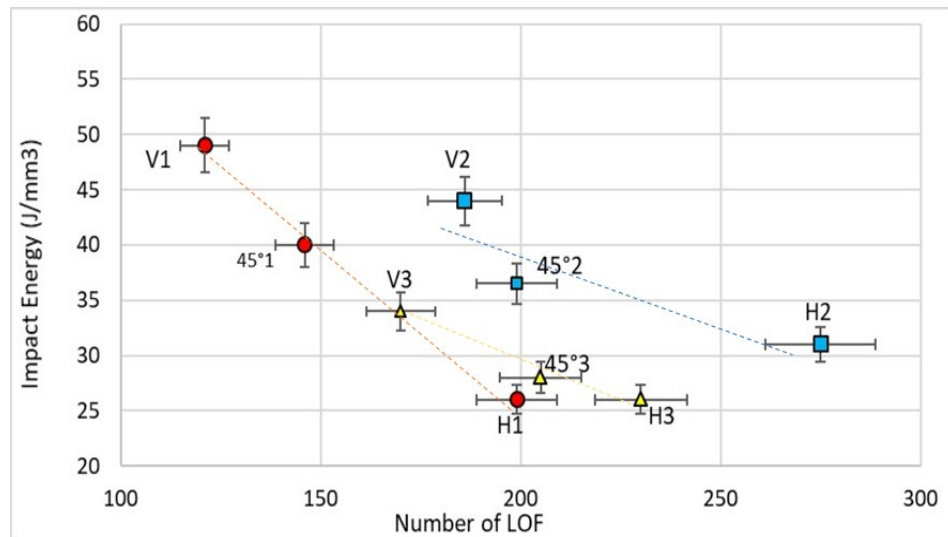
Figure 5-3 The number of LOF vs impact energy

The number of LOF values specifies that among the vertical, horizontal and 45° samples, the vertical samples with the least number of LOF have the highest impact energy or impact toughness. But by comparing each sample individually, a different result can be concluded. For instance, comparing the number of LOF in the vertical sample number 2 with 45° sample number 1, shows that although the impact toughness of the vertical sample is 44J which is higher than impact toughness in 45° sample number 1 with 40J, the number of LOF in 45° sample is 140, while in the vertical sample with higher impact toughness this value reaches 180. Therefore, this finding suggests that although there is a relationship between the number of LOF and impact energy, there could be other factors that affect the impact energy and toughness.

Figure 5-4 indicates the effect of maximum LOF area on the impact energy. In the vertical samples, the maximum LOF area increases from 0.005 to 0.113 mm^2 as the impact energy decreases from 49 to 34J. Also, in the 45° samples, the maximum LOF area increases from 0.009 to 0.125 mm^2. Unlike the vertical and 45° samples, in the horizontal samples the maximum LOF area increases from ~0 to ~0.165 mm^2 while the impact energy is in the same range. Although in the horizontal samples, the impact energy is approximately

in the same range, the maximum LOF area changes from 0.002 to 0.165mm^2. Because the orientation of the longitudinal disk-like LOF with the build direction, which is 90°, in the horizontal samples, the maximum LOF area does not readily contribute to the crack growth. Therefore, the maximum LOF area affects the impact energy when LOF is orientated in a favourable direction for crack growth. In addition, the effect of the maximum LOF area on the impact energy is a reason for the linear decrease in vertical (from V_1 to V_3) and 45° (from $45°_1$ to $45°_3$) samples, while, as the maximum LOF area does not affect the impact energy, the impact energy of horizontal samples is in the same range.
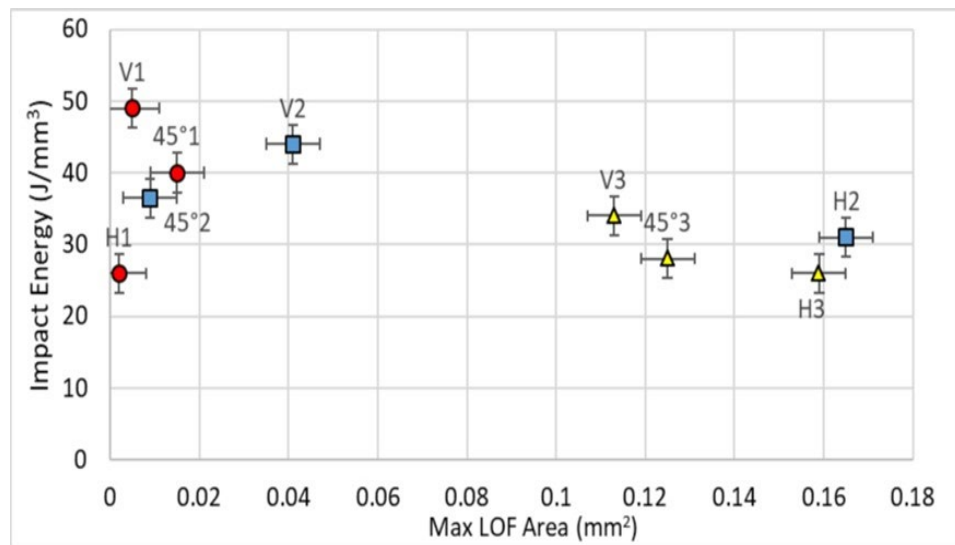
Figure 5-4 The max LOF size vs impact energy

Analysing the percentage of LOF of all batches with the impact energy results shows that although there is no relation between the percentage of LOF with impact energy, all three batch orientations have a similar behaviour. The vertical samples have the lowest percentage of LOF in all batches, as shown in Figure 5-5, while the horizontal and 45° samples have a higher percentage of LOF respectively. In the second batch, the vertical and horizontal have approximately the same value of 0.99%, while their impact energy has a large difference (31 versus 44J/mm^3). Consequently, the percentage of LOF has no correlation with the change in impact energy; however, the percentage of LOF reaches 1.05%. According to the influence of the maximum LOF size and no effect of the fraction of LOF on the impact energy indicates that the LOF size is important on the influence on the impact energy. LOF size which is less than 49μm^2 did not affect the impact energy.

In Tammas-Williams et al. and Ming-Wei Wu et al.'s work, LOF was observed, and its size was measured to be several hundred micrometres (~190 and ~300μm) (Tammas-

Williams et al., 2015; Wu et al., 2016). In these works, the effect of LOF on impact energy was investigated by analysing the number, maximum size and fraction of LOF. As mentioned before, the number of LOF affects impact energy while the percentage of LOF has no influence on the impact energy. The fraction of LOF is quite small to affect crack propagation by speeding crack propagation up by connecting to each other. Each LOF is quite small to make an easy path for the crack to propagate with lower impact energy. That means that during crack propagation, it is not important how large each area of LOF is. The effective factor is how many LOFs are in the area where the crack propagates (in the range of area and fraction of LOF of this work). Grell et al. observed LOF in their studies and explained that LOF was the cause of lowering impact energy in the Charpy samples (Grell et al., 2017). Our results showed similar findings. However, in our result, we specifically found that the number of LOF affects Charpy impact energy.
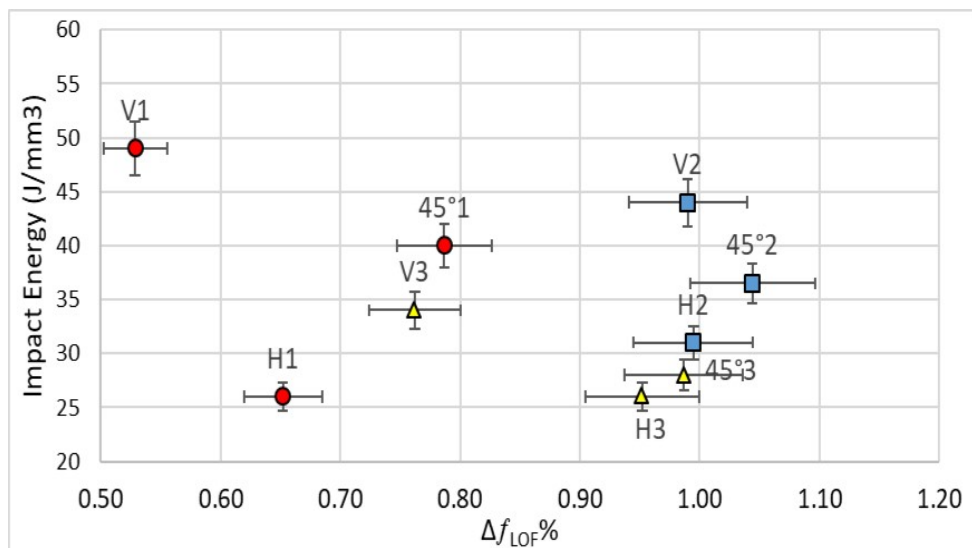
Figure 5-5 The percentage of fraction of LOF vs impact energy on fracture surface

Figure 5-6 shows the result of the number of pores with impact energy. In groups one and three, as the angle between the sample's longitudinal side and build direction decreases, not only the number of pores, but also the impact energy increases as well, while in group two, by increasing the number of pores, impact energy decreases. The contradiction among these three groups shows that impact energy is not a function of the number of pores, as shown in Figure 5-6.
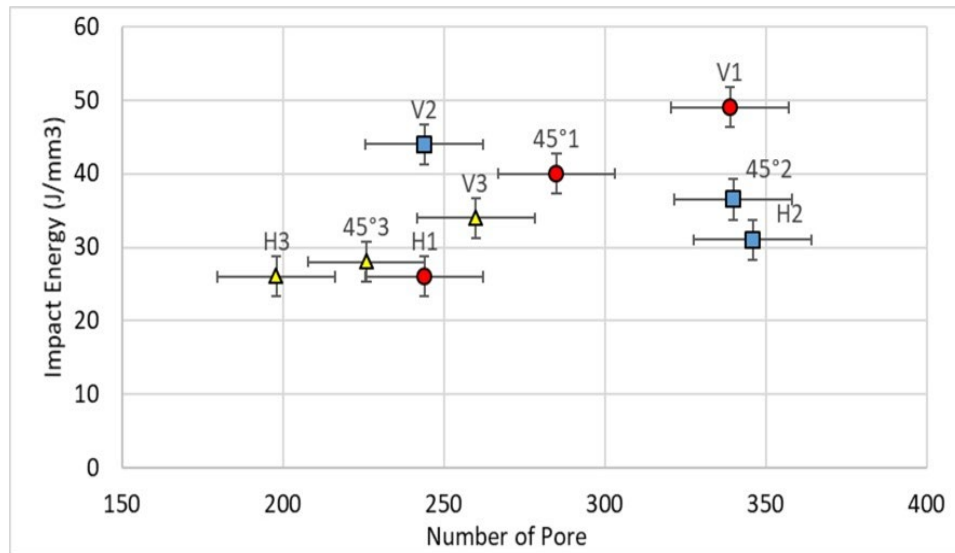
Figure 5-6 The number of pores vs impact energy on fracture surface

The range of maximum pore area in all three batches is approximately from 0.09 to 0.17 mm2. The highest maximum pore area belongs to horizontal samples with values from 0.14 to 0.17 mm^2. In the first and second groups, the vertical samples have the highest impact energies, which are 44 and 49J, respectively, and their maximum pore areas with values of ~0.13 and 0.14mm^2 are close to the horizontal samples (~0.14mm^2) with the lowest impact energies (26 and 31J).

For the percentage of pore versus impact energy, as shown in Figure 5-7, the second and third batches show that by increasing impact energy, the percentage of pore increases. However, batch one shows different behaviour. The result of related pores demonstrates that the percentage of pores in all three groups has a high range of value around 1%, while, Kristofer (Ek, 2014) measured the percentage of pores and reported it to be 0.27%. Group three has the highest percentage level of pores from horizontal to 45° and the vertical samples with values of 0.87% (26J), 0.9% (28J) and 1% (34J). Therefore, the percentage of pores does not have a substantial effect on impact energy. However, the percentage of pores in groups two and three increases when impact energy increases. The findings in Figure 5-6, and Figure 5-7 represent the effect of porosity on impact energy i.e. porosity does not significantly affect the impact energy in this work.
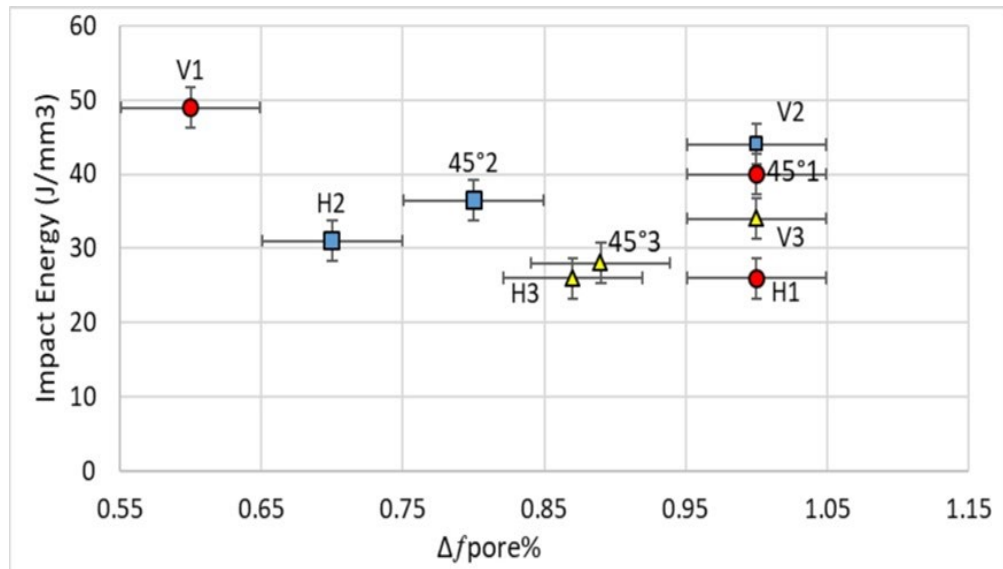
Figure 5-7 The percentage of fraction of pore versus Impact energy

As is shown in Figure 5-8 and Figure 5-9, the vertical sample continued to have the highest sub-micron voids around the fracture surface in batch one compared with other batches. The smallest size in the number, percentage of fraction and max pore is 14μm.
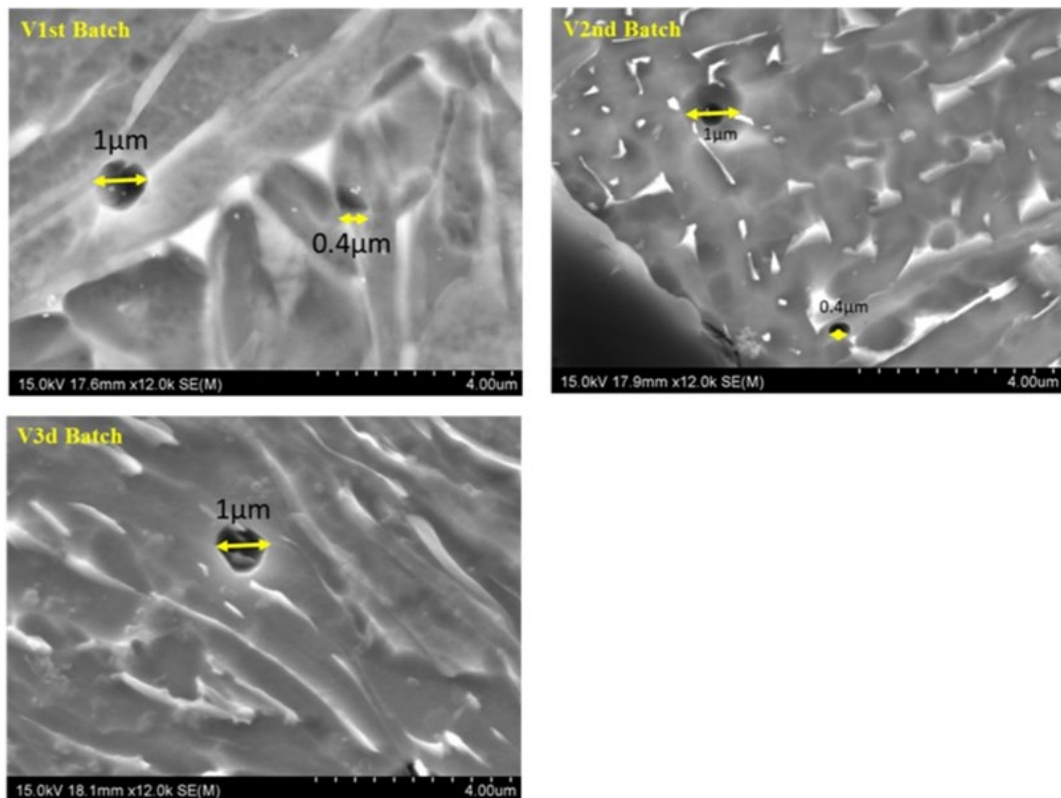
Figure 5-8 The sub-micron void in V samples close to the fracture surface.

However, there is a smaller pore, which is called a sub-micron void with a size less than 5 μm. A sub-micron void may have formed during the test. The sub-micron void

114

diameters of vertical samples in different batches have been measured, as shown in Figure 5-8 and Figure 5-9.

Figure 5-9 indicates the relationship between the sub-micron pores far from the fracture and close to the fracture surface. By decreasing the impact energy from 49J (V_1) to 44J (V_2) and 34J (V_3), the number of voids close to the fracture (in ~ 200 μm) increases from 56 to 139. These sub-micron voids are measured far from the fracture area as well where the result shows that the influence of applied load still can be seen even 2000 μm from the fracture area. However, the number of sub-micron voids is fewer than the 200 μm area close to the fracture surface. As impact energy decreases from 49J to 34J in the vertical samples, the number of micro-voids far from the fracture surface (~ 2000 μm) increases from 43 to 101. Spherical pores are too small to have a major effect, but there is a relationship between the number of sub-micron pores and the impact energy.
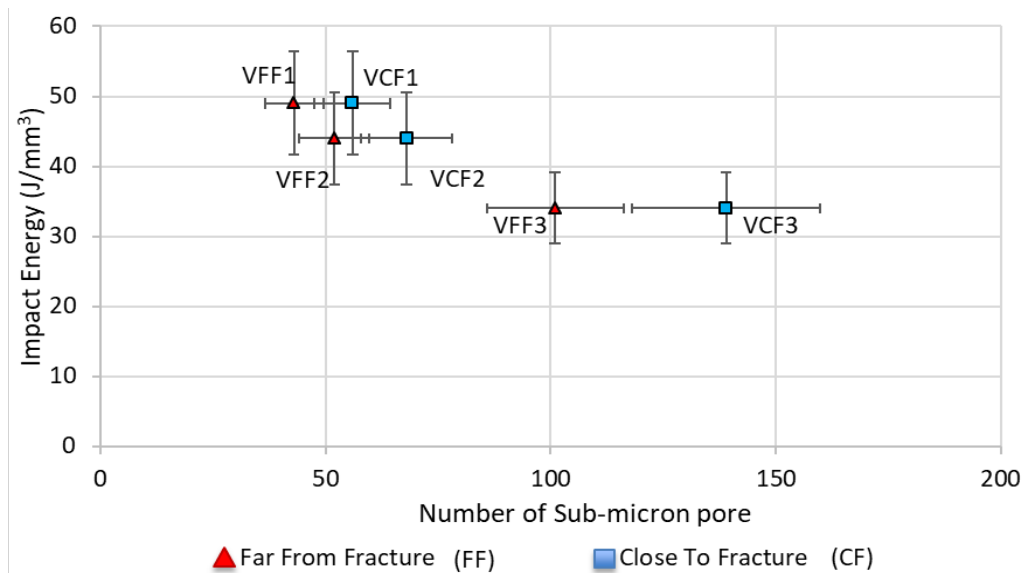
Figure 5-9 The number of sub-micron voids in vertical samples in three batches of V_1, V_2 and V_3 in two different locations, 200 μm from (close to) the fracture (VCF), and ~ 2000 μm from (far from) the fracture (VFF) surface.

5.3 Effect of Microstructure on impact energy

The structure of Ti6Al4V, which is produced by EBM, is Widmanstatten with $\alpha_+\beta$ phase microstructure. In order to investigate if the microstructure has any influence on the trend of the impact energy value, the β phase lengths of all samples were measured because the temperature differences in build height could cause different β phase lengths in EBM products. The procedure of measuring the β phase length is explained in Chapter 3, Figure

3-17, and the result is presented in Figure 5-10. It is shown that the β phase length increases as the impact energy decreases. In addition, as the angle between the longitudinal side and build direction increases (from the vertical to 45° and horizontal samples), the length of the β phase increases while impact energy decreases simultaneously. Horizontal samples have the highest length of β phase with horizontal samples 1, 2 and 3 having 4.2, 4.3 and 4.7μm, respectively. For measuring β phase length, more than eight areas in different columnar α+β grains are measured to be as precise average length. Vertical sample number 1 has the highest impact energy of 49J and has 3μm β phase length while vertical sample number 2 with 44J has the same β phase length as vertical sample 1. As the impact energy value decreases from vertical to horizontal samples, the β phase length slightly increases, however, the β phase length differences in different orientated samples (V, 45°and H) is approximately 2 μm which is narrow. In addition, measuring the width of α+β grain width shows that impact energy value decreases from vertical to horizontal samples, as the average of the α lath increases slightly (Figure 5-10). Therefore, regarding the impact energy values of the directional samples, the α lath slightly increase. The reduction impact energy from vertical to 45° and horizontal samples is due to the microstructure difference, however, this difference is really small. As the angle between the longitudinal side and the build direction increases from 0° (vertical sample) to 90° (horizontal sample), the microstructure becomes slightly coarser as the impact energy decreases. This microstructural difference is due to the directional built sample, as the height of the sample increases, the microstructure in the sample becomes finer. The impact energy decreases from vertical to 45° and horizontal samples while the average of the α+β grain width is the same in all samples (Figure 5-11). It should be mentioned that the procedures of measuring the average of α lath width, α+β grain width and β phase length are explained in Chapter 3, Figure 3-17. Besides, the microstructure of each sample is shown in Figure 5-12. The light grey needles represent β phase, and the dark grey colour is the α phase.
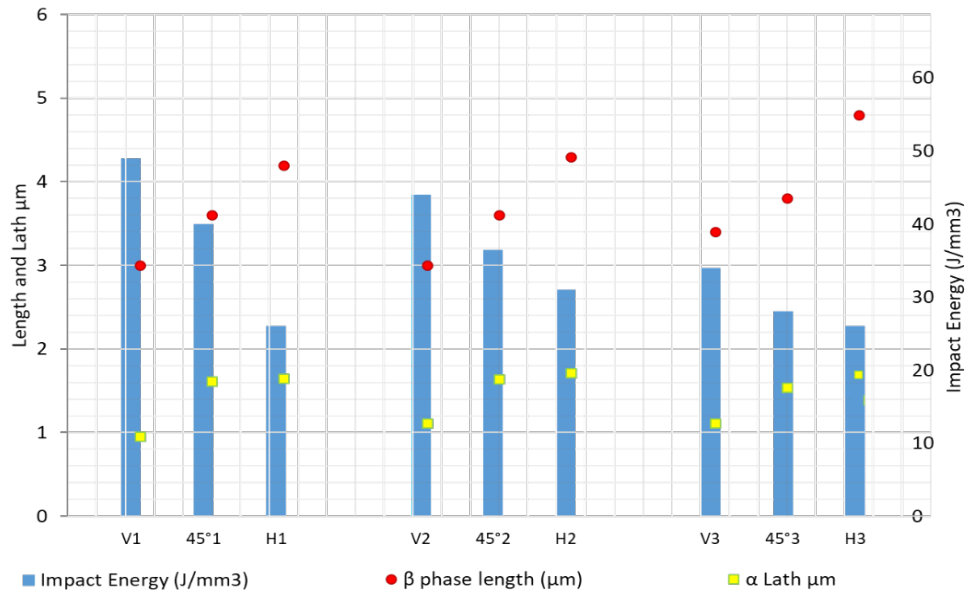
Figure 5-10 Length of β phase and the α lath for each sample vs impact energy.
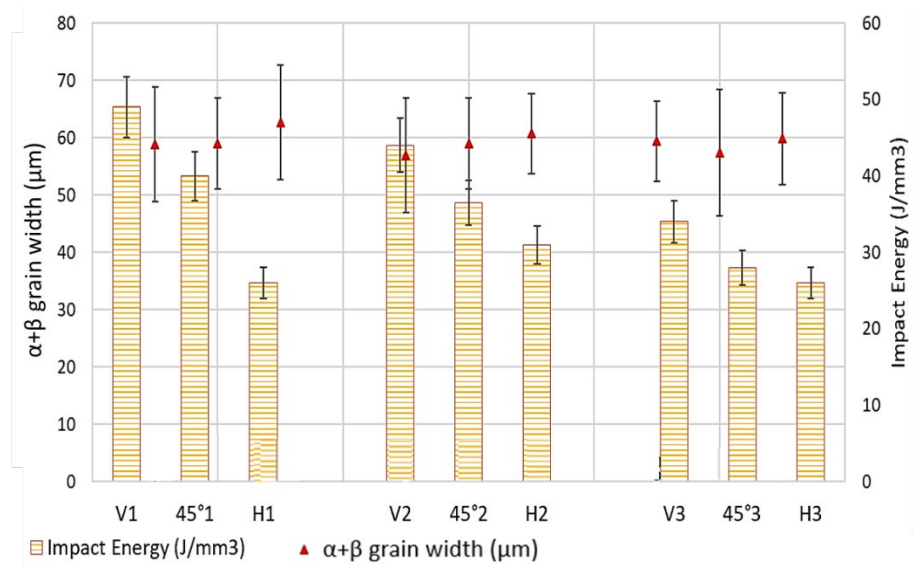
Figure 5-11 The α+β grain width for each sample vs impact energy.
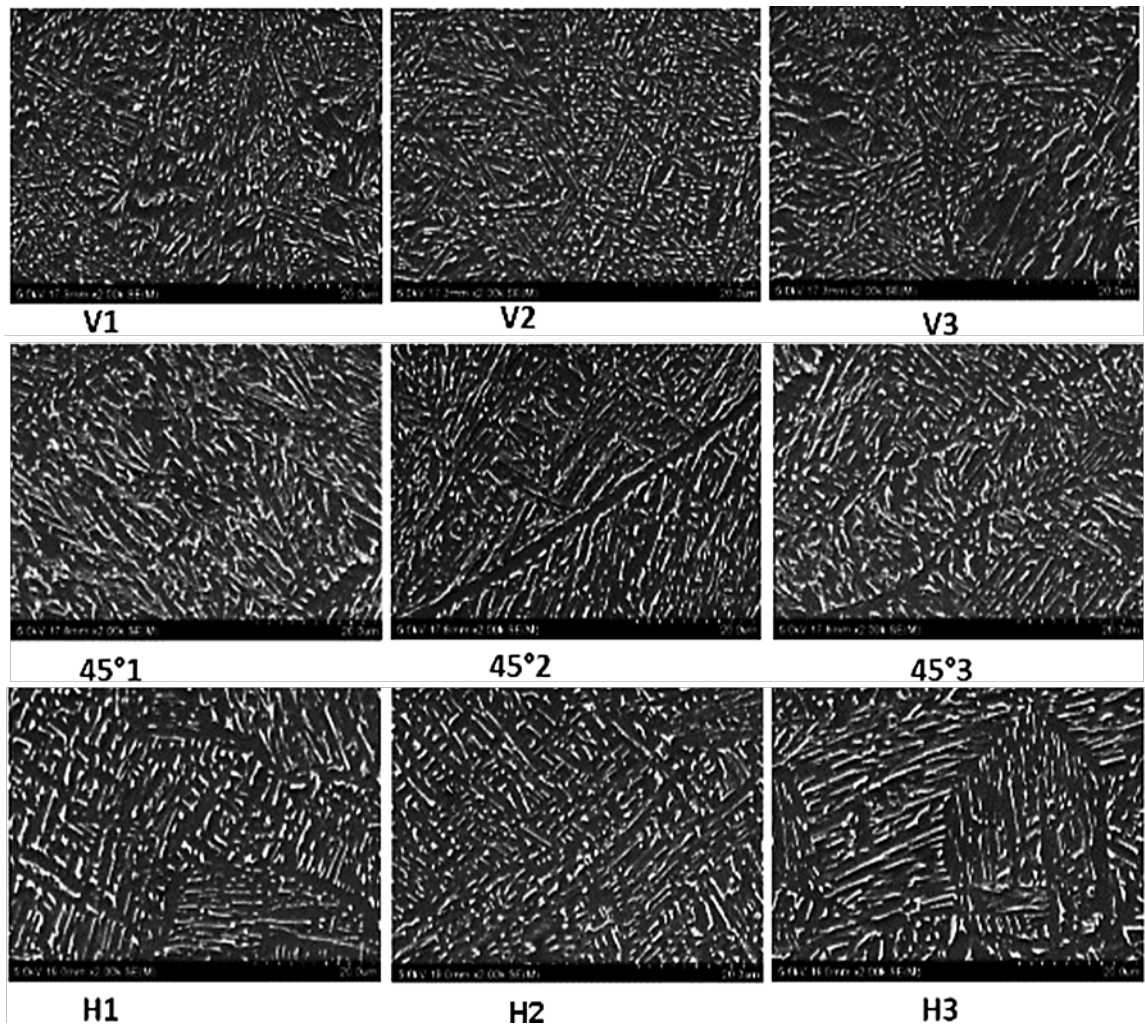
Figure 5-12 Microstructure of three batches are shown. β phase shown with white colour and α phase with dark grey.

5.4   Build direction dependent crack propagation path

The schematic of the fracture surfaces of the samples in three orientations with the notch location are presented in Figure 5-13. The cross-section of the fracture surface with microstructure is analysed and presented. By tracing the fracture path in the vertical samples, many fluctuations and deflections are observed and all of them occur inside the
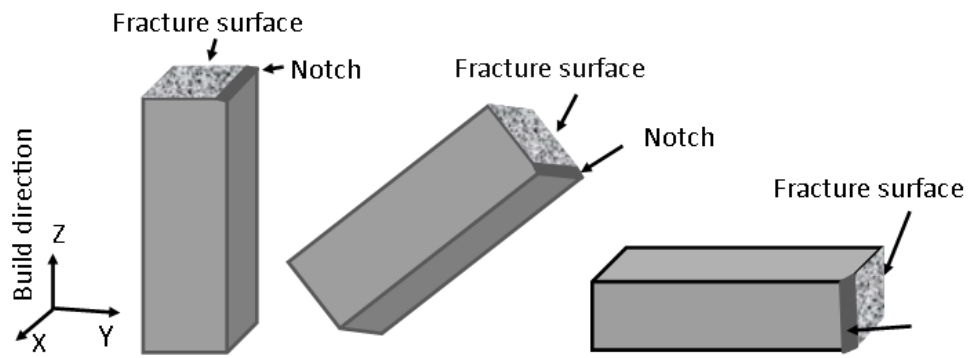
Figure 5-13 Schematic of Charpy tested samples with build direction.

α+ β phase and just pass through the α columnar phase boundaries. The crack propagates inside the colonies in the α+β columnar grains with columnar prior β phase boundaries (current columnar α phase boundaries) as shown in Figure 5-14. The columnar α phase boundaries are marked with dashed lines. The crack path from the notch to the end are observed and there is no evidence that the crack propagates along the α columnar phase boundaries.

Figure 5-14 The cross section of Charpy fracture of vertical sample.

Regarding the observation above, the results of build direction and the crack propagation path during fracture are schematically shown in Figure 5-15. The path that the crack propagates and fluctuates through the grains and just crosses the columnar α phase

119

boundaries represents transgranular propagation as Jaap Schijve and James C. Williams mentioned in their books (G. Lütjering et al., 1998; Schijve, 2009).
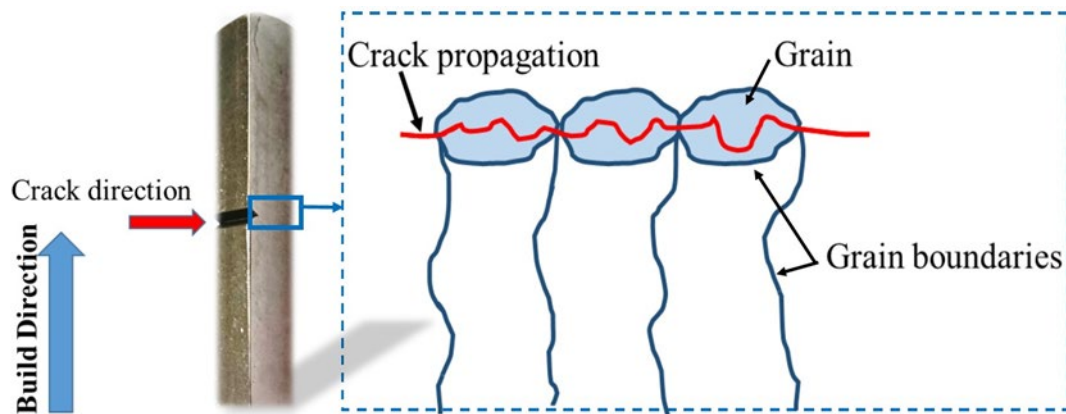
Figure 5-15 The Illustration of crack growth in the vertical samples regarding the angle of build direction with the sample's notch (crack direction).

Unlike the vertical samples' crack path, the 45° cross-section samples show that the crack propagates not only inside the α+β columnar grains, but also along the columnar α phase boundaries as shown in Figure 5-16. In some areas, the crack crosses the α phase boundaries and, in some areas, propagates along the columnar prior β phase boundaries, which are shown as dashed lines in Figure 5-16. The schematic of the crack growth path of the 45° samples is shown in Figure 5-17. This type of crack propagation is a combination of transgranular and intergranular, which Sarrazin explained as transgranular stage I propagation (Sarrazin-Baudoux, 2003). The only difference between crack propagation in the 45° samples and what Sarrazin explained is the amount of propagation of the crack along the α phase boundary which in the 45° samples is more than what Sarrazin showed in the illustration for presenting the transgranular stage I. The crack propagates not only inside the α+ β phase colonies, but also along the α phase boundaries. The columnar α phase boundaries width is usually 2μm or less; therefore, in order to recognize the columnar α phase boundaries, high magnification SEM images are used.

The comparison of the crack path of the vertical samples and the 45° samples shows that the vertical samples' cracks cross the α phase boundaries while the 45° samples' cracks propagate along the α phase boundaries and also inside the α+ β phase. Adding the impact energy result to this comparison demonstrates that the higher impact energy belongs to the crack that crosses the α phase boundaries while the lower impact energy results from the crack propagation not only along the α phase boundaries also the α+ β phase colonies. This comparison suggests that the vertical samples absorb more energy (average of ~42.33J) in order to propagate in the α+ β phase colonies while the 45° samples require

less energy (average of ~34.83J) for the crack to propagate along the α phase boundaries. It should mention that the continuous white fracture area is because the area is not completely flat and 20KV was used to take these pictures. Although the samples were mounted and ground, the mounting area is a small distance from the fracture surface.
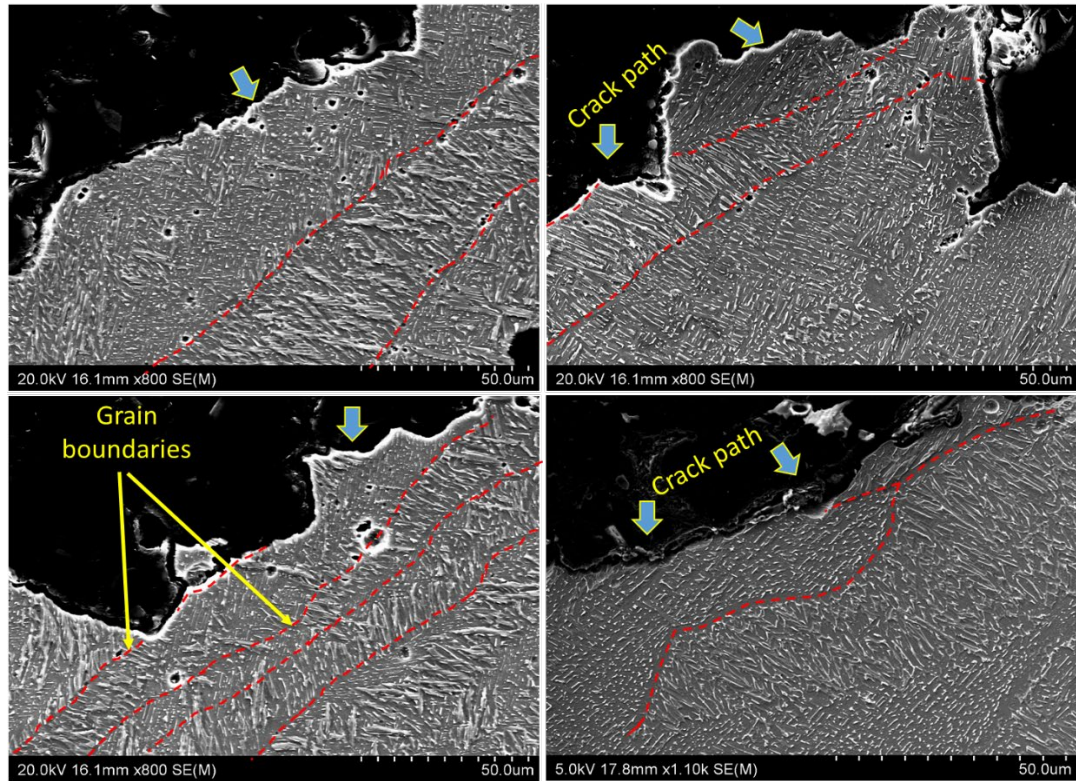
Figure 5-16 The cross section of fracture surface of the 45° samples. The white lines show the columnar α phase boundaries.
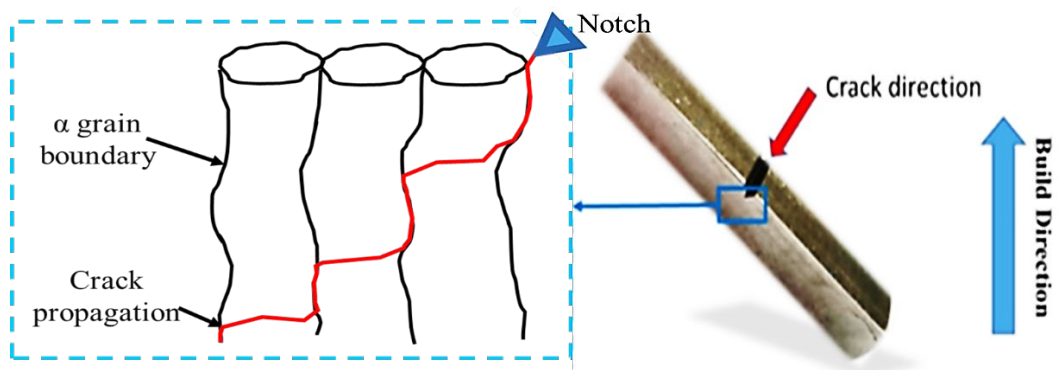
Figure 5-17 Illustration of crack growth in the 45° sample's notch position.

Figure 5-18 shows the SEM images of the horizontal sample's fracture cross-section. The columnar α+β grain width in horizontal samples is measured to be between 40 to 70μm. On the fracture surface of the horizontal sample, it is difficult to find out if the crack propagates exactly along the α phase boundaries. The applied load on the samples during

the test slightly deformed the shape of the α+β grains around the fracture area and the α phase boundaries are difficult to recognize. Some grains next to the fracture area are detected and due to the average α+β columnar grain width, it is likely the crack propagates along their boundaries while in some areas the crack propagates not exactly along the columnar α phase boundaries but close to them as shown in Figure 5-18 (a, b and c). In addition, some α phase boundaries close to the fracture are observed as shown in Figure 5-18d.
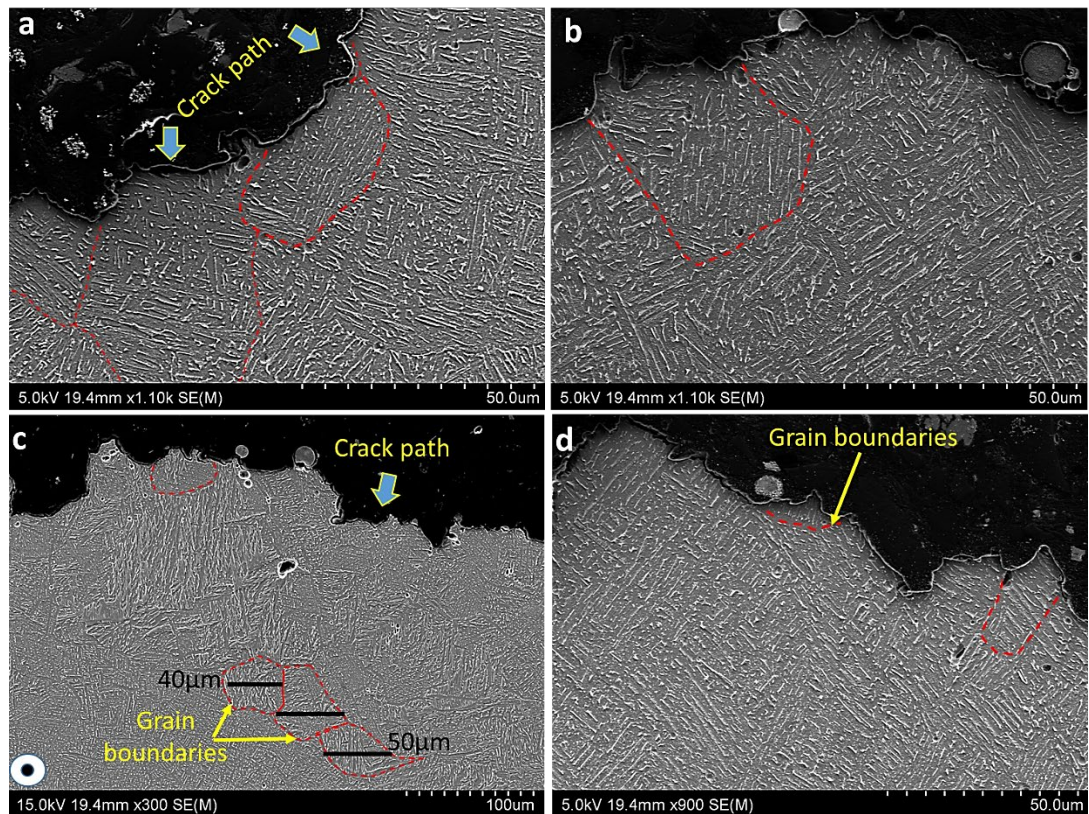
Figure 5-18 The fracture surface cross section of horizontal samples. The white lines show the columnar α phase boundaries.

Therefore, the illustration for crack growth behaviour in the horizontal sample can be seen in Figure 5-19. The observation of the crack path on the cross-section of horizontal samples suggests that the crack likely propagated along the α phase boundaries and partially the small area of α+β phase colonies. Since in the horizontal samples it is difficult to recognise if the crack propagates along the α phase boundaries more or in the α+β phase colonies. But comparing the horizontal with the vertical and the 45° samples' crack path and their impact energies shows that from the vertical with high impact energy the crack propagates in α+β phase colonies and crosses the α phase boundaries while the impact energy decreases in the 45° and the horizontal samples when the crack propagates

122

in the α+β phase colonies and the α boundaries, however, the average impact energy of the 45° sample (~34.83J) is higher than that of the horizontal one (~27.66J). The higher impact energy of the 45° samples compared to the horizontal samples could be attributed to the amount of crack propagation in α+β phase colonies. Although the crack in both samples propagates in the α+β phase colonies and crosses the columnar α phase boundaries, the distance that the crack propagates in the α+β phase colonies in the 45° samples is more than in the horizontal samples. Therefore, crack propagation in the α+β phase colonies requires more energy than in the α boundaries; which means that when the crack propagates along or through a columnar α phase boundary, the impact energy is much lower than the sample that the crack propagates partially (like the 45° sample) or completely (like the vertical sample) inside the α+β phase colonies. Hence, the α+β phase colonies are a difficult path for the crack to propagate due to the direction of the applied load. The crack propagated inside the α+β phase colonies with high abortion of energy to propagate while the crack propagates in the columnar α phase boundary with less energy absorption to propagate; consequently, an easier path for the crack to propagate. There is an agreement with our finding with the Christophe Buirette et al. result. They investigated the crack propagation of Charpy samples of Ti6Al4V alloy and explained that the crack propagated in α platelets and mentioned α+β interfaces as an obstacle (Buirette et al., 2014). Besides, Yuwei Zhai and Galarraga et al. investigated fatigue crack growth in EBM Ti6Al4V alloy and explained that the α boundary is a barrier to crack propagation (Galarraga et al., 2017; Zhai et al., 2015) while in this study during the Charpy test, the α boundary decreases the impact absorbed energy for the crack to propagate.
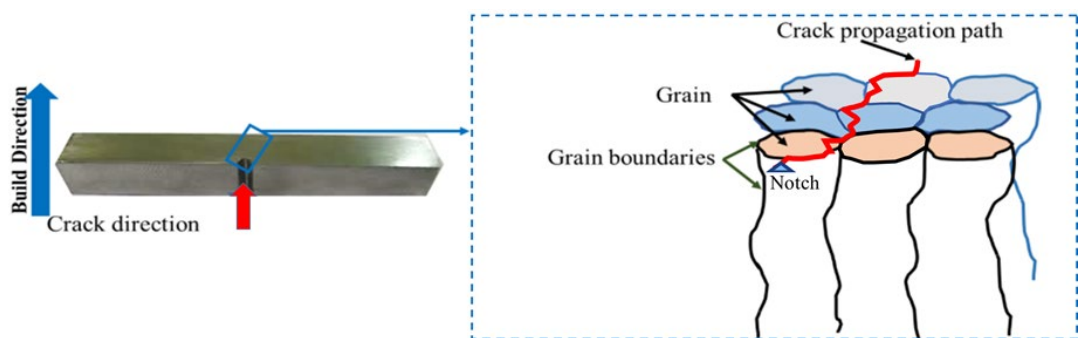
Figure 5-19 Illustration of crack growth in the horizontal sample's microstructure.

The distance that a crack travels to the end of each sample is measured by ImageJ software, and the result is shown in Figure 5-20. As the impact energy decreases in the samples and groups, the distance that the crack needs to travel until fracture, increases. However, this measurement was done on one set (one from each build direction) for each

group. Also, because for all samples, the distance that the crack travels to the end is less than 0.1%, the crack path distance does not have a significant effect on the impact energy value.
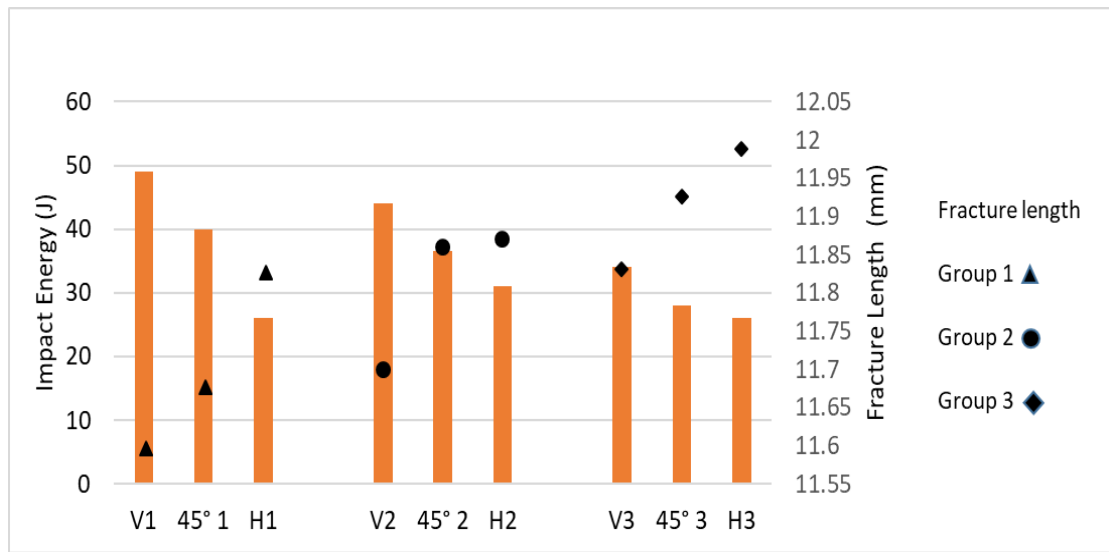
Figure 5-20 The path measurement that the crack travels in three orientated samples.

5.5   Effect of notch position on impact energy

In order to find out if the position of the notch on the different sides of the samples affects the impact energy values, different notch positions were prepared and performed. The result is shown in Table 5-1. Comparing the impact energy of different notch positions shows that the value of the impact energy has no significant difference.

Table 5-1 Impact energy of samples with different notch positions

Notch	Impact Energy (J)							
	45°				H			
Side	28	28	27	27	24	24	21	22
Up	-	-	-	-	23	23	-	-
Down	27	28	26	26.5	22	22	-	-

5.6   Effect of oxygen level on directional built samples' toughness

The oxygen level of each sample was measured in three different areas by a LECO machine and the result is plotted versus impact energy in Figure 5-21. The oxygen level

in the vertical samples is comparable, however, the impact energy decreases from 49J to 44J and 34J. Like the vertical samples, the 45° and horizontal samples have a comparable oxygen level too. In the 45° samples, when the impact energy decreases from 40J to 36.5 and 28J, the oxygen level is ~0.185%.

The oxygen level in the horizontal samples is ~0.225% while the impact energy values are different (26, 31 and 26J). The level of oxygen in the horizontal sample H3 reaches ~0.225%, which is the highest oxygen level among all samples, and in the horizontal sample, H1 reaches 0.2% whose oxygen level is ~0.025% lower than H3. However, the impact energy of H3 and H1 is the same (26J). This level of oxygen did not have a significant effect on the impact energy.
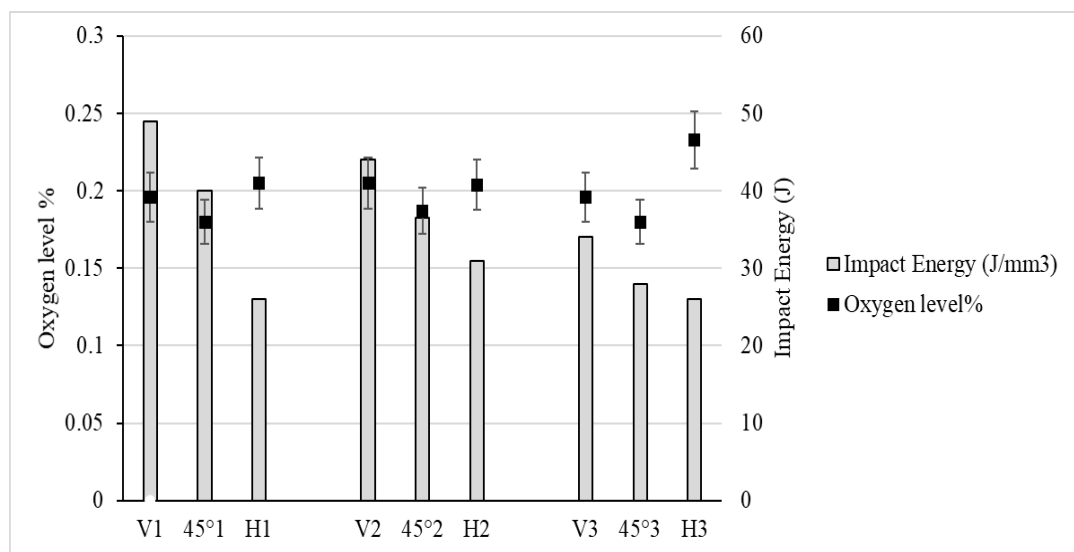
Figure 5-21 Comparison between the percentage of oxygen level and impact energy with directional built samples.

Since some literature explained that oxygen level can affect the strength of the product (Grell et al., 2017; Takahashi et al., 2010; Tang et al., 2015) and Grell et al. (Grell et al., 2017) stated that impact energy is a function of oxygen level, the oxygen level in each sample was measured. The analysis reveals that although the oxygen level of the same orientated samples such as the vertical samples is comparable, their impact energy is different which confirms the fact that oxygen level is not a factor for having different impact energy values in the same directed samples in this study.

5.7 Summary

It has been observed that the number of LOF increases with the increase of the angle between longitudinal sides with build direction increases. This result demonstrates that the impact energy is affected by the build direction, thus, the impact energy is a function of the number of LOF. The vertical samples with the fewest number of LOF have the highest (~49J), and the horizontal samples have the highest number of LOF with the lowest impact toughness (~26J) among all orientated samples. This result confirms that build direction is the most effective factor affecting impact toughness. In addition, the maximum LOF size affects impact energy when LOF is orientated in a favourable direction for crack growth.

On the fracture surface of all Charpy samples, LOF and porosity were observed; however, it was indicated that the impact energy does not have a relationship with LOF orientation. Furthermore, the number of porosities does not significantly affect the impact energy in this work. Although there is no relation between the fraction of LOF and impact energy, all three batch orientations had similar behaviour. The horizontal and 45° samples have a higher percentage of LOF than the vertical samples. The fraction of not only LOF but also porosity had no significant influence on the impact energy of this work. This result is valid for a fraction of not more than 1.1% for LOF and 0.175% for porosity.

In addition, the reduction of the impact energy from vertical to 45° and horizontal samples is due to the microstructure difference, however, this difference is really small. As the angle between the longitudinal side and build direction increases from 0° (vertical sample) to 90° (horizontal sample), the microstructure becomes slightly coarser as the impact energy decreases. This microstructural difference is due to the directional built sample, as the height of the sample increases, the microstructure in the sample becomes finer. The crack propagation in the vertical samples occurred inside the $\alpha+ \beta$ phase colonies and just passes through the columnar α phase boundaries which represents transgranular propagation with the highest impact toughness (average of ~42.33J), while in the 45° and horizontal samples, the crack propagated along the columnar α phase boundaries also inside the $\alpha+ \beta$ phase colonies, which represents a mixture of transgranular and intergranular propagation. However, the amount of crack propagation in the $\alpha+\beta$ phase colonies in the 45° samples with average impact energy ~34.83J is more than the horizontal samples with ~27.66J. Therefore, as the angle between the crack growth direction and the α columnar phase boundaries, which is parallel to the build

126

direction, becomes close to zero, the energy that the sample absorbs decreases due to crack propagation along the columnar α phase boundary. Therefore, the crack propagated inside the α+β phase colonies with high absorption of energy to propagate while the crack propagates in the α boundary with less energy absorption to propagate; consequently, an easier path for the crack to propagate.

In addition, it is confirmed that the different notch positions on the different sides of the samples had no significant effect on the value of impact energy. Besides, the oxygen level of all orientated samples is comparable while their impact energy is different which confirms the fact that oxygen level is not a factor for having different impact energy values in the same directed samples in this study.

6. CHAPTER. Effect of build direction and defects on the crack growth rate and propagation path of Ti6Al4V alloy in region II

A fatigue crack growth (FCG) test was carried out to study the effect of LOF and anisotropic microstructural behaviour of EBM Ti6Al4V alloy for different crack directions. Crack growth behaviour in fatigue regions I and II depends on the microstructural features of a material. Many investigations have been done on region I, however, the crack path behaviour in region II was not studied well. In addition, the influence of LOF and porosity on fatigue crack growth on the linear behaviour of region II was not quantified. Therefore, in this work, it is intended to study the fatigue crack growth behaviour and crack path in region II microstructurally. Then, the LOF and porosity levels are quantified and analysed by the fatigue crack growth graph. In addition, the crack propagation paths in different orientations are microstructurally studied, and the β phase behaviour against crack propagation is investigated. Furthermore, the relationship between β phase and striations on the fracture surface is studied in order to understand if β phase orientation has any relation to generating the striation direction. And finally, with the help of EDS an attempt is made to identify the α columnar phase and colony boundaries.

6.1 FCG data in three different build directions and crack propagations

Twelve samples were prepared for the three notch orientations in relation to the build directions vertical, horizontal and 45°. Four samples were made for each direction. When the notch direction is parallel to the build direction of a sample, it is called horizontal H (the notch direction with 0° to the build direction), while, as the angle of the notch direction with the build direction increases to 45° and 90° it is called 45° and vertical, respectively. A schematic drawing of the notch and build directions is shown in Figure 6-1.
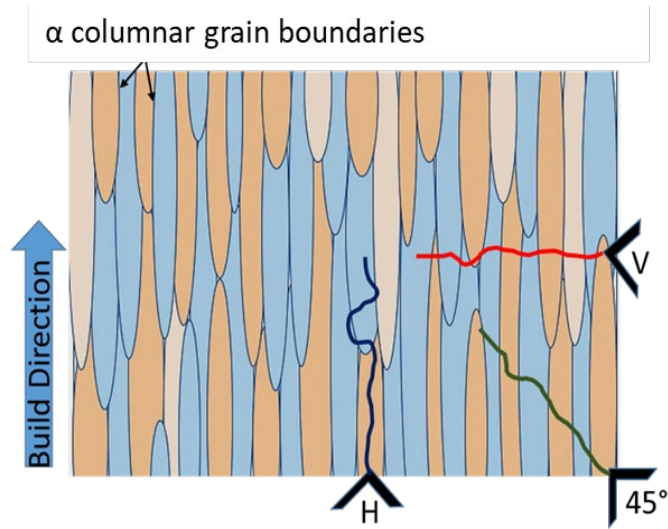
Figure 6-1 Schematic of an as-built sample with three directions of crack growth orientations.

In order to investigate the crack growth path in region II, a total of nine fatigue crack growth (FCG) data were generated after three sets of fatigue crack growth tests. Each set of FCG tests included three orientations: vertical, horizontal and 45°. For a better observation of FCG data, one set of FCG test results was plotted separately and shown in Figure 6-2.
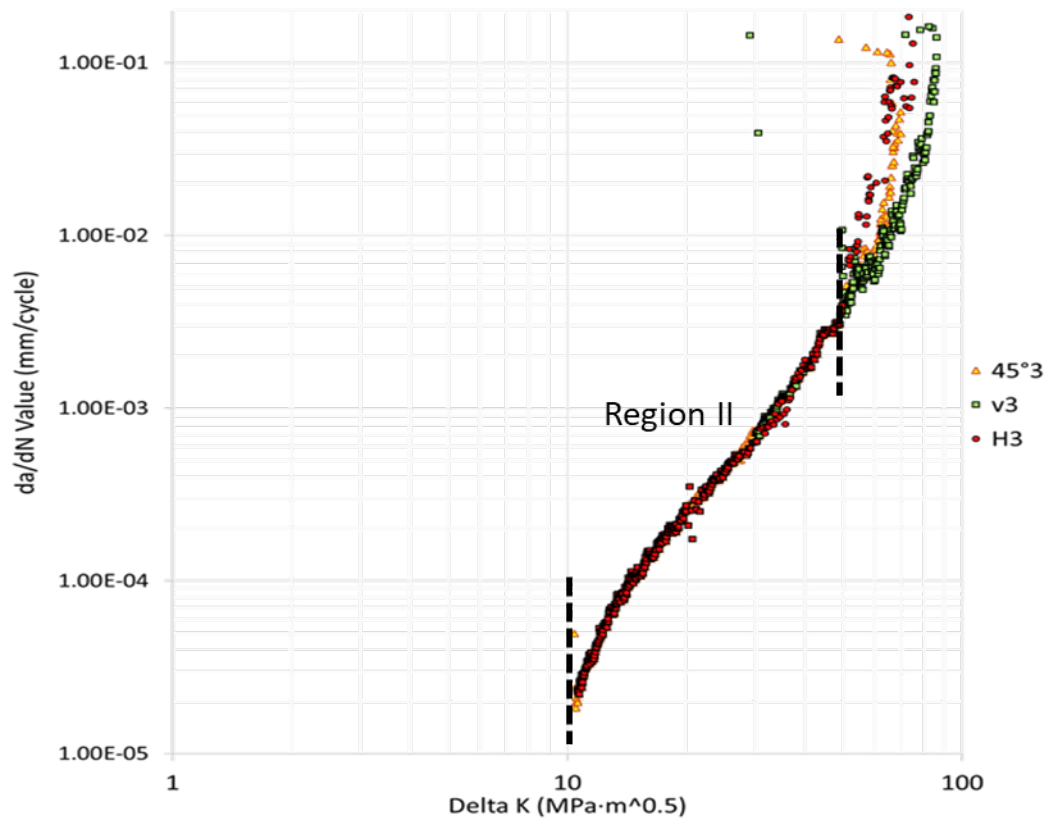
Figure 6-2 FCG of three V, H and 45° samples

The plotted graphs demonstrated two regions: the Paris law (region II) and Kc (region III). Region II started from 2×10^{-5} mm/cycle with ΔK 10 MPa.m$^{0.5}$ and finished at 3.5×10^{-2} mm/cycle with ΔK 50MPa.m$^{0.5}$ which is the starting point of region III where the crack grows rapidly. The fracture completed with different fracture toughness K_{IC} in the horizontal sample with 65 and in vertical sample with 92 MPa.m$^{0.5}$ at $\sim 2\times10^{-1}$ mm/cycle.

The FCG graph indicated that the behaviour of all three orientations in linear region II is identical. It is suggested that, although the angle between crack growth direction and build direction in the samples is different, crack propagation has the same response in each cycle with the same applied stress intensity factor range, ΔK, in region II for all samples. According to the Paris law equation for the linear region, for the three notch orientations in relation to the build direction the exponential constants were determined to be m = 3.1 and C = 1×10^{-8} mm/cycle.

In region II, many LOFs and porosities were observed in all samples as shown in Figure 6-3 and some of the LOF lengths reached 500 μm. The fraction of porosity and LOF for each direction were evaluated in region II and shown in Figure 6-4 and 6-5. The fraction of porosity in the 45° and horizontal samples is comparable while the fraction of porosity has approximately 0.1% increase in the vertical sample (0.24%, 0.108% and 0.137% respectively). However, the difference in the fraction of porosity in samples is not noticeable which is shown in Figure 6-4. Moreover, the fraction of LOF from vertical to 45° and horizontal samples decreases from 0.997% to 0.746% and ~0.397% respectively. The fraction of LOF differs in three orientated samples, but these differences are about 0.15% which is too narrow to make a difference in the fatigue crack growth graph, as shown in Figure 6-5. Combing the results of Figure 6-4 and Figure 6-5 with the FCG plotted data of Figure 6-2 indicates that having porosities and LOFs on the fracture surfaces and identical FCG curves for all three orientated samples confirms that, although the fraction of LOF and porosities in the samples are different, the differences are small enough not to change the fatigue crack growth graph in region II. Therefore, despite LOF's favourable orientation for crack growth, da/dN vs ΔK is the same. This may suggest that the crack resistance for the vertical sample material may be lower because the percentage of LOF is higher than the rest of orientated samples. Regardless of crack growth direction and the number of boundaries that the crack travels, all three directional samples show the same crack growth length for each given ΔK in region II. In the

identical region toward that the existence of LOFs and their longitudinal side with the crack propagation direction did not affect region II.
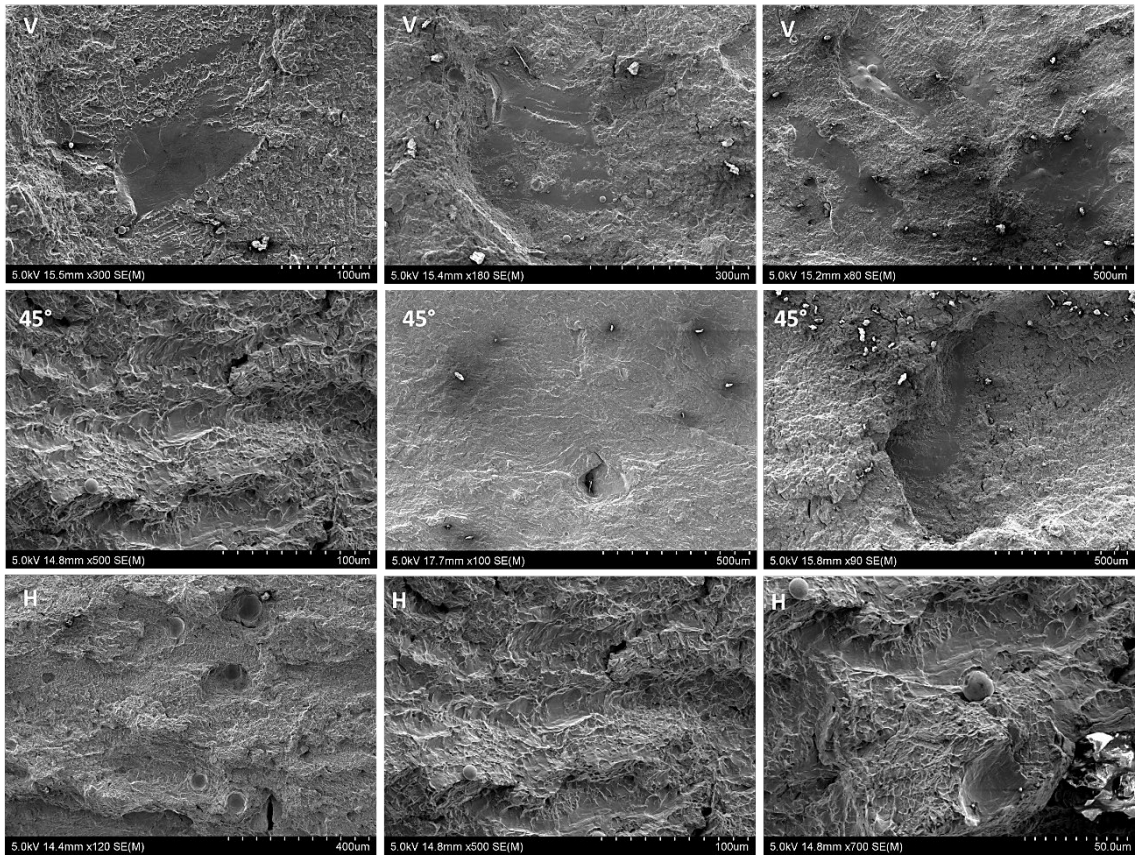
Figure 6-3 LOF and porosity on the fracture surface of three V, H and 45° samples in region II.
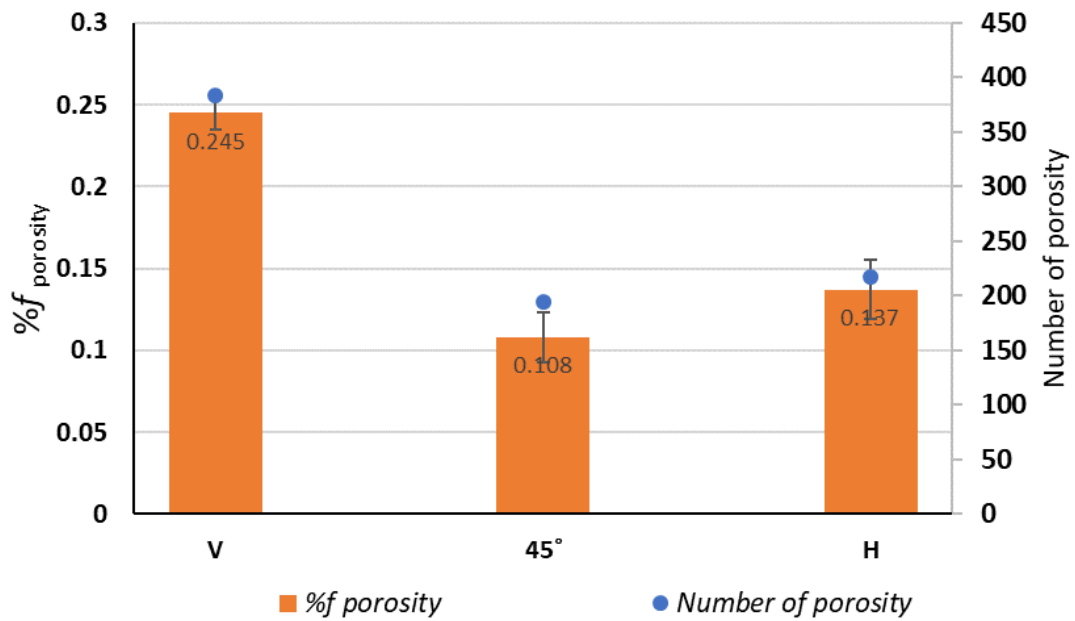
Figure 6-4 The percentage of a fraction of porosity and the number of porosities of different orientated samples in region II.
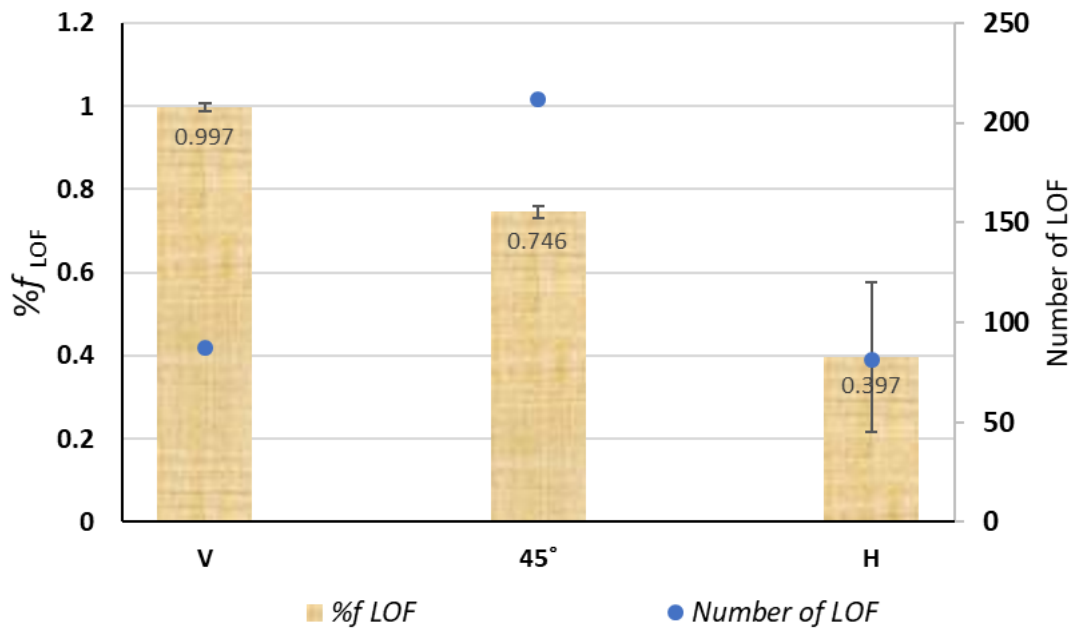
Figure 6-5 The percentage of a fraction of LOF and the number of LOF of different orientated samples in region II on fracture surface.

Although Greitemeier et al. (Greitemeier et al., 2017) reported that the fatigue performance is controlled by defects in the Ti6Al4V alloy, our results of FCG in three different directions in region II show that LOF did not have any effect on different crack propagation directions. This finding is in agreement with Edwards et al. (Edwards et al., 2013) who concluded that there was no noticeable difference in crack growth rates for samples as a function of the directed built sample. Also, in region II, a horizontal and vertical sample of Yuwei Zhai et al.'s (Zhai et al., 2015) work was identical to our results as well. There was no significant effect of the defect on different build orientations of samples (Ghonem, 2010; Greitemeier et al., 2017; Leuders et al., 2013; Nicoletto, 2017). The fracture surface of the FCG test in three orientated samples, V, H and 45°, are shown in Figure 6-6, in which the notches of all samples is located to the left side of the pictures. The fatigue crack growth path in the 45° sample in Figure 6-6 suggests that in region II, the crack growth path did not change to the orientation of the LOF direction while in the high ΔK (in region III), the crack growth direction changes to the orientation of the LOF direction.
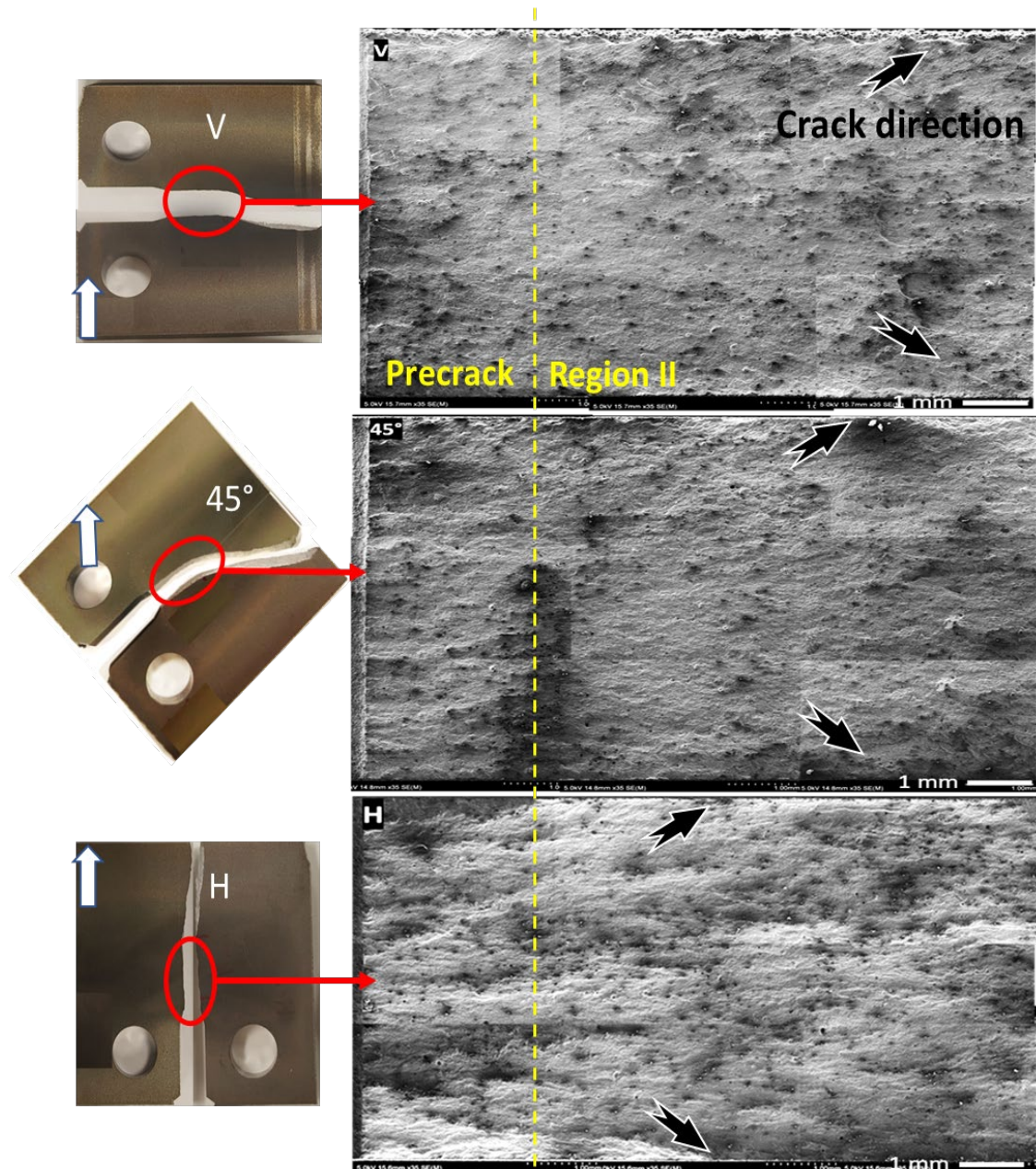
Figure 6-6 SEM image of the fracture surface of FCG of two regions pre-crack and Region II for three sample orientations are shown. The build direction is indicated at the left of the image with white arrows.

6.2 Crack growth path and microstructure

The microstructure of the as-built EBM Ti-6Al-4V consists of α+β grains that are parallel to the build direction with α+β lamellar phases inside the α columnar phase boundaries (Figure 6-7). In this structure, except for individual α phase and β phase with lamellae structure, there is another combination of compact α+β phases area that can be seen in the dashed red circle that both lamellae α phase β phases and compact α+β phases together show the Widmanstatten structure. The α+β phase area is the same as α and β phases with

a little difference which is the amount of vanadium content that is sometimes more than 4% (wt%) and in some areas it reaches 8% which makes the density of the β phase different in comparison to the rest of the areas (see Figure 6-8). It should be mentioned that vanadium is a β phase stabilizer and aluminium is an α stabilizer. In EDS analysis, the weight percentage of vanadium increase shows the existence of β phase increase and the high percentage of aluminium shows the existence of the α phase rising in that area.
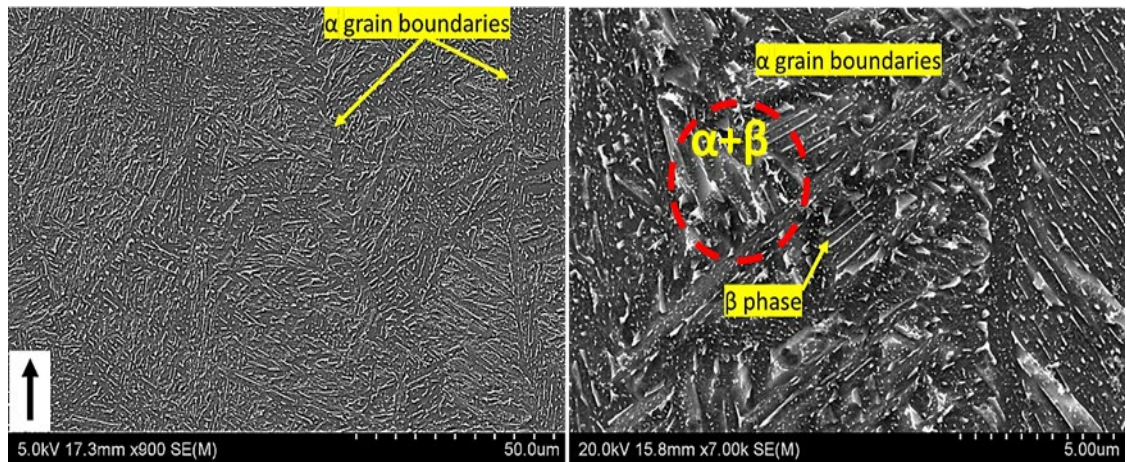
Figure 6-7 Microstructure of as-built vertical sample with showing α, β and α+β phases.

Point	Weight %		
	Al	Ti	V
1	5.92	90.42	3.65
2	5.72	90.23	4.04
3	4.96	86.40	8.03
4	5.92	90.04	4.04
5	5.35	90.54	4.11
6	5.56	90.20	4.96
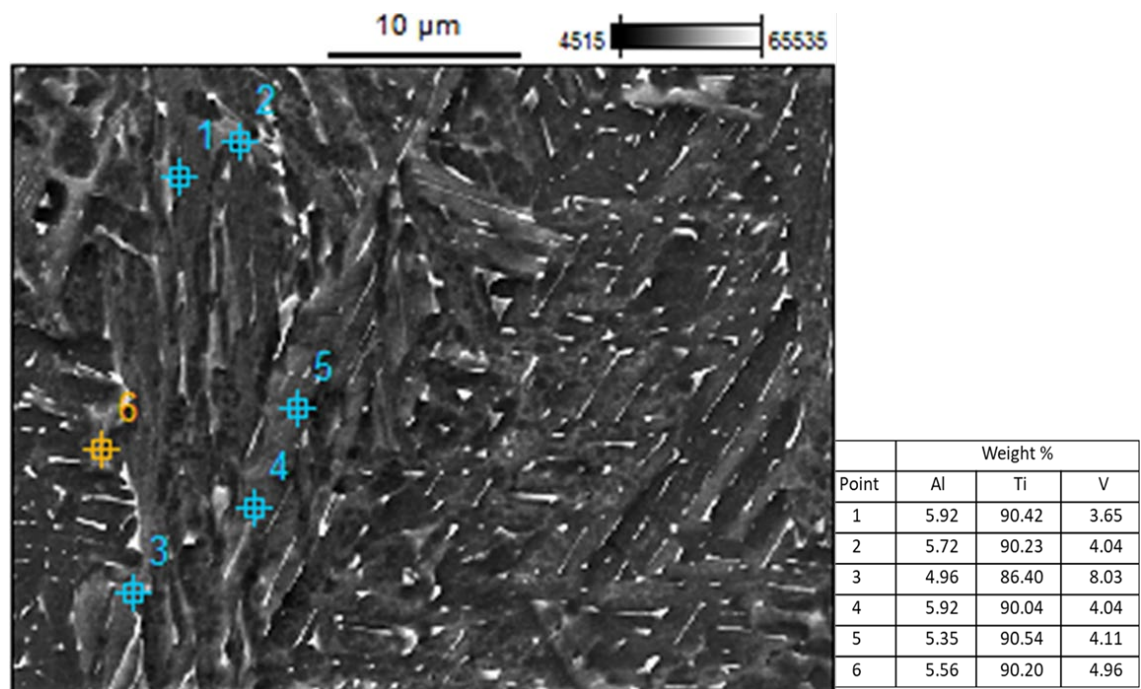
Figure 6-8 The weight percentage of Ti6Al4V alloy composition elements.

During crack propagation in a sample, the crack needs to pass through α+β phases and columnar α phase boundaries. Because in the vertical, 45° and horizontal samples, crack growth direction regarding the build direction is different as shown in Figure 6-1, the crack propagation in different samples was examined by stopping the test at the point of

ΔK 30MPa.m$^{0.5}$ and da/dN 7×10^{-4} mm/cycle in region II. It is clear in the vertical sample that crack direction has a 90° angle with the build direction, which is parallel to α columnar grain boundaries, and the crack passes the columnar α phase boundaries and has the shortest crack propagation between two adjacent grain boundaries as shown in Figure 6-9, while, in the horizontal sample, the crack travels inside the columnar α+β grains and sometimes crosses the α columnar grain boundaries. The crack propagation behaviour in the 45° sample is a combination of both vertical and horizontal samples.
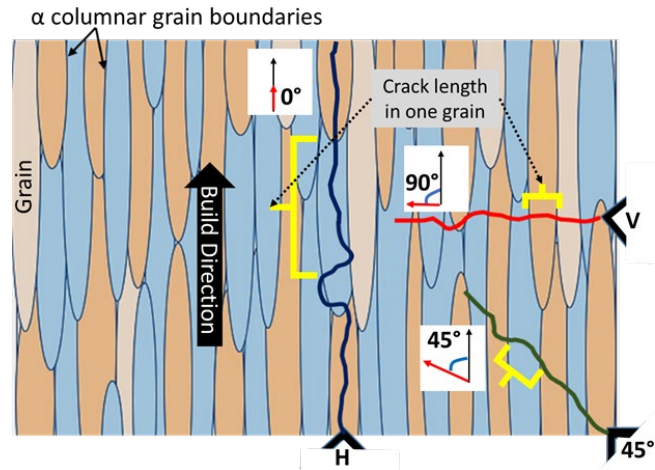
Figure 6-9 Illustration of the build direction and the crack propagation direction with the crack propagation path from one boundary to the another.

In some areas, crack just crosses the columnar α boundaries as shown in Figure 6-10 and in other areas like Figure 6-11, it propagates inside an α+β grain twice the width of the grains. The crack crosses two adjacent grain boundaries in the shortest distance like the vertical sample and in some areas, it propagates inside a grain and travels twice the width of an average grain (~70µm) or travels more likely parallel to some grain boundaries like H samples as shown in Figure 6-12. By comparing the crack paths with the result of the FCG graphs in region II, the crack propagated differently in each sample while the FCG graph in region II is identical (Figure 6-2). It can be suggested that in this region, the grain boundaries of the Ti6Al4V alloy did not act as a barrier because, in each sample, the travelled distance between two adjacent grain boundaries and the number of grain boundaries that the crack crosses are different.
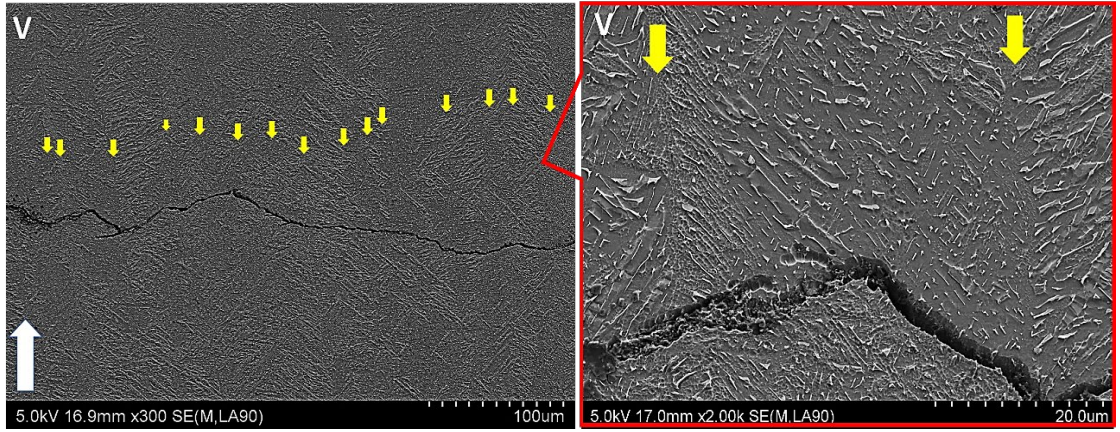
Figure 6-10 Crack path in V sample, grain boundaries are shown with yellow arrows and build direction is shown with a white arrow.
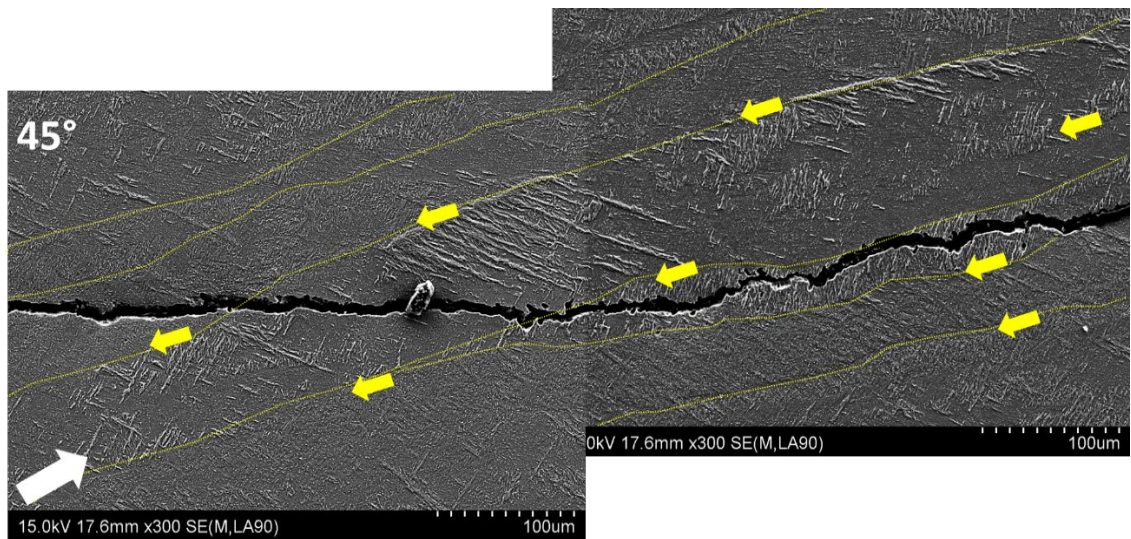
Figure 6-11 Crack path in the 45° sample, grain boundaries are shown with yellow arrows and build direction is shown with a white arrow.
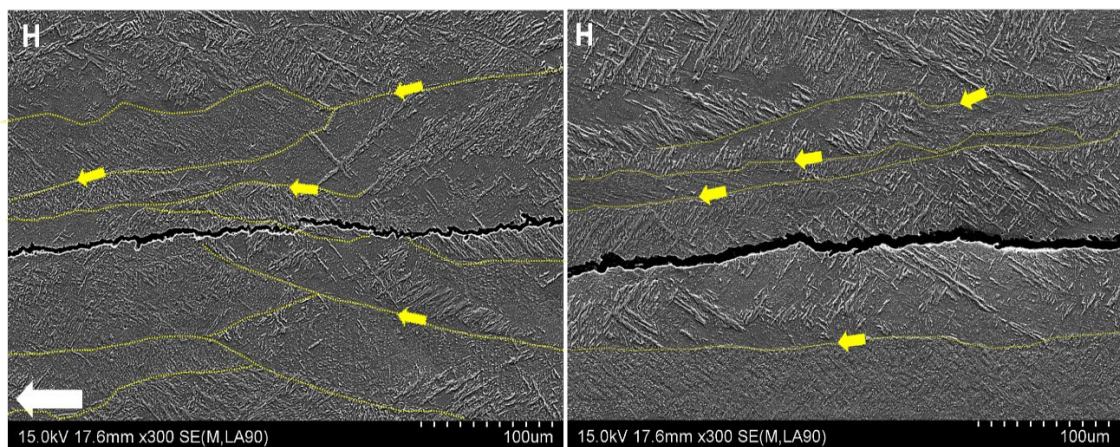
Figure 6-12 Crack path in the horizontal sample, grain boundaries are shown with yellow arrows and build direction is shown with a white arrow.

The interaction between columnar α phase boundaries and crack propagation can be seen in Figure 6-13. The crack grew inside the α+β phases (inside the α+β grain) and crossed some columnar grains in the horizontal sample. It should be mentioned that the grain that has the α columnar boundaries is called the α+β grain because of the high percentage of the material covered by α phase (matrix) with a small portion of β phase.
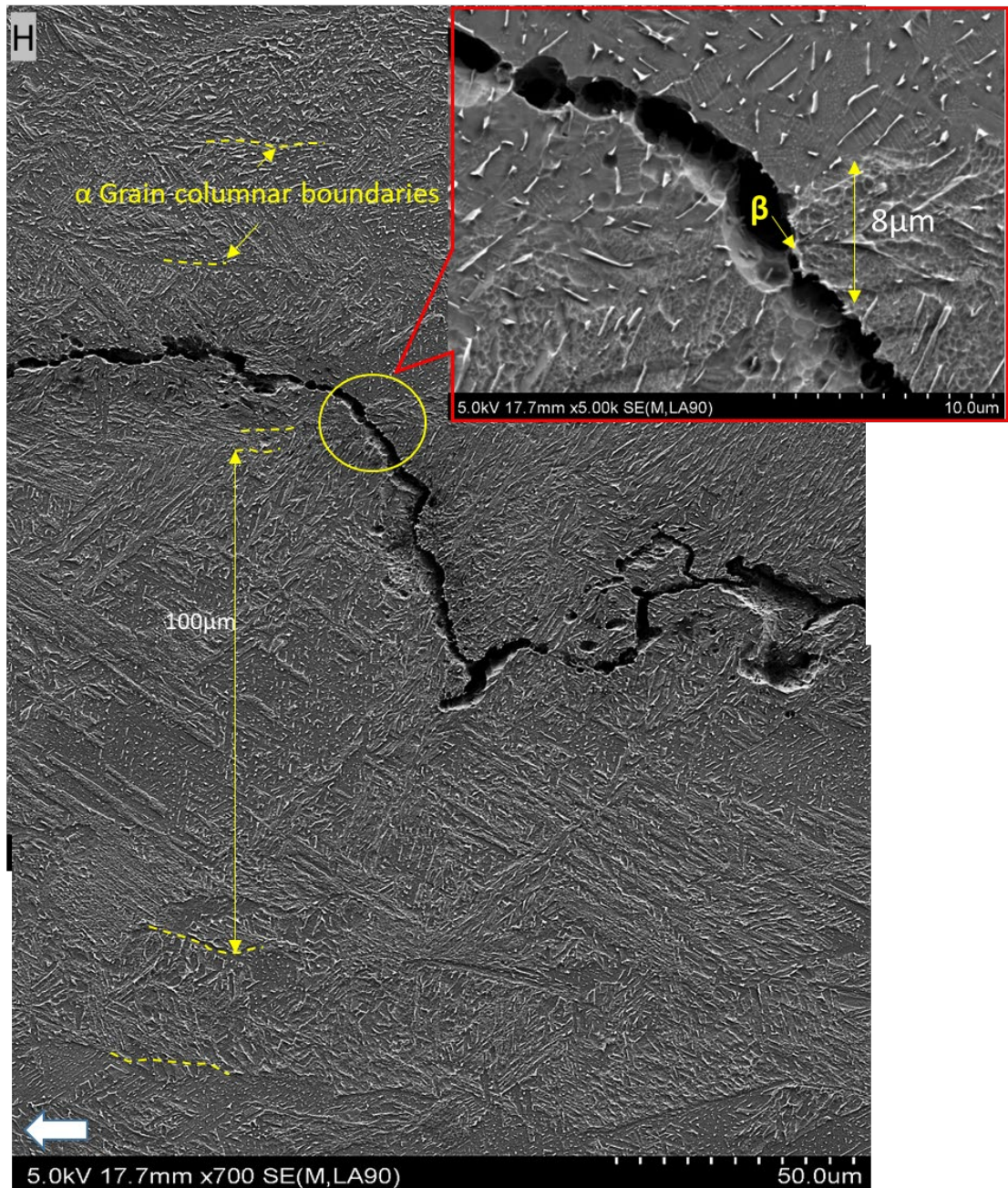
Figure 6-13 the crack propagation path with α columnar grain boundaries in the horizontal sample.

The crack propagated in one wide α+β grain with 100μm width while it continued to just cross an α+β grain with 8μm width without propagating inside the grain with high β phase density and small grain boundary width in comparison to other grain boundaries. The small width of the α+β grain is shown with a yellow circle in Figure 6-13 and its high magnification area. This observation suggests that the crack propagation path could be based on the density of the β phase inside the α+β phases colony. Therefore, the crack preferably propagates in the grain with low β phase density. In the high magnification image in Figure 6-13, the crack propagated from the interface of the α+β phases during crossing the small grain boundary. The interaction between crack propagation and β phase in different angles is shown in Figure 6-14. β phase at the contact with the crack shows different behaviour based on its angle with the crack. When the crack direction, and β phase has a 0° angle, the crack grows at the α and β interface along with the β phase as shown in Figure 6-14a. When this angle increases from 0° to 30° and 90° during crack propagation, the β phase is cut without any significant deformation, (Figure 6-14b and Figure 6-14d). As the angle of β phase and the crack growth direction increases to more than 90° (Figure 6-14c), the β phase is cut with a small noticeable deformation on the fracture tip.
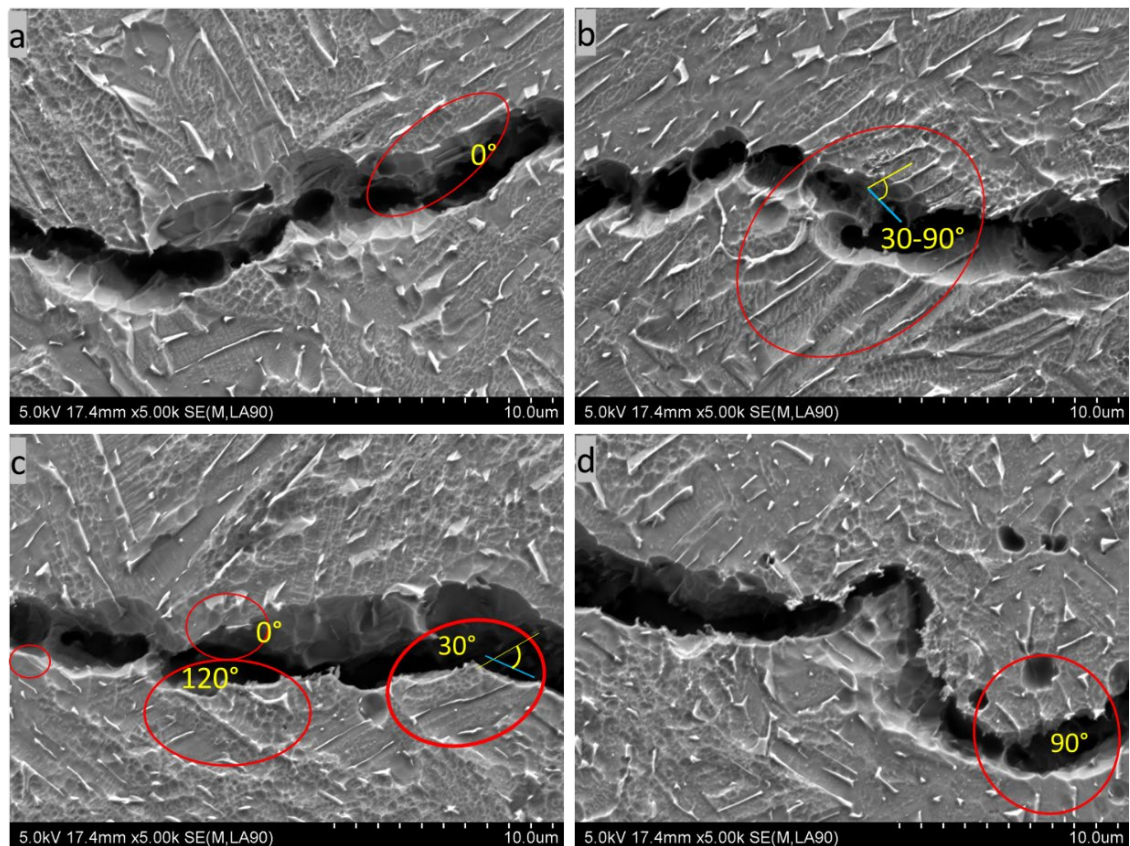
Figure 6-14 The angles between crack and β phases are shown.

In higher magnification of the fracture area, a part of the β phase is left outside the α matrix as shown in Figure 6-15. A small deformation of the β phase is observed and shown in Figure 6-15a while in some other cases, the β phase does not deform during fracture as shown in Figure 6-15b-f in the samples.
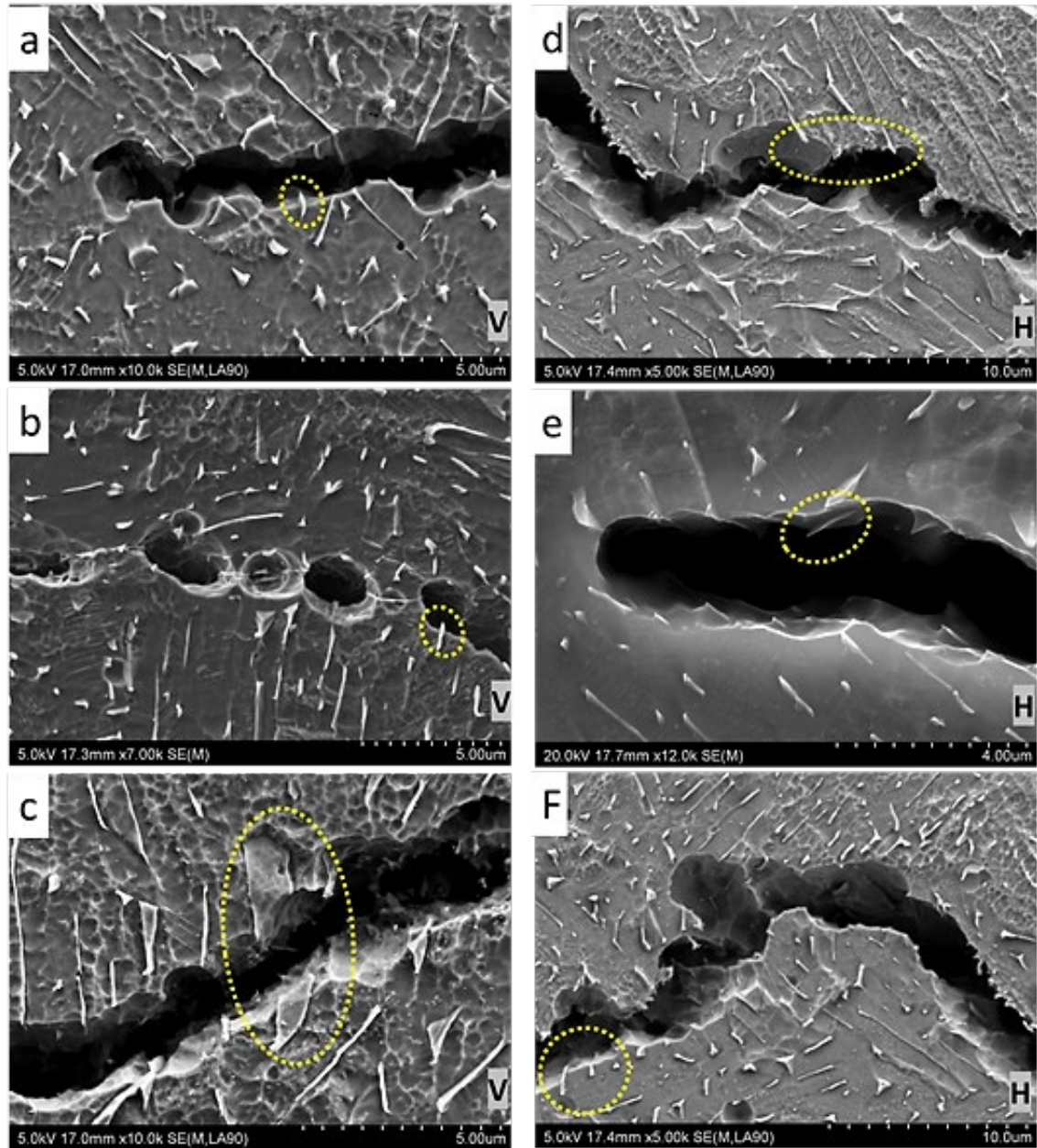
Figure 6-15 High magnification of vertical (a, b and c) and horizontal (d, e and f) samples, the fracture area of the vertical sample that the β phase without deformation cut and disjoined from the α phase.

This kind of behaviour was observed in the vertical sample as well. In Figure 6-16, the low magnification of crack propagation of the vertical sample inside the grain is shown at the left side, and the high magnification of those areas is shown on the right side. The crack grows along the β phase intersection with the α phase, as long as the angle between

the β phase longitudinal side with crack growth direction is not more than 5°, as shown in Figure 6-16b. During crack propagation, the crack passes through many areas like boundaries, colonies, and phases inside a grain. One of the areas where the crack started branching is the α+β phase with a high average size of the grains of the retained β phase. Figure 6-16c and d show that the crack, after passing the α+β phase, begins branching. This branch is attributed to the two adjacent areas where the density of the β phase is different and the crack entering from the high density of the β phase area to low density with more α phase leads to the crack branching and propagating freely. After splitting, one of the branched cracks is arrested by the β phase, and the crack continues propagating from another branch as shown with the yellow arrow in Figure 6-16d. It is good to note that the arrested crack is inside the grain. Branching can occur in areas with no β phase density differences. Because one cycle of the fatigue crack growth is a combination of tension (loading) and compression (un-loading) together, during each cycle of loading, the crack propagates in the α phase if it is not arrested by the β phase as shown in Figure 6-16E and F with blue arrows.
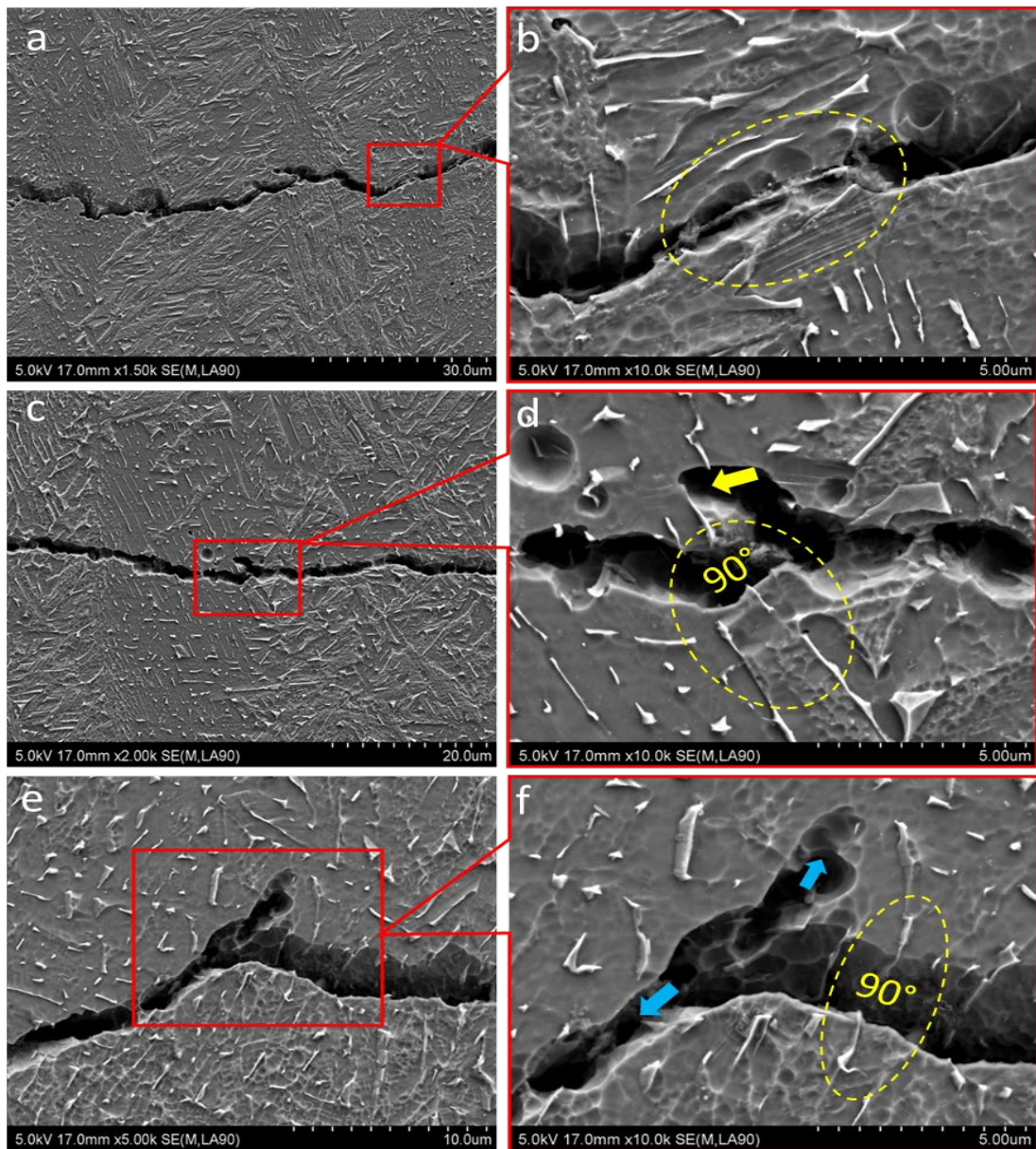
Figure 6-16 The intersection between crack propagation and β phases in V sample.

In all samples, branching occurred mostly inside the grains and not on α columnar boundaries as shown in Figure 6-17a. In other words, the crack did not branch because of passing through the α columnar boundaries; it occurred inside the grains. This finding suggests that α columnar boundaries are not crack barriers, while β phase in a particular crystal orientation act as a crack barrier and makes the crack branched.

The crack propagated inside the colony which is shown with dashed circles in Figure 6-17b and d. Sometimes the crack grows on the α colony boundary in Figure 6-17c which is shown with red circles. One grain can have a crack growth on the colony boundaries and inside the colonies together as shown in Figure 6-17d.

141
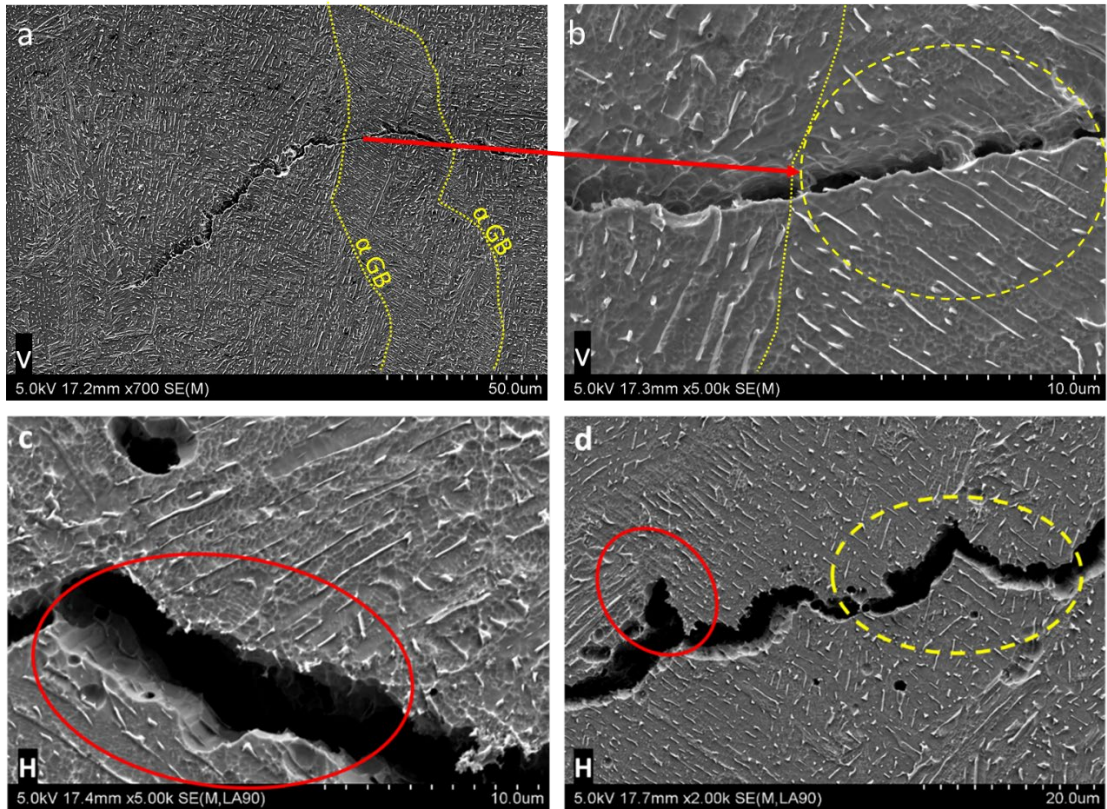
Figure 6-17 Crack propagation in different areas: a) inside α grains, b) inside α colonies, c) on the α colony boundary and d) on the α colony boundaries and inside the α colony, both occur in one α grain.

It should be mentioned that the crack growth behaviour of region II in all three samples was the same, thus, for explaining crack growth, a mixture of all samples' SEM images were used. By observing the crack path in the samples, the crack branching occurs in the α+β grain and just after crossing the α columnar boundaries. The crack crossed the α columnar boundaries without changing direction which can be seen in the crack path in Figure 6-18. In addition, during crack propagation, the crack crossed α grain boundaries like Figure 6-19 and changed direction.
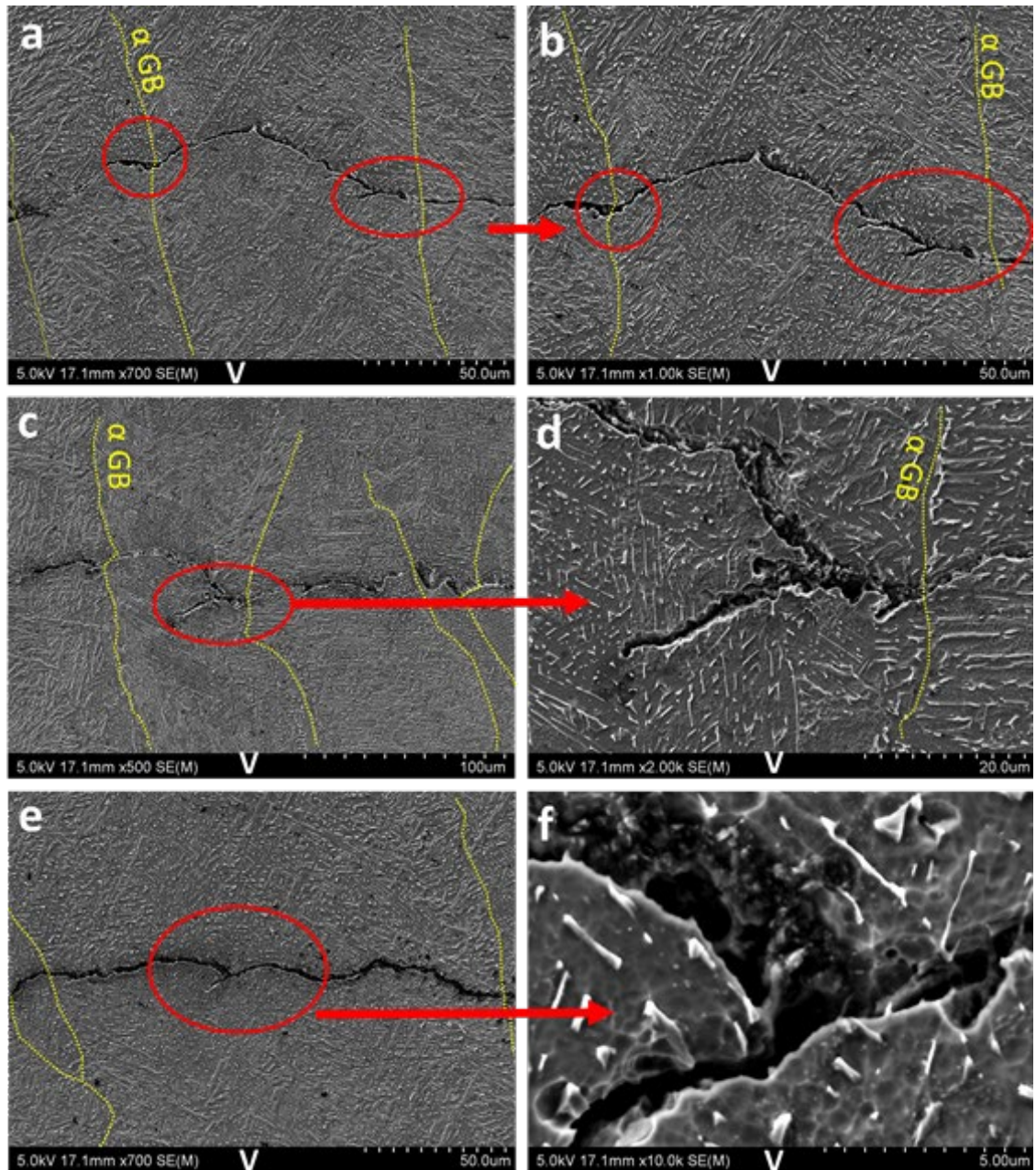
Figure 6-18 The crack branches inside the α+β grain and crosses the α columnar boundaries without branching. α grain boundaries (α GB) are shown by dashed lines.

This crack change on the grain boundary is due to the β phases around the grain boundary. When a crack propagates from one grain to another, during passing the grain boundary, it needs to pass the β phases around it. As Figure 6-19 shows, when the crack reaches the β phases around the α columnar grain boundary, it changes direction. The β phase acts as a barrier in the Ti6Al4V alloy and changes the crack growth direction before the crack reaches the α grain boundary. Galarraga et al. and Yuwei Zhai et al. reported that grain boundaries acted as a barrier; however, in this study the observation shows that the α phase boundary in the Ti6Al4V alloy is not a barrier and the β phase plays an important

role to change the direction of crack propagation (Galarraga et al., 2017; Zhai et al., 2015). As shown in Figure 6-2, fatigue crack growth in region II is identical for three different directions of crack propagation and the number of grain boundaries for samples are not the same. Also, the β phases change the direction of crack propagation as shown in Figure 6-19. Therefore, it is suggested that the β phases act as a barrier while the columnar α phase boundaries do not perform as a barrier.
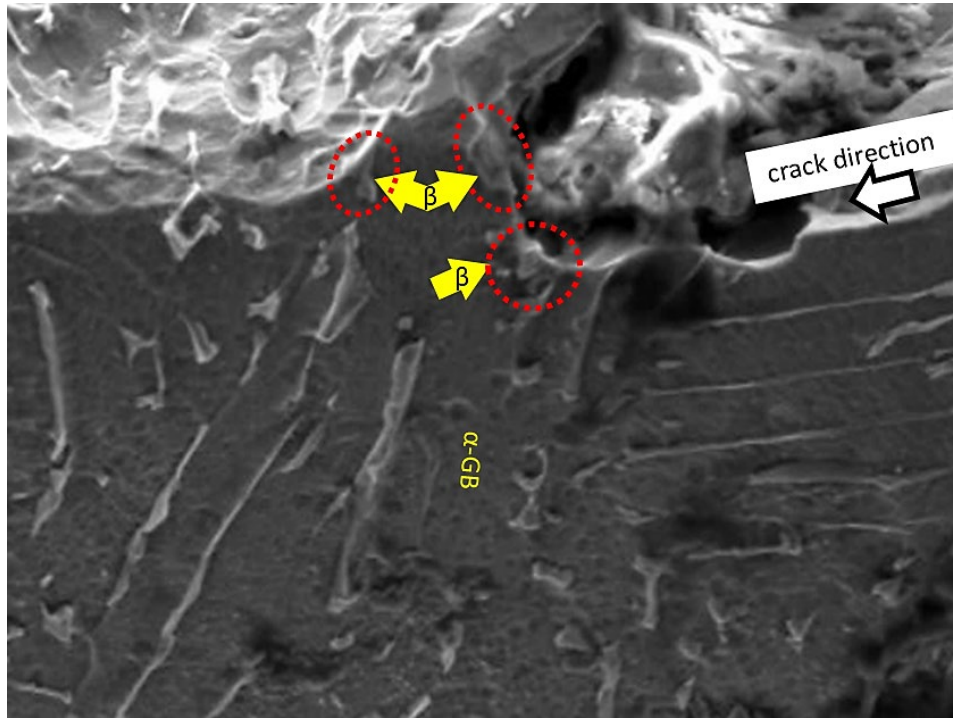
Figure 6-19 Crack propagation path that passes the α grain boundary.

6.3 Fatigue crack growth data relationship with striation

In the fracture surface of the Paris region, striations were observed, and some of them are shown in Figure 6-20. Striation spacing demonstrates the crack propagation per cycle. Thus the local da/dN can be replaced with striation spacing / cycle. The average of the striation spacing values was calculated and characterised by the quotient of the length of a line and the number of intercepting striations. The average striation space in Figure 6-20a is 6.79×10^{-4} mm with a crack size of 13.15 mm. As crack size increased from 13.15 mm to 35.6 mm, the average striation space value reached 0.003. It should be mentioned that the crack size was calculated with the first crack length of 10 mm plus the crack growth length created by the test in the samples. The crack propagation direction is perpendicular to the striation orientation. Therefore, striation spaces indicate the direction of crack growth.
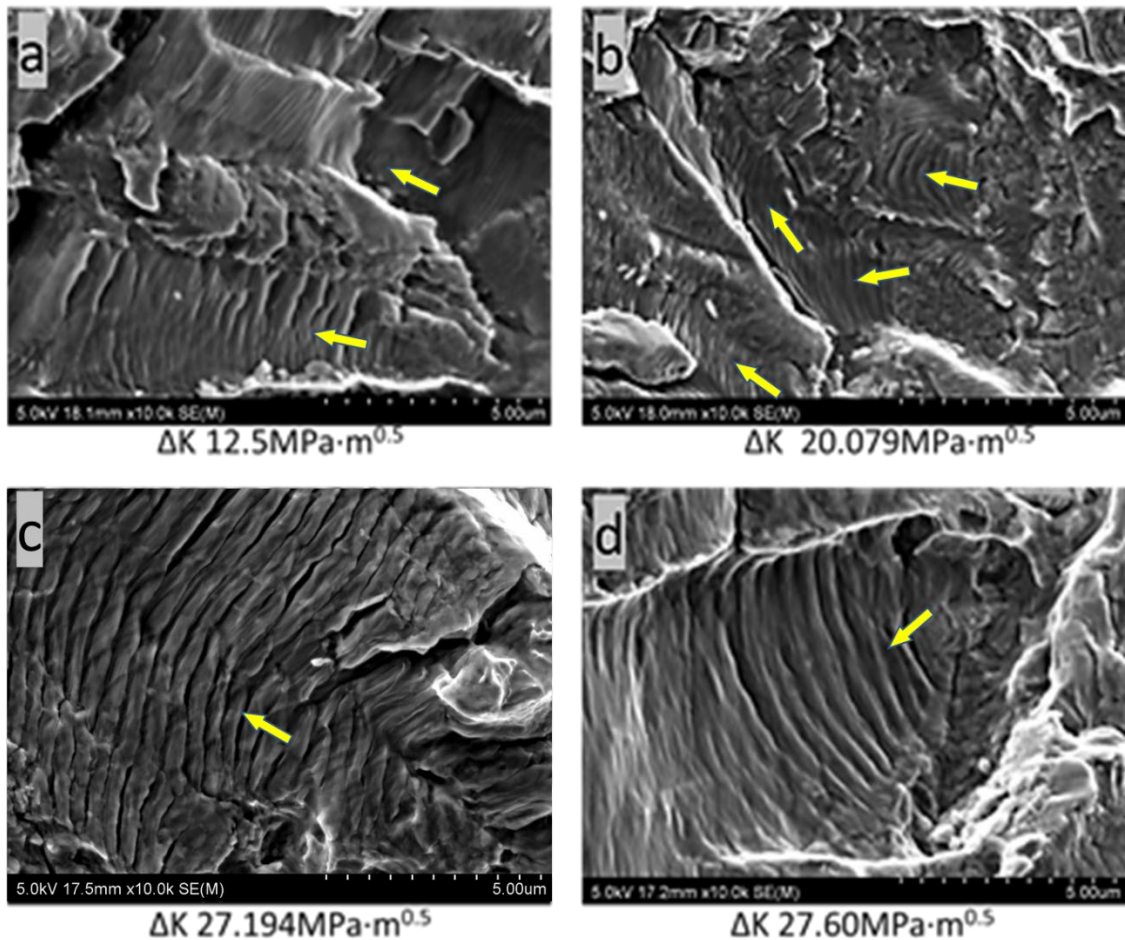
Figure 6-20 Striations in region II of 45° sample with a crack size of a) 6.79×10^{-4} mm with 13.15 mm, b) 2.55×10^{-4} mm with 24.22 mm, c) 5.22×10^{-4} mm with 28.69 mm and d) 5.35×10^{-4} mm with 28.95 mm. Striation direction is indicated by the arrow.

Striation spacing values that were measured in the ImageJ analysis software are compared with the data which the machine provided during the FCG test, represented in Figure 6-21. The finer striation spacing of Ti6Al4V indicates a slower propagation rate. From the start point of region II and getting close to region III, ΔK increases from 12MPam$^{0.5}$ to 50 MPam$^{0.5}$; consequently, the striation space increases as well, which means a faster propagation rate. These observations are not in complete agreement with the FCG data which was carried out from the machine shown in Figure 6-21.
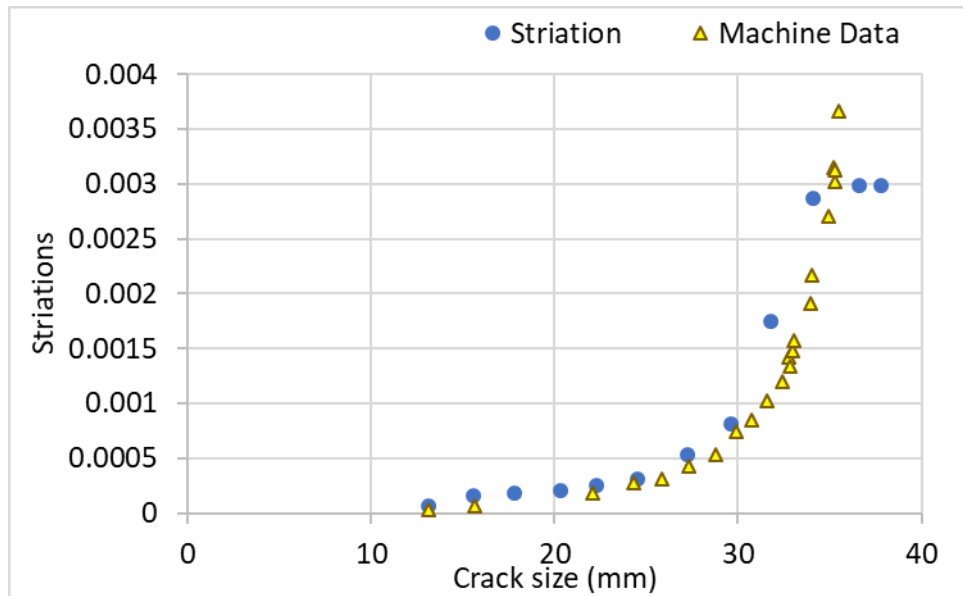
Figure 6-21 The measured striations on the fracture surface in region II of the 45°
sample with the conducted data from the MTS machine.

Some of the striation spacing values do not precisely correspond to the data that the
fatigue machine provided which could be because one striation was not generated by one
load cycling. In addition, the measured striation spacings compared with the FCG graph
show a good correlation between the macroscopic crack growth rate and fatigue striation
spacing for crack growth rates ranging from 6×10^{-5} mm/cycle to 3×10^{-3} mm/cycle. This
observation shows a good agreement with the FCG data in crack growth of the lower
Paris region II and a consistent connection to the microstructurally long crack growth data
in stress ratio 0.1 towards lower ΔK values, while the striation spacing for crack growth
rates ranging more than 3×10^{-3} mm/cycle does not correlate with crack growth rates that
were provided by the FCG data because the fatigue machine records the average of the
crack growth rate while measuring striations represents the local orientation of the crack.
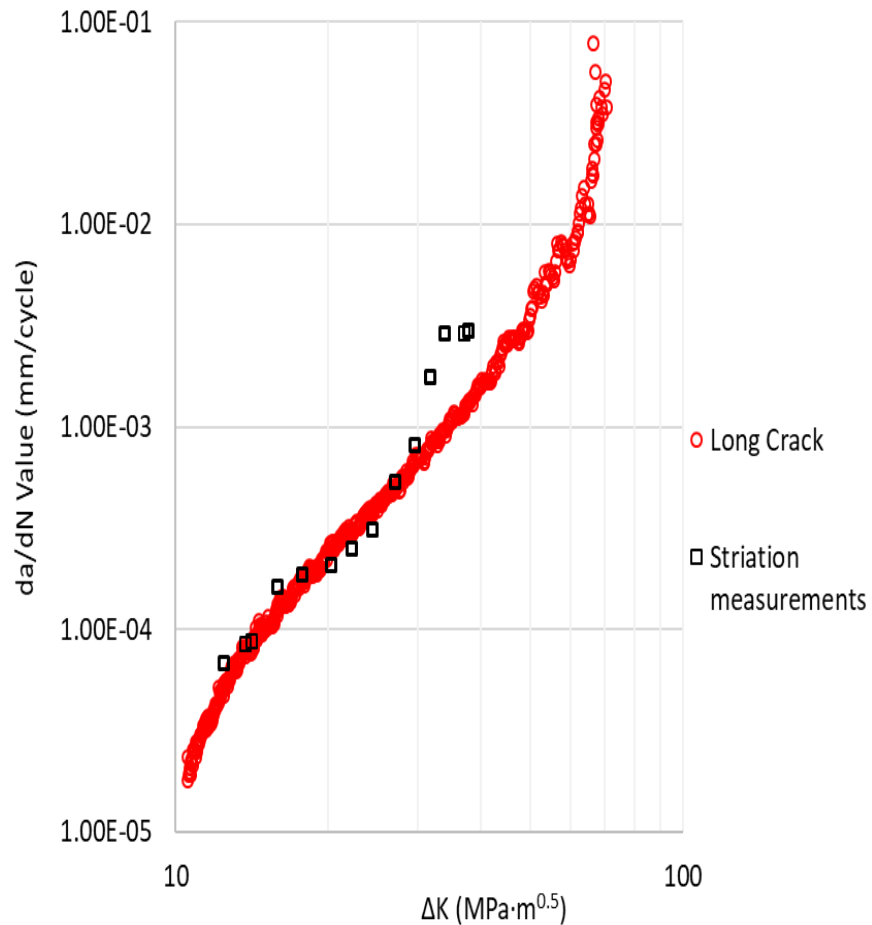
Figure 6-22 Comparison of FCG data with measured striations from SEM images.

6.4 Striation and microstructure relationship

As mentioned before, the crack propagation direction is related to striation spacing and sometimes striation direction (Dubey et al., 1997; Schijve, 2009); therefore, to investigate if β phase orientations have any role and effect on crack propagation and accordingly on striation direction, striations with its microstructure beneath were analysed by positioning the sample at an angle of 40° in order to have the striations and the microstructure in the cross-section, as illustrated in Chapter 3, Figure 3-23 and Figure 6-23. Accordingly, the relationship between β phase orientation and striation direction can be studied in SEM images.
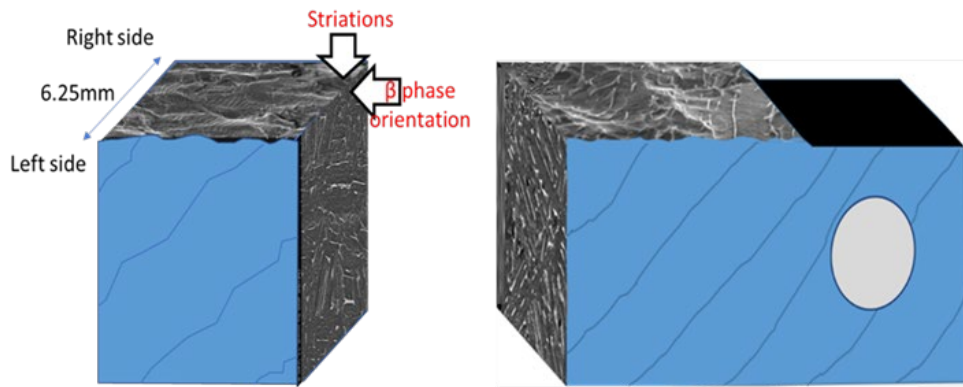
Figure 6-23 The analysed microstructure area beneath striations in the 45° sample.

In Figure 6-24 the SEM image of a fracture surface and its microstructure beneath with 3.652 mm from the left side of FCG cross-sectioned sample, a couple of chains of striations are observed, and by matching the striations with the microstructure beneath, it is clear that striations are located inside colonies. It should be mentioned that the average size of α+β grains is 0.053- 0.011 mm and the α colony size is 0.012- 0.026 mm. Also, on the grain boundaries, no striation was observed. In Figure 6-24, there are striations with two different directions with each striation group belonging to an individual columnar grain. However, these two directed striation groups belong to two adjacent columnar grains. The α grain boundary that separates these two directed striation groups does not have any striation on the fracture surface. The separated area between the two directed striation groups is an α grain boundary indicated with green arrows in Figure 6-24. The overall crack direction with the local direction of striations in Figure 6-24 area is different. This difference indicates that the local striation direction must be affected by the local α and β orientations of that area. There is another explanation explaining the difference between the local striation direction and the overall crack direction: it could be because of a secondary crack that propagated and joined the main crack. In addition, by tracking the grain boundary between the two green arrows, it is clear that α columnar grain boundary number 2 can be traced on the fracture surface. In contrary, the next α columnar boundary number 1 cannot be found easily on the fracture surface. Therefore, in order to identify the α and β phases, EDS software can be helpful and will be provided later in this chapter.
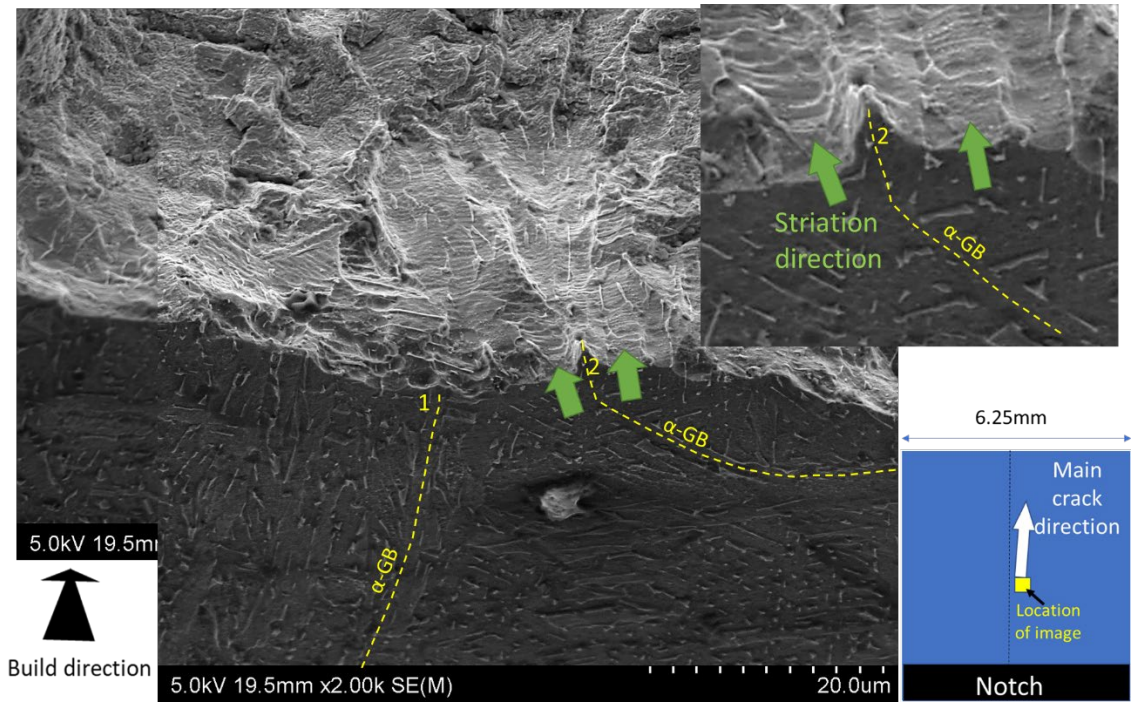
Figure 6-24 The cross-sectioned FCG of the 45° sample where α grain boundaries with dashed lines and crack growth direction with green arrows are shown.
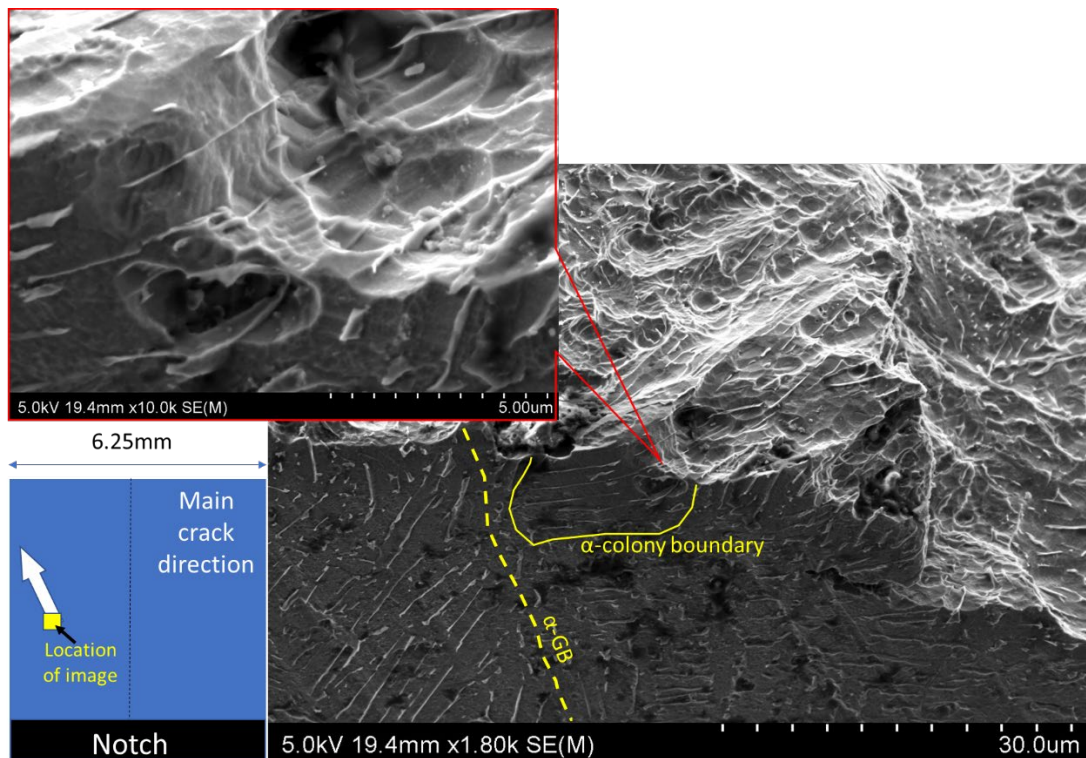
Figure 6-25 SEM image of striations of the 45° sample that are formed inside the α colony boundary.

In some areas like Figure 6-25, striations were found in the α phase between the β phases which are located inside the α colonies. Striation tracks, which demonstrate the direction

149

of crack propagation, have a different orientation with β phase plates. However, β phase appears with many different shapes such as needles, irregular thick and plate forms, which some of them are shown in Figure 6-26. As Figure 6-26c and Figure 6-24 show, striations occur on α phases. Since β phases were observed on the fracture surface due to the fracture being slightly etched, there is no sign of striation prints on the β phases (Figure 6-26d). However, the β phases are a part of the striations. The reason for not observing any interruptions of the β phases on the striations (because of the β phase position on the striations spaces) could be attributed to the small thickness of the β phases which cannot be seen in any interruption on the striations. Regarding striations' locations on the α phase, it was expected to detect striations on the α boundaries, but they were not observed perhaps because the thickness of the α boundaries was less than 2μm, which are surrounded by β phases.
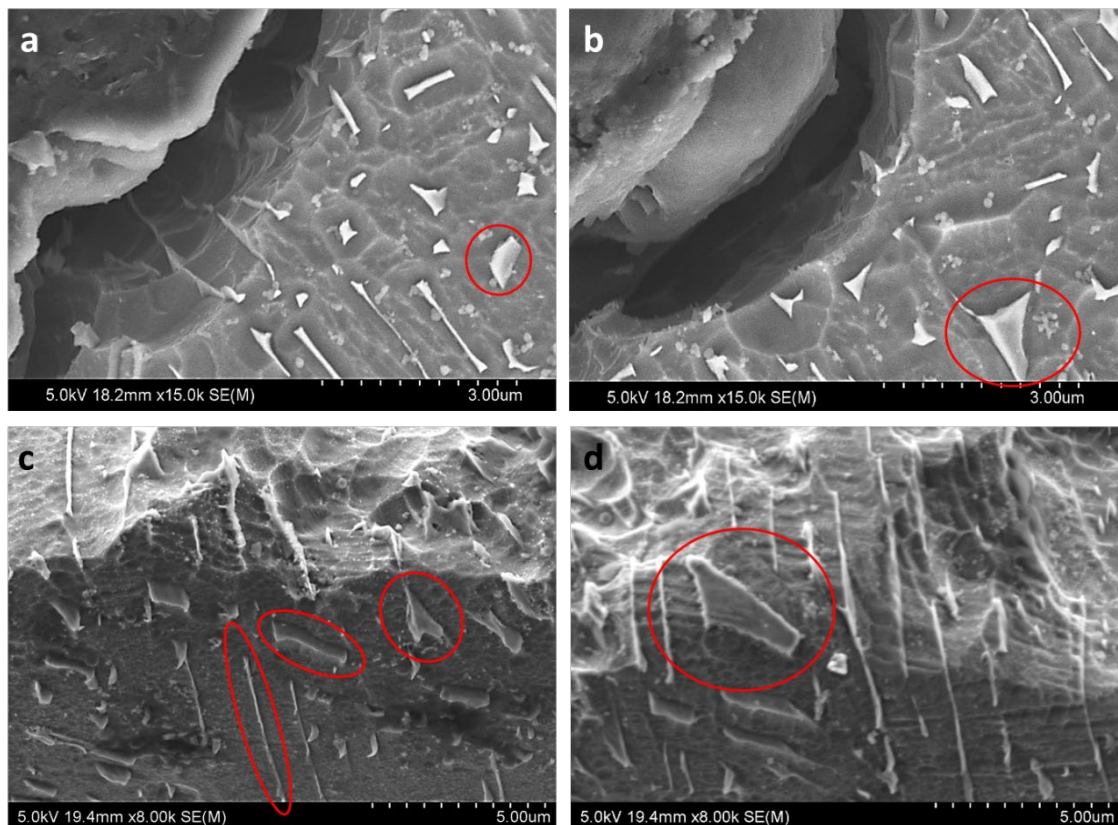
Figure 6-26 Micrograph of β phase with different shapes in fractured cross-section of Ti6Al4V alloy.

By observing the fracture surface of the samples, the striation directions were illustrated in Figure 6-27. As shown in Figure 6-27, the angle of the striation direction, which is called NS, near edges depends on the local crack orientation. Moving towards the centre of the sample, the angle between striation and notch direction (NS and NN) gets smaller

until reaching $0°$, which means the orientated striation is getting close to becoming normal to the notch. But because the striation orientation shows the direction of the local crack, sometimes the striation direction and the main crack propagation direction are not the same.
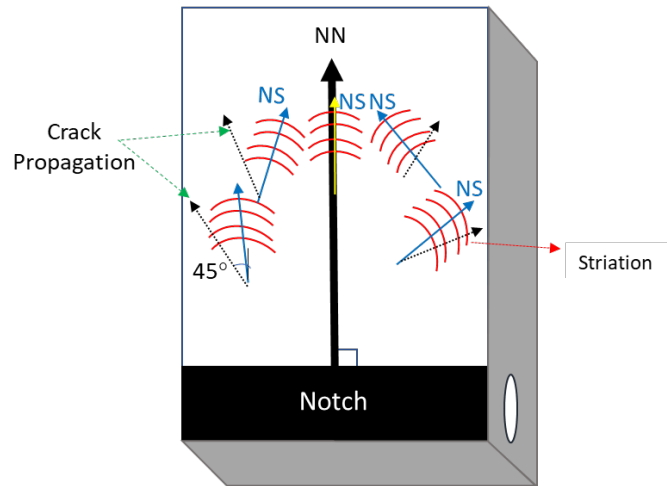
Figure 6-27 Schematic of the fracture surface of the FCG sample with an axis normal to the notch, NN, and the main striation direction, NS, normal to the striations.

By observing striation orientations with the orientation of the β phases, a schematic drawing of the striation direction and β phases is illustrated in Figure 6-28. In Figure 6-28a, the SEM image shows the fracture surface near the edge of the sample (0.988 mm from the left edge) where the angle between striations and β phases is almost $90°$. Closer to the centre, 3.125 mm from the edge, this angle decreases as shown in Figure 6-28b (2 mm from the left edge). In an area with a distance of 4.8 mm from the left edge, which is close to the middle of the sample, the striation direction becomes more or less parallel to NN, as shown in Figure 6-28c. As the distance from the left edge increases to 6 mm and gets close to the right-side edge, the angle between NS and NN increases again (Figure 6-28d).

In addition, observation of striations on the fracture surface and the β phase beneath suggests that the striation direction and the longitudinal side of the β phase have an angle of more than approximately 20°. It should be mentioned that the reason for the observed β phases on the fracture surface close to the joined area with the cross-sectioned area, is that the Kroll's etchant solution permeated inside the mounting area during etching the cross-section side of the sample. Hot glue was used instead of resin during the mounting process to protect the striations on the tested sample's fracture surface.
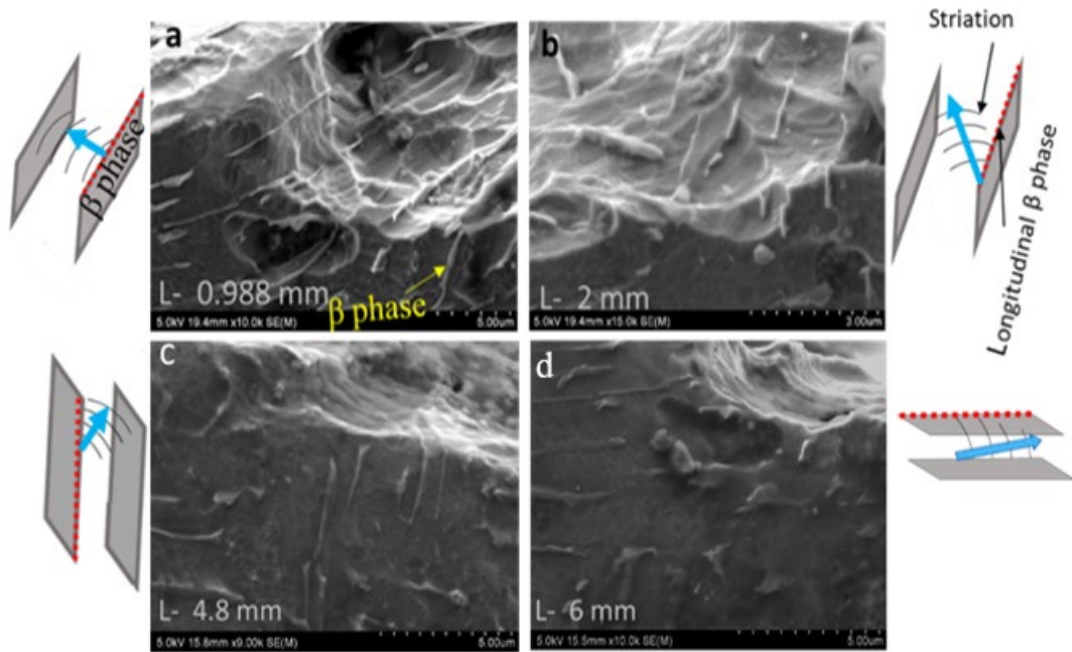
Figure 6-28 The SEM images of the fracture surface in the 45° sample with microstructure beneath and the illustration of orientated striations between two adjacent β phases.

The behaviour of β phases with striations was consistent in the whole fracture area. The observation showed that usually striations are normal to the β phase plane. In addition, the angle between the β phase direction on the cross-section side (ZX of the image) and the Z axis in Figure 6-29a and Figure 6-29b is similar. That means that by observing from the cross-section side, it seems that the β phases in these two figures have the same direction, but by adding the orientation of the β phases on the fracture surface side, the β platelet orientations are different. The same situation is seen in Figure 6-29c-d.
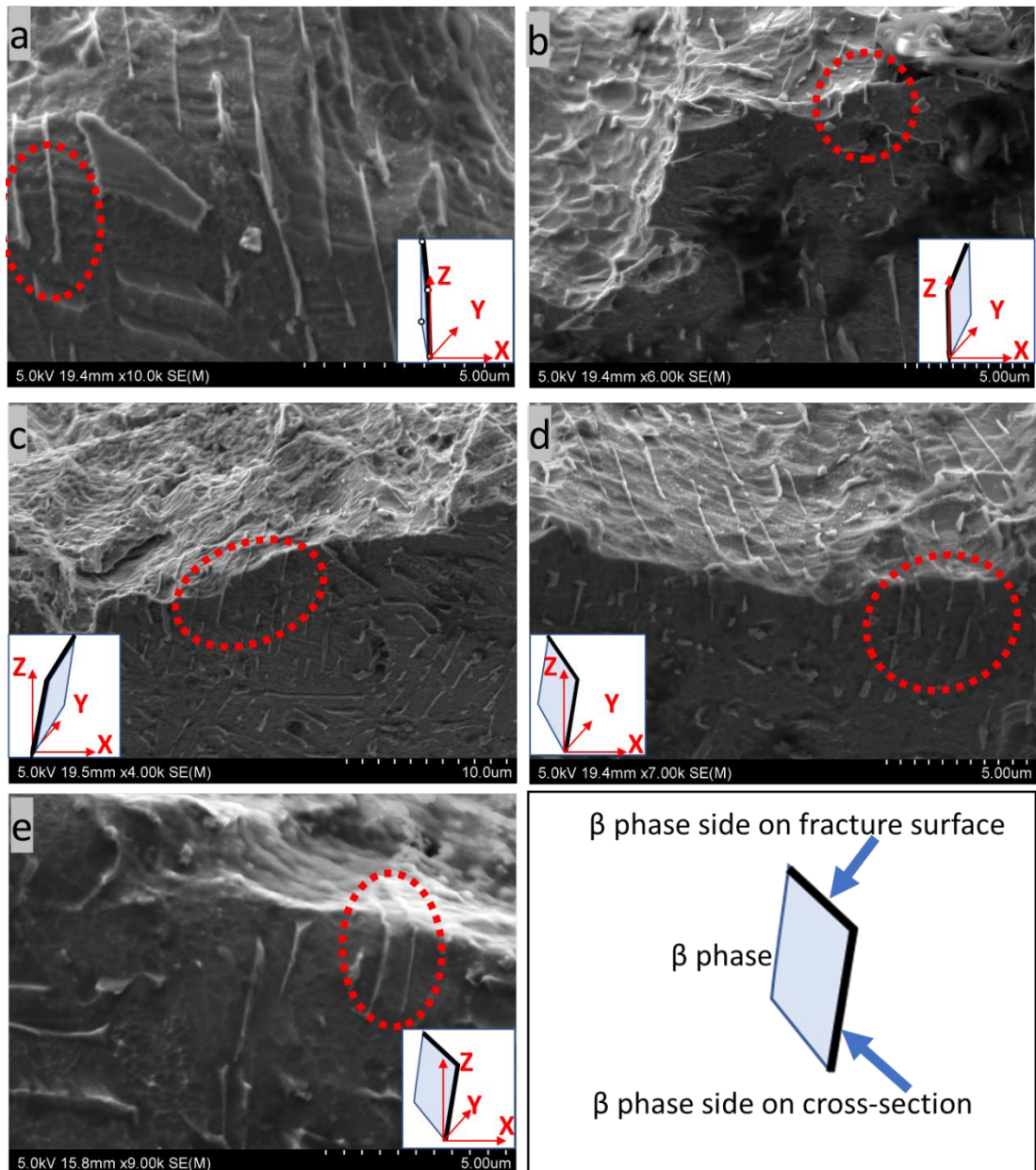
Figure 6-29 The comparison of the β phase directions on the cross-section side (ZX of the image) and β phase directions on the fracture surface side. In a) and b) the β phases on the cross-section side have the same angle with the Z direction; the same in c), d) and e) together in region II.

Most β phase orientations in the Ti6Al4V alloy are more or less at a 45° angle to the build direction. However, some β phases were observed at 90° and 0° angles to the build direction. These β phase orientations are repeated in whole samples for different build orientated samples which means that the build direction does not change the orientation of the β phase. In addition, as mentioned by Williams et al., the α phase and β phase have a burger relationship which means that when the directions of the β phase, which is shown in Figure 6-30d, are repeated in whole samples, regardless of the build direction, the α

phase directions have the same situation as the β phase (Gerd Lütjering et al., 1998). As mentioned before, the build direction does not have any influence on the fatigue crack growth graph in the Paris region as shown in Figure 6-2. Also, LOF and the porosity level are not effective factors in this region. In addition, Figure 6-18 and Figure 6-19 indicated that the β phase might affect the crack propagation path. Therefore, the linear Paris region is dependent on the α and β orientations. Furthermore, the α and β orientations are similar in all three different build samples (as shown in Figure 6-30d), and the crack growth demonstrates a similar behaviour in region II for all three samples.
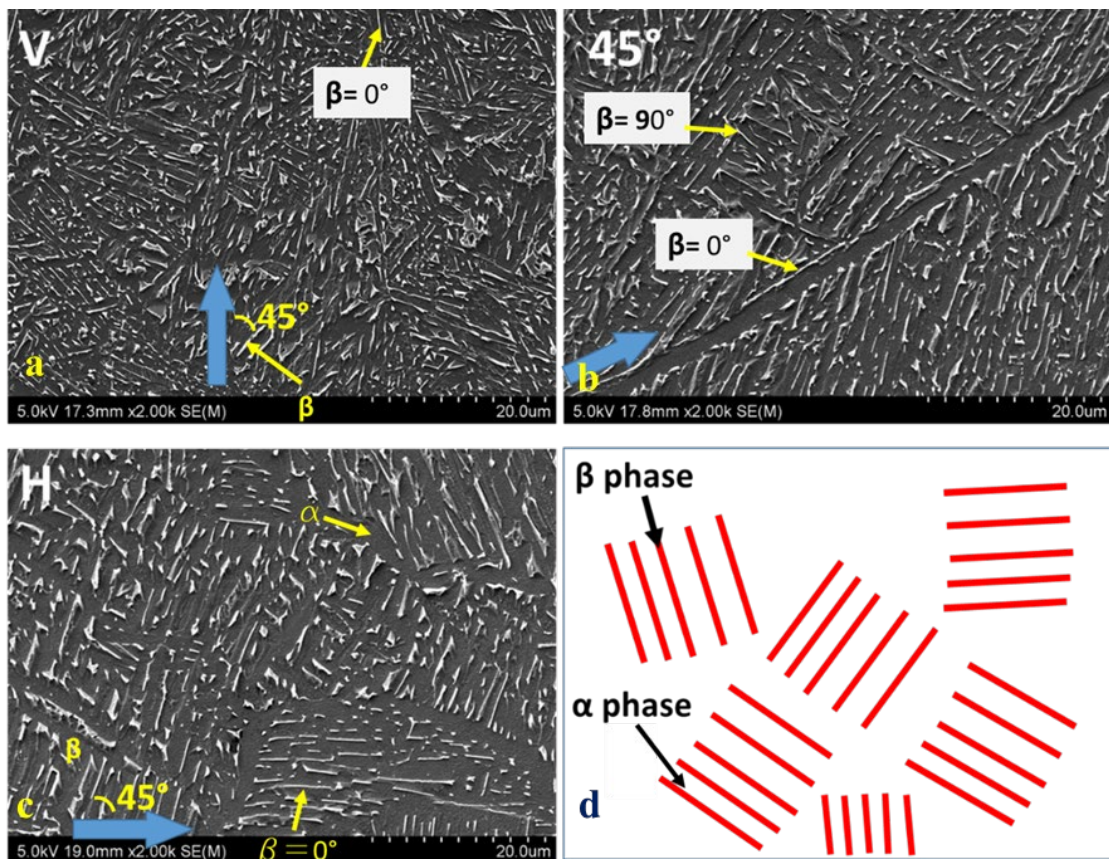
Figure 6-30 The common orientations of the β phase in all three directional samples' microstructure. Blue arrows indicate the building directions.

Therefore, an identical region II graph and the direction of the β phase is a barrier for the crack directional; therefore, several areas such as Figure 6-29 leads to the illustration in Figure 6-31 which shows the striation directions in respect of the orientations of the β phases inside the colonies. The independence of crack growth rate on build direction suggests that α-phase along the prior β-phase grain boundaries has not acted as a favoured path for crack growth during fatigue loading. The local crack advancing in a specific orientation in a α+β colony and thus the striation orientation in one colony is different

from another. The combined growth direction is then the same as the direction that the global crack front moves during crack growth. This crack growth feature is suggested to be the reason for the lack of the dependence of Paris law constants on notch and build direction relationship. It should be mentioned that in Figure 6-29 the β platelet is sketched in a rectangular shape to show the orientation of the β phase side inside the α matrix. The platelet β phase has different shapes as explained in Figure 6-26.
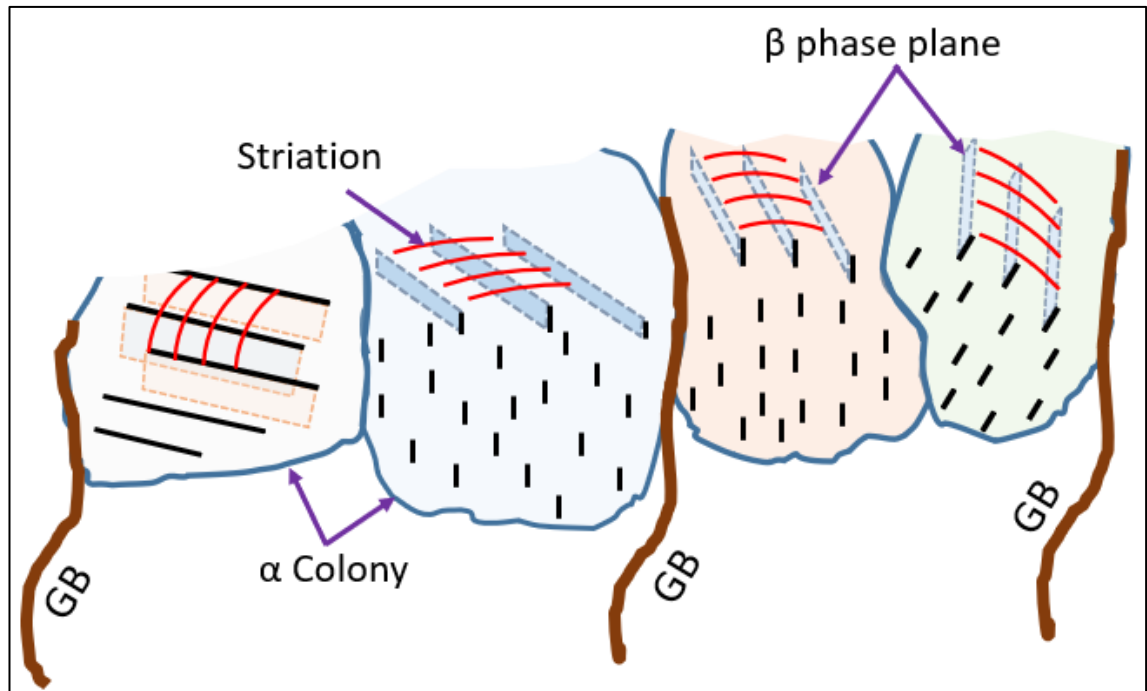
Figure 6-31 Schematic micrograph of the relationship between striations inside the colonies and the β phase plate orientations.

Since the fatigue crack growth graph in Figure 6-2 showed an identical behaviour for the vertical, horizontal and 45° orientated samples, it is concluded that not only LOF and porosity but also the build direction does not affect the Paris region (region II). After analysing the crack growth path and the observation on two sides of the cross-section side and the fracture surface together, the effective factor in the Paris region is the orientation of α and β phases (when the stress intensity is low enough to be sensitive to the microstructure in which the Paris region is included). This observation, as Figure 6-19 suggests, shows that the β phase, depending on the shape, could change the crack propagation direction. Therefore, the crack propagation in the Paris region depends on the orientation of the α and β phases. In addition, the columnar α phase boundaries and the α colony boundaries do not act as a barrier in the Ti6Al4V alloy.

6.5　Phase identification on the fracture surface

Some literature introduced some facet-like areas that separated striations on the fracture surface as grain boundaries or α colony boundaries (Sandgren et al., 2016; Zhai et al., 2015). Therefore, in order to identify the white facet-like areas or the ones that seem they could be boundaries or colonies were examined. By EDS analysis, the percentage of aluminium or vanadium concentrations were revealed to identify which area belonged to α colonies or boundaries or β phases. It should be mentioned that although the smoother the tested surface, the more accurate the recognition of elements, it was attempted to find the area that the EDS technique could detect without any obstructions in the X-rays deflection (Nasrazadani et al., 2016).

One of the facet-like areas that separated two different orientated striation areas was tested as shown in Figure 6-32. The percentage of elements suggests that this area is not an α boundary, but is more likely α-β phase inside an α+ β colony.

Weight %	Al	Ti	V
pt1	8.34	88.24	3.42
pt2	7.80	87.38	4.83
pt3	7.00	89.55	3.45
pt4	6.31	87.59	6.10
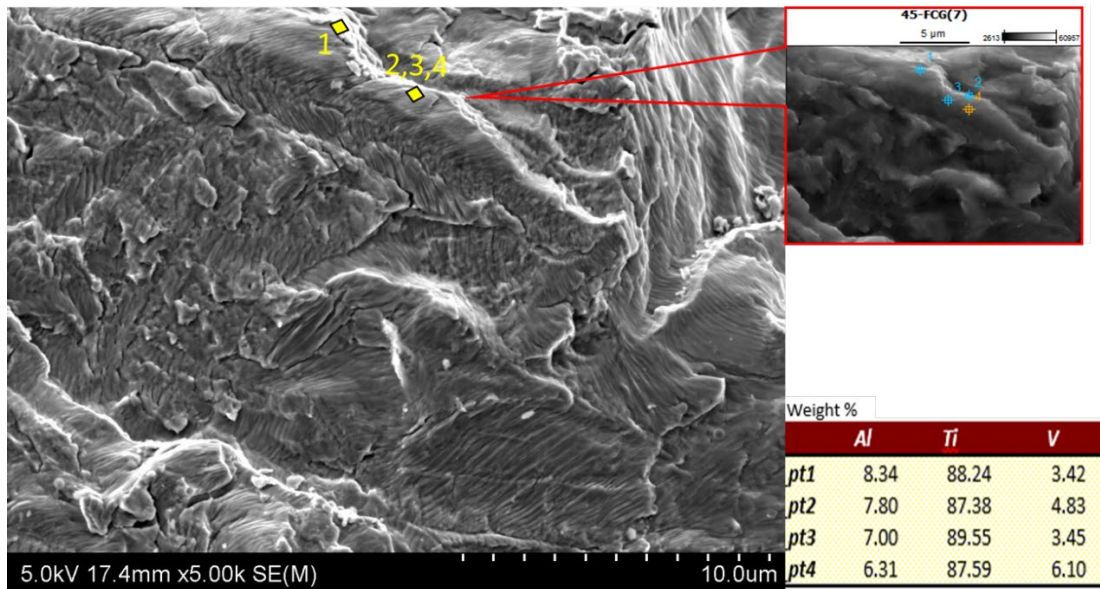
Figure 6-32 SEM image of the fracture surface of the 45° sample and EDS test result.

The SEM image in Figure 6-33 shows striation chains with different directions and some possible areas of α boundaries. So, after the EDS test, it was clear that the area numbers 10 and 11 are located in the β phase because these areas are enriched in vanadium and depleted in aluminium. In addition, the concentration of vanadium in area number 4 is higher than the average value of 4%. Consequently, it probably belongs to the β phase. In area number 9, α phase is detected, and due to the shape of the area and the striation print, it is probable that this α phase belongs inside the α colony. Like area number 9, the areas

of numbers 5, 6, 8 and 12 belong to α phase, and it seems that numbers 5 and 8 are inside one colony and each number 6 and 12 is inside the other α colonies separately.

Weight %	Al	Ti	V
pt1-No Data.			
pt2-No Data.			
pt3	2.49	50.21	47.30
pt4	1.94	39.74	58.33
pt5	4.90	95.10	0.00
pt6	4.31	95.69	0.00
pt7	5.05	91.15	3.81
pt8	5.54	94.46	0.00
pt9	4.94	95.06	0.00
pt10	4.78	57.23	37.99
pt11	4.78	57.23	37.99
pt12	4.76	95.24	0.00
pt13	10.86	89.14	0.00
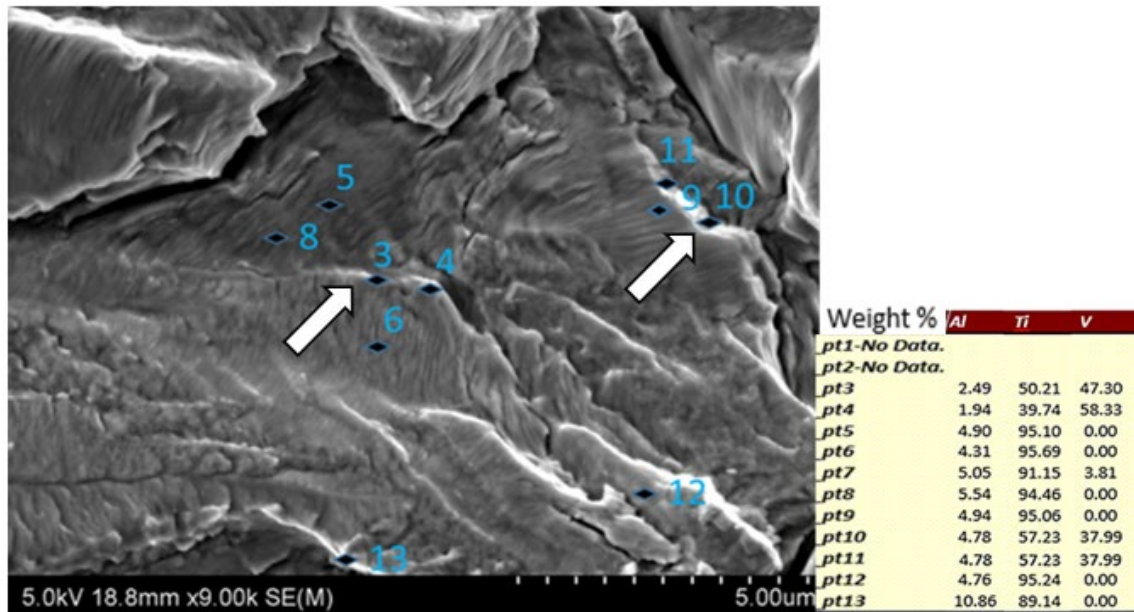
Figure 6-33 SEM image of the fracture surface of the 45° sample and EDS test result.

During observing the fracture surface of the FCG sample, in some areas like number 1 in Figure 6-34 there are some barriers that a crack cannot pass through. So, after reaching these barriers, the crack direction was redirected or got branched at that point. This behaviour of the crack was concluded because the striations orientation redirected around the area as shown in the red circle which was examined by EDS and the elements result shows that this area has α and β phases. It seems that the structure for this area is too strong for a crack to propagate through so the striations were redirected. In addition, the percentage of aluminium as an α stabilizer and vanadium as a β stabilizer suggests that the white line which shows with an arrow cannot belong to an α boundary. Therefore, by observing the white lines that separate the two striation directions, it cannot be concluded as an α boundary.
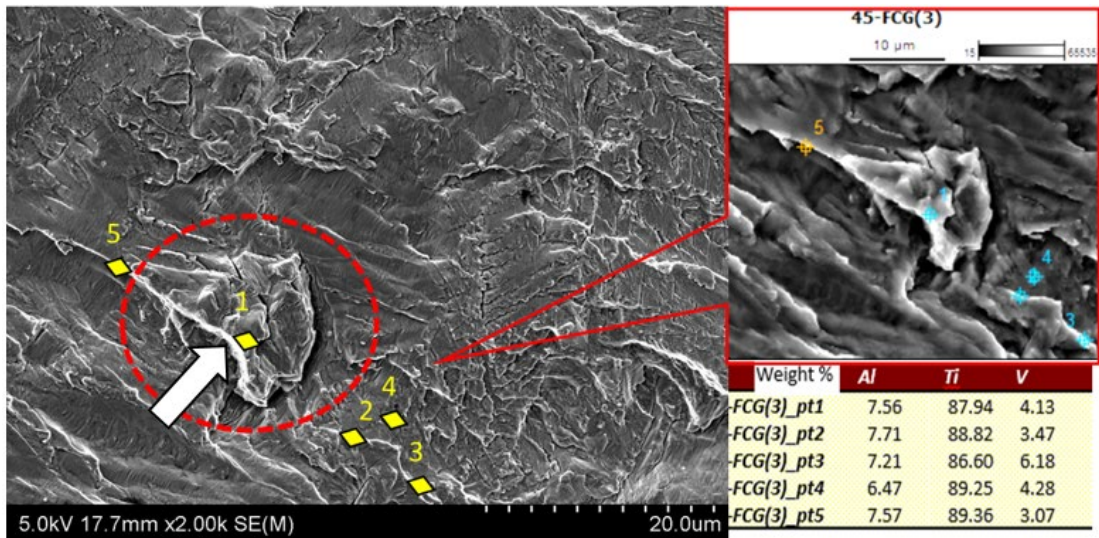
Figure 6-34 SEM image of an area where all striations changed direction on the fracture surface of the 45° sample and EDS test result.

Weight %	Al	Ti	V
FCG(3)_pt1	7.56	87.94	4.13
FCG(3)_pt2	7.71	88.82	3.47
FCG(3)_pt3	7.21	86.60	6.18
FCG(3)_pt4	6.47	89.25	4.28
FCG(3)_pt5	7.57	89.36	3.07

Weight %	Al	Ti	V
45-FCG(5)_pt1	6.62	88.98	4.40
45-FCG(5)_pt2	7.23	89.13	3.64
45-FCG(5)_pt3	6.80	89.46	3.74
45-FCG(5)_pt4	5.48	89.93	4.58
45-FCG(5)_pt5	6.65	89.62	3.56
45-FCG(5)_pt6	7.23	88.90	3.87
45-FCG(5)_pt7	7.74	88.37	3.90
45-FCG(5)_pt8	8.21	87.70	4.10
45-FCG(5)_pt9	3.87	92.52	3.60
45-FCG(5)_pt10	3.94	92.56	3.50
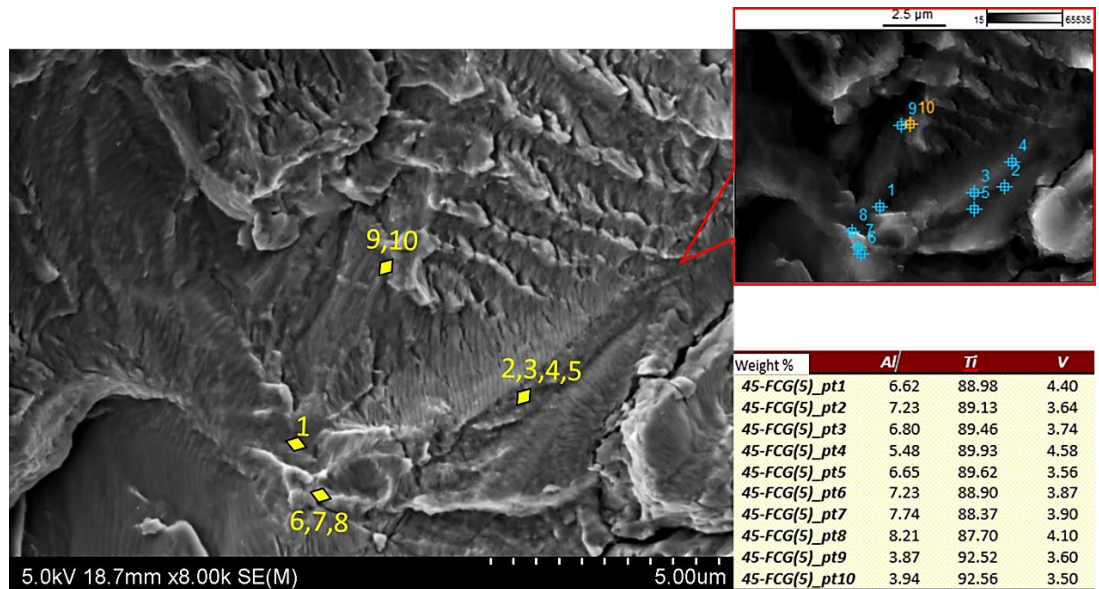
Figure 6-35 SEM image of an area on the fracture surface of the 45° sample and EDS test result.

In Figure 6-35 ten points were tested by EDS, and the result did not show any significant change in the stabilizer elements to identify these areas as belonging to which of the phase areas.

6.6   Summary

It was revealed that although the angle between crack growth direction and build direction is different, crack propagation has the same response in each cycle with the same given ΔK in region II for all samples. According to the Paris law equation for region II, the exponential constants of all three directed samples was determined to be m = 3.1 and C = 1×10^{-8} mm/cycle. Region II started from 2×10^{-5} mm/cycle with ΔK 10 MPa.m$^{0.5}$ and finished at 3.5×10^{-2} mm/cycle with ΔK 50MPa.m$^{0.5}$ which is the starting point of region III.

In region II, many LOFs and porosities were observed which could reach 500 μm. The fractions of porosity in the samples with vertical, 45° and horizontal crack growth were evaluated to be 0.24%, 0.108% and 0.137%, respectively. The difference in the fraction of porosity in the samples was not noticeable. Moreover, the fraction of LOF from vertical to 45° and horizontal samples decreased from 0.997% to 0.746% and ~0.397%, respectively. Having porosities and LOFs on the fracture surfaces and identical FCG curves for all three orientated samples confirms that although the fraction of LOF and porosities in the samples are different, the differences are small enough that no change in the fatigue crack growth graph was caused in region II. Therefore, despite LOF's favourable orientation for crack growth, da/dN vs ΔK is the same. This may suggest that the crack resistance for the vertical sample material may be higher or the percentage of LOF is low.

The micrograph observation suggests that the crack propagation path could be based on the density of the β phase inside the α+β colonies. The crack preferably propagated in the α+β grain with low β phase density. The crack propagated from the interface of the α and β phases during crossing the small α+β grain. The interaction between crack propagation and β phase shows different behaviour based on its angle with the crack. When crack direction and β phase has a 0° angle, the crack grows at the α and β interface along with the β phase. When this angle increases from 0° to 30° and 90° during crack propagation, the β phase is cut without any significant deformation. As the angle of β phase and crack growth direction increases to more than 90°, the β phase is cut with a small noticeable deformation on the fracture tip.

This observation demonstrates that crack branching occurs in the α+β grain and just after crossing the columnar α phase boundaries. The crack crossed the columnar α phase boundaries without branching or deflecting. This finding suggests that columnar α phase

boundaries are not crack barriers, while β phases in a specific crystal orientation act as a crack barrier and makes the crack branch. In addition, when the crack reaches β phases around the α columnar grain boundary, it changes direction. The β phase acts as a barrier in the Ti6Al4V alloy and changes the crack growth direction before crack reaches the α grain boundary.

The striation direction and the β phase have an angle of more than approximately 20°. Also, the striations are normal to the β phase plane. Striations occur on the α phases inside the α+β colonies since the β phases were observed on the fracture surface with no sign of a striation print which was attributed to the small thickness of the β phases which cannot be seen as an interruption on the striations. It has been found that locally a crack advances in a specific orientation in an α+β colony and thus the striation orientation in one colony is different from another. The crack direction with the local direction of striations differs due to the influence of the local α and β orientations in an α+β colony and the local secondary crack.

7. CHAPTER. Conclusion

7.1 Objectives and Achievements

Ti6Al4V alloy products processed by EBM are popular commercially and used in many industries including aerospace and biomedical. Extensive investigations carried out by the researchers showed that there were some limitations in the mechanical properties leading to poor performance and a shorter life in comparison with traditional techniques. A threshold mechanical property standard including impact toughness and fatigue crack growth resistance is required for the application of Ti6Al4V components in the industry. In metal additive manufacturing LOF formation was seen to be a critical property, hindering the widespread use of the technology. Due to the high aspect ratio of LOF, there is the possibility of LOF/defects acting as the source of crack propagation, unfavourably affecting the mechanical properties of the EBM parts. Due to unclarity in the melt pool shape formation of EBM processed Ti6Al4V, the melt pool size and formation of defects, particularly LOF, was studied with respect to the melt pool shape and size. Further knowledge gaps in the effect of the fracture path and LOF at different build orientations on impact toughness were examined, determining the effect of build orientations and LOF on the impact energy. Finally, regarding EBM processing, there was a shortage of understanding on the effect of LOF on gradually applied loads such as fatigue crack growth, with samples tested at three different build directions in region II.

7.2 General Conclusions

From this study, it was revealed that an increase in scan speed led to an increase in the size and change the shape of LOF. An increase in the surface roughness with an increase in scan speed resulting in an overall melt pool size decrease. As the overall melt pool size decreased, the melt pool body depth (depth without the crown) decreased, however, the melt pool crown height was seen to increase. Hence, the melt pool crown increases the top surface roughness, increasing the possibility of LOF formation in the components.

Two significant effects on the impact energy values, found to vary between 26J and 49J, have been identified in this work. The first is LOF (the maximum size and the number of LOF) and the second is the build direction. Additional minor influences were observed in the impact energy from microstructural variances.

In fatigue testing, it was revealed that region II is independent of the build direction and LOF, therefore, resulting in identical Paris law constants for all three build directions. Further, β phase in α+β colonies act as a barrier during crack propagation in region II, however, α columnar grain boundaries were not seen to act as a barrier.

7.3 Detailed conclusion

7.3.1 Effect of scan speed on melt pool and lack of fusion (LOF)

- In the 5m/s sample, a semi-circular melt pool with the width of more than 750 μm, and the depth of ~700 μm was produced at an energy input of ~16.8 J/mm^3 from the beam 400 μm in diameter. As scan speed increases from 9m/s to 18m/s, the melt pool shape becomes more conical due to the energy input decreasing from 9.33 to 4.66 J/mm^3. Thus, resulting in a melt pool width decrease from 750 μm to ~ 614 μm, and the depth decrease from ~410 μm to 145 μm respectively.

- Across the scan speeds tested, the reduction in the depth of the melt pool is ~ 61% greater than that of the width.

- The effect of Marangoni phenomenon becomes stronger as the melt pool size decreases with increasing scan speed leading to Rayleigh instability breaking the melt pool track into discontinuous balls.

- Increased Marangoni effect at high scan speeds leads to molten metal overflowing and solidifying generating type 4 LOF defects.

- The fraction of LOF is inverse proportional to the scanning speed with the fraction of LOF increasing sharply from 0 to 45% from 5 to 18m/s as the energy input drops.

- The top surface roughness has a direct relationship with the fraction of LOF due to instability in the melt pool increasing the top surface roughness. Surface roughness increased from <0.05 mm to 0.2mm from 5m/s to 12m/s.

- As scan speeds above 12m/s, the discontinuity between melt pools is observed along the top surface with a greater fraction of LOF.

- A direct relationship between the top surface track width and the scan speed is observed. Less overlapping between the adjacent melt pools results from increasing the scan speed from 5m/s to 12m/s, due to the decreasing the melt pool size, increasing the distance between two tracks (track width).

- The unevenness of track width results due to the instability of the melt pool shape, increasing in instability with increasing scan speed.

7.3.2 Effect of defects/LOF and build direction on Impact Toughness

- A decreasing trend in impact toughness is witnessed in decreasing level of energy from the vertically orientated samples to the samples at 45° and finally the horizontal samples.

- Impact energy absorbed is attributed to the number of LOF, as the angle between longitudinal sides and the build direction increases, the number of LOF increases with the vertical samples having the highest impact energy with the fewest number of LOF.

- The trend of the impact energy for identical samples in different batches is attributed to the maximum LOF size. Increasing LOF in vertical samples ~0.108 mm^2 leads to an impact energy decrease from 49 to 34J. Similarly, for 45° samples, the maximum LOF size increases by ~ 0.116 mm^2 with impact energy decreasing from 40 to 28J. While in the horizontal samples, despite a change in the maximum LOF size in the samples, the impact energy does not change as LOF is orientated in a favourable direction for crack growth, with the maximum LOF size affecting the impact energy. However, LOF <49μm^2 was seen to not affect the impact energy.

- As the angle between longitudinal side and the build direction increases, the impact energy decreases from an average of ~42J in vertical samples (0°) to ~27J in horizontal samples (90°).

- Build direction has the most influence on impact toughness.

- Impact energy is directly influenced by the microstructure, as the microstructure slightly coarsens with the angle between longitudinal sides and the build direction increasing from vertical sample to horizontal sample, the impact energy is seen to reduce marginally.

- Crack propagation in the vertical samples occurred inside the α+ β phase colonies and crossed passing through columnar α grain boundaries, representing transgranular propagation with the highest impact toughness of ~42J.

- Crack propagation in the 45° and horizontal samples occurred along the columnar α phase boundaries and inside the α+ β phase colonies, representing a mixture of transgranular and intergranular propagation.

- As the angle between the crack growth direction and the α columnar phase boundaries becomes close to zero, the energy that the sample absorbs decreases thus, average impact energy of ~34J is observed in the 45° samples as compared to ~27J in the horizontal samples.

163

- The fraction of LOF and porosity was seen to insignificantly influence the energy absorbed for a volume of LOF and porosity below 1.1% and 0.175% respectively.

7.3.3 Effect of build direction and defects on the crack growth rate and propagation path of Ti6Al4V alloy in region II

- The lack of dependence of Paris law constants in the build direction resulted in similar Paris law constants of m = 3.1 and C = 1×10^{-8} mm/cycle in the three different notch orientations.
- LOF and porosity did not increase the crack propagation rate significantly as a low 0.4 - 1.0% LOF and ~0.1% porosity was observed on the fracture surface.
- β phases interaction with crack propagation differs based on its angle with the crack direction. When the angle between crack direction and the β phase is 0°, the crack grows at the α and β interface along with the β phase. The β phase fractured without significant deformation when the β phase angle increases to 30° and 90°. If the angle between the β phase longitudinal side with crack growth direction is <5°, the crack growth propagates along the intersection of the β phase and α phase. The β phase is fractured with a small deformation on the fracture tip, as the angle of the β phase and the crack growth direction > 90°.

- β phase in Ti6Al4V orientated predominantly at an angle of 45° to the build direction, however, β phases orientated at 90° and 0° to the build direction was observed in all samples. Hence, the build direction does not affect the orientation of the β phase.

- β phase acted as a barrier to crack propagation with cracks deflecting away. Conversely, cracks were seen to propagate through the α grain boundaries with no deflection.

- An angle greater than ~20° was seen between the striation direction and the β phase. Striations occur on the α phase inside the α+β colonies, normal to the β phase plane. In a single colony, local crack advancing at a specified orientation within a α+β colony and striation orientation is different from another. The combined growth direction is identical to the global crack front direction during crack growth. Hence, the Paris law constants are independent of the crack growth and the build direction.

164

Future work

From these studies, further investigation is in need as follow:

- Regarding the melt pool shape in EBM produced Ti6Al4V alloy, the cross-sectioned melt pool shapes perpendicular to the scan lines (showing the width and depth side) were investigated. However, future work is required investigating the melt pool shape along the scan line length (showing the length and depth) in order to establish an overall picture of the melt shape.

- With respect to the crack path in fatigue crack growth samples, Electron backscatter diffraction (EBSD) analysis was attempted several times with limited success in order to establish crystal orientation patterns of α and β phase during crack propagation. Thus, further work establishing the appropriate sample preparation stages for EBSD analysis and crystal orientation patterns is proposed.

8. References

Aboulkhair, N. T., Everitt, N. M., Ashcroft, I., & Tuck, C. (2014). Reducing porosity in AlSi10Mg parts processed by selective laser melting. *Additive Manufacturing*, *1*, 77–86. https://doi.org/10.1016/j.addma.2014.08.001

Al-Bermani, S. S. (2011). *An Investigation into Microstructure and Microstructural Control of Additive Layer Manufactured Ti-6Al-4V by Electron Beam Melting*. The University of Sheffield. Retrieved from http://etheses.whiterose.ac.uk/14694/1/555712.pdf

Arcam AB. (2014). EBM machines and designs, http://www.arcam.com/technology/products/arcam-q10/.

Arce, A. N. (2012). *Thermal Modeling and Simulation of Electron Beam Melting for Rapid Prototyping of Ti6Al4V Alloys*. North carolina state department.

Attar, E. (2011). *Simulation of Selective Electron Beam Melting Processes*. *Processing*.

AZONetwork. (n.d.). AZO Materials. Retrieved from http://www.azom.com/article.aspx?ArticleID=9107

Balasubramanian, T. S., Balakrishnan, M., Balasubramanian, V., & Manickam, M. A. M. (2011). Influence of welding processes on microstructure, tensile and impact properties of Ti-6Al-4V alloy joints. *Transactions of Nonferrous Metals Society of China (English Edition)*, *21*(6), 1253–1262. https://doi.org/10.1016/S1003-6326(11)60850-9

Benedetti, M., & Fontanari, V. (2004). The effect of bi-modal and lamellar microstructures of Ti-6Al-4V on the behaviour of fatigue cracks emanating from edge-notches. *Fatigue and Fracture of Engineering Materials and Structures*, *27*(11), 1073–1089. https://doi.org/10.1111/j.1460-2695.2004.00825.x

Buirette, C., Huez, J., Gey, N., Vassel, A., & Andrieu, E. (2014). Study of crack propagation mechanisms during Charpy impact toughness tests on both equiaxed and lamellar microstructures of Ti-6Al-4V titanium alloy. *Materials Science and Engineering A*, *618*, 546–557. https://doi.org/10.1016/j.msea.2014.09.048

Cheng, B., & Chou, K. (2013). Melt Pool Geometry Simulations for Powder-Based Electron Beam Additive Manufacturing. In *Proceedings of the Solid Freeform*

Fabrication Symposium (pp. 644–654). Retrieved from
http://utwired.engr.utexas.edu/lff/symposium/proceedingsArchive/pubs/Manuscript
s/2013/2013-51-Cheng.pdf

Cheng, B., & Chou, K. (2014). Thermal Stresses Associated with Part Overhang
Geometry in Electron Beam Additive Manufacturing: Process Parameter Effects.
In *Solid Freeform Fabrication Symposium* (pp. 1076–1087). Texas , Austin, TX:
University of Texas. https://doi.org/10.1017/CBO9781107415324.004

Cheng, B., Price, S., Gong, X., Lydon, J., Cooper, K., & Chou, K. (2014). Speed
function effects in electron beam additive manufacturing. In *ASME International
Mechanical Engineering Congress and Exposition, Proceedings (IMECE)* (Vol.
2A, pp. 1–9). https://doi.org/10.1115/IMECE2014-36664

Cheng, B., Price, S., Lydon, J., Cooper, K., & Chou, K. (2014). On Process
Temperature in Powder-Bed Electron Beam Additive Manufacturing: Model
Development and Validation. *Journal of Manufacturing Science and Engineering*,
136(6), 061018. https://doi.org/10.1115/1.4028484

Connors, W. C. (1994). Fatigue striation spacing analysis. *Materials Characterization*,
33(3), 245–253. https://doi.org/10.1016/1044-5803(94)90046-9

Cunningham, R., Narra, S. P., Ozturk, T., Beuth, J., & Rollett, A. D. (2016). Evaluating
the Effect of Processing Parameters on Porosity in Electron Beam Melted Ti-6Al-
4V via Synchrotron X-ray Microtomography. *Jom*, *68*(3), 765–771.
https://doi.org/10.1007/s11837-015-1802-0

Donachie, M. J. (2000). *Titanium - A Techinacal Guide*. *ASM International*.
https://doi.org/10.5772/1844

Dubey, S., Soboyejo, A. B. O., & Soboyejo, W. O. (1997). An investigation of the
effects of stress ratio and crack closure on the micromechanisms of fatigue crack
growth in Ti6Al4V. *Acta Mater*, *45*(7), 2777–2787.

Edwards, P., O'Conner, A., & Ramulu, M. (2013). Electron Beam Additive
Manufacturing of Titanium Components: Properties and Performance. *Journal of
Manufacturing Science and Engineering*, *135*(6), 061016.
https://doi.org/10.1115/1.4025773

Ek, K. (2014). *Additive Manufactured Material*. 19 MKN 109 KTH Industrial

Engineering and Management Machine Design SE-100 44 STOCKHOLM.

Facchini, L., Magalini, E., Robotti, P., Molinari, A., Höges, S., & Wissenbach, K. (2010). Ductility of a Ti-6Al-4V alloy produced by selective laser melting of prealloyed powders. *Rapid Prototyping Journal*, *16*(6), 450–459. https://doi.org/10.1108/13552541011083371

Galarraga, H., Warren, R. J., Lados, D. A., Dehoff, R. R., & Kirka, M. M. (2017). Fatigue crack growth mechanisms at the microstructure scale in as-fabricated and heat treated Ti-6Al-4V ELI manufactured by electron beam melting (EBM). *Engineering Fracture Mechanics*, *176*, 263–280. https://doi.org/10.1016/j.engfracmech.2017.03.024

Galati, M., & Iuliano, L. (2018). A literature review of powder-based electron beam melting focusing on numerical simulations. *Additive Manufacturing*, *19*, 1–20. https://doi.org/10.1016/j.addma.2017.11.001

Ge, W., Lin, F., & Guo, C. (2014). The effect of scan pattern on microstructure evolution and mechanical properties in electron beam melting Ti47Al2Cr2Nb. In *Solid Freeform Fabrication Proceedings* (pp. 501–513).

Ghonem, H. (2010). Microstructure and fatigue crack growth mechanisms in high temperature titanium alloys. *International Journal of Fatigue*, *32*(9), 1448–1460. https://doi.org/10.1016/j.ijfatigue.2010.02.001

Gil, F. J., Ginebra, M. P., Manero, J. M., & Planell, J. A. (2001). Formation of α-Widmanstätten structure: Effects of grain size and cooling rate on the Widmanstätten morphologies and on the mechanical properties in Ti6Al4V alloy. *Journal of Alloys and Compounds*, *329*(1–2), 142–152. https://doi.org/10.1016/S0925-8388(01)01571-7

Gong, H. (2013). *Generation and detection of defects in melting parts fabricated by SLM and EBM and their effects on mechancal properties*. University of Louisville.

Gong, H., Rafi, K., Gu, H., Starr, T., & Stucker, B. (2014). Analysis of defect generation in Ti-6Al-4V parts made using powder bed fusion additive manufacturing processes. *Additive Manufacturing*, *1*, 87–98. https://doi.org/10.1016/j.addma.2014.08.002

Gong, H., Rafi, K., Starr, T., & Stucker, B. (2013). The Effects of Processing

Parameters on Defect Regularity in Ti-6Al-4V Parts Fabricated By Selective Laser Melting and Electron Beam Melting. In *24th Annual Solid Freeform Fabrication Symposium* (pp. 424–439). https://doi.org/10.1007/s11665-013-0658-0

Greitemeier, D., Palm, F., Syassen, F., & Melz, T. (2017). Fatigue performance of additive manufactured TiAl6V4 using electron and laser beam melting. *International Journal of Fatigue*, *94*, 211–217. https://doi.org/10.1016/j.ijfatigue.2016.05.001

Grell, W. A., Solis-Ramos, E., Clark, E., Lucon, E., Garboczi, E. J., Predecki, P. K., … Kumosa, M. (2017). Effect of powder oxidation on the impact toughness of electron beam melting Ti-6Al-4V. *Additive Manufacturing*, *17*, 123–134. https://doi.org/10.1016/j.addma.2017.08.002

Gusarov, A. V., Yadroitsev, I., Bertrand, P., & Smurov, I. (2007). Heat transfer modelling and stability analysis of selective laser melting. *Applied Surface Science*, *254*(4), 975–979. https://doi.org/10.1016/j.apsusc.2007.08.074

Hebert, R. J. (2016). Viewpoint: metallurgical aspects of powder bed metal additive manufacturing. *Journal of Materials Science*, *51*(3), 1165–1175. https://doi.org/10.1007/s10853-015-9479-x

Helmer, H. E., Körner, C., & Singer, R. F. (2014). Additive manufacturing of nickel-based superalloy Inconel 718 by selective electron beam melting: Processing window and microstructure. *Journal of Materials Research*, *29*(17), 1987–1996.

Hernández-Nava, E., Smith, C. J., Derguti, F., Tammas-Williams, S., Leonard, F., Withers, P. J., … Goodall, R. (2016). The effect of defects on the mechanical response of Ti-6Al-4V cubic lattice structures fabricated by electron beam melting. *Acta Materialia*, *108*, 279–292. https://doi.org/10.1016/j.actamat.2016.02.029

Jamshidinia, M., Kong, F., & Kovacevic, R. (2013). Numerical Modeling of Heat Distribution in the Electron Beam Melting ® of Ti-6Al-4V. *Journal of Manufacturing Science and Engineering*, *135*(6), 061010. https://doi.org/10.1115/1.4025746

Janeček, M., Nový, F., Harcuba, P., Stráský, J., Trško, L., Mhaede, M., & Wagner, L. (2015). The very high cycle fatigue behaviour of Ti-6Al-4V alloy. *Acta Physica Polonica A*, *128*(4), 497–502. https://doi.org/10.12693/APhysPolA.128.497

Joshi, G. V., Duan, Y., Neidigh, J., Koike, M., Chahine, G., Kovacevic, R., … Griggs, J. A. (2013). Fatigue testing of electron beam-melted Ti-6Al-4V ELI alloy for dental implants. *Journal of Biomedical Materials Research - Part B Applied Biomaterials*, *101 B*(1), 124–130. https://doi.org/10.1002/jbm.b.32825

Juechter, V., Scharowsky, T., Singer, R. F., & Körner, C. (2014). Processing window and evaporation phenomena for Ti-6Al-4V produced by selective electron beam melting. *Acta Materialia*, *76*, 252–258. https://doi.org/10.1016/j.actamat.2014.05.037

Karlsson, J., Sjögren, T., Snis, A., Engqvist, H., & Lausmaa, J. (2014). Digital image correlation analysis of local strain fields on Ti6Al4V manufactured by electron beam melting. *Materials Science and Engineering A*, *618*, 456–461. https://doi.org/10.1016/j.msea.2014.09.022

Kirchner, A., Kloden, B., Luft, J., Weisgarber, T., & Kieback, B. (2014). Process Window for Electron Beam Melting of Ti-6Al-4V. *Euro PM2014 - AM:Technologies*, 6–11. https://doi.org/10.1179/0032589915Z.000000000244

Körner, C. (2016). Additive manufacturing of metallic components by selective electron beam melting - A review. *International Materials Reviews*, *61*(5), 361–377. https://doi.org/10.1080/09506608.2016.1176289

Kruth, J. P., Froyen, L., Van Vaerenbergh, J., Mercelis, P., Rombouts, M., & Lauwers, B. (2004). Selective laser melting of iron-based powder. *Journal of Materials Processing Technology*, *149*(1–3), 616–622. https://doi.org/10.1016/j.jmatprotec.2003.11.051

Léonard, F., Tammas-williams, S., Prangnell, P. B., Todd, I., Withers, P. J., Moseley, H., & Facility, X. I. (2012). Assessment by X-ray CT of the effects of geometry and build direction on defects in titanium ALM parts. In *Conference on Industrial Computed Tomography* (pp. 85–93).

Leuders, S., Thöne, M., Riemer, A., Niendorf, T., Tröster, T., Richard, H. A., & Maier, H. J. (2013). On the mechanical behaviour of titanium alloy TiAl6V4 manufactured by selective laser melting: Fatigue resistance and crack growth performance. *International Journal of Fatigue*, *48*, 300–307. https://doi.org/10.1016/j.ijfatigue.2012.11.011

Levy, G. N., Schindel, R., & Kruth, J. P. (2003). Rapid manufacturing and rapid tooling

with layer manufacturing (LM) technologies, state of the art and future perspectives. *CIRP Annals - Manufacturing Technology*, *52*(2), 589–609. https://doi.org/10.1016/S0007-8506(07)60206-6

Liu, Q., Elambasseril, J., Sun, S., Leary, M., Brandt, M., & Sharp, P. (2014). The effect of manufacturing defects on the fatigue behaviour of Ti-6Al-4V specimens fabricated using selective laser melting. *Advanced Materials Research*, *891892*, 1519–1524. https://doi.org/https://doi.org/10.4028/www.scientific.net/AMR.891-892.1519

Liu, Y. J., Li, S. J., Wang, H. L., Hou, W. T., Hao, Y. L., Yang, R., … Zhang, L. C. (2016). Microstructure, defects and mechanical behavior of beta-type titanium porous structures manufactured by electron beam melting and selective laser melting. *Acta Materialia*, *113*, 56–67. https://doi.org/10.1016/j.actamat.2016.04.029

Lodes, M. A., Guschlbauer, R., & Körner, C. (2015). Process development for the manufacturing of 99.94% pure copper via selective electron beam melting. *Materials Letters*, *143*, 298–301. https://doi.org/10.1016/j.matlet.2014.12.105

Lütjering, G. (1998). Influence of processing on microstructure and mechanical properties of (α+β) titanium alloys. *Materials Science and Engineering: A*, *243*(1–2), 32–45. https://doi.org/10.1016/S0921-5093(97)00778-8

Lütjering, G., & Williams, J. C. (1998). *Titanium*. (B. Derby, Ed.), *Engineering Materials and Processes* (Revised, Vol. 243). Berlin, Germany: Springer. https://doi.org/10.1007/978-3-540-73036-1

Mahale, T. R. (2009). *Electron beam melting of advanced materials and strucutres*. North Carolina State University.

Mladenov, G., Koleva, E., Koleva, L., & Dzharov, V. (2016). State of the art of additive manufacturing by selective electron beam melting (PDF Download Available), (June). Retrieved from https://www.researchgate.net/publication/307580909_State_of_the_art_of_additive_manufacturing_by_selective_electron_beam_melting

Mohammadhosseini, A., Masood, S. H., Fraser, D., & Jahedi, M. (2012). Mechanical properties investigation of HIP and as-built EBM parts. *Advanced Materials Research*, *576*, 216–219. https://doi.org/10.4028/www.scientific.net/AMR.576.216

Murr, L. E., Esquivel, E. V., Quinones, S. A., Gaytan, S. M., Lopez, M. I., Martinez, E. Y., … Wicker, R. B. (2009). Microstructures and mechanical properties of electron beam-rapid manufactured Ti-6Al-4V biomedical prototypes compared to wrought Ti-6Al-4V. *Materials Characterization*, *60*(2), 96–105. https://doi.org/10.1016/j.matchar.2008.07.006

Murr, L. E., Gaytan, S. M., Medina, F., Martinez, E., Hernandez, D. H., Martinez, L., … Collins, S. (2009). Effect of build parameters and build geometries on residual microstructures and mechanical properties of Ti-6Al-4V components built by electron beam melting (EBM). In *20th Annual International Solid Freeform Fabrication Symposium, SFF 2009* (pp. 374–397).

Muthu, Subramanian Senthilkannan, Limited, S. H. K., Kong, H., & SAR, H. K. (2016). *Handbook of Sustainability in Additive Manufacturing*. (S. S. Muthu & M. M. Savalani, Eds.). Springer.

Narra, S. P., Cunningham, R., Beuth, J., & Rollett, A. D. (2018). Location specific solidification microstructure control in electron beam melting of Ti-6Al-4V. *Additive Manufacturing*, *19*, 160–166. https://doi.org/10.1016/j.addma.2017.10.003

Narra, S. P., Cunningham, R., Christiansen, D., Beuth, J., & Rollett, A. D. (2015). Toward Enabling Spatial Control of Ti-6Al-4V Solidification Microstructure in the Electron Beam Melting Process. In *Proceedings of Solid Freeform Fabrication Symposium* (pp. 626–635). Retrieved from http://www.arcam.com/technology/electron-beam-melting/

Nasrazadani, S., & Hassani, S. (2016). Modern analytical techniques in failure analysis of aerospace, chemical, and oil and gas industries. *Handbook of Materials Failure Analysis with Case Studies from the Oil and Gas Industry*, 39–54. https://doi.org/10.1016/B978-0-08-100117-2.00010-8

Nicoletto, G. (2017). Anisotropic high cycle fatigue behavior of Ti–6Al–4V obtained by powder bed laser fusion. *International Journal of Fatigue*, *94*, 255–262. https://doi.org/10.1016/j.ijfatigue.2016.04.032

Parry, L., Ashcroft, I. A., & Wildman, R. D. (2016). Understanding the effect of laser scan strategy on residual stress in selective laser melting through thermo-mechanical simulation. *Additive Manufacturing*, *12*, 1–15.

https://doi.org/10.1016/j.addma.2016.05.014

Perez, N. (2004). *Fracture Mechanics*. New York, Boston, Dordrecht, London, Moscow: Kluwer Academic Publishers.

Pilchak, A. L., Bhattacharjee, A., Rosenberger, A. H., & Williams, J. C. (2009). Low ΔK faceted crack growth in titanium alloys. *International Journal of Fatigue*, *31*(5), 989–994. https://doi.org/10.1016/j.ijfatigue.2008.03.036

Prabhakar, P., Sames, W. J., Dehoff, R., & Babu, S. S. (2015). Computational modeling of residual stress formation during the electron beam melting process for Inconel 718. *Additive Manufacturing*, *7*, 83–91. https://doi.org/10.1016/j.addma.2015.03.003

Puebla, K., E. Murr, L., M. Gaytan, S., Martinez, E., Medina, F., & B. Wicker, R. (2012). Effect of Melt Scan Rate on Microstructure and Macrostructure for Electron Beam Melting of Ti-6Al-4V. *Materials Sciences and Applications*, *03*(05), 259–264. https://doi.org/10.4236/msa.2012.35038

Pushilina, N., Syrtanov, M., Kashkarov, E., Murashkina, T., Kudiiarov, V., Laptev, R., … Koptyug, A. (2018). Influence of manufacturing parameters on microstructure and hydrogen sorption behavior of electron beam melted titanium Ti-6Al-4V alloy. *Materials*, *11*(5). https://doi.org/10.3390/ma11050763

Rafi, H. K., Karthik, N. V., Gong, H., Starr, T. L., & Stucker, B. E. (2013). Microstructures and mechanical properties of Ti6Al4V parts fabricated by selective laser melting and electron beam melting. *Journal of Materials Engineering and Performance*, *22*(12), 3872–3883. https://doi.org/10.1007/s11665-013-0658-0

Ritchie, R. O., Boyce, B. L., Campbell, J. P., Roder, O., Thompson, A. W., & Milligan, W. W. (1999). Thresholds for high-cycle fatigue in a turbine engine Ti-6Al-4V alloy. *International Journal of Fatigue*, *21*(7), 653–662. https://doi.org/10.1016/S0142-1123(99)00024-9

Sandgren, H. R., Zhai, Y., Lados, D. A., Shade, P. A., Schuren, J. C., Groeber, M. A., … Gavras, A. G. (2016). Characterization of fatigue crack growth behavior in LENS fabricated Ti-6Al-4V using high-energy synchrotron x-ray microtomography. *Additive Manufacturing*, *12*, 132–141. https://doi.org/10.1016/j.addma.2016.09.002

Sarrazin-Baudoux, C. (2003). Environmentally Influenced Fatigue Crack Path in Titanium Alloys. *Fatigue Crack Paths (Fcp 2003)*. Retrieved from http://www.gruppofrattura.it/index.php?option=com_docman&task=doc_download&gid=85&Itemid=228

Schijve, J. (2009). *Fatigue Structures and Materials* (2nd ed.). Amsterdam/North-East Polder, The Netherlands The: © 2009 Springer Science+Business Media, B.V.

Seifi, M., Dahar, M., Aman, R., Harrysson, O., Beuth, J., & Lewandowski, J. J. (2015). Evaluation of Orientation Dependence of Fracture Toughness and Fatigue Crack Propagation Behavior of As-Deposited ARCAM EBM Ti-6Al-4V. *Jom*, *67*(3), 597–607. https://doi.org/10.1007/s11837-015-1298-7

Seifi, M., Salem, A., Satko, D., Shaffer, J., & Lewandowski, J. J. (2017). Defect distribution and microstructure heterogeneity effects on fracture resistance and fatigue behavior of EBM Ti–6Al–4V. *International Journal of Fatigue*, *94*, 263–287. https://doi.org/10.1016/j.ijfatigue.2016.06.001

Semiatin, S. L., & Bieler, T. R. (2001). The effect of alpha platelet thickness on plastic flow during hot working of Ti-6Al-4V with a transformed microstructure. *Acta Materialia*, *49*(17), 3565–3573. https://doi.org/10.1016/S1359-6454(01)00236-1

Shrestha, S., & Chou, K. (2017). A build surface study of Powder-Bed Electron Beam Additive Manufacturing by 3D thermo-fluid simulation and white-light interferometry. *International Journal of Machine Tools and Manufacture*, *121*(February), 37–49. https://doi.org/10.1016/j.ijmachtools.2017.04.005

Soylemez, E., Beuth, J. L., & Taminger, K. (2010). Controlling Melt Pool Dimensions over a Wide Range of Material Deposition Rates in Electron Beam Additive Manufacturing. In *Proceedings 2010 Solid Freeform Fabrication Symposium* (pp. 571–582). https://doi.org/10.1007/s11837-016-2234-1

Svensson, M., & Ackelid, U. (2009). Titanium Alloys Manufactured with EBM - Mechanical and Chemical Properties. In *Proceedings from the Material @ Processes for Medical Devices Conference 2009* (pp. 189–194). Minneapolis, Minnesota, USA.

Takahashi, K., & Sato, E. (2010). Influence of Surface Treatments on Fatigue Strength of Ti6Al4V Alloy. *Materials Transactions*, *51*(4), 694–698. https://doi.org/10.2320/matertrans.MA200901

Tammas-Williams, S., Zhao, H., Léonard, F., Derguti, F., Todd, I., & Prangnell, P. B. (2015). XCT analysis of the influence of melt strategies on defect population in Ti-6Al-4V components manufactured by Selective Electron Beam Melting. *Materials Characterization*, *102*, 47–61. https://doi.org/10.1016/j.matchar.2015.02.008

Tan, X., Yihong, K., Tor, S. B., & Chua, C. K. (2014). Application of electron beam melting (EBM) in additive manufacturing of impller. In *Proceedings of the International Conference on Progress in Additive Manufacturing* (pp. 193–201). https://doi.org/10.3850/978-981-09-0446-3

Tang, H. P., Qian, M., Liu, N., Zhang, X. Z., Yang, G. Y., & Wang, J. (2015). Effect of Powder Reuse Times on Additive Manufacturing of Ti-6Al-4V by Selective Electron Beam Melting. *Jom*, *67*(3), 555–563. https://doi.org/10.1007/s11837-015-1300-4

Thijs, L., Verhaeghe, F., Craeghs, T., Humbeeck, J. Van, & Kruth, J. P. (2010). A study of the microstructural evolution during selective laser melting of Ti-6Al-4V. *Acta Materialia*, *58*(9), 3303–3312. https://doi.org/10.1016/j.actamat.2010.02.004

Tudose, L. M., & Popa, C. O. (2016). Stress intensity factors analysis cracks in the hertzian stresses field of teeth gears. In *The 10th International Conference on Tribology*. Bucharest, Romania.

Wang, D., Wu, S., Fu, F., Mai, S., Yang, Y., Liu, Y., & Song, C. (2017). Mechanisms and characteristics of spatter generation in SLM processing and its effect on the properties. *Materials and Design*, *117*, 121–130. https://doi.org/10.1016/j.matdes.2016.12.060

Wu, M. W., Lai, P. H., & Chen, J. K. (2016). Anisotropy in the impact toughness of selective laser melted Ti-6Al-4V alloy. *Materials Science and Engineering A*, *650*, 295–299. https://doi.org/10.1016/j.msea.2015.10.045

Yan, M., Dargusch, M. S., Ebel, T., & Qian, M. (2014). A transmission electron microscopy and three-dimensional atom probe study of the oxygen-induced fine microstructural features in as-sintered Ti-6Al-4V and their impacts on ductility. *Acta Materialia*, *68*, 196–206. https://doi.org/10.1016/j.actamat.2014.01.015

Yasa, E., Deckers, J., Kruth, J.-P., Rombouts, M., & Luyten, J. (2010). Charpy impact testing of metallic selective laser melting parts. *Virtual and Physical Prototyping*, *5*(2), 89–98. https://doi.org/10.1080/17452751003703894

Yunlian, Q., Ju, D., Quan, H., & Liying, Z. (2000). Electron beam welding, laser beam welding and gas tungsten arc welding of titanium sheet. *Materials Science and Engineering A*, *280*(1), 177–181. https://doi.org/10.1016/S0921-5093(99)00662-0

Zäh, M. F., & Lutzmann, S. (2010). Modelling and simulation of electron beam melting. *Production Engineering*, *4*(1), 15–23. https://doi.org/10.1007/s11740-009-0197-6

Zhai, Y., Galarraga, H., & Lados, D. A. (2015). Microstructure Evolution, Tensile Properties, and Fatigue Damage Mechanisms in Ti-6Al-4V Alloys Fabricated by Two Additive Manufacturing Techniques. *Procedia Engineering*, *114*, 658–666. https://doi.org/10.1016/j.proeng.2015.08.007

Zhai, Y., Lados, D. A., Brown, E. J., & Vigilante, G. N. (2016). Fatigue crack growth behavior and microstructural mechanisms in Ti-6Al-4V manufactured by laser engineered net shaping. *International Journal of Fatigue*, *93*, 51–63. https://doi.org/10.1016/j.ijfatigue.2016.08.009

Zhong, Y., Rännar, L. E., Liu, L., Koptyug, A., Wikman, S., Olsen, J., … Shen, Z. (2017). Additive manufacturing of 316L stainless steel by electron beam melting for nuclear fusion applications. *Journal of Nuclear Materials*, *486*, 234–245. https://doi.org/10.1016/j.jnucmat.2016.12.042

Zhou, X., Wang, D., Liu, X., Zhang, D. D., Qu, S., Ma, J., … Liu, W. (2015). 3D-imaging of selective laser melting defects in a Co-Cr-Mo alloy by synchrotron radiation micro-CT. *Acta Materialia*, *98*, 1–16. https://doi.org/10.1016/j.actamat.2015.07.014

Li, Qizhen., Chen, Edward Y., Bice, Douglas R., Dunand, David C. (2008). Mechanical properties of cast Ti-6Al-4V lattice block structures. *Metallurgical and Materials Transactions A: Physical Metallurgy and Materials Science*.

Yasa, E., Deckers, J., Kruth, J.-P., Rombouts, M., Luyten, J. (2010). *4th International Conference on Advanced Research in Virtual and Physical Prototyping, VRAP 2009.*
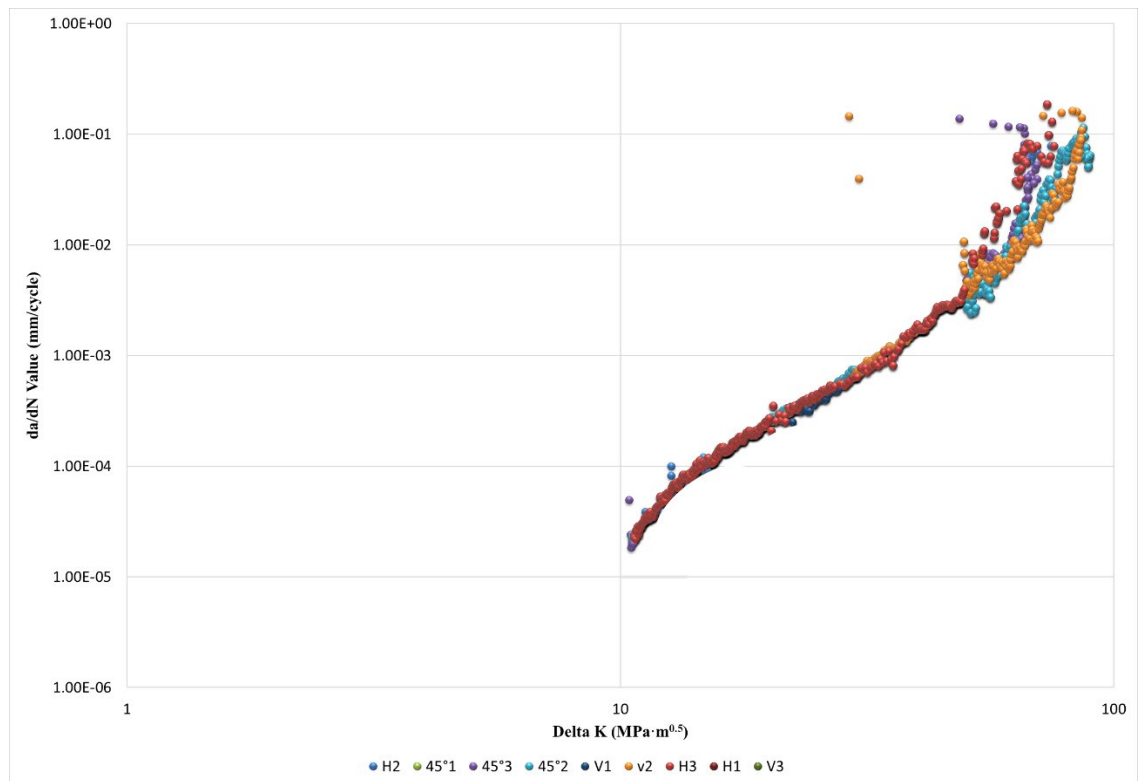
Appendix

Figure 8-1 FCG of nine vertical, 45° and horizontal samples